

NORTHWESTERN UNIVERSITY

Manipulating Light-Matter Interactions with Plasmonic Nanoparticle Lattices

A DISSERTATION

**SUBMITTED TO THE GRADUATE SCHOOL
IN PARTIAL FULFILLMENT OF THE REQUIREMENTS**

For the degree of

DOCTOR OF PHILOSOPHY

Field of Applied Physics

by

Danqing Wang

EVANSTON, ILLINOIS

June 2019

© Copyright by Danqing Wang 2019

All Rights Reserved

ABSTRACT

Manipulating Light-Matter Interactions with Plasmonic Nanoparticle Lattices

Danqing Wang

Rationally assembled nanostructures exhibit distinct physical and chemical properties beyond their individual units. The development of nanofabrication tools enables precise structural defining of nanomaterials scalable to large areas. This dissertation focuses on plasmonic nanoparticle arrays that show unique diffractive coupling with lattice spacings engineered close to the wavelength of light. Collectively coupled plasmonic nanoparticles induce sharp, intense lattice plasmon resonances upon optical excitations compared to the broad resonances of individual nanoparticles, and the electromagnetic fields are strongly enhanced and localized near the sub-wavelength vicinity of the nanoparticles. By harnessing different lattice structural designs and materials systems, various light-matter interactions can be engineered including nanoscale lasing, nonlinear optics, and quantum optics. The structured plasmonic nanoparticle lattices can serve as a versatile, scalable platform for enhanced photochemistry, large-scale quantum optics and nontrivial topological photonics.

The first half of the thesis describes the structural engineering of plasmonic nanocavity arrays for various functionalities in nanoscale lasing. Integrated with organic dye molecules, high-quality band-edge lattice plasmons (quality factor > 200) can contribute to single-mode lasing at room-temperature with directional emission. Beyond the dipolar lattice plasmons, Chapter 2 discusses a robust, stretchable nanolaser platform that can preserve its high mode quality under strain based on hybrid quadrupole lattice plasmons as a new lasing feedback mechanism. Chapter 3 describes multi-scale plasmonic superlattices can support multiple band-edge modes capable of multi-modal

nanolasing at programmed emission wavelengths and with large mode spacings. Chapter 4 introduces the scaling behaviors for lasing from plasmonic nanocavity arrays, where the number of nanoparticles in plasmonic nanocavity arrays plays a critical role in lasing action in terms of ultrafast dynamics and lasing thresholds.

In the final two chapters, we discussed the light-matter interactions between plasmonic nanocavities and photo-active materials systems beyond dye molecules. Chapter 5 covers continuous-wave upconverting lasing at room temperature with record-low thresholds and high photostability by integrating $\text{Yb}^{3+}/\text{Er}^{3+}$ -co-doped upconverting nanoparticles with Ag nanopillar arrays. Chapter 6 discusses the emerging applications of plasmonic nanocavity arrays in nonlinear optics, quantum optics and topological photonics. Second harmonic generation signal was greatly increased up to 450 times by the propagating lattice plasmons. Quantum emitters in 2D hexagonal boron nitride can be deterministically coupled to plasmonic nanocavity arrays with preserved single photon emission. The delocalized lattice plasmons can also serve a versatile platform for long-range quantum entanglement and parity-time symmetric nanophotonics.

ACKNOWLEDGEMENTS

I would like to start by thanking my advisors, Professor Teri W. Odom and Professor George C. Schatz for their dedicated, great mentoring in the past six years. Teri and George are always supportive and provide plenty of resources and significant freedom in pursuing various exciting projects. Teri always encourages me to challenge myself and step outside of my comfort zone for more creative ideas and effective delivery. Her rigorous training in writing and presenting will benefit my research in the longer term. George is passionate and knowledgeable on an unbelievably wide range of research areas. The fruitful discussions I had with him inspired me to solve many of the theoretical challenges in the past. The co-advising opportunity expanded the research scopes and deepened my understanding of experiments and theory. Both Teri and George are the role models for me towards being an independent researcher. I could not imagine a better place for doing graduate research without them.

I would like to acknowledge my Ph.D. thesis and proposal committee members - Professor Koray Aydin, Professor Hooman Mohseni, Professor Richard D. Schaller, Professor Pulak Dutta - for their critical reviews and insightful advice on my research work. I also appreciated much the advice from Professor Lin X. Chen on deciding on graduate school. I would like to thank my undergraduate advisors Professor Tao Li and Professor Shining Zhu, who offered me research opportunities during my junior and senior years at Nanjing University, which inspired my enthusiasm in science and research.

I want to thank my collaborators, who have made many of the current projects possible. The research groups are from both inside and outside of Northwestern, including those led by Professor Peter J. Schuck from Columbia University, Professor Richard D. Schaller from Argonne National

Lab, Professor Igor Aharonovich from University of Technology Sydney, Professor Ventsislav K. Valev from University of Bath, Professor Bruce E. Cohen and Professor Emory M. Chan from Lawrence Berkeley National Laboratory. I would like to thank my collaborators Dr. Angel Fernandez-Bravo, Dr. Toan Trong Tran, Dr. Zai-Quan Xu, Dr. Ayelet Teitelboim, Dr. Cheryl Tajon, and David C. Hooper for their significant contributions. I enjoyed many of our Skype and on-site meetings in the past for brainstorming ideas.

I would like to thank all the Odom group and Schatz groups members both past and present, who provide a motivating and enjoyable environment for me. I am grateful to Dr. Ankun Yang, Dr. Montacer Dridi, Dr. Alexander J. Hryn, and Dr. Yi Hua, who provided tremendous help when I started my research, and Dr. Wei Zhou and Dr. Joel Henzie, who initiated the plasmon lasing and multi-scale patterning projects in the Odom group. I would like to acknowledge the other coworkers that contributed to my projects and allowed me to work together on theirs: Marc R. Bourgeois, Dr. Weijia Wang, Dr. Michael P. Knudson, Dr. Jingtian Hu, Dr. Yuanhai Lin, Dr. Xianyu Ao, Dr. Jianxi Liu, Dr. Won-Kyu Lee, Dr. Ahmad Fumani, Dr. Dhara J. Trivedi, Ran Li and Jun Guan. I want to thank Lindsay Haukebo and Lisa Gugwor for their great administrative help. I also want to thank Dr. Claire Deeb, Dr. Jun Yue, Dr. Jian Zhang, Tingting Liu, Dongjoon Rhee, Thaddeus Reese, Dr. Shikai Deng, Nicolas Watkins, Priscilla Choo, Xitlali Juarez and Alexander Sample for enjoyable time in the group.

Finally, I would like to show gratitude to my family and friends. My father Wenxian Wang and mother Hongjuan Li have always been there, providing their unconditioned love and support to me in pursuing my dream. They accompanied me through the good time and the bad, and are my strongest motivators and the biggest comfort. I also want to thank my friends, who have brought me a beautiful and colorful life besides research. Thank you all.

List of Abbreviations

SPP	Surface Plasmon Polariton
LSP	Localized Surface Plasmon
NP	Nanoparticle
DL	Dipole Lattice Plasmons
HQL	Hybrid Quadrupole Lattice Plasmons
Q-Factor	Quality Factor
CDA	Coupled Dipole Approximation
RA	Raley Anomaly
FWHM	Full Width at Half Maximum
TE	Transverse Electric
TM	Transverse Magnetic
SEM	Scanning Electron Microscopy
LDOS	Local Density of States
FDTD	Finite-difference Time-domain
PEP	Pauli Exclusion Principle
PSP	Phase-Shifting Photolithography
PEEL	PSP + Etching + Electron-beam evaporation + Lift-off
SANE	Solvent Assisted Nanoscale Embossing
PDMS	Poly(dimethylsiloxane)
CW	Continuous-wave
UCNP	Upconverting Nanoparticles

NIR	Near-Infrared
SHG	Second Harmonic Generation
2D	Two-Dimensional
hBN	Hexagonal Boron Nitride
PT	Parity-Time

Table of Contents

ABSTRACT.....	3
ACKNOWLEDGEMENTS.....	5
List of Abbreviations	7
List of Figures.....	12
Chapter 1. Introduction on Plasmonic Nanocavity Array	26
1.1 Principles of Ultra-sharp Lattice Plasmons.....	27
1.2 Sub-wavelength Plasmon Lasing.....	30
1.2.1 Small lasers	30
1.2.2 Nanoscale Lasing from Sub-wavelength Plasmons.....	32
1.2.3 Lasing from Spaser Nanoparticle Arrays.....	35
1.2.4 Semi-quantum Modeling of Nanoscale Lasing.....	40
1.3 Parity-time Symmetric Photonics and Quantum Optics.....	42
1.4 Scope of This Thesis.....	46
Chapter 2. Stretchable Lasing from Hybrid Quadrupole Plasmons	48
2.1 Introduction.....	49
2.2 Hybrid Quadrupole Plasmons from Engineered Nanoparticle Size	50
2.3 Stretchable Lasing from Au Nanoparticle Arrays	60
2.4 Semi-quantum Modeling of Plasmon Nanolasing Buildup	62
2.5 Summary and Outlook	64
Chapter 3. Structural Engineering in Plasmonic Superlattices	65
3.1 Introduction.....	67
3.2 Multiscale Patterning of Superlattice Arrays.....	69
3.3 Superlattice Plasmons in Hierarchical Arrays	71
3.4 Controlled Multi-modal Nanolasing from Plasmonic Superlattices.....	79
3.5 Band-edge Engineering from Structural Designs	98

	10
3.5.1 2D Superlattice Arrays.....	98
3.5.2 Symmetry-breaking Superlattice Line Patches	101
3.6 Microscale Superstrate Molding of Plasmonic Nanoparticle Arrays	108
3.7 Summary and Outlook	114
Chapter 4. Scaling Behavior for Lasing from Plasmonic Nanocavity Arrays	115
4.1 Introduction.....	116
4.2 Narrowed Lattice Plasmons with Increased Nanoparticle Number	117
4.3 Scaling Behavior for Lasing from Finite-sized Nanocavity Arrays	119
4.4 Summary and Outlook	121
Chapter 5. Continuous-wave Upconverting Plasmon Nanolasing	123
5.1 Introduction.....	124
5.2 Low-threshold Upconverting Nanolasing.....	126
5.3 Upconverting Lasing under Pulsed Pumps.....	135
5.4 Six-level System for Modeling Upconverting Lasing	138
5.5 Summary and Outlook	141
Chapter 6. Emerging Applications of Strongly Coupled Nanocavities.....	142
6.1 Enhanced Second Harmonic Generation from Propagating Lattice Plasmons.....	142
6.1.1 Introduction.....	144
6.1.2 Determined SHG enhancement from lattice plasmons.....	146
6.1.3 Enhanced SHG quadrupolar contributions from gold Nanoparticle arrays	157
6.2 Deterministic Coupling of Quantum Emitters to Plasmonic Nanocavity Arrays	163
6.2.1 Introduction.....	163
6.2.2 Enhanced Single-photon Emission by Plasmonic Nanocavities.....	164
6.3 Topology and Parity-time Symmetry in Plasmonics	174
6.3.1 Introduction.....	174
6.3.2 Mode Splitting in Stacked Plasmonic Nanoresonator Arrays.....	175

6.3.3 Parity-time Symmetry with Spatial Engineering of Gain and Loss.....	179
6.4 Summary and Outlook	180
Reference	181
CV (Danqing Wang).....	196

List of Figures

Figure 1.1. Surface plasmons in metals. (a) Surface plasmon polariton from a thin metal film. (b) Localized surface plasmons from metal NPs.....	27
Figure 1.2. Lattice plasmons with sharp resonances in periodic metal nanoparticle arrays. (a) Large-scale fabrication of plasmonic NP arrays by soft photolithography process. (b) Experimental demonstration of sharp lattice plasmon resonances from gold nanorod arrays. (c) Simulated extinction spectra of a 1D chain of silver nanoparticles with varying spacings by coupled dipole method.....	29
Figure 1.3. A conventional laser supporting Fabry-Pérot modes between two end mirrors (length L) and gain medium inside the cavity.	31
Figure 1.4. Development timeline of plasmon nanolasers. (a) The first plasmon laser using SPP modes as optical feedback for lasing at cryogenic temperatures, including CdS semiconducting nanowires on a silver film separated by a MgF ₂ layer. (b) Plasmon laser operated at room temperature with CdS nanosquares on a Ag film separated by a MgF ₂ layer. (c) Plasmon nanolaser using epitaxially grown silver film for lower lasing threshold. (d) The first theoretical study of spaser arrays for directional emission using split-ring resonators at mid-infrared wavelengths. (e) The first experimental realization of directional emission from spaser NP arrays at near-infrared wavelengths. (f) Plasmonic superlattice arrays with controlled multi-modal nanolasing. (g) Timeline of plasmon nanolasers.	33
Figure 1.5. Array coupling for directional emission in various plasmonic unit cell designs. (a) Directional lasing from asymmetric split-ring resonator arrays on a gain medium slab. (b) Directional lasing from a metal hole array on a semiconductor layer. (c) Unidirectional lasing from template-stripped 2D plasmonic crystals consisting of gold NP arrays on a gold film. Figures adapted with permission.	36
Figure 1.6. Directional lasing from spaser NP arrays. (a) Scheme of a laser device including gold NP arrays embedded in liquid or solid-state gain media. (b) Calculated optical band structure.	

(c) Simulated phase profile at lattice plasmon resonances. **(d-e)** Power dependent lasing emission and input-power output-intensity curves. **(f)** Far-field beam profile with a highly directional lasing spot.37

Figure 1.7. Real-time tunable nanolasing from plasmonic nanoparticle arrays by refreshing liquid dye solutions. **(a)** Scheme of a lasing device consisting of gold NP arrays sandwiched between liquid dye solutions and a glass coverslip. **(b)** Statically tuned lasing wavelengths can span the entire emission bandwidth of the dye. **(c)** Scheme of the dynamic laser with a microfluidic channel. **(d)** Continuous shifting of lasing emission to longer wavelengths and then back to shorter wavelengths.39

Figure 1.8. Modeling of nanoscale energy transfer with semi-quantum four-level system for lasing action. **(a)** Scheme of the energy transfer process from four-level gain media to lattice plasmon resonances in spaser NP arrays. **(b)** Calculated distribution maps of spontaneous transition rate (left) and stimulated transition rate (right) in the middle plane of NP arrays below threshold (top) and above threshold (bottom).41

Figure 1.9. Modeling of nanoscale energy transfer with semi-quantum four-level system for lasing action. **(a)** Scheme of a pair of coupled whispering-galley-mode resonators with gain in one ring. **(b)** Collapsing of two eigenstates to a single mode after exceptional point by tuning the coupling coefficient. **(c)** Experimentally observed unidirectional transmission for PT-symmetric microresonators at the symmetry-broken phase.44

Figure 2.1. Stretchable nanolasing from hybrid quadrupole lattice plasmons (HQLs) in metal nanoparticle (NP) arrays. **(a)** Scheme of out-of-plane HQL oscillations that are robust to lateral lattice changes. **(b)** Scheme of a wavelength tunable nanolaser with strain ε applied on the elastomeric substrate.50

Figure 2.2. Asymmetric charge distributions along z suggest a non-zero dipole momentum at HQL resonance. **(a)** Simulated charge distribution of Au NPs in an array with diameter $d = 260$ nm, spacing $a_0 = 600$ nm and height $h = 120$ nm. **(b)** Simulated charge distribution of Au NPs in an array with diameter $d = 300$ nm, spacing $a_0 = 600$ nm and height $h = 120$ nm.52

Figure 2.3. Sharp HQL resonance in arrays of large Au NPs. (a) SEM image of large Au NP arrays on glass with lattice spacing $a_0 = 600$ nm and measured transmission spectra with different NP height h . (b) Simulated charge distribution of HQL mode for cylinder NP arrays (diameter $d = 260$ nm and height $h = 120$ nm). (c) Decomposition of transmission spectrum into dipolar and quadrupolar contributions based on coupled dipole-quadrupole method with a simplified spherical NP array ($d = 260$ nm and refractive index $n = 1.44$).53

Figure 2.4. Spectral overlap between electric dipole lattice resonance and HQL increases with sphere diameter. (a) Decomposition of extinction spectrum to quadrupole and dipole contributions for spherical Au NP arrays with diameter $d = 260$ nm and, (b) $d = 300$ nm with refractive index $n = 1.44$. Notably, the width of the lattice plasmon resonance is determined by the imaginary part of $(1/\alpha_{NP} - S)$, which becomes larger on the blue side of the spectrum for the dipole resonance.55

Figure 2.5. Quadrupole and dipole localized surface plasmons both exist in large single Au NPs. (a) Scattering cross section spectra of a single Au NP with $d = 260$ nm and $h = 120$ nm. (b) The near-field and charge distributions at the quadrupole localized surface plasmon (top) and the dipole localized surface plasmon (bottom).56

Figure 2.6. Sharp HQL resonance in arrays of large Au NPs robust to lateral stretching. (a) The scheme for depositing Au NPs on top of soft PDMS with a Au hole film mask. (b) The cross-section height profile of patterned Au NPs on PDMS. (c) Photograph of a flexible laser device loaded onto a stretching apparatus. The edges of the PDMS slab were stretched uniaxially with control over the applied strain. (d) Photograph of the patterned Au NP arrays on PDMS. The AFM image and cross-sections can be found in Figure S8. (e) Wavelength tunable HQL modes under strain $\varepsilon = 0-0.05$57

Figure 2.7. Distinct out-of-plane standing waves were preserved at the band-edge state under stretching. (a-b) Measured and simulated dispersion diagrams of large Au NP arrays on glass under TE polarization with $a_0 = 600$ nm, $d = 260$ nm $h = 120$ nm and $n = 1.44$. (c-d) Near-field (E_z , with units of V/m) and phase distributions ($\Phi(E_z)$, with units of rad) at the band-edge HQL mode under strains $\varepsilon = 0$ and 0.1.58

Figure 2.8. Multiple resonant modes exist simultaneously in large Au NP arrays. (a) Simulated optical band structures under TE polarization. **(b)** Charge distributions at resonances denoted in panel a.59

Figure 2.9. Nanolasing from HQL cavity resonance showed localized build-up at the plasmonic hot spots. (a) Scheme of the lasing detection where emission was collected normal to the sample surface. **(b)** Simulated near-field enhancement $|E|^2$ confined around plasmonic hot spots at HQL mode with units of V^2m^{-2} . **(c)** Measured emission spectra with increased pump power for Au NP arrays on glass (dye concentration 3 mM). **(d)** Spatial distribution of spontaneous emission rate (N_2/τ_{21}) and stimulated emission rate $\frac{1}{\hbar\omega}E\frac{dP}{dt}$ when lasing occurred with units of $s^{-1}m^{-3}$60

Figure 2.10. Reversibly tunable nanolasing from HQL mode by stretching and releasing the elastomeric substrate. Measured reversible, tunable nanolasing under strain $\varepsilon = 0.02-0.05$61

Figure 2.11. Reversibly tunable nanolasing from HQL mode by stretching and releasing the elastomeric substrate. (a) Scheme of the energy transfer process from four-level gain media to lattice plasmon resonances in metal NP arrays. **(b)** Simulated tunable lasing emission from HQL resonance with a fixed pump power under strain $\varepsilon = 0.02-0.05$. **(c)** Simulated near-field enhancement $|E|^2$ confined around plasmonic hot spots at HQL mode, with units of V^2m^{-2} . **(d)** Spatial distribution of spontaneous emission rate (N_2/τ_{21}) and stimulated emission rate $\frac{1}{\hbar\omega}E\frac{dP}{dt}$ when lasing occurred, with units of $s^{-1}m^{-3}$63

Figure 3.1. Scheme of the multiscale patterning technique. Typical NP periodicity $a_0 = 600$ nm, patch side length $l = 6$ μm and patch periodicity $A_0 = 9$ μm70

Figure 3.2. Comparison of transmission spectra between infinite arrays and 2D hierarchical Au NP arrays. (a) SEM images of an infinite NP array with NP periodicity $a_0 = 600$ nm and NP diameters d around 140 nm. **(b)** SEM images of 2D hierarchical NP arrays with $a_0 = 600$ nm, patch side length $l = 6$ μm , patch periodicity $A_0 = 9$ μm and NP $d = 140$ nm.72

Figure 3.3. Orientation-dependent transmission properties of 1D Au NP patches. (a) SEM image of fabricated 1D Au NP patches on top of glass, with patch side length $l = 6$ μm , patch

periodicity $A_0 = 9 \mu\text{m}$ along x and NP diameter $d = 160 \text{ nm}$. **(b)** Evolution of transmission spectrum with increasing polarization angle θ from 0° (x direction) to 90° (y direction).74

Figure 3.4. Far-field transmission, near-field electric field, and charge distribution of hierarchical Au NP arrays indicating the origin of superlattice plasmons. **(a)** Linear optical properties of a single NP, a single patch, and periodic patches with the same NP diameter $d = 160 \text{ nm}$, height $h = 50 \text{ nm}$ and spacing $a_0 = 600 \text{ nm}$. Periodic patches had side length $l = 6 \mu\text{m}$ and periodicity $A_0 = 9 \mu\text{m}$. **(b)** Near-field electric field distributions of superlattice plasmons at $\lambda_{\text{SL}}^{15} = 944 \text{ nm}$, $\lambda_{\text{SL}}^{14} = 981 \text{ nm}$, and $\lambda_{\text{SL}}^{13} = 1056 \text{ nm}$ within plotted area of $1.2 \mu\text{m} \times 9 \mu\text{m}$. **(c)** Charge distribution of superlattice plasmons at $\lambda_{\text{SL}}^{15} = 944 \text{ nm}$ and $\lambda_{\text{SL}}^{14} = 981 \text{ nm}$ within plotted area of $1.2 \mu\text{m} \times 9 \mu\text{m}$75

Figure 3.5. Superlattice plasmons in hierarchical Au NP arrays can be tuned by varying patch periodicity A_0 and side length l . **(a)** Experimental and simulated linear properties of hierarchical arrays with $l = 6 \mu\text{m}$, $A_0 = 12 \mu\text{m}$ and $d = 140 \text{ nm}$. **(b)** Experimental and simulated linear properties of hierarchical arrays with $l = 18 \mu\text{m}$, $A_0 = 24 \mu\text{m}$ and $d = 140 \text{ nm}$. **(c)** Experimental and simulated linear properties of hierarchical arrays with $l = 18 \mu\text{m}$, $A_0 = 36 \mu\text{m}$ and $d = 140 \text{ nm}$78

Figure 3.6. Multi-modal nanolasing in gold nanoparticle superlattices surrounded by liquid dye solutions. Schemes, SEM images and measured lasing emission from **(a)** NP superlattices with NP spacing $a_0 = 600 \text{ nm}$, NP diameter $d = 120 \text{ nm}$, height $h = 50 \text{ nm}$, patch side length $l = 18 \mu\text{m}$ and patch periodicity $A_0 = 24 \mu\text{m}$ embedded in IR-140-DMSO (concentration $C = 0.6 \text{ mM}$) and **(b)** single-lattice arrays with the same NP diameter $d = 120 \text{ nm}$, height $h = 50 \text{ nm}$ and spacing $a_0 = 600 \text{ nm}$ as superlattices in (a).80

Figure 3.7. Multiple band-edge modes are observed in the band structures of plasmonic NP superlattices. Measured (left) and simulated (right) band structures in gold NP superlattices with $l = 18 \mu\text{m}$, $A_0 = 24 \mu\text{m}$, and $d = 125 \text{ nm}$ under **(a)** unpolarized light, **(b)** TE polarized light, and **(c)** TM polarized light.83

Figure 3.8. Light excited at off-normal angles can couple to NP superlattices and form standing waves.84

Figure 3.9. Only lower-energy band-edges appear in single-lattice gold NP arrays with two orders stronger near-field enhancement compared with dielectric NPs.86

Figure 3.10. Experiments and simulations of band-edge modes at zero and non-zero wavevectors supporting standing waves for multi-modal nanolasing. (a) Measured band structure of two-dimensional (2D) superlattice arrays. (b) Measured angle-resolved emission of multi-modal lasing, with emission signals collected within $\pm 3.5^\circ$ relative to the sample surface normal. (c) Satellite spots around a central spot were detected in the far-field beam profile, where the center represented $\theta_D = 0^\circ$ along x and y88

Figure 3.11. Single mode lasing from band-edge state at $k_{//} = 0$ in single-lattice arrays. (a) (left) Measured band structure with varying incident angle θ_i in single-lattice arrays; (middle) simulated band structure based on FDTD Lumerical method with $a_0 = 600$ nm and $d = 120$ nm; (right) emission map of lasing from a single band-edge mode. (b) Superlattice arrays with $A_0 = 24$ μm , $l = 18$ μm , and $d = 120$ nm.89

Figure 3.12. Multiple lasing beams showed minor divergence in the far field and angle-resolved emission along x and y identified the wavelength distribution. (a) Far-field beam profiles from single-lattice arrays with plotted area 6.2 mm \times 4.8 mm at detection distance $z = 4$ cm, 5 cm, and 6 cm away from the sample plane. (b) Far-field beam profiles from superlattices ($l = 18$ μm , $A_0 = 24$ μm) under TE polarization. (c) Angle-resolved emission under TE polarization (d) Angle-resolved emission under TM polarization.90

Figure 3.13. Both four-level one-electron systems without and with the Pauli exclusion principle can describe lasing action in single-lattice arrays with population inversion in real-time. (a) Lasing from FDTD method with the PEP at pump 0.37 mJ cm^{-2} and (b) corresponding real-time population inversion. (c) Lasing from FDTD method without PEP at the same pump power range and (d) corresponding real-time population inversion.92

Figure 3.14. Multi-modal nanolasing was observed in simulations from 2D plasmonic superlattices above lasing threshold. (a) Lasing spectra from band-edges at (upper panel) $k_{//} = 0$, (middle panel) $k_{//} = \pm 0.13$ μm^{-1} , and (lower panel) $k_{//} = \pm 0.26$ μm^{-1} by FDTD simulations. (b) Simulated lasing spectrum from 2D superlattices (patch side length $l = 18$ μm , periodicity $A_0 = 24$

μm , NP size $d = 120 \text{ nm}$) slightly above lasing threshold at 0.11 mJ cm^{-2} and (c) above lasing threshold at 0.26 mJ cm^{-2}93

Figure 3.15. Multi-modal nanolasing from plasmonic superlattices with controlled output behaviors and spatial coherence.

(a) Measured output profiles of multi-modal lasing with dye concentration and increased pump power at $0.2\text{-}0.8 \text{ mJ cm}^{-2}$ for 2D superlattices with $d = 120 \text{ nm}$. (b) Experimental threshold curve of multi-modal lasing with $d = 120 \text{ nm}$. (c) (left panel) Experimental and (right panel) simulated output behaviors of $\lambda_{\text{SL}}^{\text{I}}$ and $\lambda_{\text{SL}}^{\text{III}}$ with $d = 120 \text{ nm}$. Experimental data are a zoom-in of (b). (d) Output profiles of larger NP size $d = 125 \text{ nm}$ with increased pump power at $0.3\text{-}0.6 \text{ mJ cm}^{-2}$. (e) Experimental threshold curve of multi-modal lasing with $d = 125 \text{ nm}$. (f) (left panel) Experimental and (right panel) simulated output behaviors of $\lambda_{\text{SL}}^{\text{I}}$ and $\lambda_{\text{SL}}^{\text{III}}$ with $d = 125 \text{ nm}$96

Figure 3.16. Modulation of the ultrafast decay dynamics of multi-modal lasing by micron patch-patch coupling.

Time-correlated single-photon counting of multi-modal lasing from NP superlattice arrays at (a) 0.03 mJ cm^{-2} , (b) 0.38 mJ cm^{-2} , and (c) single-lattice NP arrays at 0.30 mJ cm^{-2} (2 kHz, 800-nm fs-pulsed laser).97

Figure 3.17. Plasmonic NP superlattices with arbitrary geometric parameters can be fabricated by multiscale patterning.

(a) $l = 18 \mu\text{m}$, $A_0 = 24 \mu\text{m}$ arrays. (b) $l = 12 \mu\text{m}$, $A_0 = 18 \mu\text{m}$ arrays. (c) $l = 18 \mu\text{m}$, $A_0 = 36 \mu\text{m}$ arrays. (d) $l = 18 \mu\text{m}$, $A_0 = 24 \mu\text{m}$ line patches.99

Figure 3.18. Spectral spacing of band-edge lasing modes can be manipulated by varying patch periodicities.

(a) SEM images of superlattice array with $(l, A_0) = (12 \mu\text{m}, 18 \mu\text{m})$, $(l, A_0) = (18 \mu\text{m}, 24 \mu\text{m})$ and $(l, A_0) = (18 \mu\text{m}, 36 \mu\text{m})$ (from top to bottom). (b) Measured band structure of superlattice arrays under TE polarization with spectral spacing of band-edges at 14 nm, 11 nm, and 7 nm. (c) Controlled lasing spacing from band-edge modes. Dashed lines depict the outline of the patches.100

Figure 3.19. Dynamic control of band-edge modes in symmetry-broken plasmonic line patches leading to switchable nanolasing between single and multiple modes.

(a) Scheme of lasing measurement on NP line patches with the same $a_0 = 600 \text{ nm}$, $l = 18 \mu\text{m}$ and $A_0 = 24 \mu\text{m}$ along x as in 2D superlattice arrays. (b) Orientation-dependent lasing under TE polarization. \mathbf{e}_{line}

and \mathbf{e}_{pump} represent the directions of line axis and pump polarization, respectively. (c) Angle-resolved mapping of lasing emission by sweeping θ_x with (upper panel) $\mathbf{e}_{\text{line}} \perp \mathbf{e}_{\text{pump}}$ and (lower panel) $\mathbf{e}_{\text{line}} // \mathbf{e}_{\text{pump}}$. (d) Far-field beam profiles from line patches under in-plane rotation of the sample.103

Figure 3.20. Dynamical tuning of band structure in NP line patches by sample orientation.

Measured band structures of NP line patches with \mathbf{e}_{line} oriented at (a) 0° (x direction), (b) 30° , (c) 45° , (d) 60° , and (e) 90° (y direction).104

Figure 3.21. Switching between multiple and single lasing modes is detected in simulation of line patches with population inversion distributed at dipolar hot-spots.105

Figure 3.22. Polarization of output lasing emission was aligned with polarization of pump source.

(a) Angle-resolved PL emission map from line patches with \mathbf{e}_{pump} along y and \mathbf{e}_{line} along y , and (b) \mathbf{e}_{pump} along y and \mathbf{e}_{line} along x . (c) Measured multiple lasing modes from line patch with \mathbf{e}_{pump} along y , and \mathbf{e}_{line} orientated along y , and (d) \mathbf{e}_{pump} along y and \mathbf{e}_{line} orientated along x106

Figure 3.23. Orientation-dependent and polarization-dependent lasing were observed in NP line patches.

Measured switchable lasing from line patches with (a) pump polarization direction \mathbf{e}_{pump} and line axis \mathbf{e}_{line} both along x , (b) \mathbf{e}_{pump} along x and \mathbf{e}_{line} along y , (c) \mathbf{e}_{pump} along y and \mathbf{e}_{line} along x , and (d) \mathbf{e}_{pump} and \mathbf{e}_{line} both along y107

Figure 3.24. Microscale superstrate molding of plasmonic NP arrays.

(a) Large scale superstrate patterning on Au NP arrays (b) The optical images of patterned superstrate with (6 μm , 9 μm) line patches and (12 μm , 18 μm) 2D arrays.109

Figure 3.25. Superlattice plasmons from patterned superstrate on NPs.

(a) Superlattice modes from patterned superstrate, (b) superlattice modes from spaced patches.110

Figure 3.26. Polarization-dependent linear properties for symmetry-breaking line patches.

(a) Superlattice resonance from molded line patches when the light was polarized parallel to the line axis, (b) single-lattice resonance when the light was polarized perpendicular to the line axis.112

Figure 3.27. Tunable superlattice modes from flexible micro-photoresist molding.113

Figure 4.1. Lattice plasmons showed stronger resonances with increasing NP numbers in a finite-sized patch. (a) Scheme of infinite NP arrays to finite-sized NP arrays with spacing $a_0 = 600$ nm. (b) Simulated spectra of lattice plasmons in a single patch showed narrowed resonances with increased NP number N . (c) Near-field enhancement $|E|^2$ with increased N in a patch from 10×10 , 30×30 to 50×50117

Figure 4.2. Sharper lattice plasmons were detected in experiments with increased NP numbers. (a) Optical setups of a dark-field microscope for imaging and spectroscopy. (b) Image of single patches with side length $l = 18$ μm and patch spacing $A_0 = 180$ μm under the microscope and the detection with an inserted slit. (c) Measured transmission spectra from single patches with varying N118

Figure 4.3. Lasing action from single patches of plasmonic nanoparticles. (a-b) Measured single lasing mode from a plasmonic lattice with patch size and patch spacing $(l, A_0) = (12$ $\mu\text{m}, 18$ $\mu\text{m})$ and $(18$ $\mu\text{m}, 180$ $\mu\text{m})$, respectively. (c) The optical set-up with objective lens of beam focusing, and the input-output curves for the single plasmonic NP patches.119

Figure 4.4. Lasing emission intensity and ultrafast dynamics depend strongly on NP number N within a single patch from simulations. (a) Set-up of FDTD simulation scheme. (b) N -dependent lasing build-up with a constant pump power of 0.9 mJ/cm^2 . (c) Time-dependent population inversion with different N120

Figure 4.5. Near-field NP coupling in unpumped regions contributes to enhanced lasing emission. Simulated lasing emission from (a) a finite lattice arrays with 40×40 NPs all covered by dye solvent, (b) a finite lattice arrays with 30×30 NPs all covered by dye solvent and, (c) a finite 40×40 lattice array with 30×30 NPs covered by dye solvent.122

Figure 5.1. Continuous-wave (CW) upconverting nanolasing on Ag nanopillar arrays at room temperature. (a) Schematic of the upconverting nanoparticle (UCNP) coating on top of Ag arrays with spacing $a_0 = 450$ nm. (b) Scanning electron micrograph showing the Ag nanopillar array with partial conformal coating (right) with a film of 14 nm core-shell UCNP (NaYF₄:Yb³⁺, Er³⁺). (c) Representative near-field $|E|^2$ plot for the 450-nm spaced Ag nanopillars at resonance ($n = 1.46$) from a finite-difference time-domain method simulation. (d) Yb³⁺, Er³⁺ energy levels and

coupling mechanism to the lattice plasmons. (e) Power-dependent lasing spectra from lattice plasmon resonances at $\lambda = 664$ nm for Ag nanopillar arrays with $a_0 = 450$ nm. (f) Input-output curves in log-log scale with emission linewidth narrowing, showing a low lasing threshold of 70 W/cm².127

Figure 5.2. Transmission electron micrograph of core/shell UCNPs.129

Figure 5.3. Preserved lattice plasmon resonances after coating Ag nanopillars with UCNP emitters. (a) The resonance lineshape and position of lattice plasmons showed only slight modifications after coating Ag NP arrays with Yb³⁺/Er³⁺-based UCNPs. Measured transmission spectra of Ag nanopillar arrays with $a_0 = 450$ nm in DMSO (left) and coated with UCNPs (right). (b) The dispersion property of a thin Er-UCNP film measured by ellipsometry, suggesting that the refractive index of Er-UCNPs is close to the fused silica substrate ($n = 1.48$) at 650 nm ($n = 1.50$). (c) The dispersion diagram of lattice plasmons after UCNP coating shows that the plasmon resonance follows the Bragg mode defined by the lattice.129

Figure 5.4. Resolving plasmon-enhanced emission from UCNP-coated Ag nanopillar arrays with high numerical aperture (NA) wide-field imaging.130

Figure 5.5. Er³⁺ red-band emission and pump intensity dependence for a UCNP film. (a) Intensity-dependent spectra of upconverted emission from the same UCNPs used in the lasing experiments. (b) Light-in-light-out curve for the emission intensity, showing the expected nonlinear behavior typical of a pseudo 2-to-3 photon process, followed by the onset of saturation at higher pump fluences.131

Figure 5.6. Upconverting nanolasing showed spatial and polarization coherence, as well as high photo-stability. (a) Schematic of the experimental optics setup to measure the far-field beam profile. (b) Far-field beam profile of lasing emission above threshold, with the camera detector placed 2 cm away from the sample plane, showing a beam divergence of ca. 0.5°. (c) Polarization-dependent lasing emission with pump polarized at 90°. (d) The polar plot represents the emission intensity of the 664 nm lasing mode and the spontaneous emission (SE) as a function of the polarization angle θ . (e-f) Stability of lasing spectra, intensity and wavelength (red and blue

curves) over the course of 6 hours of uninterrupted irradiation, exhibiting stable emission intensity and modest mode shift (< 0.15 nm).134

Figure 5.7. Upconverting CW nanolasing under a pulsed laser and semi-quantum modeling in the time domain. (a) Lasing spectra with lasing modes at $\lambda = 650$ and 660 nm from UCNPs coupled to Ag nanopillar arrays with spacing $a_0 = 450$ (blue) and 460 nm (red), respectively. (b) Input-output curves in log-log scale show a slightly lower laser threshold for the mode at 660 nm.136

Figure 5.8. Temporal coherence of upconverting nanolasing by $g^{(2)}$ measurements under CW and pulsed pump. (a) $g^{(2)}(t)$ for 10000 ns window and bin size 100 ns for the plasmon laser at 664 nm under CW excitation above threshold (112 W/cm²) in red, and pulsed excitation (230 W/cm²) in black showing the values of 1 for the entire window. (b) $g^{(2)}(t)$ for 100 ns window and bin size 1 ns for the plasmon laser at 664 nm under pulsed excitation above threshold (230 W/cm²), showing CW emission and no modulation with the 80 MHz excitation (12.5 ns delay between pulses) and with values close to 1 for the entire window.137

Figure 5.9. The semi-quantum system used for modeling the upconverting plasmon nanolasing in the time domain. The energy diagram showed that the six-level UCNP system was coupled to the lattice plasmon resonance.139

Figure 5.10. The semi-quantum system used for modeling the upconverting plasmon nanolasing in the time domain. (a) The simulated upconverting nanolasing showed single-mode lasing emission determined by the lattice constant a_0 of the array. (b) Simulated input-output curve showing a threshold-like power dependence with laser thresholds comparable to the experimental values. (c) No population inversion between different energy levels was observed in our semi-quantum simulations below the lasing threshold. (d) Simulated time-dependent evolution of population density describing upconverting nanolasing and the associated population inversion above threshold at 27 kW/cm².140

Figure 6.1. Our large-area gold nanoparticle arrays exhibit clear surface lattice resonances. (a) Sample schematic and dimensions showing gold nanoparticles on a fused silica substrate and capped with photoresist (SU8). (b) Scanning electron micrograph of the fabricated nanoparticle

array before capping with SU8. (c) Photograph of an investigated sample, the large-area nanostructured array appears green. (d) Experimental mapping of transmission spectra versus changing angle of incidence, upon illumination with vertically polarized light (S_{IN}).147

Figure 6.2. Numerical simulations illustrating the near-field enhancement at lattice plasmons. (a) For the 600 nm period gold array, the transmission at normal incidence clearly displays a lattice plasmon resonance at 872 nm. (b) The electric near-field at the surface of the nanoparticle, away from resonance at 780 nm. (c) The electric near-field at the surface of the nanoparticle, at 872 nm, the wavelength of lattice plasmon.148

Figure 6.3. The second harmonic generation signal clearly stands out from the multiphoton background. (a) Experimental configuration for the SHG measurements, where θ is the angle of incidence, RG is an RG665 Schott glass filter, BP is bandpass filter and, PMT is a photomultiplier tube. (b) For illumination with 780 nm fundamental light, the multiphoton emission is plotted versus wavelength.151

Figure 6.4. Due to the strong near-fields of lattice plasmons, SHG enhancements (up to 450 times) occur by tuning fundamental wavelength, angle of incidence and lattice constant of the arrays. (a) SHG enhancement from a lattice plasmon resonance occurs near the Rayleigh anomaly corresponding to the fundamental wavelength of 810 nm for the 600 nm period array. (b-c) Enhanced SHG at different fundamental wavelengths for the 600 nm and 580 nm period gold nanoparticle arrays, respectively. (d) Enhanced SHG at different fundamental wavelengths for the 600 nm period silver nanoparticle array.155

Figure 6.5. Measurements of silver nanoparticle arrays. (a-b) Transmission spectra versus angle of incidence, upon illumination with vertically polarized light (S_{IN}), for the 600 nm and 580 nm period arrays, respectively. (c) The SHG intensity, as a function of the angle of incidence, at different fundamental wavelengths for the 580 nm period silver nanoparticle array.156

Figure 6.6. Lattice plasmon causes an enhancement of the SHG quadrupolar contributions for the gold arrays. (a) For S_{IN} - P_{OUT} (dots) the SHG signal is attributable to electric dipolar contributions. The fundamental light is at 870 nm (at the Rayleigh anomaly) and the peaks correspond to the lattice plasmons. (b) Measuring SHG spectra, for S_{IN} - S_{OUT} and at normal

incidence, these higher-order contributions to SHG peak at the normal incidence lattice plasmon wavelength, for both the 600 nm and 580 nm period arrays.161

Figure 6.7. Hexagonal boron nitride flakes and their transfer process onto plasmonic lattice substrates. (a) Schematic illustration of the wet process used to transfer a selected hBN flake with an emitter of choice (exemplified by the red dot) from a thermal silicon oxide substrate onto a plasmonic nanoparticle array using PMMA as the carrier. (b) SEM image of the mechanically exfoliated hBN flake positioned atop of a silver plasmonic lattice on silica and, (c) optical image of the same flake on the plasmonic lattice. (d) FDTD simulation of the lateral (in-plane) electric field intensity distribution $|E|^2$ of a 400 nm-spaced silver NP lattices.165

Figure 6.8. Coupling between a quantum emitter in a tape exfoliated hBN flake and a gold NP array on silica. (a) PL confocal map of a flake containing a single photon emitter (red circled). Inset, SEM image of part of the flake on top of the gold plasmonic lattice. (b) PL spectra of the pristine (red trace) and coupled (blue trace) single photon emitter, and a transmission spectrum of the plasmonic lattice (green trace) with the plasmonic resonance at 640 nm. (c) Second-order autocorrelation functions obtained from the pristine (red circles) and coupled (blue open squares) system. (d) Time-resolved PL measurements from the pristine (red open circles) and coupled (blue open squares) systems.169

Figure 6.9. Coupling between a quantum emitter in a solvent exfoliated hBN flake and a gold NP array on a silica substrate. (a) PL spectra of a pristine (red trace) and coupled (blue trace) single photon emitter, and a transmission spectrum of the gold lattice (green trace). (b) Second-order autocorrelation functions obtained from the pristine (red open circles) and coupled (blue open squares) systems. (c) Time-resolved PL measurements from the pristine (red open circles) and coupled (blue open squares) systems. Red and blue solid lines are double exponential fits. (d) Fluorescence saturation curves obtained from the pristine (red open circles) and coupled (blue open squares) systems.170

Figure 6.10. Coupling between a quantum emitter in a solvent exfoliated hBN flake and a silver NP array on a silica substrate. (a) PL spectra of a pristine (red trace) and coupled (blue trace) single photon emitter, and a transmission spectrum of the silver lattice (green trace). (b)

Second-order autocorrelation functions obtained from the pristine (red open circles) and coupled (blue open squares) systems. (c) Time-resolved PL measurements from the pristine (red open circles) and coupled (blue open squares) systems. (d) Fluorescence saturation curves for obtained from the pristine (red open circles) and coupled (blue open squares) systems.172

Figure 6.11. Splitting modes were observed in stacked plasmonic NP arrays. Near-field mode coupling in stacked NP arrays results in mode splitting in simulations. (a) Scheme of stacked NP arrays with gain in one layer for PT symmetry breaking. (b) Splitting modes were observed in stacked NP arrays without gain. (c) The electric field and phase distributions suggest that NP arrays work as a pair of resonators with distinct phases between two splitting modes.176

Figure 6.12. Mode splitting was sensitive to NP size and interlayer spacing. (a) Evolution of splitting modes with increased NP diameter, which enhanced the oscillator strength of NP array. (b) Evolution of splitting modes with increased interlayer spacing, which tuned the coupling efficiency.177

Figure 6.13. The split modes followed the diffraction orders of a square array at high incident angles. The dispersion diagrams under TE (a) and TM (b) polarization for NP diameter $D = 130$ nm and interlayer spacing $d = 330$ nm.177

Figure 6.14. Mode splitting was observed in the dispersion diagram of stacked NP arrays. (a) Measured transmission spectrum at $k_{\parallel} = 0$ for stacked Au NP arrays with interlayer spacing around 100 nm. (b-c) Measured dispersion diagrams under unpolarized light.178

Figure 6.15. Revival of single mode with tunable NP interlayer spacing in semi-quantum simulations. (a) Scheme of stacked NP arrays with dye molecule solvents in one layer. (b-d) Evolution from single to two modes with increased interlayer spacing ($d = 330$ nm to 430 nm) to tune the coupling efficiency.179

Chapter 1. Introduction on Plasmonic Nanocavity Arrays

Abstract

This chapter provides a review on ultra-sharp resonances in metal nanoparticle arrays, and the structural engineering of lasers from the macroscale to the nanoscale. Plasmon nanolasers can overcome the diffraction limit of light and incorporate unique structural designs to engineer cavity geometries and optical band structure. Plasmon nanolasers designed by band-structure engineering open prospects for manipulation of lasing characteristics such as directional emission, real-time tunable wavelengths, and controlled multi-mode lasing. In addition, we expand scope of the discussions to the fields of quantum optics, parity-time symmetry and topological photonics, which provides a foundation to the emerging applications of plasmon nanoresonators.

Related references

Wang, D.; Wang, W.; Knudson, M.P.; Schatz, G.C.; Odom, T.W. “Structural Engineering in Plasmon Nanolasers,” *Chemical Reviews* **118**, 2865–2881 (2018)

Wang, D.; Wang, W.; Odom, T.W et al. “Roadmap on Plasmonics: Nanoarray Lasing Spasers,” *Journal of Optics* **20**, 043001 (2018)

1.1 Principles of Ultra-sharp Lattice Plasmons

Surface plasmons—collective oscillations of surface conduction electrons—can squeeze light into sub-wavelength volumes.^{1,2} Surface plasmon polaritons (SPPs) are propagating modes excited at planar metal-dielectric interfaces when external light couples to surface plasmons (**Figure 1.1**).³ Electromagnetic (EM) fields are tightly confined perpendicular to the interface and penetrate less into the metal than into the dielectric because of the negative permittivity of the metal.¹ Localized surface plasmons (LSPs) are supported by metal nanoparticles (NPs) whose lateral dimensions are much smaller than the wavelength of light. Their EM fields are localized in all three dimensions within tens of nanometers from the particle surface.

Lattice plasmons—hybrid modes from coupling of LSPs of individual NPs to diffraction modes in a periodic array—can suppress radiative loss with characteristic ultrasharp resonances.^{4,5} Periodic plasmonic NP arrays with sub-wavelength NP spacing can be generated over cm^2 areas using multi-scale nanofabrication (**Figure 1.2a**).⁶ High-quality (quality factor, $Q > 200$) lattice plasmon resonances can be supported in metal NP arrays in a uniform refractive index

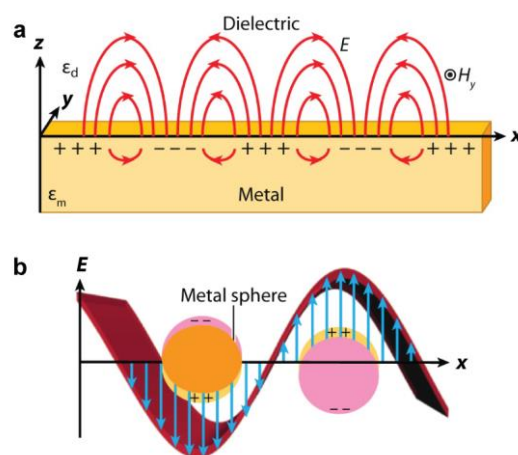


Figure 1.1. Surface plasmons in metals. (a) Surface plasmon polariton from a thin metal film. **(b)** Localized surface plasmons from metal NPs. Figures adapted from ref. 3 with permission.

environment, and their wavelengths are determined by the LSP of the NPs, refractive index, and NP spacing.⁷⁻⁹

At resonance, the NPs reside at the antinodes of standing waves, and all NPs exhibit in-phase oscillations of electromagnetic waves with each other. Diffractive scattering of photons by one NP can be collected by adjacent NPs as plasmons instead of radiatively decaying as free-space light; hence, lattice plasmons support modes with large Q and ultra-narrow linewidths (< 1 nm).⁴ Narrow lattice plasmon resonances have been observed experimentally in arrays of cylindrical NPs⁷ and nanorods.^{5,10} For gold nanorod arrays, the measured extinction spectra showed sharp linewidths that were sensitive to particle size and polarization direction (**Figure 1.2b**). Based on the coupled dipole approximation (CDA), the sharp lattice resonances arose from partial cancellation of the single particle linewidth by the negative imaginary part of the radiative dipolar interactions⁴ (**Figure 1.2c**). In this model, each NP was considered as a dipole, and the net dipolar moment was the sum of the incident field and radiation from all other dipoles.^{5,9,11} The imaginary part of the normalized dipolar sum (Figure 1.2c, inset) was zero at a Rayleigh anomaly, an in-plane diffractive scattering mode.⁴ In comparison, lattice plasmon resonances were slightly red-shifted, where the real part of the dipolar moment showed a peak while the imaginary part dropped to a minimum.

Varying the lattice geometry in NP arrays is a straight-forward way to engineer the optical band structure. Square arrays of NPs support band-edge modes at zero wavevector—the Γ point in the band structure—with a large local density of optical states.¹² Slow light with a nearly-zero group velocity can be trapped at band-edge states to manipulate strong light-matter interactions.^{13,14} In honeycomb lattices, an effective Dirac Hamiltonian can be derived, and interacting LSPs in the lattice structure can yield massless Dirac-like bosonic collective plasmons in the vicinity of two Dirac points in the Brillouin zone.^{15,16} These edge states can provide

propagation channels for light at targeted frequency ranges. By tuning the polarization of the incident light, the Dirac points in the Brillouin zone could be manipulated to produce a band gap at certain polarization angles.¹⁶ Because of the in-phase oscillation of the NPs in the array, the local field around each NP is enhanced by two orders of magnitude compared to that of an isolated NP at resonance, which offers prospects in nonlinear optics, photocatalysis and other light-matter

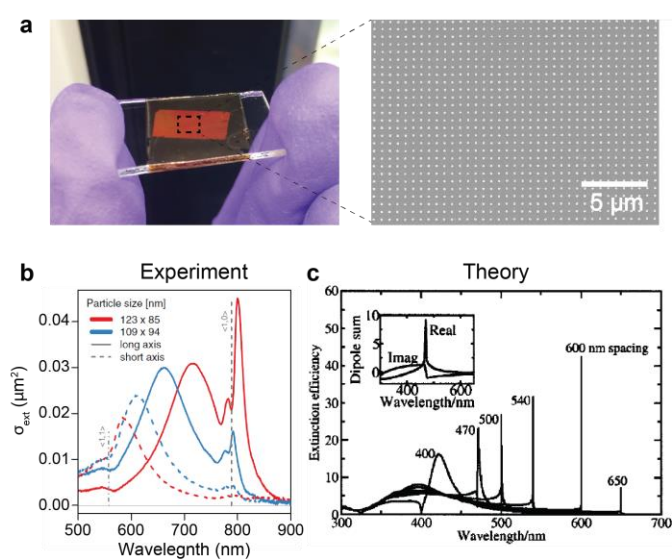


Figure 1.2. Lattice plasmons with sharp resonances in periodic metal nanoparticle arrays. (a) Large-scale fabrication of plasmonic NP arrays by soft photolithography processes. (b) Experimental demonstration of sharp lattice plasmon resonances from gold nanorod arrays.⁵ (c) Simulated extinction spectra of a 1D chain of silver nanoparticles with varying spacings by coupled dipole method.⁴ Inset shows the real and imaginary parts of the normalized dipole sum. Panels b-c adapted with permission.

interactions.

1.2 Sub-wavelength Plasmon Lasing

1.2.1 Conventional Lasers

Lasers are coherent light sources that are driving discoveries in ultrafast spectroscopy and sub-femtosecond chemical reactions¹⁷⁻¹⁹ and are widely used in optical communications,²⁰ biomedical imaging²¹⁻²³ and laser printing.²⁴ Small lasers—those with sizes close to half the lasing wavelength, or the diffraction limit—can be widely applied in nanoscale applications. For example, they can serve as coherent light sources in on-chip electro-photonics circuits^{25,26} and be implanted in tissues for in-situ cellular imaging.²⁷⁻²⁹ Shrinking coherent light sources to sub-wavelength scales can also provide new insight into light-matter interactions such as fluorescence, photocatalysis, quantum optics and nonlinear optical processes.^{22,30,31}

Traditional lasers are composed of gain sandwiched between parallel mirrors that support Fabry-Pérot modes within the optical cavity (**Figure 1.3**). Photons generated by optical or electrical pumping travel back and forth through the gain media in the cavity and are amplified to build up stimulated emission with spatial and temporal coherence.³² For a Fabry-Pérot cavity of length L and mirror reflectivities R_1 and R_2 , the electric field amplitude of the light returning to its original value after a round trip forms a standing wave that can be expressed as:

$$E_0 \sqrt{R_1 R_2} e^{(G-\alpha)L} e^{i4\pi n L / \lambda_0} = E_0 \quad (1.1)$$

where G is the optical gain for a specific cavity mode, α the absorption loss, λ_0 the resonance wavelength in free space, and n the effective index of the medium.²² Therefore, $4\pi n L / \lambda_0$ must be a multiple of 2π in **Equation 1**, leading to:

$$L = \frac{\lambda_0}{2n} m \quad (1.2)$$

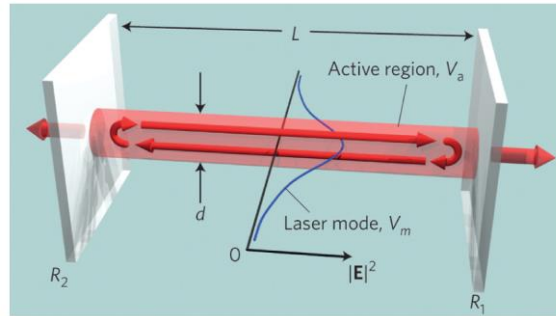


Figure 1.3. A conventional laser supporting Fabry-Pérot modes between two end mirrors (length L) and gain medium inside the cavity. Figure adapted from ref. 22 with permission.

where m is an integer indexing the lasing mode. The shortest possible cavity length for traditional lasers is $\frac{\lambda_0}{2n}$ ($m = 1$), which represents the diffraction-limit. Additionally, sufficient gain is needed to overcome the absorption losses (α) and mirror losses ($R_1, R_2 < 1$) in one round trip, resulting in:

$$L = \frac{-\ln(R_1 R_2)}{2(G - \alpha)} \quad (1.3)$$

Therefore, the cavity sizes of conventional lasers need to be large enough to provide sufficient gain to overcome the losses.

Based on propagation and reflection losses of the cavity, the quality factor (Q) can indicate the residence time of photons. The Purcell factor F is typically used to quantify enhanced spontaneous emission rate in dielectric resonators and influences the build-up dynamics of population inversion for lasing.³³ A simplified expression for F is³²

$$F = \frac{3}{4\pi^2} \left(\frac{Q}{V}\right) \left(\frac{\lambda}{2n}\right)^3 \quad (1.4)$$

where Q depends on linewidth, and mode volume V defines electromagnetic field confinement.

Unlike the process of spontaneous emission, where photons are emitted with random direction and phase, stimulated emission is the result of coherent amplification of photons by interaction with the excited states of gain media.³² The critical characteristics of lasing include spatial and temporal coherence, where emitted photons from the lasing cavity share the same wavelength, phase, amplitude, polarization, and directionality.³² As generally agreed upon in the community,³⁴ criteria for lasing include: (1) a deterministic lasing threshold in the input power-output intensity curves; (2) linewidth narrowing (full-width at half-maximum (FWHM) < 1-2 nm) above threshold; (3) a non-linear increase in the output intensity above threshold; and (4) minor divergence of the emission beam. Other competing phenomena such as amplified spontaneous emission (ASE) need to be eliminated to verify lasing action, especially in unconventional nanolasers.^{34,35}

1.2.2 Nanoscale Lasing from Sub-wavelength Plasmons

In past decade, unconventional architectures of plasmon nanolasers appeared that are different from traditional Fabry-Pérot mode cavities. Intense, localized electric fields at plasmonic hotspots can overcome the diffraction limit of light and enable ultrafast operation at terahertz frequencies.^{12,36,37} Since the concept of the spaser (surface plasmon amplification by stimulated emission of radiation)³⁸ was proposed, plasmon nanolasers based on either surface plasmon polariton (SPP) modes on metal films^{30,36,39-41} or localized surface plasmon (LSP) modes from metal NPs^{12,42} have been reported (**Figure 1.4**).

Spasers exploit LSP excitations to beat the diffraction limit and to confine electric fields within deep sub-wavelength scales.^{38,43} As first proposed, spasers excite nanoscale localized radiation by stimulated emission of two-level emitters.³⁸ When gain materials are pumped into an excited state (optically, electrically, or chemically), instead of emitting light, they can transfer energy non-

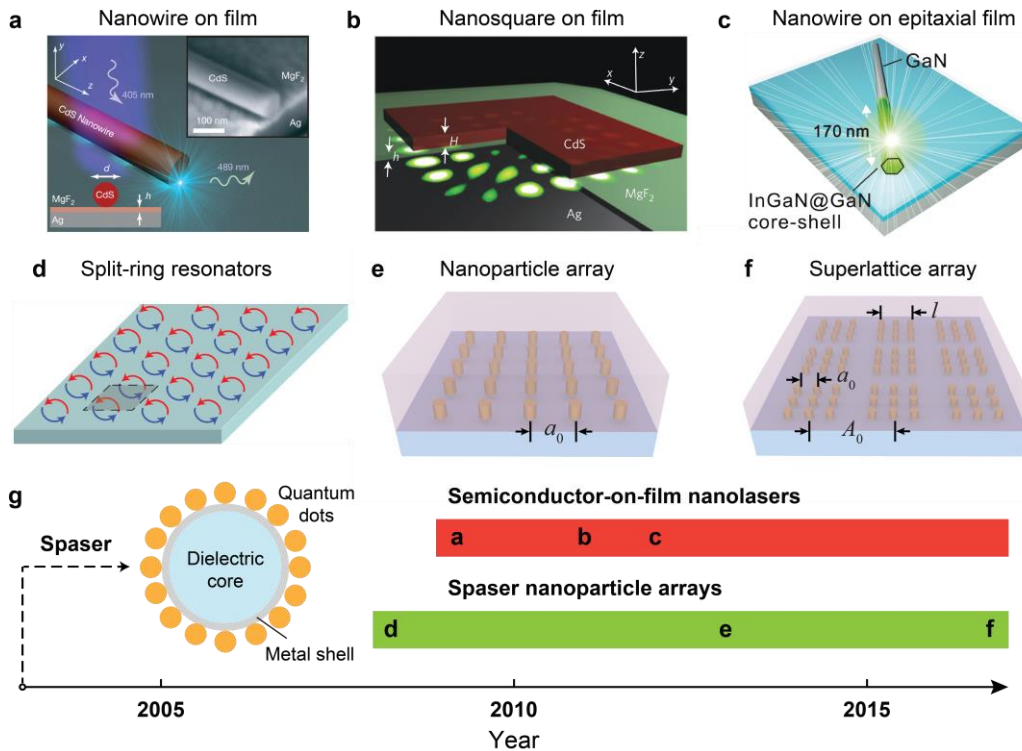


Figure 1.4. Development timeline of plasmon nanolasers. (a) The first plasmon laser using SPP modes as optical feedback for lasing at cryogenic temperatures, including CdS semiconducting nanowires on a silver film separated by a MgF₂ layer.³⁶ (b) Plasmon laser operated at room temperature with CdS nanosquares on a Ag film separated by a MgF₂ layer.³⁹ (c) Plasmon nanolaser using epitaxially grown silver film for lower lasing threshold.⁴⁹ (d) The first theoretical study of spaser arrays for directional emission using split-ring resonators at mid-infrared wavelengths.⁴² (e) The first experimental realization of directional emission from spaser NP arrays at near-infrared wavelengths.¹² (f) Plasmonic superlattice arrays with controlled multi-modal nanolasing.⁵³ (g) Timeline of plasmon nanolasers. Figures adapted with permission.

radiatively to the resonant surface plasmons of NPs. Stimulated emission generates coherent surface plasmons, and energy accumulated in the plasmon oscillations can emit into free space resulting in a lasing spaser.³⁸ In experiments, single-particle spasers were originally conceived as nanostructures with a dielectric NP core and silver shell supporting an LSP mode surrounded by

nanocrystal quantum dots as gain^{43,44}. Although emission from nanostructures composed of a gold core surrounding a silica shell embedded with organic dye has been realized experimentally, follow-up work has been surprisingly sparse, and demonstrations need to be better differentiated from other phenomena such as random lasing.^{45,46}

Although the first theoretical paper on spasers³⁸ focused on plasmon amplification of LSPs in single metal NPs, semiconducting nanowires on metal films (**Figure 1.4a**) were one of the first designs realized using SPP modes as optical feedback for lasing at cryogenic temperatures.³⁶ To compensate for large ohmic losses at optical frequencies in metal structures,⁴⁷ incorporating a dielectric layer between metal and semiconductor materials could reduce losses while maintaining ultra-small mode volumes.⁴⁸ When the dielectric spacer is reduced to nanoscale dimensions (< 10 nm), a hybrid mode is confined in the gap having features of both a waveguide mode from the nanowire and an SPP mode from the metal. Room-temperature operation was later achieved using nano-squares (**Figure 1.4b**) as resonators.³⁹ Additionally, a larger contact area at the nanowire-insulator interface such as hexagonal and triangular cross-sections⁴⁰ and integration of epitaxially-grown metal films with atomic smoothness^{49,50} decreased the scattering losses and further improved SPP lasers by lowering lasing thresholds (**Figure 1.4c**).

As a result of the short spontaneous carrier recombination lifetimes of plasmon modes, plasmonic systems can achieve lasing pulse widths < 800 fs, around ten times shorter than their photonic counterparts.³⁷ Because lasers based upon SPPs tend to exhibit high ohmic losses from the metal, early work required cryogenic temperatures.^{36,49} Improvements in design and fabrication, however, have since lowered the lasing thresholds and allowed operation at room temperature.^{37,40,51} Another limitation for nanowire-on-film lasers is their lack of directional emission in the far-field since the light is scattered from the end-facets of the nanowire because of

the momentum mismatch of SPPs and free-space light, while the harnessing of coherent, directional beam is critical for on-chip photonic devices.³⁶

Nearly ten years ago, the concept of using an array structure to couple sub-units for directional lasing emission was proposed for split-ring resonators⁴² at mid-infrared wavelengths (**Figure 1.4d**). However, experimental realization¹² was only recently achieved and with a simpler system (**Figure 1.4e**). Periodic arrays of metal NPs coupled with organic gain molecules showed room-temperature operation, spatial coherence, directional emission normal to the surface, and tunability over near-infrared wavelengths.^{12,52} Advances in theoretical modeling by considering cavity modes and time-dependent lasing action have contributed to understanding and design of emerging plasmon lasers, including switchable, multi-modal nanolasers⁵³ (**Figure 1.4f**) and dark-mode lasers.^{54,55}

1.2.3 Lasing from Spaser Nanoparticle Arrays

Periodic arrangements of spaser arrays support directional lasing emission and efficient out-coupling due to constructive interference between adjacent units.^{12,52} The first proposed array was based on split-ring resonators with curved plasmonic nanowire pair subunits of different lengths.⁴² The asymmetric resonator shape prevented cancellation of dipole emission from nanowire pairs with opposite oscillating currents (**Figure 1.5a**). Each unit oscillated in phase, which resulted in a high-quality cavity mode for coupling the near-field energy into free space at mid-infrared regions.

Different unit cell designs have been pursued to engineer arrays of plasmonic hot spots.^{56,57} Three-dimensional plasmonic bowtie arrays exhibited strong near-field enhancements in the gap region with an ultra-small mode volume; integrated with gain media composed of dye mixed in a solid polymer matrix, lasing action was demonstrated at room temperature.⁵⁶ Lasing signatures

have also been realized in plasmonic hole arrays, where SPPs formed the plasmonic nanocavity.⁵⁸⁻
⁶⁰ Low temperatures were required to reach enough gain since semiconductors exhibit high non-radiative recombination rates.⁵⁹ In the far-field, the emission beam was radially polarized and ring-shaped, consistent with polarization-dependent dispersion with “dark” modes at zero wavevector, where the emission could not radiatively couple to the far field (**Figure 1.5b**). SPP modes based on a combined structure of periodic metal NPs on a planar metal film (two-dimensional plasmonic crystals) have also provided optical feedback for nanoscale lasing.⁶¹ Since the underlying gold substrate functioned like a mirror, unidirectional lasing occurred on the same side as the gold NPs and pump source (**Figure 1.5c**). High dye concentrations were required for lasing action because of large ohmic losses from the metal film.

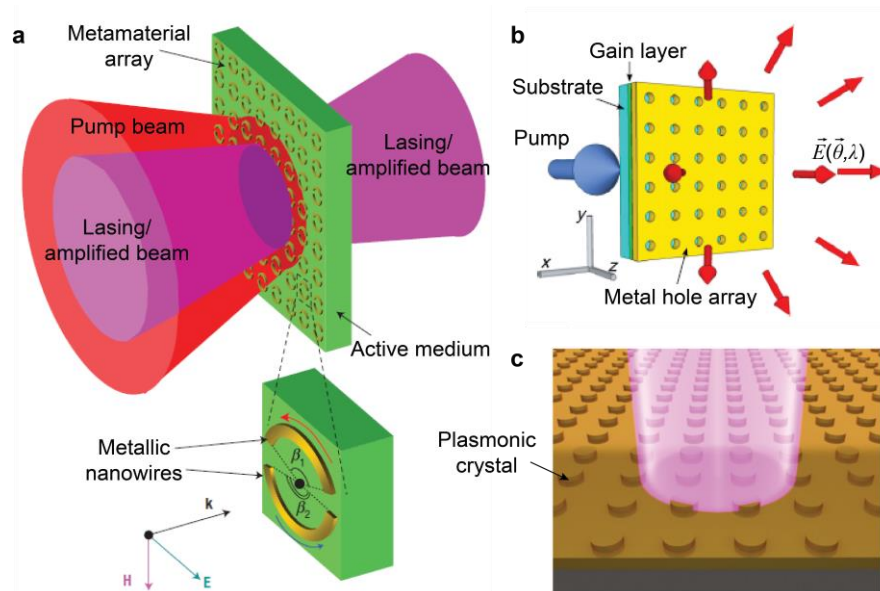


Figure 1.5. Array coupling for directional emission in various plasmonic unit cell designs.

(a) Directional lasing from asymmetric split-ring resonator arrays on a gain medium slab.⁴² (b) Directional lasing from a metal hole array on a semiconductor layer.⁵⁸ (c) Unidirectional lasing from template-stripped 2D plasmonic crystals consisting of gold NP arrays on a gold film.⁶¹ Figures adapted with permission.

The high-quality band-edge lattice plasmons in metal NP arrays can contribute to single-mode lasing at room-temperature.^{12,52} In the array, each small metal NP can be treated as a dipole emitter radiating spherical waves in the far field. Top-down, unconventional nanopatterning methods⁶ can generate NP arrays over large areas ($> \text{cm}^2$) and overcome lengthy fabrication times required of bottom-up semiconductor materials and small-area patterns by electron-beam lithography^{36,39} (**Figure 1.6a**). Nanofabrication tools such as phasing-shifting photolithography can control particle size, spacing, and lattice geometry.^{12,62,63}

In distributed feedback lasers, both upper and lower band edge modes compete for available gain, and only one mode emerges as the lasing peak above threshold.^{53,64} In contrast, metal NP arrays exhibit only a single band-edge mode at the Γ point ($k_{\parallel} = 0$, **Figure 1.6b**). Lower band

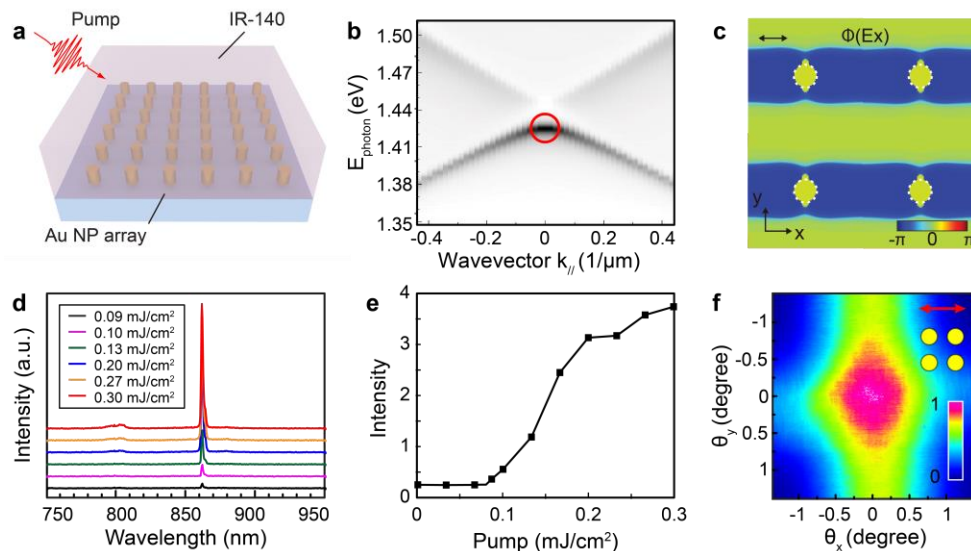


Figure 1.6. Directional lasing from spaser NP arrays. (a) Scheme of a laser device including gold NP arrays embedded in liquid or solid-state gain media. (b) Calculated optical band structure. (c) Simulated phase profile at lattice plasmon resonances.¹² (d-e) Power dependent lasing emission and input-power output-intensity curves.⁵² (f) Far-field beam profile with a highly directional lasing spot.⁵² Figures adapted with permission.

edges are suppressed due to destructive near-field interference. At zero wavevector, band-edge modes form standing waves, where each NP has the same phase profile, and optical fields are localized at the dipolar hot spots (**Figure 1.6c**). Au NP arrays showed over two-orders of magnitude higher and more localized near-field enhancements compared to silicon NP arrays. At non-zero wavevectors, in-plane lattice plasmon modes are dispersive and follow the $(0, \pm 1)$ Rayleigh anomaly lines under transverse electric (TE) polarization⁵³ and $(\pm 1, 0)$ under transverse magnetic (TM) polarization.¹²

The first nanoscale lasing devices were constructed from two-dimensional arrays of Au NPs on transparent substrates covered by a solid gain layer of dye in a polymer matrix¹² or by a liquid gain medium in subsequent work.^{52,53} Optically pumped with 800-nm fs-pulses (repetition rates: 1-10 kHz), spaser NP arrays emitted light normal to the surface. Above the lasing threshold, a narrow emission peak emerged with a FWHM of 1.3 nm (**Figures 1.6d-e**), and directional beam emission with a small divergence angle ($< 1.5^\circ$) was observed (**Figure 1.6f**). Distinct from other plasmon lasers, spaser NP arrays can show lasing at room temperature and with low lasing thresholds ($\sim 0.1 \text{ W cm}^{-2}$).^{12,52} In contrast, nanowire-on-film lasers generally have thresholds in the KW cm^{-2} range at low temperature³⁶ or GW cm^{-2} at room temperature because of large radiative losses.^{37,39} Spaser NP arrays are also robust to defects; even drastic changes in the lattice plasmon quality by distortions in NP shape, missing NPs in the array, and displaced NPs from the periodic lattice can still produce lasing signals.^{4,57,65}

Another advantage of spaser NP arrays is their ability to exhibit real-time tunable lasing based on the same metal NP cavity structure but different liquid gain characteristics.⁵² Dye molecules dissolved in different organic solvents will have different refractive indices. Static tuning of lasing wavelength was possible using ultra-flat polyurethane with varying index ($n = 1.42\text{-}1.50$) as

substrates and dye molecules dissolved in various solvents⁶⁶ as superstrates (**Figure 1.7a**). By changing the refractive index, lattice plasmon lasing could be tuned over the entire gain bandwidth of the dye (**Figure 1.7b**). In contrast, DFB lasers require more sophisticated methods to achieve similar wavelength tuning ranges.^{67,68}

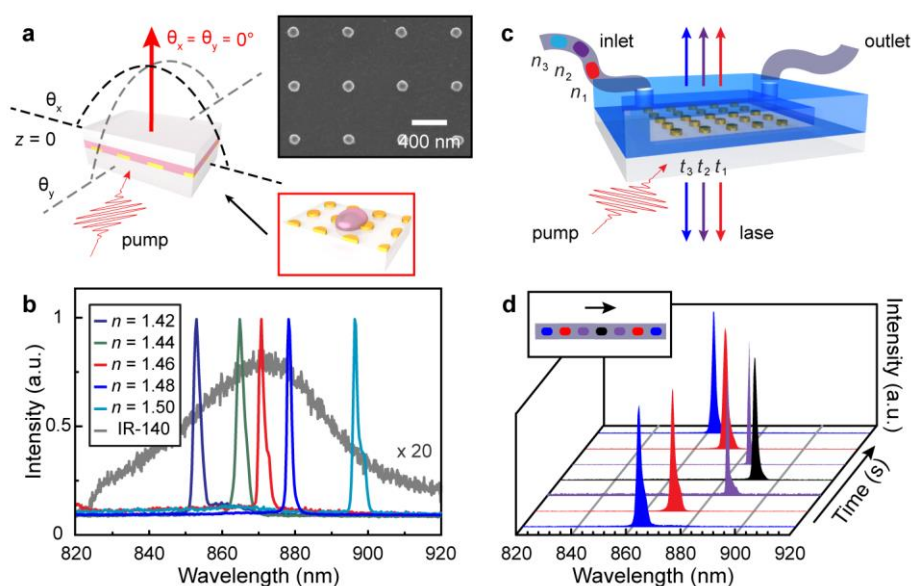


Figure 1.7. Real-time tunable nanolasing from plasmonic nanoparticle arrays by refreshing liquid dye solutions. (a) Scheme of a lasing device consisting of gold NP arrays sandwiched between liquid dye solutions and a glass coverslip. (b) Statically tuned lasing wavelengths can span the entire emission bandwidth of the dye. (c) Scheme of the dynamic laser with a microfluidic channel. (d) Continuous shifting of lasing emission to longer wavelengths and then back to shorter wavelengths. Figures adapted from ref. 52 with permission.

Large-area arrays ($> \text{cm}^2$) can be integrated with microfluidic devices to achieve dynamically tunable lasing, which is not possible in NP arrays produced by electron-beam lithography (areas: μm^2).^{54,55} Liquid gain with different indices can be introduced plug-wise into fluidic channels to tune the lattice plasmon resonance and hence the lasing wavelength (**Figure 1.7c**). Compared to

solid-state gain, dyes in solvents can be refreshed in dipolar hot spot regions and maintain their photostability under optical pumping by avoiding photo-oxidation and photobleaching.^{69,70} **Figure 1.7d** shows that the lasing emission can be continuously shifted to longer wavelengths and then back again to shorter wavelengths with no hysteresis. The real-time tunability was enabled by the tolerance of the lattice plasmon to mismatches in index between the liquid superstrate and solid ($\Delta n < 0.05$ refractive index units).⁷¹ Modeling of tunable lasing with the finite-difference time-domain (FDTD) method showed excellent agreement with experiments.⁵²

1.2.4 Semi-quantum Modeling of Nanoscale Lasing

Plasmon lasers have been predicted and inspired by theoretical models based on cavity mode analysis; however, there are remaining challenges in understanding and modeling lasing action in plasmonic cavities. In Purcell factor calculations, the traditional definition of mode volume V fails because the EM fields diverge exponentially away from the plasmonic cavity; a more accurate definition of V such as that in effective mode-volume theory is needed.^{72,73} To understand lasing action, models need to include equations describing populated states in gain and how population inversion induces stimulated emission in the presence of the plasmonic cavity.

Dye photophysics can be described by a four-level electronic state model, and the optical cavity treated with classical electrodynamics.^{74,75} In the classic work of Nagra and York,⁷⁶ who developed a theory where the FDTD method was used to numerically solve the EM fields, finite differencing was also used to describe rate equations and coupling between the field and populations. Related approaches have been applied to plasmon lasers^{27,33,77} and expanded to non-plasmonic systems such as photonic crystals and random lasers.⁷⁸⁻⁸³ The Nagra-York model⁷⁶ as well as variations that account for Pauli exclusion principle effects⁷⁹ have now been combined with standard FDTD

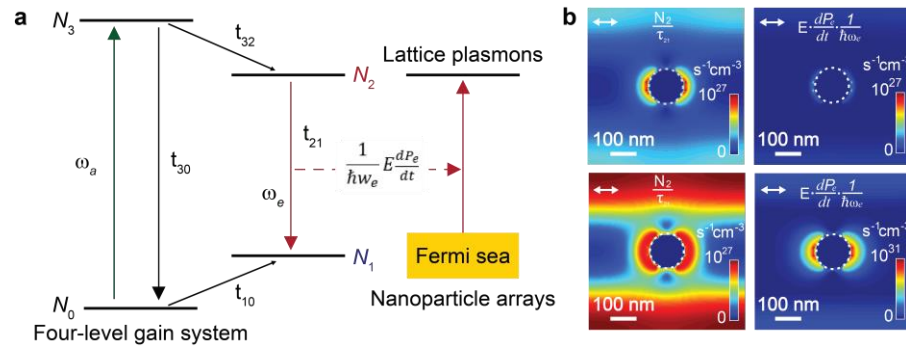


Figure 1.8. Modeling of nanoscale energy transfer with semi-quantum four-level system for lasing action. (a) Scheme of the energy transfer process from four-level gain media to lattice plasmon resonances in spaser NP arrays. (b) Calculated distribution maps of spontaneous transition rate (left) and stimulated transition rate (right) in the middle plane of NP arrays below threshold (top) and above threshold (bottom). Figures adapted from ref. 12 with permission.

codes, including commercial solvers like COMSOL and Lumerical and the public domain code MEEP.⁸⁴

Using a semi-quantum time-domain approach,^{12,33,85} lattice plasmon lasing can be simulated by stimulated energy transfer from the gain to the band-edge modes of the plasmons (**Figure 1.8a**). The lattice plasmon response from NP arrays can be described by classical electrodynamics, and Maxwell's equations can be solved numerically. Integration between the EM fields and gain can be described in auxiliary equations including both the macroscopic polarization of EM fields from population inversion and the time evolution of the population density of the gain modified by EM fields. Overall, the rate equations, Maxwell's equations, and auxiliary equations can be solved by finite differencing on an FDTD grid⁷⁶ to determine emitted power as a function of pump energy.

Below the lasing threshold, the stimulated transition rate is negligible compared to spontaneous emission (**Figure 1.8b**). Above the lasing threshold, the stimulated emission rate was four orders of magnitude higher than the spontaneous emission rate. A spatial map of the stimulation emission

revealed that population inversion leading to lasing action had maximum values in hot spot regions within 25 nm of the NPs, which was in excellent agreement with the near-field EM patterns at the band-edge plasmon resonance. This calculation confirmed that the nanoscale localization of EM fields stimulated excited state gain to resonantly transfer energy into surface plasmons.

Describing gain material merely by evolution of rate equations is incomplete in their treatment of coherence effects. At high dye concentration, the dye excitons may dephase, transfer energy to each other, or be quenched for those close to the metal NPs. Recently, more sophisticated models describing emitter photophysics have been based on the classical picture of oscillating dipoles, and quantum pictures include phonon and electron-phonon coupling as well as excited state dynamics. Time-evolution of the quantum density matrix of the emissive species can describe the dephasing of emitter states,⁸⁶ and the Maxwell-Liouville approach and variants have already been applied to non-lasing plasmonic systems.⁸⁷⁻⁹³ New theoretical models can provide insight into the plasmonic lasing processes and motivate experimental studies on fundamental light-matter interactions.

1.3 Parity-time Symmetric Photonics and Quantum Optics

Hybrid plasmonic – photonic systems are attracting increasing attention in studies of light-matter interaction at the nanoscale, coherent and incoherent light amplification, and as media for achieving enhanced emission and absorption rates.⁹⁴⁻⁹⁸ Quantum emitters in two-dimensional materials are promising candidates for studies of light-matter interaction and next generation, integrated on-chip quantum nanophotonics. To this extent, coupling of single photon emitters (SPEs), which are vital components of future quantum technologies,⁹⁹ to plasmonic cavities was demonstrated for 3D crystals including color centers in diamond,^{100,101} 1D carbon nanotubes (CNTs)¹⁰² and 0D quantum dots.¹⁰³⁻¹⁰⁵ Recently, isolated defects in two dimensional (2D)

hexagonal boron nitride (hBN)¹⁰⁶⁻¹⁰⁹ have emerged as a new class of room temperature SPEs. These emitters are embedded in 2D flakes of layered hBN and therefore offer an excellent platform for integration with photonic elements, making them promising constituents of next-generation nanophotonics and optoelectronic devices. However, due to the random locations of these defects within the 2D materials, deterministic positioning of quantum emitters within a nanophotonic cavity is critical for harnessing strong light-matter interactions.

As an analog of quantum Hall states, topological photonics that support unidirectional propagating edge states is an emerging research area.^{50,110-115} Unidirectional edge transport is highly desirable in optical devices because of robustness to device disorders.¹¹⁶ The lossy nature of metals complicates descriptions of topological effects in a plasmonic system. Dissipative losses in plasmonic systems also offer opportunities to explore the emerging fields of non-Hermitian physics and PT symmetry, which is critical in accessing the unidirectional topological edge states.¹¹⁷ A parity-time (PT) symmetric photonic system requires balanced loss and gain, where the Hamiltonian commutes with PT operators. The spatial dependence of the refractive index that leads to non-Hermitian eigenstates requires:

$$Re(n(x)) = Re(n(-x)) \quad (1.5)$$

$$Im(n(x)) = -Im(n(-x))$$

which can be achieved by spatial control of loss and gain in a device. In a PT symmetric photonic system, the unique PT symmetry-broken phase can be accessed when two eigenstates collapse to a single mode after passing an exceptional point. Coupled ring resonators^{118,119} with an active Er³⁺-doped ring and a passive ring side by side have achieved the exceptional point (**Figure 1.9a**). A

simple two-level non-Hermitian model Hamiltonian H is used for describing a PT symmetric system:

$$H = \begin{pmatrix} \delta + ig_1 & k \\ k & -ig_2 \end{pmatrix} \quad (1.6)$$

When gain g_1 and loss g_2 are balanced ($g_1 = g_2 = g$), and the un-coupled modes are degenerate ($\delta=0$), H becomes PT symmetric.¹¹⁷ By tuning parameters g and k , the system can undergo phase transitions across the exceptional point ($g/k = 1$) between the PT-exact ($g/k < 1$) and PT-broken phases ($g/k > 1$) (**Figure 1.9b**). Unidirectional light propagation is associated with the symmetry-

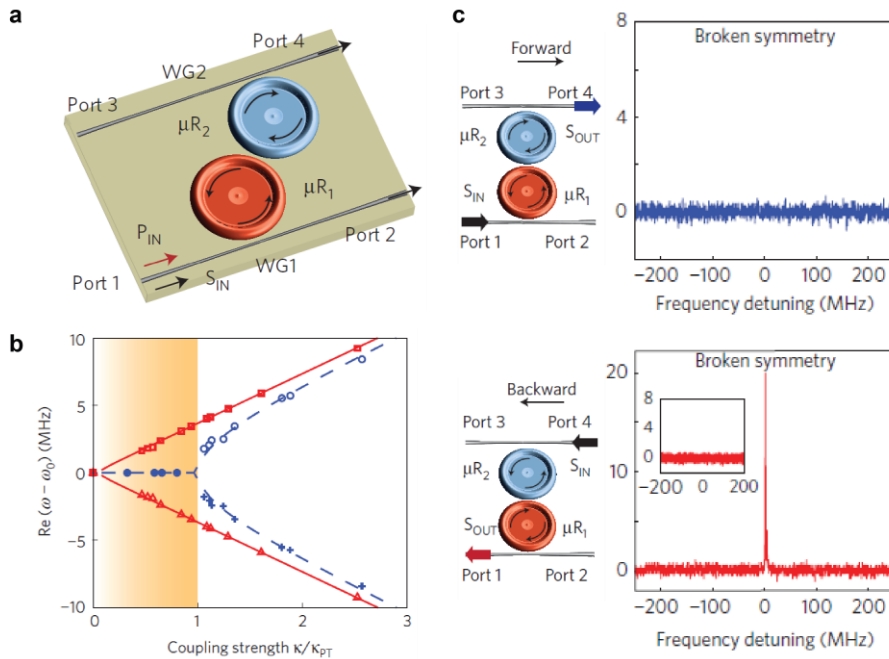


Figure 1.9. Modeling of nanoscale energy transfer with semi-quantum four-level system for lasing action. (a) Scheme of a pair of coupled whispering-galley-mode resonators with gain in one ring. (b) Collapsing of two eigenstates to a single mode after exceptional point by tuning the coupling coefficient. (c) Experimentally observed unidirectional transmission for PT-symmetric microresonators at the symmetry-broken phase. Figures adapted from ref.118 with permission.

broken phases (**Figure 1.9c**), which is important for optical communications and on-chip photonics integration.^{117,120,121}

However, a well-defined, coupled plasmonic nanoresonator system that can achieve PT symmetry-broken phases is missing. The balance of loss and gain in a plasmonic system is challenging due to the lossy plasmon damping, and the defining of active and passive resonators requires stringent development of nanofabrication processes. The development of a well-defined plasmonic nanoresonator system is desirable for achieving PT symmetric plasmonics that can balance the gain and loss and arbitrarily control the coupling efficiency in between.

1.4 Scope of This Thesis

This dissertation includes 6 chapters on the structural and materials engineering of plasmonic NP arrays. **Chapter 2** discusses a robust, stretchable nanolaser platform that can preserve its high mode quality based on hybrid quadrupole lattice plasmons (HQLs) as the lasing feedback mechanism. Increasing the size of metal NPs in an array can introduce ultra-sharp lattice plasmon resonances tolerant to lateral strain. By patterning these NPs onto an elastomeric slab surrounded by liquid gain, we realized reversible, tunable nanolasing with high strain sensitivity and no hysteresis.

Chapters 3 describes how plasmonic superlattices—finite-arrays of NPs (patches) grouped into microscale arrays—can support multiple band-edge modes capable of multi-modal nanolasing at programmed emission wavelengths and with large mode spacings. The multi-scale interactions in structured plasmon superlattices enable access to multiple tunable, on-demand optical modes for optical multiplexing in on-chip photonic devices. In addition, this chapter shows that microscale molding of dielectric superstrate on top of plasmonic NPs can produce reconfigurable, polarization-dependent superlattice plasmons.

Chapters 4 details the scaling behavior for lasing from plasmonic nanocavity arrays. This chapter shows the critical NP number N in a finite-sized lattice for lasing at room temperature. Narrowing of lattice plasmon resonances associated with stronger near fields was observed with increased N . For compact photonic integration, NP number in a finite-sized plasmonic nanocavity array plays a critical role in lasing actions in terms of ultrafast dynamics and lasing thresholds.

Chapter 5 describes continuous-wave upconverting lasing at room temperature with record-low thresholds and high photostability from sub-wavelength plasmons. We achieve selective, single-mode lasing from $\text{Yb}^{3+}/\text{Er}^{3+}$ -co-doped upconverting nanoparticles conformally coated on

Ag nanopillar arrays that support a single, sharp lattice plasmon cavity mode and sub-wavelength field confinement in the vertical dimension. The intense electromagnetic near-fields result in a threshold of 70 W/cm^2 , orders of magnitude lower than other small lasers.

Chapter 6 discusses the emerging applications of plasmonic nanocavity arrays in nonlinear optics, quantum optics and topological photonics. We show that the second harmonic generation (SHG) signal is greatly increased (up to 450 times) by the propagating lattice plasmons. Quantum emitters in 2D hexagonal boron nitride can be deterministically coupled to high-quality plasmonic nanocavity arrays to produce enhanced single photon emission. Stacked plasmonic NP arrays can serve as a pair of coupled resonators and achieve transition between PT-symmetric and PT-broken phases by partial integration with the gain in one layer.

Chapter 2. Stretchable Lasing from Hybrid Quadrupole Plasmons

Abstract

This chapter discusses a robust and stretchable nanolaser platform that can preserve its high mode quality by exploiting hybrid quadrupole plasmons as an optical feedback mechanism. Increasing the size of metal nanoparticles in an array can introduce ultra-sharp lattice plasmon resonances with out-of-plane charge oscillations that are tolerant to lateral strain. By patterning these nanoparticles onto an elastomeric slab surrounded by liquid gain, we realized reversible, tunable nanolasing with high strain sensitivity and no hysteresis. Our semi-quantum modeling demonstrates that lasing build-up occurs at the hybrid quadrupole electromagnetic hot spots, which provides a route towards mechanical modulation of light-matter interactions on the nanoscale.

Related reference

Wang, D.; Bourgeois, M.R.; Lee, W.; Li, R.; Trivedi, D.; Knudson, M.P.; Wang, W.; Schatz, G.C.; Odom, T.W. “Stretchable Nanolasing from Hybrid Quadrupole Plasmons,” *Nano Letters* **18**, 4549–4555 (June 18, 2018) DOI: 10.1021/acs.nanolett.8b01774

2.1 Introduction

Tunable, coherent, and compact light sources are critical for applications in responsive optical displays, on-chip photonic circuits, and multiplexed optical communication.^{22,25,26,28} Integrating laser cavities such as photonic crystals into a stretchable matrix has produced dynamic manipulation of photonic band structure and lasing emission as a function of applied strain.^{122,123} The spectrally narrow lasing signals allow for large spatiotemporal responses that can provide insight on local structural changes.¹²⁴⁻¹²⁷ However, one drawback of stretchable lasing from photonic cavities is their limited strain sensitivity because of the microscale device footprints.^{122,128-130} Further miniaturization of mechanically robust lasers is essential to track nanoscale structural deformations with high figures of merit and to manipulate light-matter interactions such as photocatalysis and nonlinear optical processes by external strain.^{22,131,132}

Unlike traditional photonic systems, plasmonic nanocavities can overcome the diffraction limit and confine light to subwavelength regions.^{12,36,39,43,131,133} Nanolasing has been realized from coupled arrays of metal NPs surrounded by gain media, with wavelengths tailorable by varying refractive index environment and lattice spacing.^{12,52-55,134} Metal NP lattices can readily be patterned over macroscale areas ($> \text{cm}^2$) on flexible substrates for reconfigurable, mechanical control over the lattice plasmon resonances.^{62,135} To achieve broad tuning of the lasing wavelength, however, the quality of the cavity mode needs to be maintained under applied strain, which is not possible for in-plane, electric-dipole coupled NPs.^{4,136} In contrast, large metal NPs in an array can produce a narrow quadrupole lattice resonance with unique out-of-plane charge oscillations^{21, 23} that could result in a nanoscale lasing footprint as well as preserve a high-quality nanocavity mode.

Here we report a robust, stretchable nanolaser platform based on hybrid quadrupole lattice plasmons (HQLs) as the lasing feedback. Large metal NPs in a lattice produced HQLs with sharp

resonances under different strains. We patterned Au NP arrays on elastomeric substrates to achieve mechanical control over the plasmonic nanocavity modes. Stretching the device along the polarization direction resulted in out-of-plane standing waves at the band edge that were tolerant to lateral changes in lattice spacing. We achieved reversibly tunable nanolasing with ultra-sensitive strain responses ($\Delta\lambda = 31$ nm for $\Delta\varepsilon = 0.03$) by mechanically stretching and releasing the substrate. Our semi-quantum model revealed that plasmonic nanocavities exhibited stimulated emission at the localized HQL hot spots. Small changes in strain could be monitored optically with high spatial precision compared to photonic microcavities.

2.2 Hybrid Quadrupole Plasmons from Engineered Nanoparticle Size

Figure 2.1 depicts the scheme of the stretchable nanolaser consisting of arrays of large metal NPs on an elastomeric poly-(dimethylsiloxane) (PDMS) slab. With optimized diameter and height, NP arrays can support hybrid lattice resonances with asymmetric, out-of-plane charge distributions

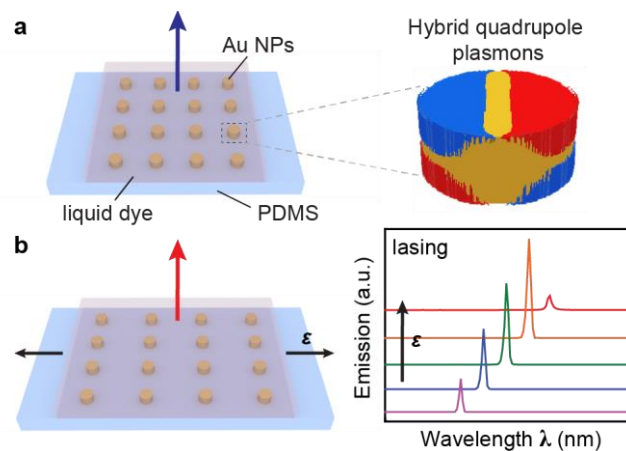


Figure 2.1. Stretchable nanolasing from hybrid quadrupole lattice plasmons (HQLs) in metal nanoparticle (NP) arrays. (a) Scheme of out-of-plane HQL oscillations that are robust to lateral lattice changes. **(b)** Scheme of a wavelength tunable nanolaser with strain ε applied on the elastomeric substrate.

because of the superposition of dipoles and quadrupoles (**Figure 2.1a**). The compact stretchable device was composed of a flexible PDMS substrate and liquid dye molecules to ensure the same dye concentration would surround the NPs upon applied and released strain. Changing interparticle distances directly modulated the cavity resonance, and thus tunable lasing emission was achieved by stretching and releasing the substrate (**Figure 2.1b**).

Based on nanopatterning processes using soft lithography tools,^{6,137,138} we fabricated arrays of large cylindrical Au NPs (NP diameter $d = 260$ nm, spacing $a_0 = 600$ nm). Arrays of large Au NPs on glass or fused silica were fabricated with a soft nanofabrication process referred to as PEEL.⁶ Briefly, we generated periodic photoresist posts on Si wafers by phase-shifting photolithography with controlled post size. The patterns were then transferred into free-standing Au nanohole films after Cr deposition, removal of PR posts, etching through the Si nanoholes and lift-off of Au film. Finally, we created Au NP arrays by metal deposition through the hole-array mask on a transparent substrate and then removal of the mask. A 2-nm Cr layer was deposited in-between for better adhesion between Au NPs and glass or PDMS.

To establish HQLs as potential feedback for stretchable lasing, we first used glass as the substrate and tested the optical properties in a static system. In the measured transmission spectra, we observed both an ultra-sharp mode at $\lambda = 877$ nm (full-width-at-half-maximum, FWHM = 4 nm) and a broad mode at $\lambda = 1006$ nm (FWHM = 115 nm) for a NP height $h = 120$ nm, consistent with simulations using FDTD methods (**Figure 2.2**). Calculated charge distributions indicated the resonance at $\lambda = 1006$ nm was a dipolar lattice plasmon (DL) since the positive and negative charges were separated in-plane. At $\lambda = 877$ nm, the resonance showed charge accumulation at four corners, which we denote as HQL since the asymmetry along z indicates the mode is not

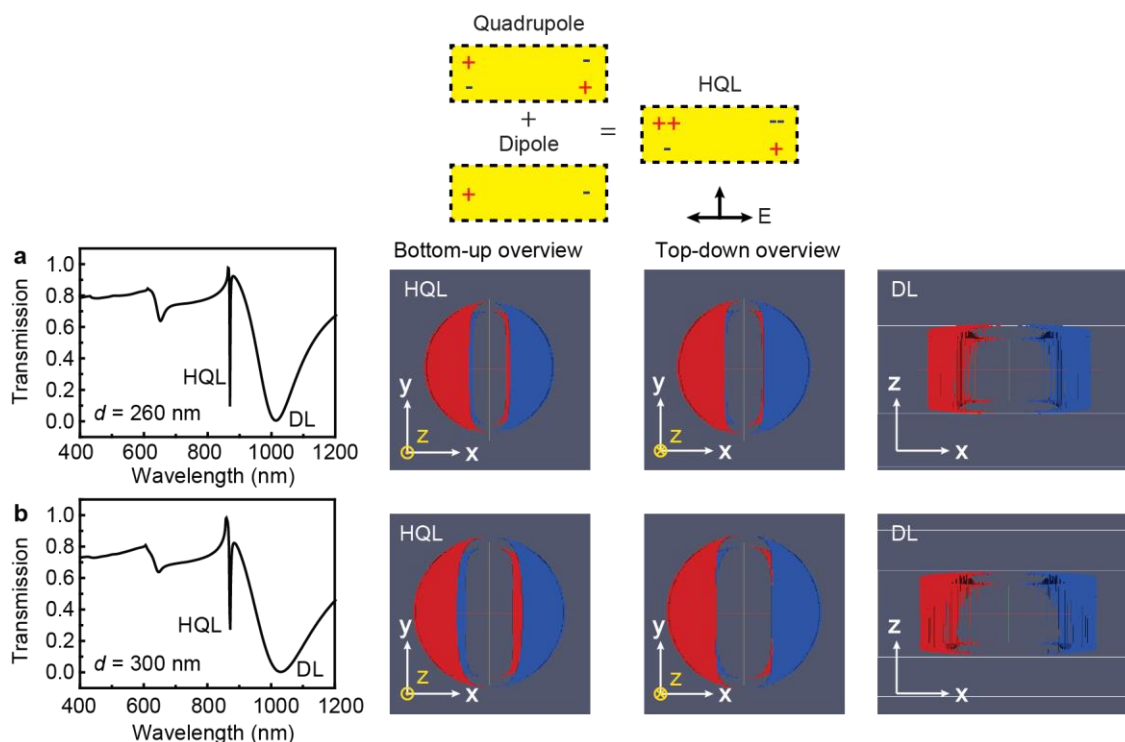


Figure 2.2. Asymmetric charge distributions along z suggest a non-zero dipole momentum at HQL resonance. (a) Simulated charge distribution of Au NPs in an array with diameter $d = 260$ nm, spacing $a_0 = 600$ nm and height $h = 120$ nm. (b) Simulated charge distribution of Au NPs in an array with diameter $d = 300$ nm, spacing $a_0 = 600$ nm and height $h = 120$ nm. The charge distributions in the top-down and the bottom-up overviews suggest that more charges accumulate at the top surface of metal NPs when the incident light comes from the bottom.

purely quadrupolar (**Figures 2.3a-b**). The excitation of high-order resonant modes is intrinsically connected to phase retardation¹³⁹ of the electric field within the large NP volume along the propagation direction z . Therefore, HQLs are very sensitive to NP height h and index difference Δn between the superstrate and the substrate; the resonance intensity dramatically decreased for $\Delta n = 0.1$. Because of the slight index-mismatch between benzyl alcohol (BA, refractive index $n = 1.52$) and glass ($n = 1.48$), sufficient NP height ($h \geq 120$ nm) was critical to support HQL (Figure

2a). In contrast, the sharp HQL mode was tolerant to changes of in-plane lattice features and can be maintained over a wide range of NP diameters ($d = 240\text{-}300\text{ nm}$).

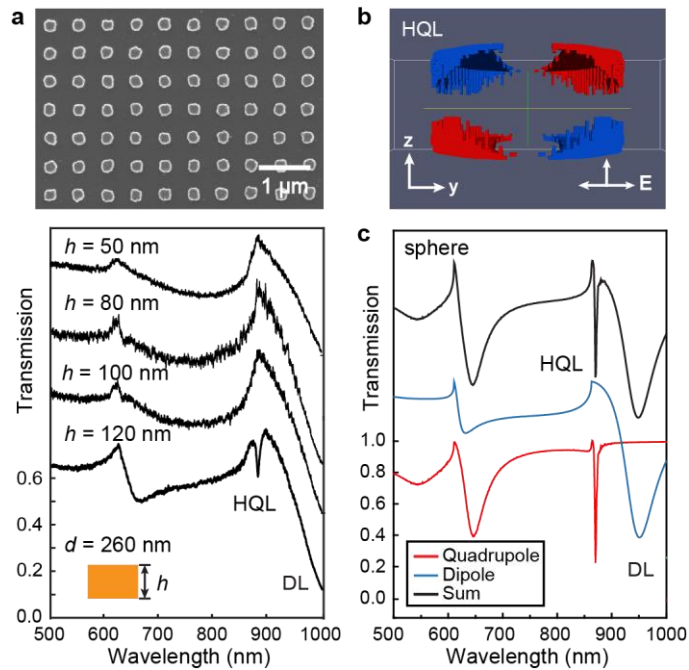


Figure 2.3. Sharp HQL resonance in arrays of large Au NPs. (a) SEM image of large Au NP arrays on glass with lattice spacing $a_0 = 600\text{ nm}$ and measured transmission spectra with different NP height h . (b) Simulated charge distribution of HQL mode for cylinder NP arrays (diameter $d = 260\text{ nm}$ and height $h = 120\text{ nm}$). (c) Decomposition of transmission spectrum into dipolar and quadrupolar contributions based on coupled dipole-quadrupole method with a simplified spherical NP array ($d = 260\text{ nm}$ and refractive index $n = 1.44$). The transmission spectra had an offset of 0.4 and 0.8, respectively.

Analytical calculations using the coupled dipole-quadrupole method¹⁴⁰ revealed the origin of HQL resonances. Within this theoretical approach, a spherical NP array was used to approximate the charge distribution of the cylinder array, and optical spectra were calculated taking into account electric dipole and quadrupole coupling between NPs (Figure 2.3c). Dipole-quadrupole cross-

coupling vanishes in infinite periodic arrays,¹⁴⁰ which enables separation of the contributions from dipole- and quadrupole-coupled modes to the total optical spectrum (**Figure 2.4**). The transmission spectrum was calculated by considering a far-field approximation of the superposition of the incident field and the electric field scattered by the NP array into the forward direction¹⁴¹

$$\mathbf{E} = \mathbf{E}_0 + \mathbf{E}_p + \mathbf{E}_Q \quad (2.1)$$

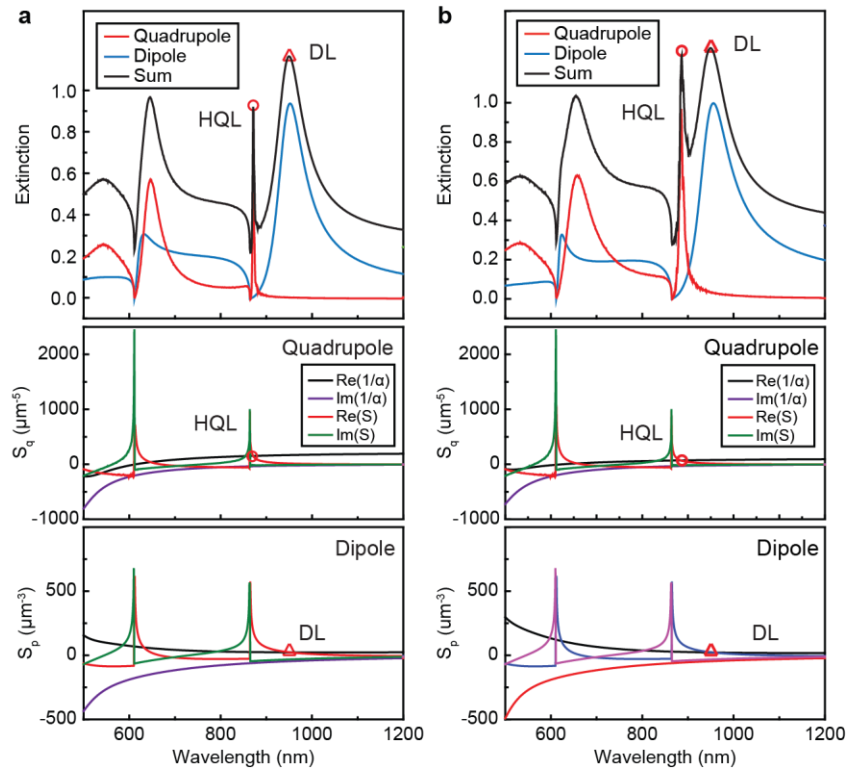


Figure 2.4. Spectral overlap between electric dipole lattice resonance and HQL increases with sphere diameter. (a) Decomposition of extinction spectrum to quadrupole and dipole contributions for spherical Au NP arrays with diameter $d = 260$ nm and, (b) $d = 300$ nm with refractive index $n = 1.44$. Notably, the width of the lattice plasmon resonance is determined by the imaginary part of $(1/\alpha_{NP} - S)$, which becomes larger on the blue side of the spectrum for the dipole resonance. Therefore, the resonance linewidth of DL mode is much broader at small lattice spacing for a fixed NP size.

where E_p and E_Q denote the fields scattered by the dipole and quadrupole multipoles, respectively. Because only the zeroth order transmission was considered, the spectrum calculated using this model is more accurate for wavelengths larger than the Rayleigh anomaly, as all higher-order transmission modes are evanescent in this spectral range. The coupled dipole-quadrupole method can analytically predict the HQL resonance, where the real part of $(1/\alpha_{\text{NP}} - S)$ vanishes, and it is slightly red-shifted compared to the Bragg mode. The quadrupole lattice plasmon contributes dominantly to the HQL resonance, while dipolar coupling still plays a role especially for large Au NPs (Figure 2.4b).

Isolated Au NPs of the same size supported a quadrupole localized surface plasmon at $\lambda = 710$ nm and a dipole one at $\lambda = 1162$ nm. Both coupled to the discrete Bragg mode to result in a hybrid HQL resonance with a Fano-type lineshape (**Figure 2.5**). The in-plane DL mode, however, originated from dipole coupling; quadrupole oscillations were not important at this wavelength. The DL mode was also red-shifted with a much broader resonance because of significant radiative damping associated with the large NPs.¹² At the HQL resonance, the collective charges from the superimposed dipole and quadrupole oscillations partially cancel at the bottom surface while accumulating on the top, which leads to asymmetric charge distributions along z (Figure 2.2). For larger NPs ($d = 300$ nm), the stronger dipolar contributions led to greater charge asymmetry, and the resulting non-zero net dipole moment in the x - y plane facilitated HQL coupling to the far-field.

To fabricate a stretchable laser cavity, we patterned Au NPs with controlled NP diameter and height onto an elastic PDMS slab by metal deposition through a Au nanohole film mask.⁶ AFM images and cross-sections confirmed that metal NPs protruded on the surface of flat PDMS, which increased access of the plasmonic nanocavities to the liquid dye (**Figures 2.6a-c**). The sharp HQL

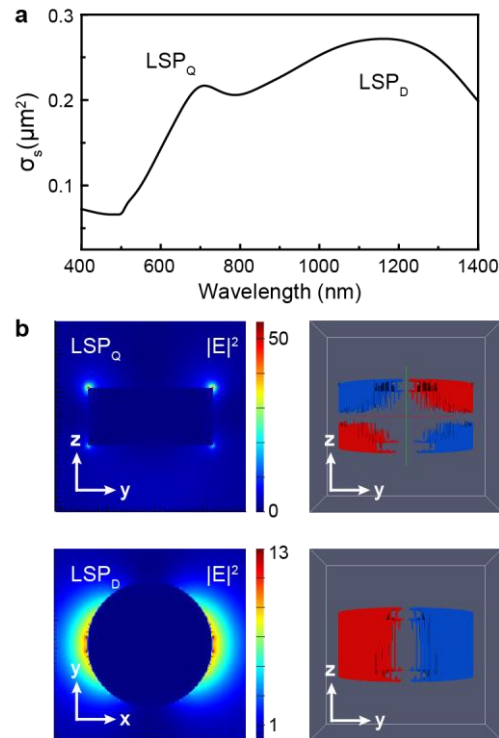


Figure 2.5. Quadrupole and dipole localized surface plasmons both exist in large single Au NPs. (a) Scattering cross section spectra of a single Au NP with $d = 260$ nm and $h = 120$ nm. (b) The near-field and charge distributions at the quadrupole localized surface plasmon (top) and the dipole localized surface plasmon (bottom).

resonance and accompanying intense near fields were robust even if the NP structure was not cylindrical. As the applied strain increased between $\varepsilon = 0$ -0.05, the HQL mode shifted approximately 45 nm yet still maintained its quality factor Q ($= \lambda/\Delta\lambda$, where λ is the resonance wavelength and $\Delta\lambda$ the linewidth) (Figures 2.6d-e). The simulated transmission spectra at the experimental strain range showed excellent agreement assuming a Poisson ratio of 0.5 for PDMS.

Preserved standing wave oscillations within a cavity³² are critical for determining whether a mode can serve as optical feedback for stretchable lasing. Tunable HQL resonances could satisfy these constraints since the lattice symmetry is maintained with strain applied along polarization

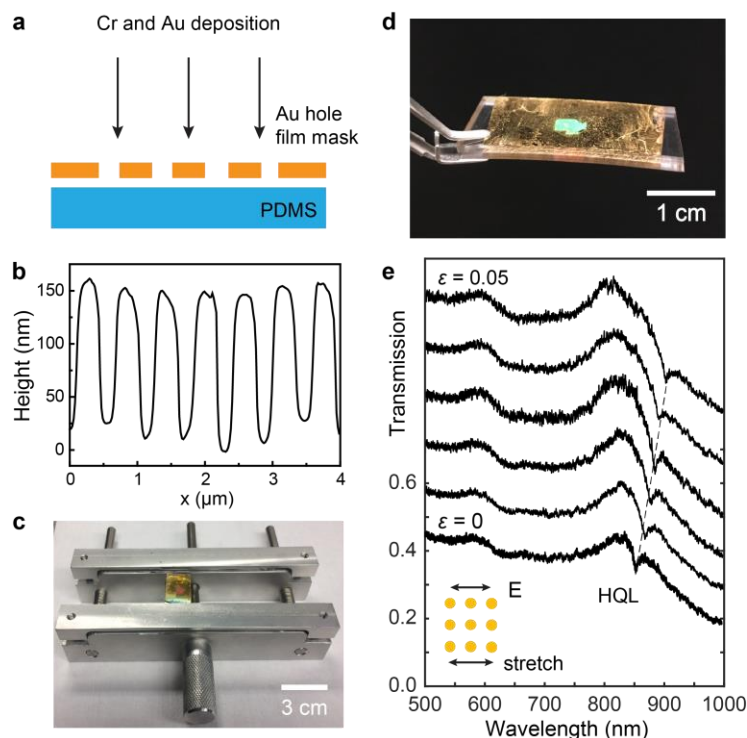


Figure 2.6. Sharp HQL resonance in arrays of large Au NPs robust to lateral stretching. (a) The scheme for depositing Au NPs on top of soft PDMS with a Au hole film mask. (b) The cross-section height profile of patterned Au NPs on PDMS. (c) Photograph of a flexible laser device loaded onto a stretching apparatus. The edges of the PDMS slab were stretched uniaxially with control over the applied strain. (d) Photograph of the patterned Au NP arrays on PDMS. The AFM image and cross-sections can be found in Figure S8. (e) Wavelength tunable HQL modes under strain $\varepsilon = 0-0.05$. Benzyl alcohol and dimethyl sulfoxide (DMSO) solvents were used on top to match the refractive index of glass and PDMS, respectively.

direction y . In the photon dispersion diagram compiled by transmission spectra at different incident angles, the HQL band edge appeared at in-plane wavevector $k_{\parallel} = 0$ with a near-zero group velocity (Figures 2.7a-b). Interestingly, the HQLs result from strong diffractive coupling between NPs along the polarization direction, compared to DL modes where NPs perpendicular to the incident light polarization interact strongly with each other.¹² Under TE polarization, out-of-plane standing

waves appeared at the HQL band edge in y - z plot with alternating phase between adjacent NPs along y (**Figure 2.7c**). The HQL followed the $(0, \pm 1)$ diffraction modes and was red-shifted slightly (8 nm), which was consistent with the HQL resonance predicted by coupled dipole-quadrupole method, and the DL resonance traced the $(\pm 1, 0)$ modes. The mode dispersions were reversed under TM polarization. Increasing interparticle spacing along the polarization direction red-shifted the cavity resonance, while the band-edge state still maintained its characteristic out-of-plane standing

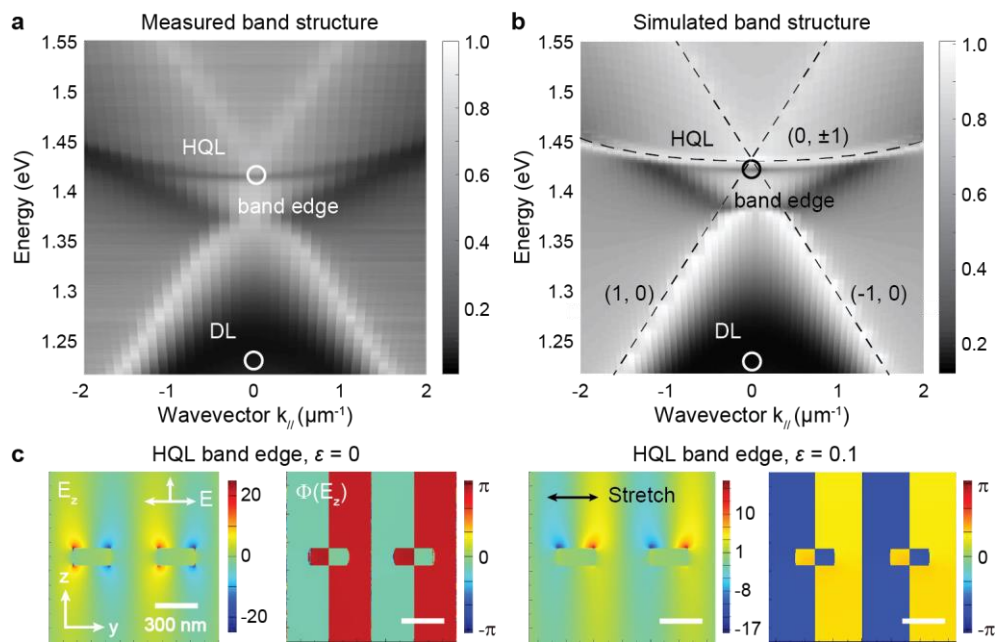


Figure 2.7. Distinct out-of-plane standing waves were preserved at the band-edge state under stretching. (a-b) Measured and simulated dispersion diagrams of large Au NP arrays on glass under TE polarization with $a_0 = 600$ nm, $d = 260$ nm $h = 120$ nm and $n = 1.44$. The dashed lines trace the dispersion of Bragg modes from the NP lattice. (c-d) Near-field (E_z , with units of V/m) and phase distributions ($\Phi(E_z)$, with units of rad) at the band-edge HQL mode under strains $\varepsilon = 0$ and 0.1. The incident field was set as 1 V/m in the simulations. Standing wave patterns with a phase shift of π between adjacent NPs were maintained under applied strain.

wave patterns with a phase shift of π between NPs (spacing $a_0 = 660$ nm at strain $\varepsilon = 0.1$). Notably, the asymmetric electric field distributions were more exaggerated under stretching since the red-shifted Bragg mode led to a larger contribution of dipole oscillations at the HQL resonance. In-plane quadrupolar oscillations also appeared at non-zero $k_{//}$ but were absent at $k_{//} = 0$, where the symmetry of the plane incident field precluded excitation of this mode (**Figure 2.8**).

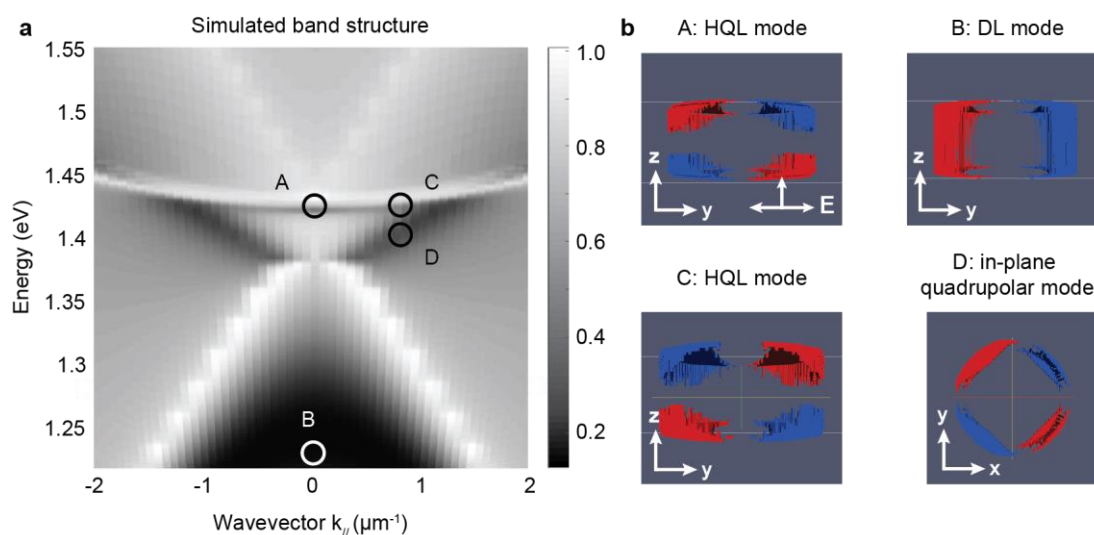


Figure 2.8. Multiple resonant modes exist simultaneously in large Au NP arrays. (a) Simulated optical band structures under TE polarization. (b) Charge distributions at resonances denoted in panel a. HQL mode appeared at both zero and non-zero wavevectors, while in-plane quadrupolar mode was absent at $k_{//} = 0$ since the symmetry of normal incident light precluded the excitation of this mode.

2.3 Stretchable Lasing from Nanoparticle Arrays

To test lasing from HQL resonances, we put a droplet of IR-140-BA solution on top of Au NP arrays on glass and pumped the dye with an 800-nm fs-pulsed laser under TE polarization (**Figure 2.9a**). In the emission spectrum collected normal to the sample surface, a narrow lasing peak (FWHM = ~ 0.3 nm) appeared at $\lambda = 871$ nm close to the HQL resonance (**Figures 2.9b-c**). Power-

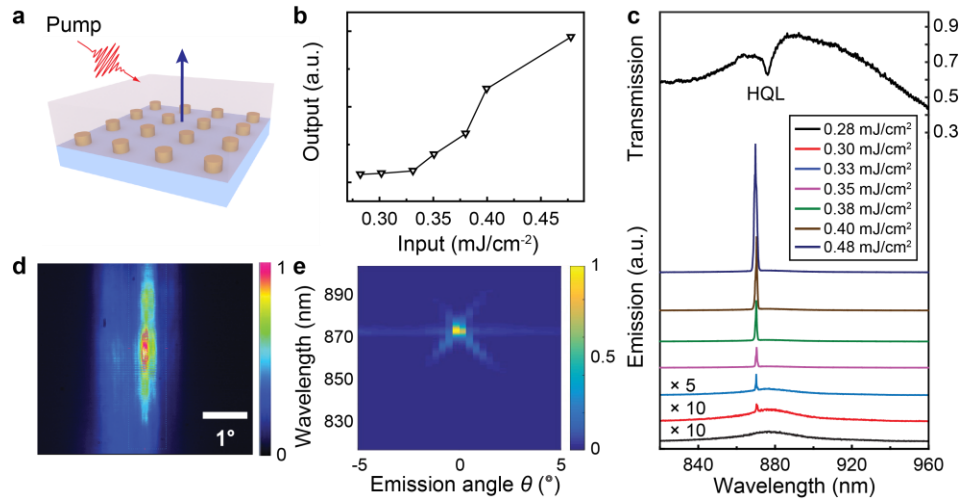


Figure 2.9. Nanolasing from HQL cavity resonance showed localized build-up at the plasmonic hot spots. (a) Scheme of the lasing detection where emission was collected normal to the sample surface. **(b)** Simulated near-field enhancement $|E|^2$ confined around plasmonic hot spots at HQL mode with units of V^2m^{-2} . **(c)** Measured emission spectra with increased pump power for Au NP arrays on glass (dye concentration 3 mM). **(d)** Spatial distribution of spontaneous emission rate (N_2/τ_{21}) and stimulated emission rate $\frac{1}{\hbar\omega}E\frac{dP}{dt}$ when lasing occurred with units of $s^{-1}m^{-3}$. Scale bar is 100 nm.

dependent output profiles showed a nonlinear increase of lasing intensity above threshold (~ 0.3 mJ/cm^2). By mapping the angle-resolved emission, we identified that the lasing mode came from the band-edge state at $k_{||} = 0$. Consistently, a directional and confined output beam spot appeared in the far-field (divergence angle $< 1^\circ$). We observed that lasing had a minor blueshift compared to the cavity resonance ($\lambda_{HQL} = 876$ nm) in experiments, which might be attributed to the optical pulling effect³² and modified refractive index environment at high pump fluences.

We prepared stretchable lasing devices by sandwiching a droplet of liquid dye IR-140-DMSO between Au NP arrays on PDMS and a glass cover slide. By stretching the PDMS and aligning the pump polarization along the symmetric axis of a square lattice, we achieved continuous tuning

over 31 nm in lasing wavelength with varying strain $\varepsilon = 0.02-0.05$ (**Figure 2.10**). At the HQL resonance, the collective coupling between NPs happens at the same direction of the pump polarization, hence only a single lasing mode showed up despite the Poisson effect of PDMS under stretching. The lasing emission exhibited excellent recovery after the strain was released with nearly zero hysteresis, and cyclic changes in strain allowed real-time modulation of the lasing output. No lasing signal was observed at $\varepsilon = 0$ since the HQL resonance ($\lambda_{\text{HQL}} = 851$ nm) deviated from the gain emission envelope (center at 875 nm, FWHM = ~ 50 nm). Our stretchable nanolaser device was robust in structural stability, and only a minor wavelength shift (< 1 nm) occurred because of shrinking of the PDMS slab in DMSO. Significantly, stretchable nanolasing from metal NP arrays achieved a much higher figure-of-merit ($\Delta\lambda = 31$ nm for $\Delta\varepsilon = 0.03$) than those based on photonic crystals with similar lattice spacings ($\Delta\lambda = 26$ nm for $\Delta\varepsilon = 0.2$).^{122,123} We attribute this improvement to the tuning of HQL wavelengths directly by small changes in submicron

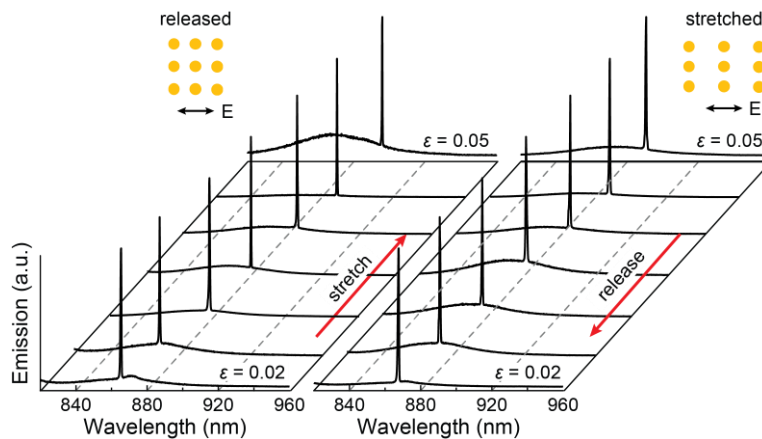


Figure 2.10. Reversibly tunable nanolasing from HQL mode by stretching and releasing the elastomeric substrate. Measured reversible, tunable nanolasing under strain $\varepsilon = 0.02-0.05$. The normalized emission intensities were multiplied by a factor of 9, 9, 1, 2, 5, 8, 17 for stretching and 2, 4, 4, 4, 2, 1, 2 for releasing, respectively from low to high strains.

interparticle spacing, while the microscale photonic cavities are less sensitive to nanoscale structural changes due to the diffraction limit. Note that the wavelength tuning range of stretchable lasing is primarily restricted by the emission bandwidth of dye molecules (< 50 nm), while the HQL cavity mode can preserve the sharp resonances over a broad spectral window from visible to near-infrared regimes.

2.4 Semi-quantum Modeling of Plasmon Nanolasing Buildup

To provide insights into the spatial- and time-dependent lasing buildup in nanocavity arrays, we developed a semi-quantum model by integrating a four-level gain system (**Figure 2.11a**) and a FDTD approach.^{12,85} The oscillator equations that depict the driven polarization field by an external pump are below:

$$\begin{aligned} \frac{d^2 P_e}{dt^2} + r_e \frac{dP_e}{dt} + w_e^2 P_e &= \xi_e (N_2 - N_1) E \\ \frac{d^2 P_a}{dt^2} + r_a \frac{dP_a}{dt} + w_a^2 P_a &= \xi_a (N_3 - N_0) E \end{aligned} \quad (2.2)$$

where \mathbf{E} and \mathbf{P} are the electric field and polarization field, w_e is the transition frequency, r_e is the bandwidth of the targeted transition including radiative, nonradiative and collision effects, and N_i is the population density at different energy levels.

Initially, we pumped the four-level system from the ground state (population density $N_0 = 1$, $N_1 = N_2 = N_3 = 0$) and collected all emitted flux with a plane monitor placed $0.3 \mu\text{m}$ away on top of the NPs. The nonradiative dephasing rate r_e in above oscillator equation introduces broadening of the radiative emission linewidth, which allows for lasing over a range of wavelengths. For simplification, the rate equation of dye molecules was as described as a four-level system to capture the dominant pump and emission processes.

$$\begin{aligned}
\frac{dN_3}{dt} &= -\frac{N_3(1-N_2)}{\tau_{32}} - \frac{N_3(1-N_0)}{\tau_{30}} + \frac{1}{\hbar\omega_a} E \frac{dP_a}{dt} \\
\frac{dN_2}{dt} &= \frac{N_3(1-N_2)}{\tau_{32}} - \frac{N_2(1-N_1)}{\tau_{21}} + \frac{1}{\hbar\omega_e} E \frac{dP_e}{dt} \\
\frac{dN_1}{dt} &= \frac{N_2(1-N_1)}{\tau_{21}} - \frac{N_1(1-N_0)}{\tau_{10}} - \frac{1}{\hbar\omega_e} E \frac{dP_e}{dt} \\
\frac{dN_0}{dt} &= \frac{N_3(1-N_0)}{\tau_{30}} + \frac{N_1(1-N_0)}{\tau_{10}} - \frac{1}{\hbar\omega_a} E \frac{dP_a}{dt}
\end{aligned} \tag{2.3}$$

Modeling with a four-level gain system and a time domain approach confirmed that lasing occurred at the same wavelength as the HQL resonance and can be tuned by the interparticle spacing in a lattice (**Figure 2.11b**). Controlling the spatial distribution of lasing build-up on the nanoscale is essential in the design of stretchable nanolasers. Radiative loss was strongly

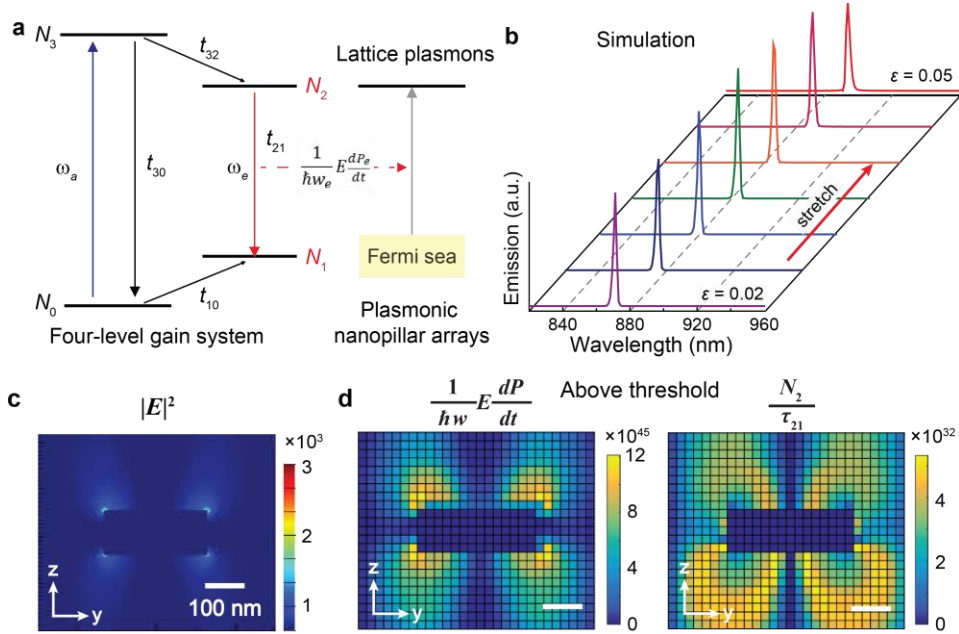


Figure 2.11. Reversibly tunable nanolasing from HQL mode by stretching and releasing the elastomeric substrate. (a) Scheme of the energy transfer process from four-level gain media to lattice plasmon resonances in metal NP arrays. (b) Simulated tunable lasing emission from HQL resonance. (c) Simulated near-field enhancement $|E|^2$ confined around plasmonic hot spots at HQL mode, with unit of V^2m^{-2} . (d) Spatial distribution of spontaneous emission rate (N_2/τ_{21}) and stimulated emission rate $\frac{1}{\hbar\omega_e} E \frac{dP_e}{dt}$ when lasing occurred.

suppressed at the HQL resonance because of coherent coupling between NPs⁴ that resulted in hybrid quadrupole oscillations with intense optical confinement and near-field enhancement ($|\mathbf{E}|^2/|\mathbf{E}_0|^2 > 3000$). Unlike in conventional photonic lasers where lasing occurs in the bulk gain,³² lasing at HQL resonances was localized to the deep subwavelength vicinity of the metal NPs (< 50 nm) (**Figure 2.11c**). Above threshold, stimulated emission ($\frac{1}{\hbar\omega} \mathbf{E} \frac{dP}{dt}$) accumulated at the HQL hot spots (**Figure 2.11d**), which could enable ultra-sensitive monitoring of local strain changes on the nanoscale. Note that population inversion was depleted in these areas after the onset of lasing, which lowered the spontaneous emission rate (N_2/τ_{21}). The strong near-field \mathbf{E} enhanced the stimulated emission rate⁸⁵ by a factor of E^2 , which can expedite the lasing emission dynamics and reduce power consumption. Modeling based on a semi-quantum method showed good agreement with the experiments, while the broader lasing peaks were attributed to a lack of dephasing in the description of the dye molecule emission.⁸⁵

2.5 Summary and Outlook

In conclusion, we realized robust stretchable nanolasing based on hybrid quadrupole plasmons in large metal NP arrays. This work offers critical insights to manipulating high-order oscillations in plasmon nanocavities. Because our stretchable laser design spatially separates the nanocavity from the gain media, different gain materials such as dye molecules, quantum dots, and 2D materials can be incorporated for wavelength tuning from the UV to near-infrared. We expect that this versatile nanolaser system will not only have wide applications in flexible photonic devices, in-situ biomedical imaging, and optical communication, but also open possibilities for mechanical modulation of strong light-matter interactions in fluorescence, photocatalysis, and quantum optics.

Chapter 3. Structural Engineering in Plasmonic Superlattices

Abstract

Single band-edge states can trap light and function as high-quality optical feedback for microscale lasers to nanolasers. However, access to more than a single band-edge mode for nanolasing has not been possible because of limited cavity designs. This chapter describes how plasmonic superlattices—finite-arrays of NPs (patches) grouped into microscale arrays—can support multiple band-edge modes capable of multi-modal nanolasing at programmed emission wavelengths and with large mode spacings. Different lasing modes showed distinct input-output light-light behavior and decay dynamics that could be tailored by NP size. Modeling the superlattice nanolasers with a four-level gain system and a time-domain approach revealed the accumulation of population inversion at plasmonic hot spots that can be spatially modulated by the diffractive coupling order of the patches. Symmetry-broken superlattices exhibited switchable nanolasing between a single mode and multiple modes. In addition, this chapter shows that beyond the microscale patterning with as-fabricated lattice features, microscale molding of dielectric superstrate on top of plasmonic NPs can produce reconfigurable, polarization-dependent superlattice plasmon resonances and optical band structures. Coherent nanoscale light sources with multiple tunable, on-demand optical modes can enable multiplexing for on-chip photonic devices and offer prospects for multi-modal laser designs.

Related references

Wang, D.; Yang, A.; Hryn, A.J.; Schatz, G.C.; Odom, T.W. "Superlattice Plasmons in Hierarchical Au Nanoparticle Arrays," *ACS Photonics* **2**, 1789 (2015)

Wang, D.; Yang, A.; Wang, W.; Hua, Y.; Schaller, R.D.; Schatz, G.C.; Odom, T.W. "Band-edge Engineering for Controlled Multi-modal Nanolasing in Plasmonic Superlattices," *Nature Nanotechnology* **12**, 889 (2017)

Wang, D; Hu, J.; Schatz, G.C.; Odom, T.W. "Plasmonic Superlattices from Superstrate Micro-molding" *In preparation*

3.1 Introduction

Band structure engineering is critical for controlling emission wavelengths and efficiency in electronic and photonic materials.¹⁴²⁻¹⁴⁴ Single band-edge states that can trap slow light have functioned as high-quality optical feedback for lasing from photonic bandgap crystals,^{13,145} metal-dielectric waveguides,¹⁴⁶ and metal NP arrays.^{12,52,61,147} However, access to more than a single band-edge mode for nanolasing has not been possible because of limited cavity designs. Here we show that plasmonic superlattices—finite-arrays of NPs (patches) grouped into microscale arrays—can support multiple band-edge modes that can serve as feedback for nanolasing with controlled and large modal spacing. The different lasing modes showed distinct output emission behavior and decay dynamics that could be tailored by NP size. Besides engineering spectral separation between lasing modes by changing patch periodicity, we designed symmetry-broken superlattices with nanolasing switchable between a single and multiple lasing modes. We expect that coherent nanoscale light sources with widely spaced, tunable, and on-demand optical modes and unprecedented tunability of output behavior can increase information storage for on-chip devices and offer prospects for multi-modal laser designs.

Engineering electronic and photonic band structures can control the emission wavelengths and output efficiencies of semiconductor materials and optical devices.¹⁴²⁻¹⁴⁴ Slow light trapped at band-edge states can support standing waves that have also functioned as high-quality optical feedback for lasing from photonic bandgap crystals,^{13,145} metal-dielectric waveguides,¹⁴⁶ and metal NP arrays.^{12,61,147} Compared to semiconducting lasers, plasmon nanolasers can support ultrasmall mode volumes that can beat the diffraction limit by exploiting localized surface plasmons from single NPs^{38,42,43} and surface plasmon polaritons on metal films;^{36,39} however, most cavity

architectures suffer from large radiative losses and lack beam directionality. Moreover, unwanted multi-modal nanolasing from plasmonic lasers exhibits both uncontrolled mode spacing and output behavior.^{36,39,49,54}

Different from periodic dielectric structures that support both upper and lower band edges in distributed feedback lasers,⁶⁴ periodic metal NP arrays in a homogeneous dielectric environment exhibit only single band-edge lattice plasmons that are characterized by suppressed radiative loss and sub-wavelength localized field enhancement around the NPs.^{4,5,9} Recently, we discovered that high-quality band-edge lattice plasmons (quality factor $Q > 200$) can contribute to single-mode lasing at room-temperature with directional emission and lasing wavelengths that can be tuned in real time.^{12,52} To achieve multiplexing, multiple optical frequencies with well-defined and separated spacings are needed to increase storage capability and facilitate optical processing.^{22,148,149} However, access to more than a single band-edge mode for nanolasing has not been possible because of limited cavity designs.

In this chapter, we demonstrate how plasmonic NP superlattices enable access to multiple band-edges at zero and nonzero wavevectors that can be exploited for multi-modal lasing with characteristics distinct from traditional photonic and plasmonic lasers. Compared to multi-modal lasing that usually lacks tunability, superlattice plasmons can achieve accurate control over the wavelength and spectral separation of multiple lasing modes. Moreover, tuning NP size can provide an additional degree of freedom for manipulating the output behavior of different lasing modes. As a result of symmetry breaking of the NP superlattice, dynamically switchable lasing between single and multiple modes was achieved. Our modeling of multi-modal lasing based on a four-level gain system and a time-domain approach not only showed excellent agreement with

experiments but also revealed that the switchable lasing can be attributed to the spatial distribution of population inversion at dipolar plasmonic hot spots.

3.2 Multiscale Patterning of Superlattice Arrays

Hierarchical plasmonic structures show unique optical properties because of the short-range nature of LSPs and the long-range nature of surface plasmon polaritons.^{6,150,151} Multiple waveguide modes with narrow resonances were observed in one-dimensional (1D) nanowire superlattices incorporating both nanowire periodicity and patch periodicity.¹⁵² In addition, for NP superlattices composed of assemblies of synthesized NP building blocks, the volume fraction of both the metal and dielectric materials in the superlattice influenced the effective permittivity of the assembly and optical properties.^{153,154} Besides three-dimensional (3D) NP superlattices made by bottom-up bio-programmable DNA assembly,¹⁵⁵ two-dimensional (2D) NP superlattices can be fabricated by top-down methods such as electron-beam lithography and photolithography, where finite-arrays of NPs (patches) are grouped into larger arrays.^{6,156} Despite this hierarchical architecture, the spectral mismatch of the LSPs of the NPs and Bragg modes from patch periodicity did not show evidence of coupling.¹⁵⁶ Also, limited overall patterned areas from e-beam lithography ($100 \times 100 \mu\text{m}^2$) only resulted in broad optical resonances (FWHM > 50 nm).

To produce NP superlattices with uniform particle sizes, we developed a multi-scale nanofabrication approach to fabricate hierarchical Au NP arrays on glass starting with a soft nanofabrication procedure referred to as PEEL (photolithography, etching, electron-beam deposition and lift-off).^{137,157,158} Briefly, hierarchical photoresist posts on Si wafers were generated by contact photolithography, Cr deposition, resist lift-off, and phase-shifting photolithography with a PDMS mask¹³⁸ (**Figure 3.1**). Here, 8-nm Cr was used as an isolation layer to create uniform

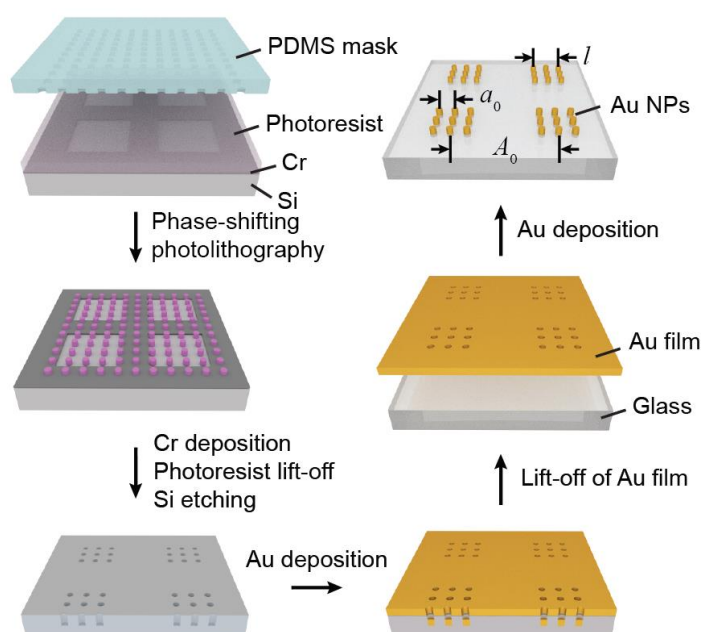


Figure 3.1. Scheme of the multiscale patterning technique. Typical NP periodicity $a_0 = 600$ nm, patch side length $l = 6 \mu\text{m}$ and patch periodicity $A_0 = 9 \mu\text{m}$.

photoresist posts within the patch. Hierarchical patterns of photoresist posts were then transferred into free-standing Au films of hierarchical nanohole arrays by PEEL. Basically, the hierarchical photoresist posts covered with Cr layer from thermal deposition were lifted off with photoresist remover. Deep reactive ion etching (DRIE) was then used to etch cylindrical pits through the microscale Cr holes (depth ~ 150 nm) inside Si. After depositing ~ 90 nm Au and etching the Cr sacrificial layer, a hierarchical Au nanohole array film was produced and floated onto glass substrate. Finally, Au deposition through the hole-array mask on glass substrates and then removal of the mask resulted in hierarchical Au NP arrays with arbitrarily designed microscale and nanoscale features.

Multiscale patterning for generating hierarchical NP arrays has two key advantages: (1) the uniform exposure of UV light ensures that the photoresist posts are homogeneous from patch

center to edge; and (2) the Cr masks and PDMS masks can be independently selected to control the patch periodicity A_0 , patch side length l , and NP periodicity a_0 . The PDMS mask determined the sub-micron NP periodicity a_0 , and the Cr mask determined the microscale patch length l and patch periodicity A_0 . In experiments, a poly (dimethylsiloxane) (PDMS) mask with square lattice periodicity $a_0 = 600$ nm was used for phase-shifting photolithography to produce photoresist posts with varying diameter. Cr masks with patch features: ($l = 6$ μm , $A_0 = 9$ μm), ($l = 6$ μm , $A_0 = 12$ μm), ($l = 18$ μm , $A_0 = 24$ μm), and ($l = 18$ μm , $A_0 = 32$ μm) were used for contact photolithography.

3.3 Superlattice Plasmons in Hierarchical Arrays

In this section, we demonstrate that superlattice plasmons can be supported in hierarchical Au NP arrays. We observed multiple narrow superlattice plasmon resonances in 2D arrays of NP patches. To confirm that the origin of the multiple resonances was from the patch periodicity, we fabricated 1D NP patches and characterized their orientation-dependent transmission properties. Moreover, we identified the specific Bragg modes that contributed to the superlattice resonances by simulating both far-field transmission and near-field properties. Similar to lattice plasmons in infinite NP arrays that are defined by NP LSP and NP periodicity, we found that the superlattice plasmons in hierarchical NP arrays can be attributed to coupling of single-patch lattice plasmons with the high-order Bragg modes of the microscale patch periodicity. Finally, we demonstrated that the resonance position and the number of dominant modes of superlattice plasmons can be tuned by varying the patch periodicity and overall patch size.

The transmission spectra of hierarchical Au NP arrays were characterized in an index-matched environment consisting of an oil superstrate ($n = 1.52$) that matched the glass substrate. With the inclusion of microscale patch periodicity in hierarchical arrays, more high-order Bragg modes fell

within the resonance envelope of metal LSP to form multiple lattice plasmons with narrow resonances. To determine the influence of patch periodicity on the lattice plasmon resonances, we compared the resonance position of hierarchical NP arrays to that of an infinite NP array. For infinite NP arrays with NP periodicity $a_0 = 600$ nm and NP diameters $d = 140$ nm, we observed a single lattice plasmon mode at $\lambda_L = 903$ nm (**Figure 3.2a**).

For 2D hierarchical NP arrays with the same NP characteristics but with $l = 6$ μm and $A_0 = 9$ μm , however, two narrow resonances appeared (**Figure 3.2b**). The shorter-wavelength superlattice resonance at $\lambda_{SL} = 904$ nm had nearly the same position and FWHM width (15 nm) as the lattice

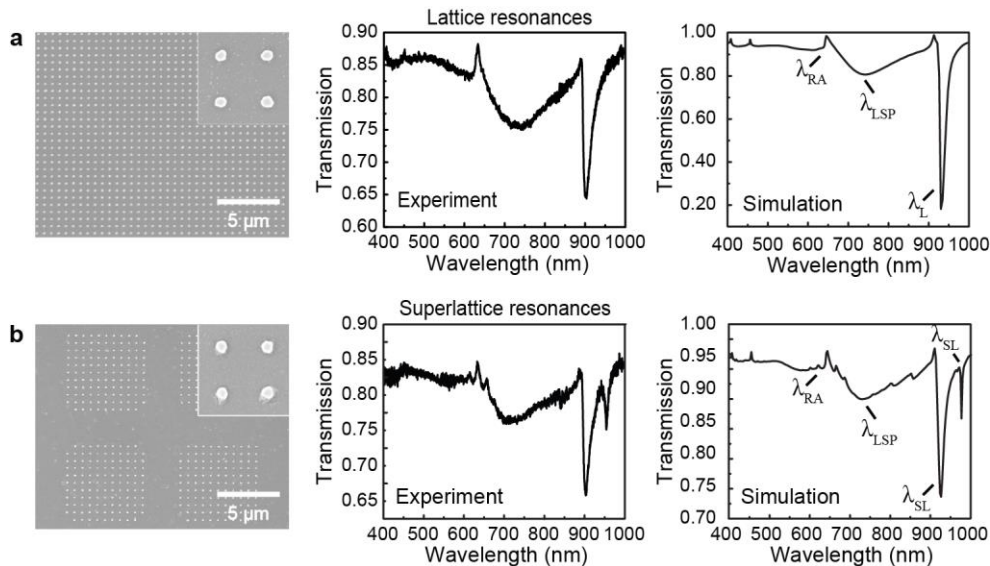


Figure 3.2. Comparison of transmission spectra between infinite arrays and 2D hierarchical Au NP arrays. (a) SEM images of an infinite NP array with NP periodicity $a_0 = 600$ nm and NP diameters d around 140 nm. Linear optical properties from experiments and FDTD simulations ($n = 1.52$) are in excellent agreement. **(b)** SEM images of 2D hierarchical NP arrays with $a_0 = 600$ nm, patch side length $l = 6$ μm , patch periodicity $A_0 = 9$ μm and NP $d = 140$ nm. Linear optical properties from experiment and simulations ($n = 1.52$) are in excellent agreement.

plasmon λ_L in the infinite NP array. The longer-wavelength superlattice resonance appeared at $\lambda_{SL} = 954$ nm, with a narrower FWHM of 7 nm. As observed in both infinite and hierarchical arrays, the broad resonance λ_{LSP} around 730 nm was the LSP of a single Au NP, and the Rayleigh anomaly peak λ_{RA} around 630 nm was from coupling with higher-order Bragg modes (Figure 3.2a). FDTD simulations were in good agreement with experiments. The small shift between simulated and experimental resonance wavelengths can be explained in part by the dispersive properties of the immersion oil used for index-matching.

To confirm that the multiple resonances were from patch periodicity, we characterized the orientation-dependent transmission properties of 1D NP patches (**Figure 3.3a**). These 1D patches had the same a_0, l , and A_0 as the 2D hierarchical arrays, but where A_0 was defined only along the x -direction. This symmetry-breaking structure shows polarization-dependent optical properties and different coupling along the x and y directions. To observe the evolution of the transmission spectra with respect to polarization angle more clearly, we fabricated NPs with larger diameters $d = 160$ nm that showed stronger longer-wavelength resonances. With the incident light polarized along x , the individual NPs exhibited dipolar oscillations also along x . The NPs aligned perpendicular to the oscillation direction coupled strongly with each other. Since only NP periodicity a_0 existed along y , the transmission spectrum showed a single narrow lattice plasmon resonance, similar to that of infinite NP array (**Figure 3.3b**). As the polarization angle θ increased from 0° (x) to 90° (y), the narrow resonance at $\lambda_{SL} = 913$ nm maintained its location and amplitude but a new resonance ($\lambda_{SL} = 958$ nm) gradually emerged and increased in intensity. The broad resonance around 730 nm was the λ_{LSP} from single Au NP, and the peak λ_{RA} around 630 nm was Rayleigh anomaly seen earlier in Figure 3.2b. Note that both were at fixed wavelengths even as θ changed.

The spectral evolution with respect to polarization angle suggests that the infinite-like resonance at $\lambda_{SL} = 913$ nm in 1D hierarchical patches and the single lattice plasmon λ_L of the infinite NP array are similar regarding resonance wavelength and intensity. In contrast, the resonance at $\lambda_{SL} = 958$ nm in the 1D NP patches, which gradually appeared and kept the same position as θ increased, can be attributed to the patch periodicity A_0 .

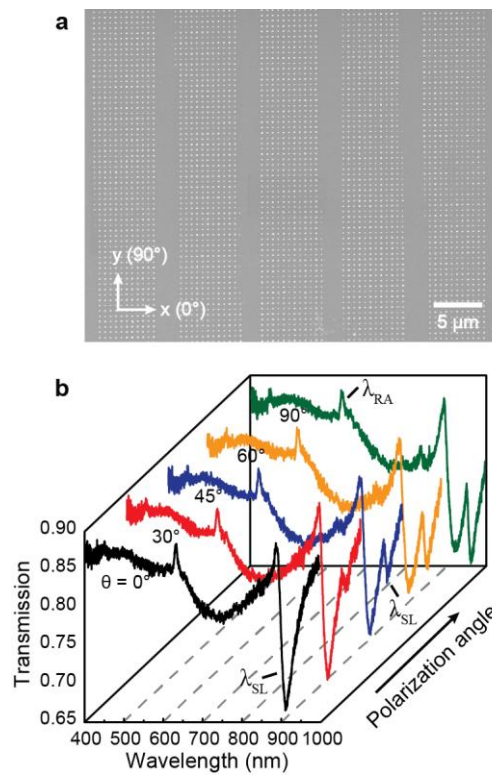


Figure 3.3. Orientation-dependent transmission properties of 1D Au NP patches. (a) SEM image of fabricated 1D Au NP patches on top of glass, with patch side length $l = 6 \mu\text{m}$, patch periodicity $A_0 = 9 \mu\text{m}$ along x and NP diameter $d = 160$ nm. (b) Evolution of transmission spectrum with increasing polarization angle θ from 0° (x direction) to 90° (y direction). The resonance at $\lambda_{SL} = 913$ nm maintained its location and amplitude but the resonance at $\lambda_{SL} = 958$ nm gradually emerged and increased in intensity, which indicated that the latter originated from patch periodicity.

To demonstrate the influence of patch periodicity on the superlattice plasmon resonances, we simulated far-field transmission spectra for a single Au NP, an isolated Au NP patch, and 2D hierarchical Au NP arrays. The simulations can study resonances from a single NP and patch and eliminate coupling effects from nearby NPs and patches, which cannot be achieved in experiments where the incident light spot ($\sim \text{mm}^2$) was much larger than the single NP or patch size. **Figure 3.4a** shows a broad LSP resonance λ_{LSP} from a single Au NP with diameter $d = 140 \text{ nm}$. For a

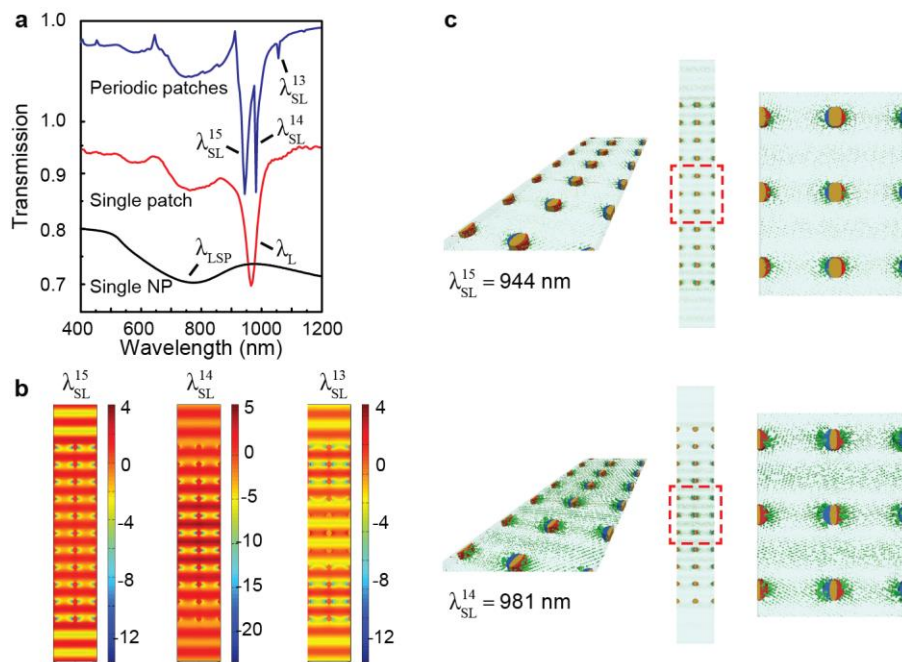


Figure 3.4. Far-field transmission, near-field electric field, and charge distribution of hierarchical Au NP arrays indicating the origin of superlattice plasmons. (a) Linear optical properties of a single NP, a single patch, and periodic patches with the same NP diameter $d = 160 \text{ nm}$, height $h = 50 \text{ nm}$ and spacing $a_0 = 600 \text{ nm}$. Periodic patches had side length $l = 6 \mu\text{m}$ and periodicity $A_0 = 9 \mu\text{m}$. **(b)** Near-field electric field distributions of superlattice plasmons at $\lambda_{\text{SL}}^{15} = 944 \text{ nm}$, $\lambda_{\text{SL}}^{14} = 981 \text{ nm}$, and $\lambda_{\text{SL}}^{13} = 1056 \text{ nm}$ within plotted area of $1.2 \mu\text{m} \times 9 \mu\text{m}$. In simulation, the amplitude of incident plane wave (polarized along x) was set as 1 V/m . The plotted electric field is the real part of E_x with units of V/m . **(c)** Charge distribution of superlattice plasmons at $\lambda_{\text{SL}}^{15} = 944 \text{ nm}$ and $\lambda_{\text{SL}}^{14} = 981 \text{ nm}$ within plotted area of $1.2 \mu\text{m} \times 9 \mu\text{m}$.

single patch containing 10×10 NPs with $a_0 = 600$ nm and $d = 140$ nm, consistent with the isolated patch in Figure 3.2b, a single lattice plasmon resonance was observed at $\lambda_L = 965$ nm (FWHM 35.7 nm). The single-patch lattice plasmon arose from the coupling of the metal LSP and the Bragg mode determined by the NP periodicity a_0 .

For 2D hierarchical NP arrays with $l = 6$ μm and $A_0 = 9$ μm , two narrow resonances were observed at $\lambda_{\text{SL}}^{15} = 944$ nm and $\lambda_{\text{SL}}^{14} = 981$ nm as well as one weak resonance at $\lambda_{\text{SL}}^{13} = 1056$ nm, whose diffraction peaks were in good agreement with the calculated Bragg modes at the $n = 15$, $n = 14$ and $n = 13$ orders from patch periodicity $A_0 = 9$ μm (at 912 nm, 976 nm and 1051 nm respectively). The FWHM of the two dominant lattice plasmons at λ_{SL}^{15} and λ_{SL}^{14} were 19.2 nm and 3.1 nm respectively, much narrower than that of the single-patch resonances. Similar to lattice plasmons in infinite arrays from coupling the NP LSP and Bragg mode from NP periodicity a_0 , superlattice plasmons in hierarchical arrays can be described by the coupling of single-patch lattice plasmons with high-order Bragg modes determined by the patch periodicity A_0 . Two-step coupling was involved in generating superlattice plasmons: (1) NP coupling within a single patch, and then (2) patch-patch coupling.

The electric field and charge distribution around NPs at the superlattice plasmon resonances illustrated the influence of patch periodicity A_0 on the near-field NP coupling. For resonances at $\lambda_{\text{SL}}^{15} = 944$ nm, $\lambda_{\text{SL}}^{14} = 981$ nm, and $\lambda_{\text{SL}}^{13} = 1042$ nm, the electric field was localized both around and between NPs but with larger enhancement at the narrower resonance at λ_{SL}^{14} than the other two modes (**Figure 3.4b**). Compared to λ_{LSP} , single-patch lattice plasmons λ_L had 10-fold local electric field $|E|$ peak enhancement, while superlattice plasmons had 15-fold and 40-fold enhancement at λ_{SL}^{15} and λ_{SL}^{14} respectively. At λ_{SL}^{15} and λ_{SL}^{14} , positive and negative charges were located around the

NP surface and distributed along the polarization direction of incident light, indicating a dipolar distribution (**Figure 3.4c**). At resonances of λ_{SL}^{15} , λ_{SL}^{14} , and λ_{SL}^{13} , there were 15, 14, and 13 phase oscillations within a single patch, which agreed with the order of the Bragg mode that coupled to single-patch lattice plasmons (Figure 3.4b). Similarly, at the lattice plasmon resonance in infinite NP arrays with $a_0 = 600$ nm, exactly 15 overall phase oscillations spanned the same length scale of patch periodicity ($A_0 = 9$ μm). Notably, although hierarchical arrays could be viewed as an infinite array with missing NPs, the in-phase oscillation between NPs at infinite-like superlattice plasmon resonance λ_{SL}^{15} was the same as that of lattice plasmon resonance λ_{L} in infinite arrays. In contrast, the resonance at λ_{SL}^{14} had single-period phase oscillations and the one at λ_{SL}^{13} had two-period phase oscillations between NPs within the single patch. For 1D NP patches at different polarization angles, the in-phase oscillations between NPs were also maintained at λ_{SL}^{15} ($\theta = 0^\circ$ to 90°), while single-period phase oscillations existed at λ_{SL}^{14} ($\theta > 0^\circ$).

To illustrate the tunability of superlattice plasmons, we increased A_0 from 9 μm to 12 μm while keeping patch side length l fixed at 6 μm (**Figure 3.5a**). Larger patch periodicity resulted in more high-order Bragg modes with smaller separations and that fell within the resonance envelope of single-patch lattice plasmons. Two dominant lattice plasmon modes at $\lambda_{\text{SL}}^{20} = 905$ nm and $\lambda_{\text{SL}}^{19} = 938$ nm were observed, corresponding to the coupling of single-patch lattice plasmons to the $n = 20$ and $n = 19$ orders of Bragg modes from the enlarged patch periodicity $A_0 = 12$ μm . Compared to the resonances with $A_0 = 9$ μm (Figure 3.2b), the shorter-wavelength resonance at λ_{SL}^{20} kept nearly the same position, and the longer-wavelength resonance at λ_{SL}^{19} blue-shifted. At the infinite-like superlattice plasmon resonance λ_{SL}^{20} , where the resonance wavelength and near-field

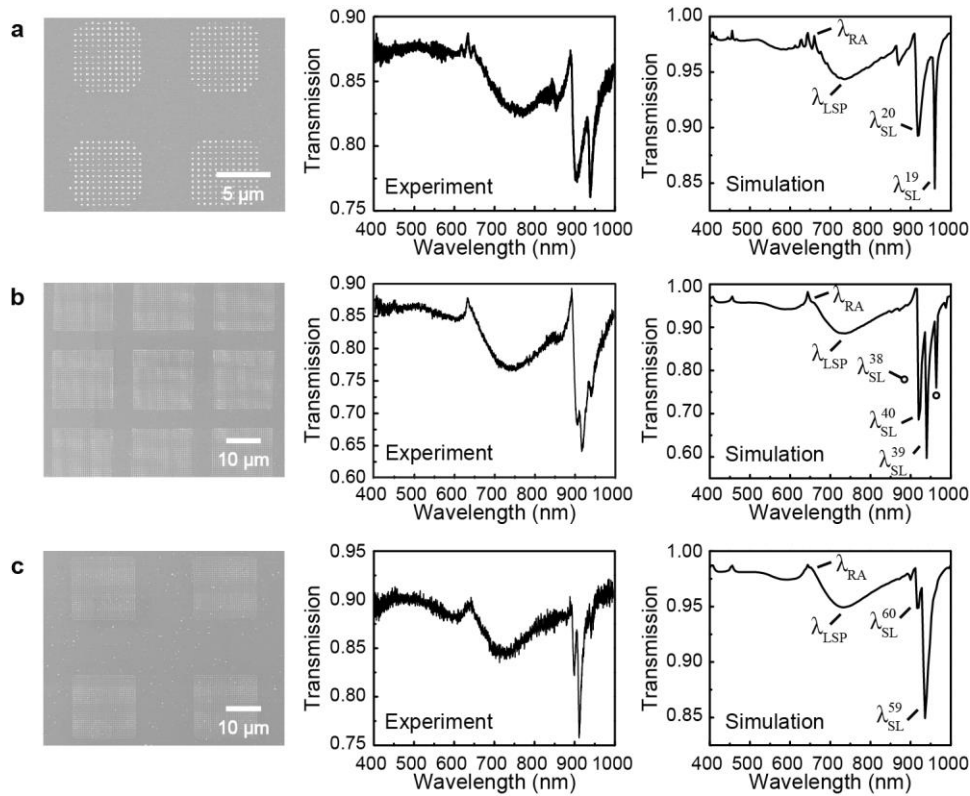


Figure 3.5. Superlattice plasmons in hierarchical Au NP arrays can be tuned by varying patch periodicity A_0 and side length l . (a) Experimental and simulated linear properties of hierarchical arrays with $l = 6 \mu\text{m}$, $A_0 = 12 \mu\text{m}$ and $d = 140 \text{ nm}$. (b) Experimental and simulated linear properties of hierarchical arrays with $l = 18 \mu\text{m}$, $A_0 = 24 \mu\text{m}$ and $d = 140 \text{ nm}$. (c) Experimental and simulated linear properties of hierarchical arrays with $l = 18 \mu\text{m}$, $A_0 = 36 \mu\text{m}$ and $d = 140 \text{ nm}$.

distribution were the same as those of lattice plasmon in infinite arrays, the NPs oscillated in-phase with each other both within an individual patch and between patches.

We further increased the number of NPs within one 2D patch from 10×10 to 30×30 to study the influence of patch side length on superlattice plasmon resonances. Notably, more NPs within one patch created narrower, more intense single-patch lattice plasmons. Three dominant lattice plasmon modes at $\lambda_{\text{SL}}^{40} = 905 \text{ nm}$, $\lambda_{\text{SL}}^{39} = 916 \text{ nm}$, and $\lambda_{\text{SL}}^{38} = 939 \text{ nm}$ were observed for patch size l

= 18 μm and patch periodicity $A_0 = 24 \mu\text{m}$, corresponding to the coupling of single-patch lattice plasmons to the $n = 40$, $n = 39$ and $n = 38$ orders of Bragg modes (**Figure 3.5b**). When the patch side length $l = 18 \mu\text{m}$ was maintained and A_0 was increased to $36 \mu\text{m}$, we observed one narrow lattice plasmon mode at $\lambda_{\text{SL}}^{59} = 911 \text{ nm}$ with a FWHM of 2 nm, and a secondary mode at $\lambda_{\text{SL}}^{60} = 899 \text{ nm}$ (**Figure 3.5c**). These two resonances originated from the $n = 59$ and $n = 60$ orders of Bragg modes. The NPs oscillate in-phase with each other at infinite-like resonances of λ_{SL}^{40} ($a_0 = 600 \text{ nm}$ and $A_0 = 24 \mu\text{m}$) and λ_{SL}^{60} ($a_0 = 600 \text{ nm}$ and $A_0 = 36 \mu\text{m}$). By varying patch side length l and patch periodicity A_0 in 2D hierarchical arrays, we were able to tune the resonance position and the number of dominant modes for superlattice plasmons.

3.4 Controlled Multi-modal Nanolasing from Plasmonic Superlattices

Figure 3.6 compares the linear optical properties and lasing emission from gold NP superlattices and single-lattice NP arrays. The NPs were supported on substrates of fused silica ($n = 1.48$) and liquid gain superstrates of IR-140 dye in dimethyl sulfoxide (DMSO, $n = 1.46$) to achieve the highest-quality lattice plasmon modes. Superlattices with NP spacing $a_0 = 600 \text{ nm}$ and patch periodicity $A_0 = 24 \mu\text{m}$ were fabricated over cm^2 -areas by multi-scale nanofabrication tools that combine contact and phase-shifting photolithography (**Figure 3.6a**).^{6,63} A_0 was selected such that the gain emission (centered at 860 nm, orange curve) overlapped with superlattice (SL) plasmons $\lambda_{\text{SL}}^a = 864 \text{ nm}$ and $\lambda_{\text{SL}}^{c1} = 881 \text{ nm}$ (blue curve), as determined by coupling of single-patch lattice plasmons and Bragg modes (λ_{SL}^a and λ_{SL}^{c1} would be λ_{SL}^{40} and λ_{SL}^{39} for $A_0 = 24 \mu\text{m}$ according to indexing based on diffractive coupling).⁶³ λ_{SL}^a exhibited the same resonance wavelength and in-phase oscillations between NPs as that of the single band-edge lattice plasmon mode λ_L in a single-lattice array, although the FWHM of the dip was larger (**Figure 3.6b**). The additional mode at λ_{SL}^{c1}

showed overall single-period phase oscillations between adjacent NPs within a single patch because of patch-patch coupling.

Consistent with previous work,^{12,52} the high-quality band-edge lattice plasmon at λ_L contributed to a single lasing mode at $\lambda_L^I = 862$ nm with directional emission and an extremely narrow linewidth (FWHM = 0.3 nm). Note the minor blue shift of lasing wavelength compared to

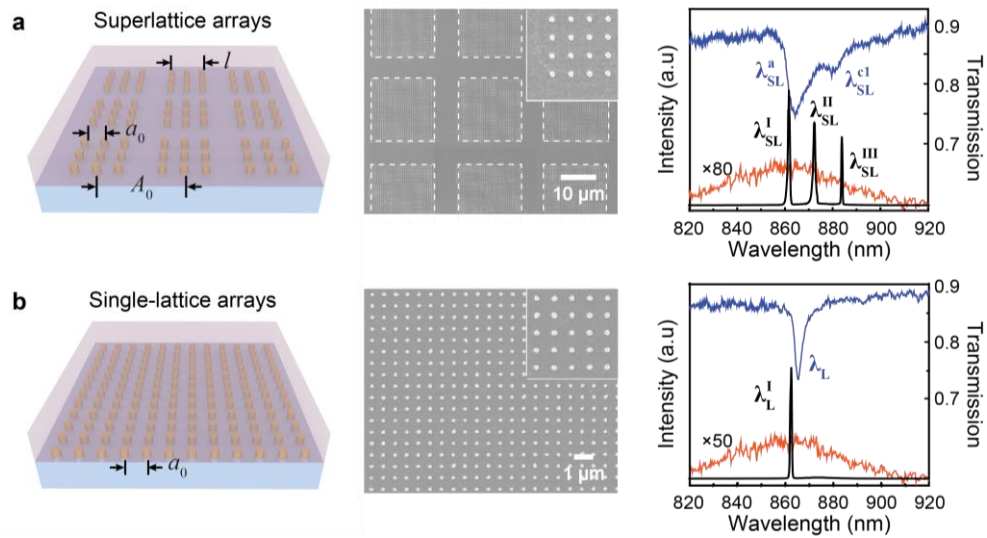


Figure 3.6. Multi-modal nanolasing in gold nanoparticle superlattices surrounded by liquid dye solutions. Schemes, SEM images and measured lasing emission from (a) NP superlattices with NP spacing $a_0 = 600$ nm, NP diameter $d = 120$ nm, height $h = 50$ nm, patch side length $l = 18$ μm and patch periodicity $A_0 = 24$ μm embedded in IR-140-DMSO (concentration $C = 0.6$ mM) and (b) single-lattice arrays with the same NP diameter $d = 120$ nm, height $h = 50$ nm and spacing $a_0 = 600$ nm as superlattices in (a). IR-140-DMSO superstrates surrounding single-lattice and superlattice NP arrays were pumped with an 800-nm fs-pulsed laser and light was collected normal to the sample surface. FWHM of lattice plasmon resonances is 6.2 nm at λ_{SL}^a and 4.2 nm at λ_L . IR-140-DMSO gain media in pink, linear optical properties in blue, and dye emission in orange with intensity rescaled and lasing emission is in black.

lattice plasmon resonance could be attributed to the slightly modified index environment around NPs at high pump fluences, and the optical pulling effect by pump source at 800 nm. In contrast, multiple lasing peaks at $\lambda_{\text{SL}}^{\text{I}} = 863$ nm, $\lambda_{\text{SL}}^{\text{II}} = 874$ nm, and $\lambda_{\text{SL}}^{\text{III}} = 884$ nm were observed in superlattices with large modal spacing ($\Delta\lambda = 10\text{-}11$ nm) and narrow spectral linewidths (FWHM < 0.5 nm). The lasing mode $\lambda_{\text{SL}}^{\text{I}}$ originated from the SL plasmon mode $\lambda_{\text{SL}}^{\text{a}}$, similar to how the wavelength of the band-edge lattice plasmon mode λ_{L} in single-lattice NP arrays determined the lasing wavelength $\lambda_{\text{L}}^{\text{I}}$.^{6,63} $\lambda_{\text{SL}}^{\text{II}}$ and $\lambda_{\text{SL}}^{\text{III}}$ were new lasing modes that can uniquely be attributed to patch-patch coupling. $\lambda_{\text{SL}}^{\text{III}}$ can be correlated with the SL plasmon at $\lambda_{\text{SL}}^{\text{c1}}$ based on good spectral overlap and emission position, but surprisingly, $\lambda_{\text{SL}}^{\text{II}}$ was absent in the transmission spectrum even though lasing emission at that wavelength was evident.

To understand the origin of the different lasing modes, we first determined the optical band structure of NP superlattices by stitching together zero-order angle-resolved transmission spectra. Compared with the single band-edge state at λ_{L} in single-lattice NP arrays (located at in-plane wavevector $k_{\parallel} = 0$), multiple band-edge modes were observed under transverse electric (TE) polarization in NP superlattices not only at $k_{\parallel} = 0$ ($\lambda_{\text{SL}}^{\text{a}}$, $\lambda_{\text{SL}}^{\text{c1}}$) but also $k_{\parallel} = \pm 0.13, \pm 0.26$ and ± 0.39 μm^{-1} ($\lambda_{\text{SL}}^{\text{b1}}$, $\lambda_{\text{SL}}^{\text{c2}}$, $\lambda_{\text{SL}}^{\text{b2}}$) (**Figure 3.7**). Band-edge modes at both zero and non-zero k_{\parallel} arose from coupling of localized surface plasmons of the NPs to different diffraction modes from the hierarchical structure (A_0). Based on FDTD methods, simulated band structures showed excellent agreement with measurements (Figure 3.7).

We indexed different Bragg modes of the superlattice as $[k_x k_y k_x' k_y']$ in reciprocal space, where k_x (k_y) and k_x' (k_y') denoted grating vectors from the NP ($k = 2\pi/a_0$) and patch spacing ($k' = 2\pi/A_0$) (**Figure 3.8**). At $\lambda_{\text{SL}}^{\text{a}}$ ($k_{\parallel} = 0$), two propagating Bragg modes $[1000]$ and $[\bar{1}000]$ with opposite

wavevectors formed a standing wave. At $\lambda_{\text{SL}}^{\text{b1}}$ ($k_{\parallel} = \pm 0.13 \mu\text{m}^{-1}$), an overall $0.5k_x$ from two coupled Bragg modes $[\bar{1}000]$ and $[10\bar{1}0]$ compensated for non-zero k_{\parallel} . Therefore, plasmonic NP superlattices can exhibit standing wave modes with very low group velocities ($v_g = \delta w / \delta k_g$) at all band-edges at $\lambda_{\text{SL}}^{\text{a}}, \lambda_{\text{SL}}^{\text{b1}}, \lambda_{\text{SL}}^{\text{b2}}, \lambda_{\text{SL}}^{\text{c1}}, \lambda_{\text{SL}}^{\text{c2}}$. The electric field enhancement was localized within the sub-wavelength vicinity of the NPs, where the fields oscillated with nearly the same phase and amplitude (Figure 3.8). Compared to dielectric NPs, only lower-energy band-edges appear in single-lattice gold NP arrays with two orders stronger near-field enhancement (**Figure 3.9**). Band-edge modes at $k_{\parallel} \neq 0$ only exist for plasmonic NP superlattices and are not observed for dielectric NPs because of weak near-field coupling between patches in the visible and NIR regions.

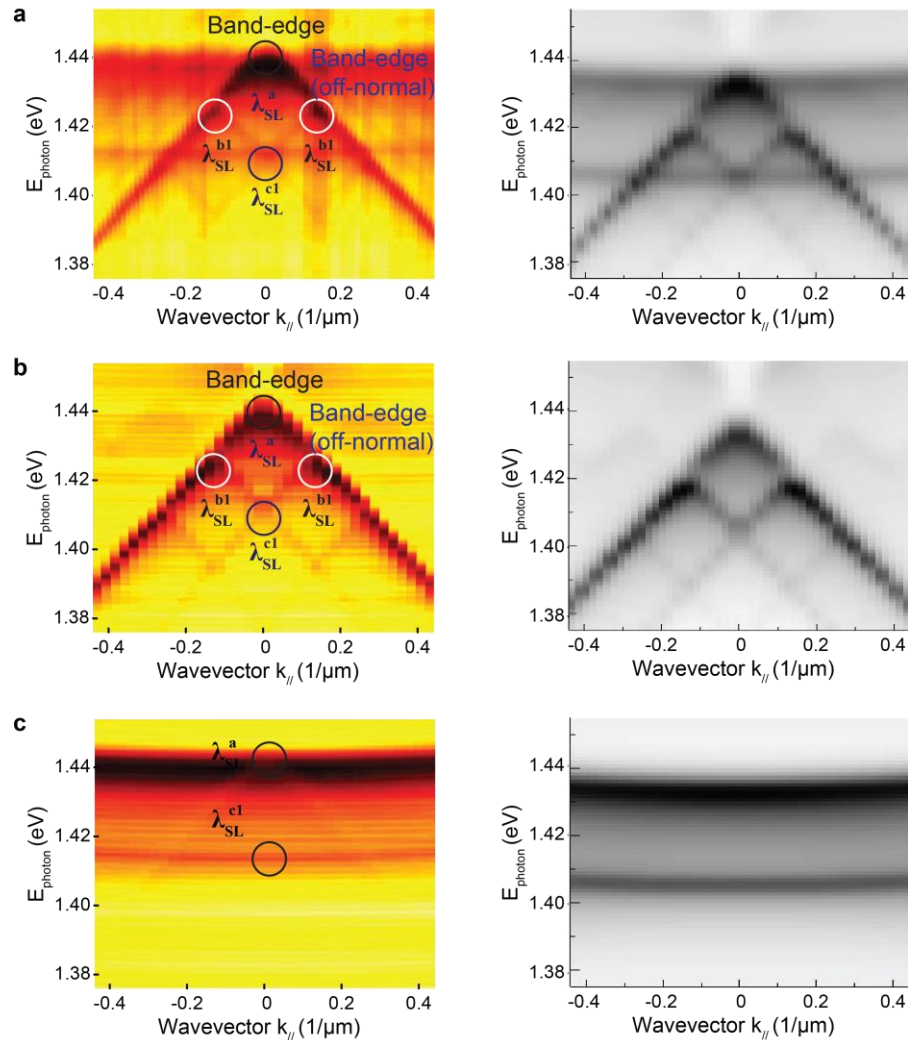


Figure 3.7. Multiple band-edge modes are observed in the band structures of plasmonic NP superlattices. Measured (left) and simulated (right) band structures in gold NP superlattices with $l = 18 \mu\text{m}$, $A_0 = 24 \mu\text{m}$, and $d = 125 \text{ nm}$ under (a) unpolarized light, (b) TE polarized light, and (c) TM polarized light. For the measurements, a droplet of DMSO was sandwiched between Au NP superlattices on fused silica and a glass coverslip to index-match the substrate. Although band-edge modes at $k_{\parallel} = 0$ are degenerate under both TE and TM polarization, band-edge states at $k_{\parallel} \neq 0$ cannot be supported by TM polarization since off-normal angle band-edges arise from coupling of Bragg modes under TE polarization, such as [1000], [1010] and [1020].

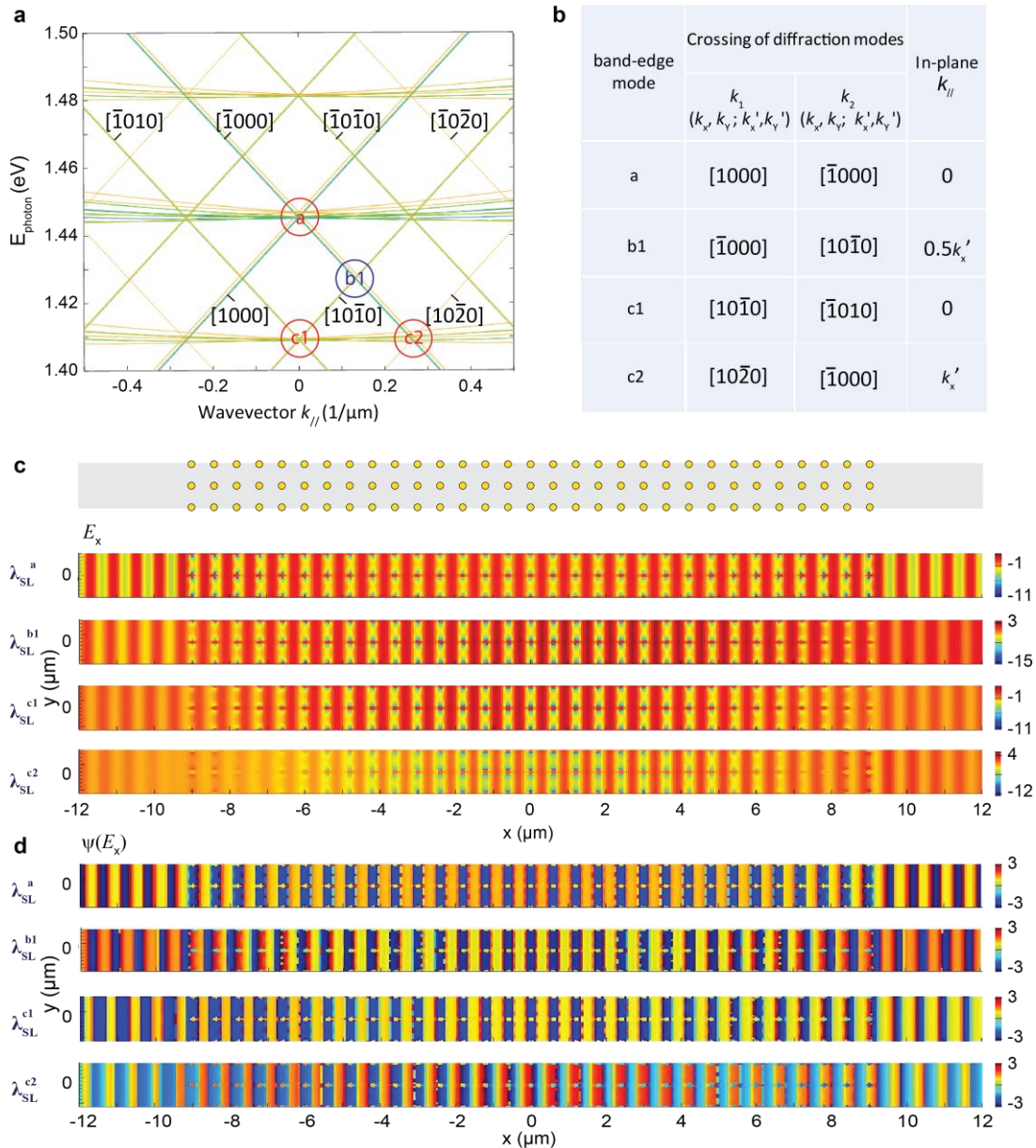


Figure 3.8. Light excited at off-normal angles can couple to NP superlattices and form standing waves. (a) Calculated dispersion diagram and indexing of different Bragg modes. **(b)** Table of Bragg modes that cross each other at different band-edges and corresponding in-plane wave vectors $k_{||}$ along x . **(c)** Simulated near field distributions E_y of multiple band-edges within plotted area of $24 \mu\text{m} \times 1.2 \mu\text{m}$ (top image) in the middle of 2D superlattices. **(d)** The phase distribution $\psi(E_x)$ at multiple band-edges, which shows standing wave patterns and in-phase oscillation of the NPs with each other. We indexed different Bragg modes in the superlattice as

$[k_x k_y k_x' k_y']$, where k_x (k_y) and k_x' (k_y') denote the grating vectors from NP spacings ($k = 2\pi/a_0$) and patch spacings ($k' = 2\pi/A_0$) along x (y) direction. At $\lambda_{\text{SL}}^{\text{a}}$ ($k_{//} = 0$), two propagating Bragg modes $k_1 = [1000]$ and $k_2 = [\bar{1}000]$ with opposite wavevectors formed a standing wave. In contrast, at $\lambda_{\text{SL}}^{\text{b}}$ ($k_{//} = \pm 0.13 \mu\text{m}^{-1}$), an overall k_x' from two coupled Bragg modes $k_1 = [\bar{1}000]$ and $k_2 = [10\bar{1}0]$ compensated for the non-zero $k_{//}$ from the off-normal incident light. In general, $(k_1+k_2)/2+k_{//}=0$ is common for all band-edge points, which indicates that plasmonic NP superlattices can exhibit standing waves with a very low group velocity ($v_g = \delta w/\delta k_g$) at zero and non-zero $k_{//}$. Here the blue, green, and yellow curves represent the first-, second-, and third-order diffraction modes from the superlattice structure, respectively. For example, the blue curves are first-order Bragg modes including $[1000]$, $[0100]$, $[\bar{1}000]$, and $[0\bar{1}00]$; green curves are second-order Bragg modes such as $[1010]$, $[\bar{1}010]$, $[\bar{1}0\bar{1}0]$, $[10\bar{1}0]$, and $[0101]$.

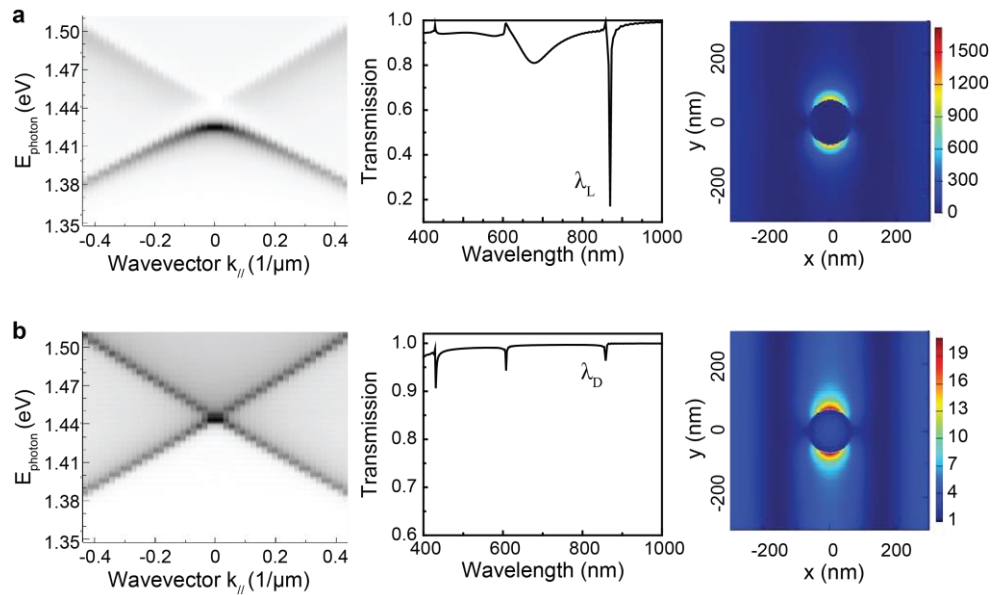


Figure 3.9. Only lower-energy band-edges appear in single-lattice gold NP arrays with two orders stronger near-field enhancement compared with dielectric NPs. Simulated band structure, normal incidence transmission spectra, and near-field enhancement $|E|^2$ at (a) lattice plasmon mode (λ_L) in single-lattice gold NP arrays and (b) photonic mode (λ_D) in single-lattice silicon NP arrays (refractive index $n = 3$) with NP spacing $a_0 = 600$ nm, NP diameter $d = 120$ nm and height $h = 50$ nm under TE polarization. Compared to both upper and lower band-edges in silicon NP arrays, we observed only lower-energy band-edges in gold NP arrays. The higher-energy band-edges at $k_{\parallel} = 0$ were suppressed because of destructive interference between NPs in the near-field. Note that the gold NP single-lattice arrays exhibited a two-order magnitude stronger near-field enhancement $|E|^2$ than dielectric ones with the same NP size and height.

Side-by-side comparison of an angle-resolved lasing emission map and band structure revealed that superlattice lasing modes had a one-to-one correspondence with the band-edge modes (**Figures 3.10a-b**). For single-lattice arrays, a single lasing mode appeared at the $k_{//} = 0$ band edge, and in the emission map, a single lasing point was observed at the detection angle $\theta_D = 0^\circ$, normal to the NP arrays (**Figure 3.11**). In contrast, for NP superlattices, lasing action at λ_{SL}^I and λ_{SL}^{III} (from band-edges at λ_{SL}^a and λ_{SL}^{c1} , respectively) emerged at $\theta_D = 0^\circ$, while λ_{SL}^{II} matched well with band-edges at $k_{//} \neq 0$, which suggests that standing waves at both zero and non-zero $k_{//}$ can support lasing action. Although the band-edge at λ_{SL}^{b2} was barely resolved in the measured band structure, lasing action at λ_{SL}^{II} was still observed in the emission map, which indicates how lasing could serve as a probe to identify band-edge points with a high local density of optical states.

Plasmonic superlattice lasers also exhibit distinct spatial coherence characteristics. Besides the central, single spot at $\theta_D = 0^\circ$ similar to single-lattice NP arrays, multiple satellite spots appeared on each side of the central beam (at $\theta_D = \pm 1.04^\circ$ and $\pm 2.08^\circ$) (**Figure 3.10c**). The angular correlation between band structure and the angle-resolved emission map along x (Figure 3.10b) identified that lasing at λ_{SL}^I and λ_{SL}^{III} appeared at $\theta_D = 0^\circ$ and $\pm 2.08^\circ$, while λ_{SL}^{II} contributed to the left and right satellite beams at $\theta_D = \pm 1.04^\circ$. All emission beams exhibited only minor beam divergence ($< 1^\circ$), which in combination with the narrow spectral linewidth (< 0.5 nm) supports the coherence of each lasing mode. The emission map acquired by sweeping θ_D along y verified that under TE polarization, the multiple spots along y resulted from diffractive effects of patch-patch interactions, and the alternating of different lasing wavelengths among spots only appeared along x (**Figure 3.12**). Since the far-field beam profiles of the four-fold symmetric 2D arrays under TE and TM polarization are spatially rotated by 90° , the wavelength distribution of multiple spots

along y under TE polarization can be identified by angle-resolved emission along x under TM polarization. Multiple flat bands were shown with low dispersion at different detection angles under TM polarization, which suggests that the spots along y are from diffractive interference effects between patches since they show the same phase profiles.

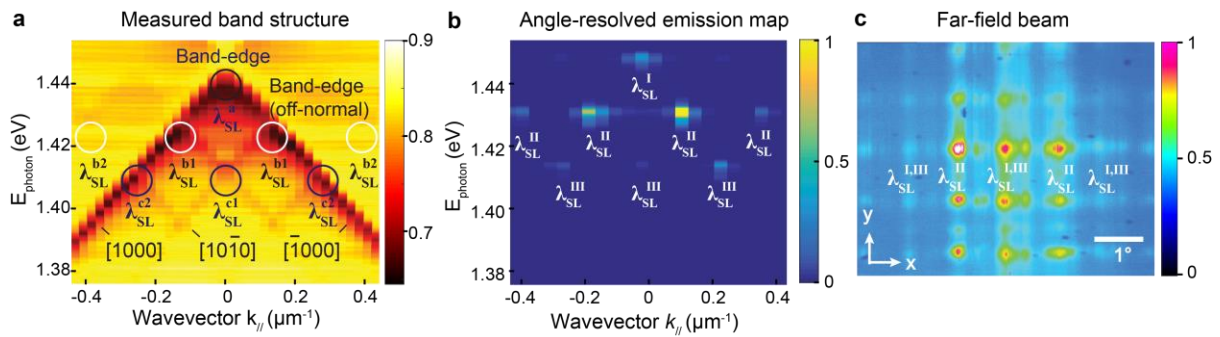


Figure 3.10. Experiments and simulations of band-edge modes at zero and non-zero wavevectors supporting standing waves for multi-modal nanolasing. (a) Measured band structure of two-dimensional (2D) superlattice arrays. (b) Measured angle-resolved emission of multi-modal lasing, with emission signals collected within $\pm 3.5^\circ$ relative to the sample surface normal. (c) Satellite spots around a central spot were detected in the far-field beam profile, where the center represented $\theta_{\text{D}} = 0^\circ$ along x and y . Intensity scale bars indicate normalized emitted photon intensity, increasing from blue to yellow or red.

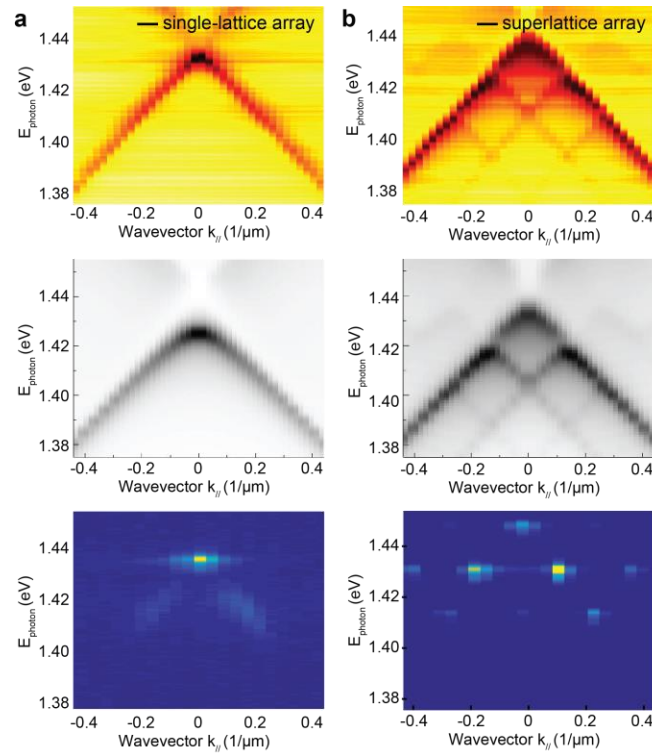


Figure 3.11. Single mode lasing from band-edge state at $k_{//} = 0$ in single-lattice arrays. (a) (left) Measured band structure with varying incident angle θ_i in single-lattice arrays; (middle) simulated band structure based on FDTD Lumerical method with $a_0 = 600$ nm and $d = 120$ nm; (right) emission map of lasing from a single band-edge mode. (b) Superlattice arrays with $A_0 = 24$ μm , $l = 18$ μm , and $d = 120$ nm. All data acquired under TE polarization. The correlation between the band structure (linear optical properties) and angle-resolved lasing map is consistent with previous work, where the only lasing mode in single-lattice NP arrays was at the single band-edge state at $k_{//} = 0$. In contrast, multi-modal lasing originates from multiple band-edges at $k_{//} = 0$ and $k_{//} \neq 0$ in plasmonic superlattices.

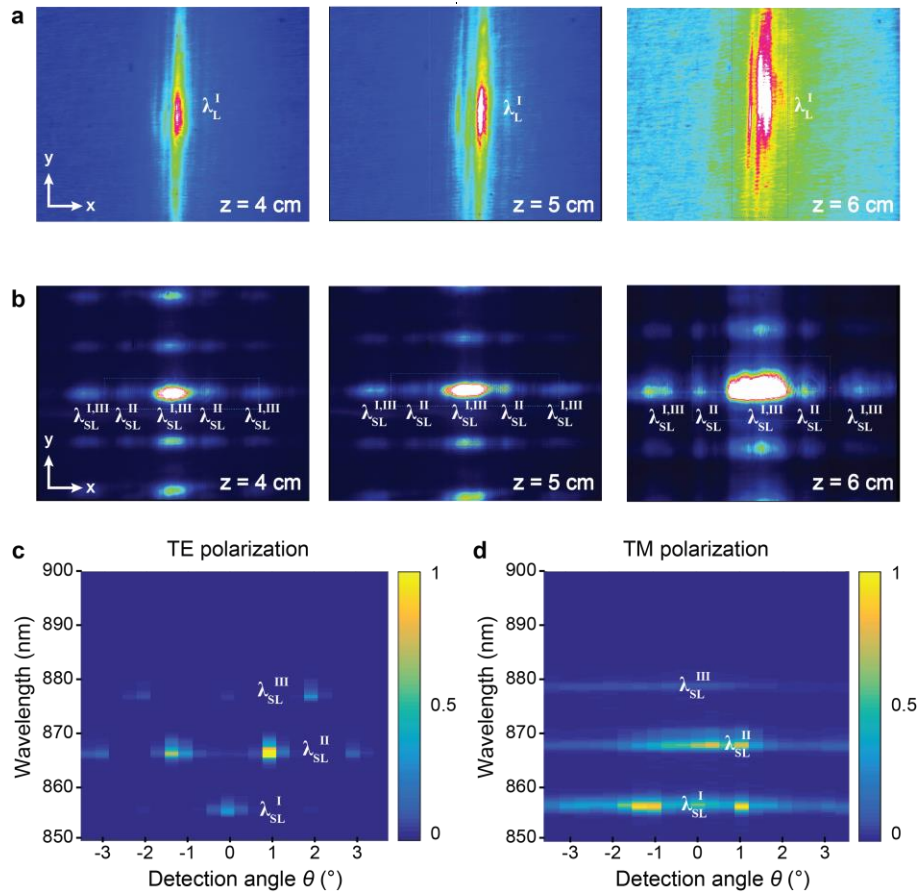


Figure 3.12. Multiple lasing beams showed minor divergence in the far field and angle-resolved emission along x and y identified the wavelength distribution. (a) Far-field beam profiles from single-lattice arrays with plotted area $6.2 \text{ mm} \times 4.8 \text{ mm}$ at detection distance $z = 4 \text{ cm}$, 5 cm , and 6 cm away from the sample plane. Minor stretching of the emission spot was observed along the light polarization, which is consistent with the previous reports and could originate from amplified spontaneous emission (ASE) at minor off-normal. **(b)** Far-field beam profiles from superlattices ($l = 18 \text{ } \mu\text{m}$, $A_0 = 24 \text{ } \mu\text{m}$) under TE polarization. **(c)** Angle resolved emission under TE polarization. The angular correlation between the far-field beam pattern and angle-resolved emission map helped to identify that lasing at λ_{SL}^I and λ_{SL}^{III} appeared at $\theta_D = 0^\circ$ and $\pm 2.08^\circ$ along x , while λ_{SL}^{II} contributed to the left and right satellite beams at $\theta_D = \pm 1.04^\circ$. **(d)** Angle resolved emission under TM polarization.

Modeling of lasing action from large-unit cell lattices (tens of microns) and at non-zero $k_{//}$ was not possible in our home-built FDTD codes because of limited computational efficiency.^{12,159} To improve the computation speed, we integrated the four-level one-electron model with a commercial software (FDTD Solutions, Lumerical Inc.) and modeled dye molecules subject to the Pauli exclusion principle.⁵³ FDTD simulations with the Pauli exclusion principle showed lasing action in single-lattice arrays comparable to that of our previous method⁷ that did not consider electron spin; only a minor change of oscillation amplitude in the time-dependent population inversion was observed (**Figure 3.13**).

By pumping from the ground level ($N_0 = 1$), we observed lasing modes above threshold that were strongly correlated with superlattice plasmon resonances. Pumping of the ground electronic state resulted in lasing modes at $\lambda_{\text{SL}}^{\text{I}}$ and $\lambda_{\text{SL}}^{\text{III}}$ for $k_{//} = 0$ with wavelengths that can be correlated with SL plasmons $\lambda_{\text{SL}}^{\text{a}} + \lambda_{\text{SL}}^{\text{c1}}$ and $\lambda_{\text{SL}}^{\text{c2}}$ (**Figure 3.14a**). Note that the output spectrum only showed two lasing modes $\lambda_{\text{SL}}^{\text{I}}$ and $\lambda_{\text{SL}}^{\text{III}}$ at $k_{//} = 0$ and could not reveal $\lambda_{\text{SL}}^{\text{II}}$ because this time-domain approach cannot represent SL plasmons at different $k_{//}$ simultaneously. However, simulations with a plane-wave incident at $\theta_{\text{I}} = \pm 1.04^\circ$ and $\pm 2.08^\circ$ could produce lasing at $\lambda_{\text{SL}}^{\text{II}}$ (from $\lambda_{\text{SL}}^{\text{b1}}$ at $k_{//} = \pm 0.13 \mu\text{m}^{-1}$) and $\lambda_{\text{SL}}^{\text{III}}$ (from $\lambda_{\text{SL}}^{\text{c1}}$ at $k_{//} = \pm 0.26 \mu\text{m}^{-1}$) by introducing a phase shift at the microscale unit-cell boundary (**Figures 3.14b-c**).

The simulated linewidths of the lasing peaks are typically ~ 2 nm, but in the experiments, we detected sharp peaks as narrow as 0.5 nm. The broadening of the simulated lasing modes can be attributed to: (1) the semi-quantum model used to describe lasing actions without including dephasing of the dye molecules over time; (2) the short simulation time (within 2 ps). Additionally, in (a), the photoluminescence (PL) of dyes is not captured at low pump power because: (1) in

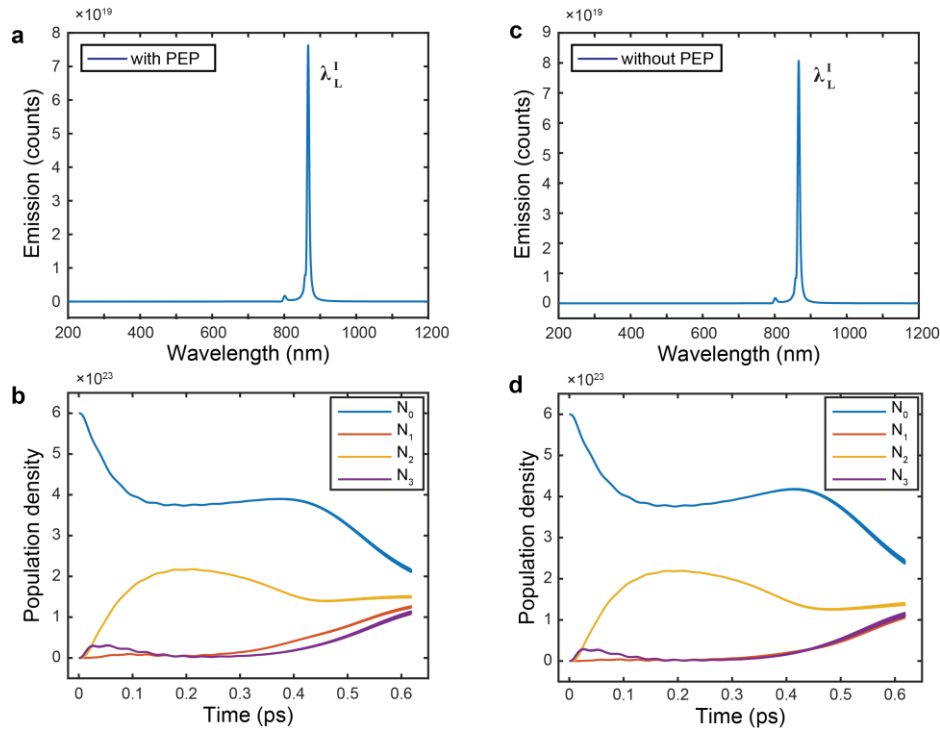


Figure 3.13. Both four-level one-electron systems without and with the Pauli exclusion principle can describe lasing action in single-lattice arrays with population inversion in real-time. (a) Lasing from FDTD method with the PEP at pump 0.37 mJ cm^{-2} and (b) corresponding real-time population inversion. (c) Lasing from FDTD method without PEP at the same pump power range and (d) corresponding real-time population inversion. Previously we used a four-level one-electron model without PEP to describe lasing action in single-lattice arrays. Lumerical only allows a four-level model with PEP to model the micron superlattices. Here we compared the influence of the PEP to the model of lasing action based on our home-built FDTD codes. By slightly changing the description of the rate equation defined by PEP, we can compare the two models side-by-side. We found that the two models showed robust lasing action within 1 ps with the population inversion accumulated at the plasmonic hot spot regions. Only a minor change of oscillation amplitude in the time-dependent population inversion was observed, where the model with PEP had a slightly slower transition rate.

simulation, there are fewer dye molecules (1 mM dye in unit cells $600 \text{ nm} \times 600 \text{ nm} \times 2 \text{ }\mu\text{m}$) for strong PL than experiments ($\sim 1\text{-mm}$ gain thickness); and (2) simulation time of 2 ps is too short to capture emission from dyes with much longer intrinsic decay lifetime ($\sim 800 \text{ ps}$).

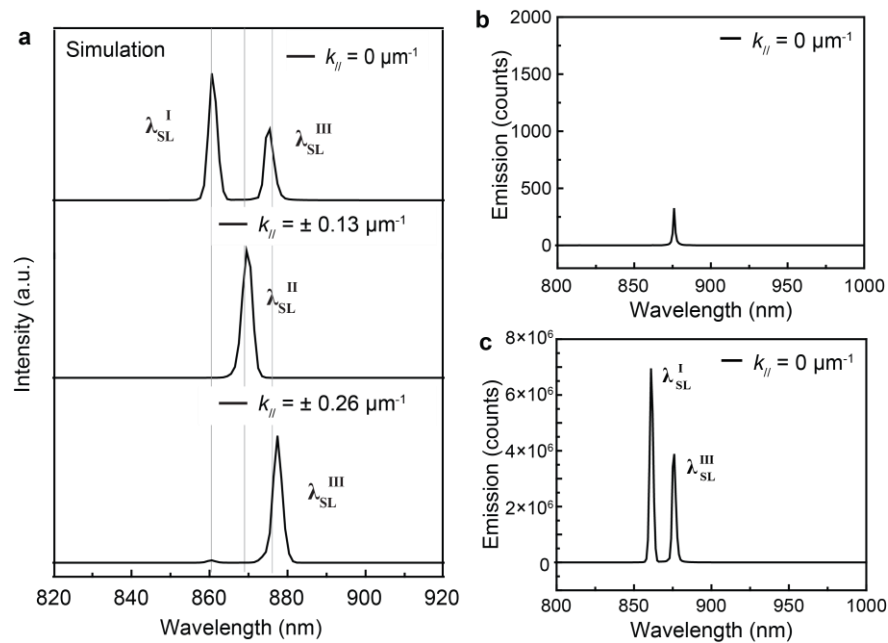


Figure 3.14. Multi-modal nanolasing was observed in simulations from 2D plasmonic superlattices above lasing threshold. (a) Lasing spectra from band-edges at (upper panel) $k_{//} = 0$, (middle panel) $k_{//} = \pm 0.13 \text{ }\mu\text{m}^{-1}$, and (lower panel) $k_{//} = \pm 0.26 \text{ }\mu\text{m}^{-1}$ by FDTD simulations. All results under TE polarization. (b) Simulated lasing spectrum from 2D superlattices (patch side length $l = 18 \text{ }\mu\text{m}$, periodicity $A_0 = 24 \text{ }\mu\text{m}$, NP size $d = 120 \text{ nm}$) slightly above lasing threshold at 0.11 mJ cm^{-2} and (c) above lasing threshold at 0.26 mJ cm^{-2} .

Mode competition is common in semiconductor lasers, where multiple cavity modes compete for available gain; hence, oscillations in one mode generally reduce and suppress gain for others.³² Distinct from traditional systems, plasmonic NP superlattices can support multiple lasing modes simultaneously because of a combination of factors: (i) the large gain bandwidth of the dye (~50 nm); (ii) the short pulsed laser excitation (~90 fs) that avoids accumulation of mode competition over limited photon traveling cycles; (iii) widely separated spectral resonances of SL plasmons (~10 nm); and (iv) different near-field spatial overlap of SL modes with the gain media.³² Since all band-edge wavelengths for this particular NP superlattice ($A_0 = 24 \mu\text{m}$; $l = 18 \mu\text{m}$) -- $\lambda_{\text{SL}}^{\text{a}}$, $\lambda_{\text{SL}}^{\text{b1}}$, $\lambda_{\text{SL}}^{\text{b2}}$, $\lambda_{\text{SL}}^{\text{c1}}$, $\lambda_{\text{SL}}^{\text{c2}}$ -- were within the gain envelope, multi-modal lasing could exist and be captured simultaneously by a single detector (collection angle around 3°).

At low pump powers, $\lambda_{\text{SL}}^{\text{II}}$ at $k_{\parallel} \neq 0$ and $\lambda_{\text{SL}}^{\text{III}}$ at $k_{\parallel} = 0$ emerged with lasing thresholds lower than $\lambda_{\text{SL}}^{\text{I}}$ (**Figure 3.15a**). Interestingly, $\lambda_{\text{SL}}^{\text{I}}$ surpassed $\lambda_{\text{SL}}^{\text{III}}$ at 0.35 mJ cm^{-2} and continued to increase, while $\lambda_{\text{SL}}^{\text{II}}$ and $\lambda_{\text{SL}}^{\text{III}}$ saturated at high pump fluence (**Figures 3.15b-c**); these trends were similar for all NP superlattices tested. In FDTD modeling at $k_{\parallel} = 0$, we also observed an early rise of $\lambda_{\text{SL}}^{\text{III}}$ but dominant growth of $\lambda_{\text{SL}}^{\text{I}}$ at high pump power (Figure 3.15c). These power-dependent output behaviors may be attributed to the near-field enhancement of SL plasmons and their mode quality Q ($= \frac{\lambda}{\Delta\lambda}$, where λ represents the resonance wavelength and $\Delta\lambda$ the linewidth). $Q_{\lambda_{\text{c1}}} = 197$ is slightly larger than $Q_{\lambda_{\text{a}}} = 139$, which suggests that photons from $\lambda_{\text{SL}}^{\text{c1}}$ are trapped within the cavity for more cycles than $\lambda_{\text{SL}}^{\text{a}}$ such that there is more available gain at $\lambda_{\text{SL}}^{\text{c1}}$ at low pump powers. Thus, lasing action was first observed at $\lambda_{\text{SL}}^{\text{II}}$ and $\lambda_{\text{SL}}^{\text{III}}$ (from band edges at $\lambda_{\text{SL}}^{\text{b1}}$, $\lambda_{\text{SL}}^{\text{b2}}$, $\lambda_{\text{SL}}^{\text{c1}}$ and $\lambda_{\text{SL}}^{\text{c2}}$). At high

pump powers, $\lambda_{\text{SL}}^{\text{I}}$ dominated since the mode at $\lambda_{\text{SL}}^{\text{a}}$ exhibited a seven-fold stronger local field that enhanced the stimulated emission term $\frac{1}{\hbar\omega} E \frac{dP}{dt}$ in the rate equations.

Unlike existing photonics and plasmonic lasers that exhibit fixed intensity ratios across the different modes³⁰ or a single, dominant mode with increased pump power,³⁹ the output behavior of SL plasmon lasing peaks can be uniquely controlled by manipulating the near-field intensity of the individual modes. For example, by increasing NP size from $d = 120$ nm to $d = 125$ nm (**Figure 3.15d**), all band-edge modes red-shifted and those at longer wavelengths had higher intensity. The stronger local E field at $\lambda_{\text{SL}}^{\text{c1}}$ led to stronger stimulated emission at $\lambda_{\text{SL}}^{\text{III}}$; thus, $\lambda_{\text{SL}}^{\text{II}}$ and $\lambda_{\text{SL}}^{\text{III}}$ showed a dominant increase at high pump powers while $\lambda_{\text{SL}}^{\text{I}}$ remained relatively weak and did not surpass $\lambda_{\text{SL}}^{\text{III}}$ in simulation or experiment (**Figures 3.15e-f**). Note that $\lambda_{\text{SL}}^{\text{II}}$ was located closer to the dye emission center and could show stronger lasing emission than $\lambda_{\text{SL}}^{\text{I}}$ and $\lambda_{\text{SL}}^{\text{III}}$. Moreover, we could modify the available gain by changing dye concentration and also achieve tailored output behavior of the different lasing modes. The output behavior was sensitive to dye concentration, where only $\lambda_{\text{SL}}^{\text{I}}$ and $\lambda_{\text{SL}}^{\text{II}}$ appeared at low dye concentration (0.56 mM), while $\lambda_{\text{SL}}^{\text{I}}$, $\lambda_{\text{SL}}^{\text{II}}$ and $\lambda_{\text{SL}}^{\text{III}}$ all arose at high dye concentration (0.63 mM and 0.75 mM). The observation can be attributed to the red-shifting of the dye emission (~ 8 nm) with increased dye concentration (from 0.5 mM to 1 mM). This unprecedented, modular control over the input-output light curves of each lasing mode based on cavity resonances and gain can provide insight into unconventional designs of multi-modal lasers.

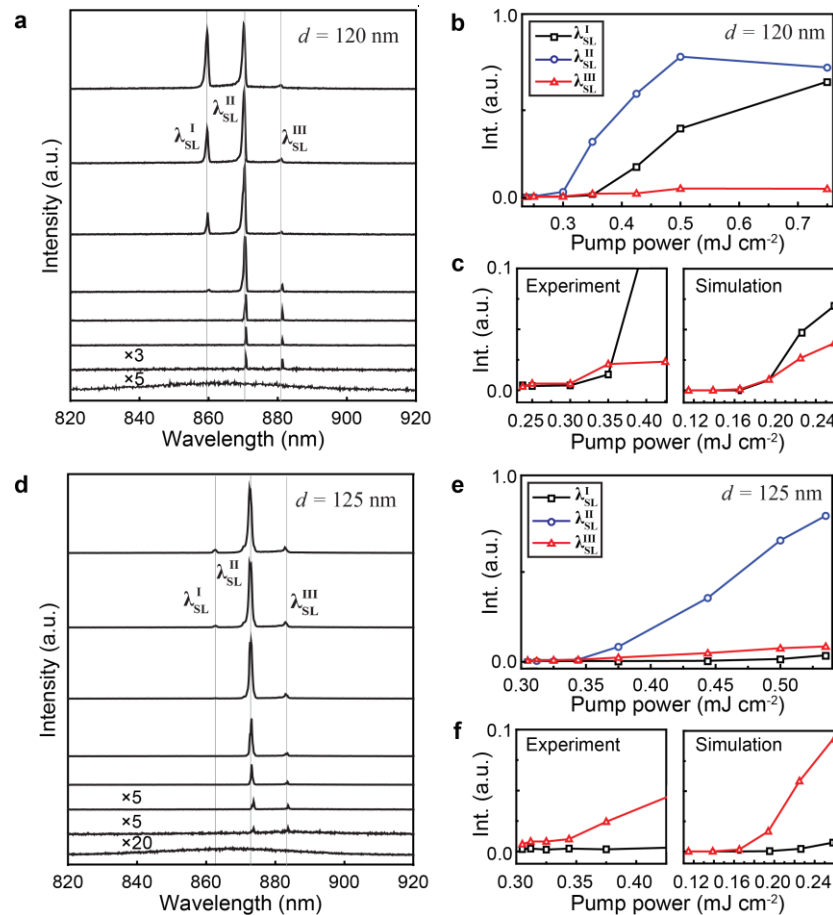


Figure 3.15. Multi-modal nanolasing from plasmonic superlattices with controlled output behaviors and spatial coherence. (a) Measured output profiles of multi-modal lasing with dye concentration and increased pump power at 0.2-0.8 mJ cm^{-2} for 2D superlattices with $d = 120$ nm. (b) Experimental threshold curve of multi-modal lasing with $d = 120$ nm. (c) (left panel) Experimental and (right panel) simulated output behaviors of λ_{SL}^I and λ_{SL}^{III} with $d = 120$ nm. Experimental data are a zoom-in of (b). (d) Output profiles of larger NP size $d = 125$ nm with increased pump power at 0.3-0.6 mJ cm^{-2} . (e) Experimental threshold curve of multi-modal lasing with $d = 125$ nm. (f) (left panel) Experimental and (right panel) simulated output behaviors of λ_{SL}^I and λ_{SL}^{III} with $d = 125$ nm. Experimental data are a zoom-in of (e). $C = 0.63$ mM for both superlattice lasers.

Time-correlated photoluminescence (PL) measurements revealed distinct ultrafast decay dynamics of the different superlattice lasing modes (Methods). Below the lasing threshold, PL from the IR-140-DMSO on NP superlattices exhibited an intrinsically long decay lifetime (834 ps) (**Figure 3.16**). Above threshold, the decay lifetime of photons from the dye can be significantly reduced by the faster process of stimulated emission^{12,52} and modulated by the near-field distribution and mode quality of SL plasmons. $\lambda_{\text{SL}}^{\text{a}}$ and λ_{L} showed the same in-phase NP oscillations in the near field, and we observed similar ultra-short decay lifetimes between $\lambda_{\text{SL}}^{\text{I}}$ (16 ps) and $\lambda_{\text{L}}^{\text{I}}$ (13 ps) (**Figures 3.16b-c**). In contrast, the $\lambda_{\text{SL}}^{\text{II}}$ lasing mode from patch-patch coupling exhibited a longer decay lifetime (41 ps) because photons could be trapped in the $\lambda_{\text{SL}}^{\text{b1}}$ mode for a longer time ($Q_{\lambda_{\text{b1}}} > Q_{\lambda_{\text{a}}}$). Specifically, $\lambda_{\text{SL}}^{\text{I}}$ emerged earlier (at 27 ps) than $\lambda_{\text{SL}}^{\text{II}}$ (at 35 ps) in part because the stronger near field at $\lambda_{\text{SL}}^{\text{a}}$ led to faster population inversion build-up for lasing; $\lambda_{\text{SL}}^{\text{I}}$ also decayed faster since these $\lambda_{\text{SL}}^{\text{I}}$ photons did not exhibit long cavity lifetimes through non-radiative decay from the metal NPs.

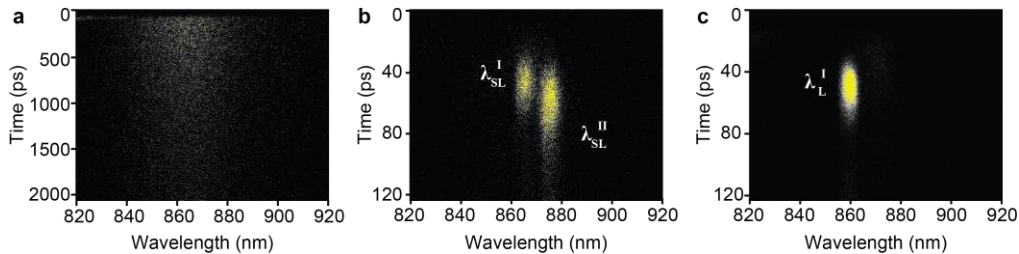


Figure 3.16. Modulation of the ultrafast decay dynamics of multi-modal lasing by micron patch-patch coupling. Time-correlated single-photon counting of multi-modal lasing from NP superlattice arrays at (a) 0.03 mJ cm⁻², (b) 0.38 mJ cm⁻², and (c) single-lattice NP arrays at 0.30 mJ cm⁻² (2 kHz, 800-nm fs-pulsed laser). Only two peaks were observed at this pump power because of power-dependent multi-modal lasing.

3.5 Band-edge Engineering from Structural Designs

3.5.1 2D Superlattice Arrays

Plasmonic superlattices can be fabricated with precise control over patch-patch spacing; hence, we can define the spectral location and spacing of the multiple lasing modes. **Figure 3.17** depicts the plasmonic NP superlattices with different patch periodicities fabricated by a multiscale patterning process. As we increased A_0 from 18 μm to 24 μm to 36 μm in the real space, the spectral separation between band-edges in the reciprocal space was reduced, as was the lasing modal spacing (from 14 nm to 11 nm to 7 nm, respectively, **Figure 3.18**). Consistent with Figure 3.15a, $\lambda_{\text{SL}}^{\text{II}}$ ($k_{//} \neq 0$) and $\lambda_{\text{SL}}^{\text{III}}$ ($k_{//} = 0$) saturated at high pump powers while $\lambda_{\text{SL}}^{\text{I}}$ ($k_{//} = 0$) continued to increase. For superlattice arrays, with increased pump power, lasing peaks $\lambda_{\text{SL}}^{\text{II}}$ and $\lambda_{\text{SL}}^{\text{III}}$ became broader and were "pulled" by the rising of $\lambda_{\text{SL}}^{\text{I}}$ on the blue side as a result of the pulling effect;³² thus, the peaks had extended tails to the blue side. Similarly, in single-lattice arrays, lasing peaks became broader and unsymmetrical to the red side, which can be correlated to the excitation of ASE modes on the red side.

The far-field spatial distribution of the different lasing modes could also be tailored by changing A_0 . For example, at $A_0 = 36 \mu\text{m}$, multiple satellite spots over smaller detection angles ($\theta_{\text{D}} = \pm 0.69^\circ$ at $\lambda_{\text{SL}}^{\text{b1}}$) were observed compared to that for $A_0 = 24 \mu\text{m}$ ($\theta_{\text{D}} = \pm 1.04^\circ$). The lasing beam spots appeared as symmetric along both x and y direction, where the emission wavelength variation corresponding to different band-edge states happened along x direction.

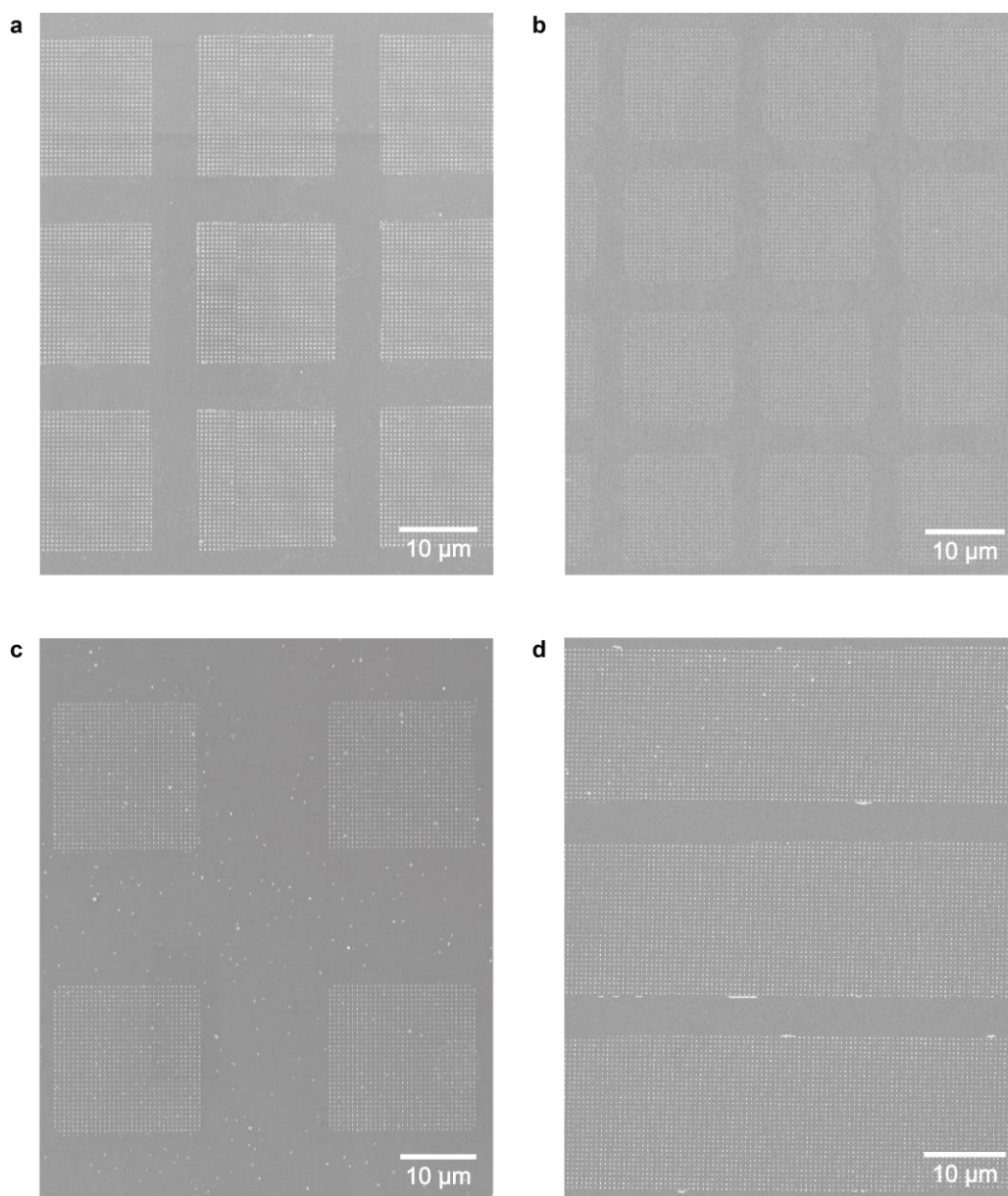


Figure 3.17. Plasmonic NP superlattices with arbitrary geometric parameters can be fabricated by multiscale patterning. (a) $l = 18 \mu\text{m}$, $A_0 = 24 \mu\text{m}$ arrays. (b) $l = 12 \mu\text{m}$, $A_0 = 18 \mu\text{m}$ arrays. (c) $l = 18 \mu\text{m}$, $A_0 = 36 \mu\text{m}$ arrays. (d) $l = 18 \mu\text{m}$, $A_0 = 24 \mu\text{m}$ line patches.

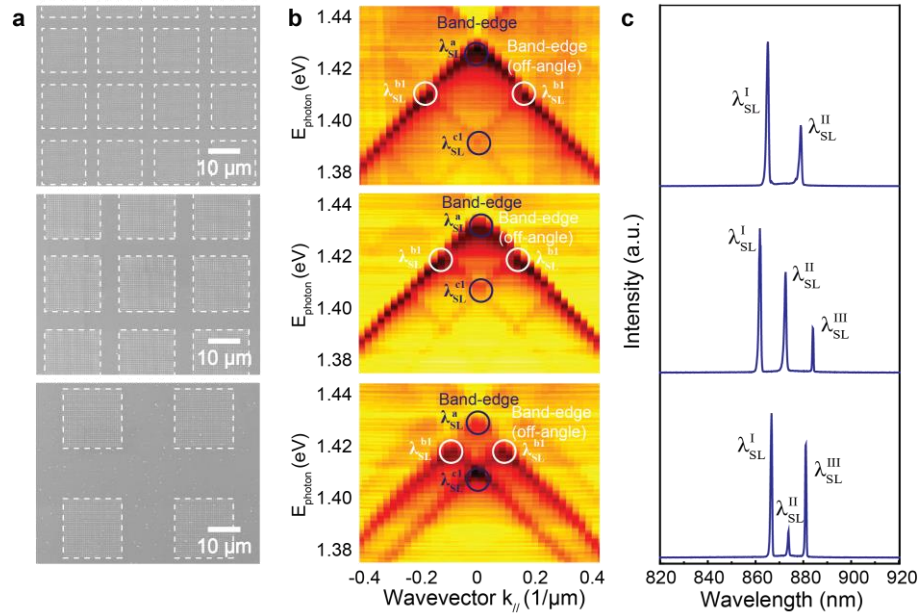


Figure 3.18. Spectral spacing of band-edge lasing modes can be manipulated by varying patch periodicities. (a) SEM images of superlattice array with $(l, A_0) = (12 \mu\text{m}, A_0 = 18 \mu\text{m})$, $(l, A_0) = (18 \mu\text{m}, A_0 = 24 \mu\text{m})$ and $(l, A_0) = (18 \mu\text{m}, A_0 = 36 \mu\text{m})$ (from top to bottom). (b) Measured band structure of superlattice arrays under TE polarization with spectral spacing of band-edges at 14 nm, 11 nm, and 7 nm. (c) Controlled lasing spacing from band-edge modes. Dashed lines depict the outline of the patches. Notably, we observed unsymmetrical shapes of lasing peaks at high pump power.

3.5.2 Symmetry-breaking Superlattice Line Patches

Besides exquisite spectral control of multiple nanolasing modes by tuning patch-patch spacing, we also spatially engineered band-edge modes with a symmetry-broken superlattice. We designed NP line patches with the same a_0 and A_0 as the 2D case (Figure 3.6) along x , while the structure along y only had a periodicity a_0 , the same as the single-lattice array (**Figure 3.19a**). Since plasmonic NPs exhibit dipolar oscillations along the direction of incident light, symmetry-broken cavity structures enable polarization- and orientation-dependent band structures with either single or multiple band-edge modes. With pump polarization \mathbf{e}_{pump} along y and line axis \mathbf{e}_{line} along x ($\mathbf{e}_{\text{line}} \perp \mathbf{e}_{\text{pump}}$), we observed a single lasing mode at $\lambda_{\text{SL}}^{\text{I}} = 862$ nm (**Figure 3.19b**) from the single band-edge ($k_{//} = 0$) and multiple spots along y from patch-patch diffractive interference (**Figures 3.19c-d**). Conversely, when $\mathbf{e}_{\text{line}} // \mathbf{e}_{\text{pump}}$ (sample rotated in plane), multiple lasing modes arose at $\lambda_{\text{SL}}^{\text{I}} = 860$ nm ($k_{//} = 0$), $\lambda_{\text{SL}}^{\text{II}} = 871$ nm ($k_{//} \neq 0$), and $\lambda_{\text{SL}}^{\text{III}} = 881$ nm ($k_{//} = 0$) from the multiple band-edges. In the far field, these lasing modes were distributed along x , and no satellite spots appeared along y because there was no A_0 ; the power-dependent output behavior was similar to that of 2D superlattices. As the sample was rotated in the x - y plane, switchable nanolasing between single and multiple lasing modes agreed with the evolution of band structure from single to multiple band-edges (**Figure 3.20**).

The underlying mechanism of switchable lasing in the NP line patches can be attributed to the asymmetric spatial distribution of population inversion at the plasmonic hot spots. The four-level model showed that population inversion accumulated only at dipolar hot spots along the pump polarization (y) and increased faster when $\mathbf{e}_{\text{line}} \perp \mathbf{e}_{\text{pump}}$ as a result of larger numbers of NPs coupling along x (**Figure 3.21**). In Figure 3.24c, monitor A (at the dipolar hot spot) showed the real-time

population inversion and energy decay. In contrast, monitor B (far away from the hot spot) showed no change of dN at different energy levels over time. When we fixed \mathbf{e}_{pump} along y and varied \mathbf{e}_{line} to be along x , the dipolar oscillation was distributed still along y and hence, we observed the real-time population inversion only in monitor A. Since there are more NPs along x that coupled with each other, the population inversion accumulated faster, and lasing output happened earlier in (f) (~ 1250 fs) compared to (c) (~ 2300 fs).

Although dye molecules were randomly orientated and incoherent PL emission was independent of sample orientation, molecules with transition dipole moments along the pump polarization were preferentially excited; hence, the polarization of output lasing emission was along the polarization of the pump source (**Figure 3.22**). Different from orientation-dependent lasing output from line patches, we observed orientation-independent PL emission following the $[\pm 1, 0]$ Bragg modes (Figures 3.22a-b). In contrast, for superlattice lasing under TE polarization (along y), we found that the output lasing emission was polarized preferentially along y for both single-mode and multi-modal lasing, which suggested the coherence of polarization in superlattice lasing emission (Figures 3.22c-d). By fixing the sample orientation and changing the pump polarization, we also observed tunable lasing between single and multiple modes (**Figure 3.23**). Therefore, the lasing output can be dynamically manipulated in rationally designed NP superlattices.

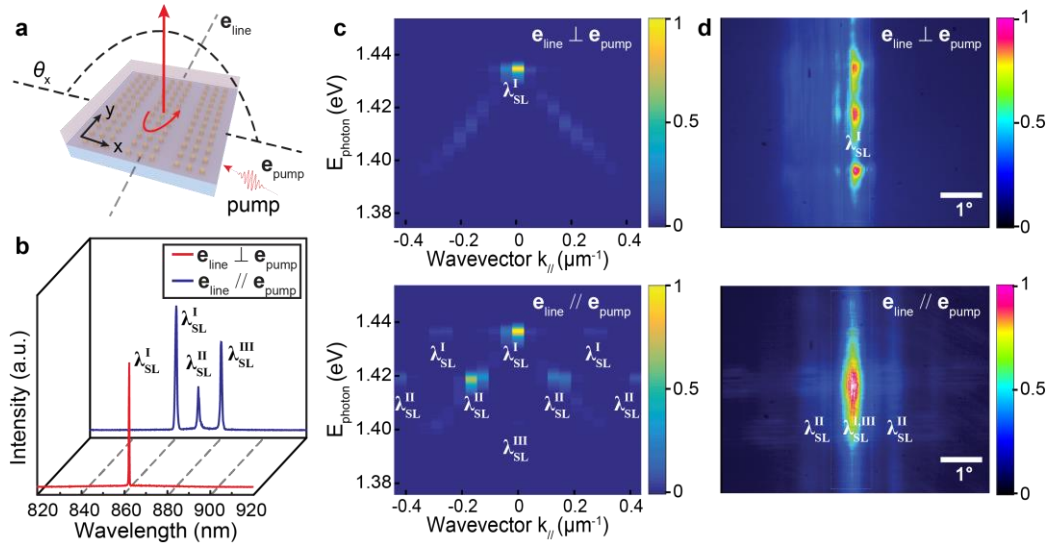


Figure 3.19. Dynamic control of band-edge modes in symmetry-broken plasmonic line patches leading to switchable nanolasing between single and multiple modes. (a) Scheme of lasing measurement on NP line patches with the same $a_0 = 600$ nm, $l = 18$ μm and $A_0 = 24$ μm along x as in 2D superlattice arrays. (b) Orientation-dependent lasing under TE polarization. \mathbf{e}_{line} and \mathbf{e}_{pump} represent the directions of line axis and pump polarization, respectively. (c) Angle-resolved mapping of lasing emission by sweeping θ_x with (upper panel) $\mathbf{e}_{\text{line}} \perp \mathbf{e}_{\text{pump}}$ and (lower panel) $\mathbf{e}_{\text{line}} // \mathbf{e}_{\text{pump}}$. (d) Far-field beam profiles from line patches under in-plane rotation of the sample. For $\mathbf{e}_{\text{line}} \perp \mathbf{e}_{\text{pump}}$, a single lasing mode at $\lambda_{\text{SL}}^{\text{I}}$ produced multiple spots along y from patch-patch diffractive interference. For $\mathbf{e}_{\text{line}} // \mathbf{e}_{\text{pump}}$, with pump power slightly above lasing threshold, $\lambda_{\text{SL}}^{\text{III}}$ appeared in the middle while $\lambda_{\text{SL}}^{\text{II}}$ showed up as two weak spots on the left and right. Intensity scale bars indicate normalized emitted photon intensity, increasing from blue to yellow or red.

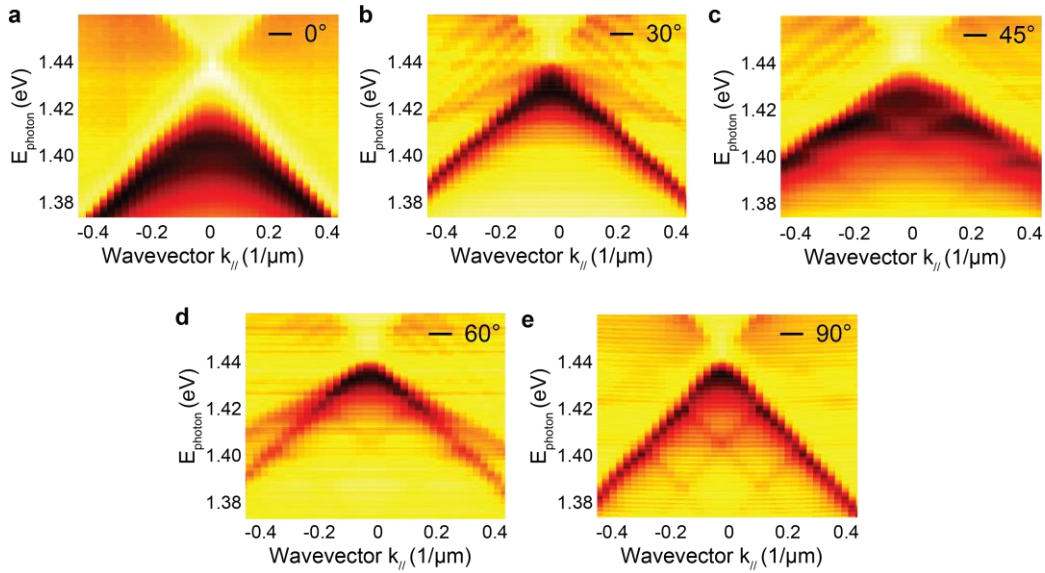


Figure 3.20. Dynamical tuning of band structure in NP line patches by sample orientation.

Measured band structures of NP line patches with \mathbf{e}_{line} oriented at (a) 0° (x direction), (b) 30° , (c) 45° , (d) 60° , and (e) 90° (y direction). In the angle-resolved band structure measurement, the pump was kept as TE polarized (along y direction) and θ_l was swept in x - z plane. Band structures gradually evolved from a single band-edge to multiple band-edges as the line patch lattice was rotated in x - y plane.

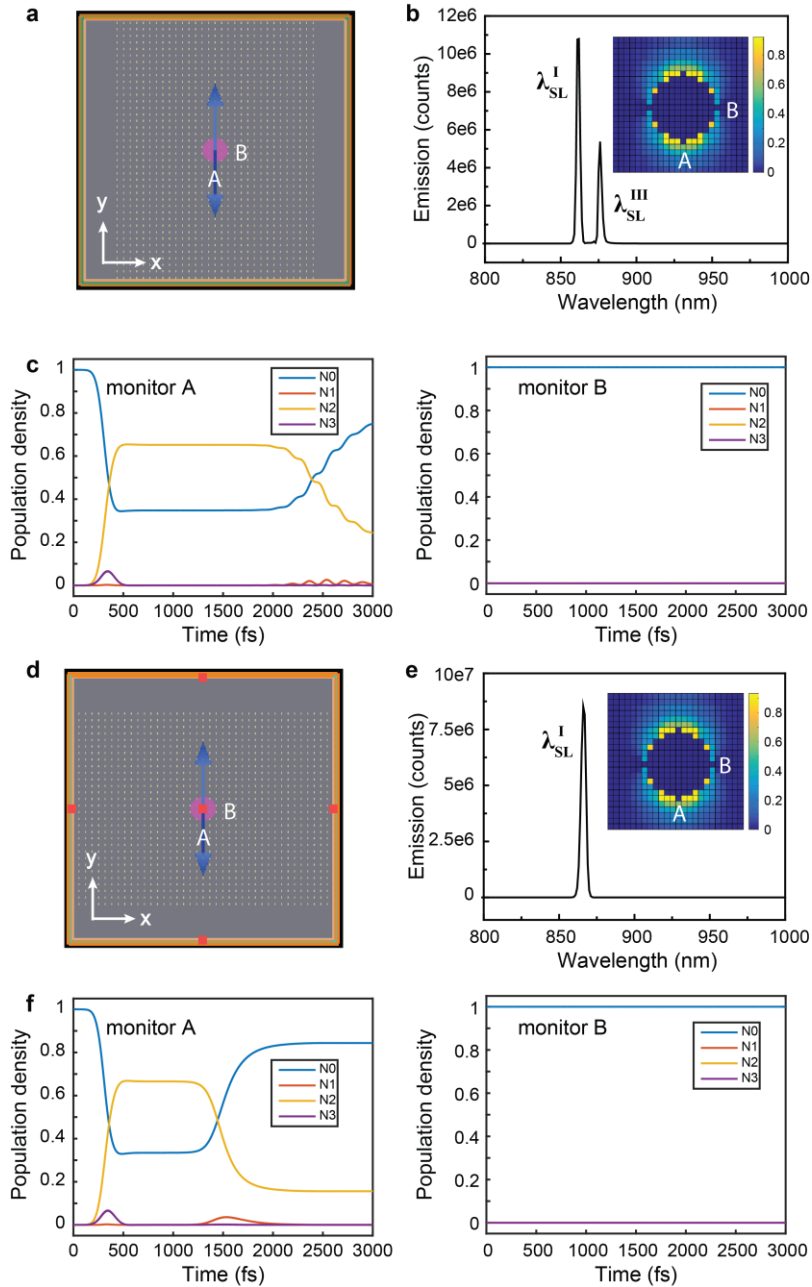


Figure 3.21. Switching between multiple and single lasing modes is detected in simulation of line patches with population inversion distributed at dipolar hot-spots. (a) Simulation setup for lasing from line patches with \mathbf{e}_{pump} along y and \mathbf{e}_{line} along y . **(b)** Multi-modal lasing emission $\lambda_{\text{SL}}^{\text{I}}$ and $\lambda_{\text{SL}}^{\text{III}}$ from simulation at $k_{\parallel} = 0$. **(c)** Real-time evolution of population inversion at monitor A (left panel) and monitor B (right panel). Monitors A and B were placed 20 nm away from the NP edge along y and x directions, respectively. Inset shows the spatial distribution of population inversion ($dN = N_2 - N_1$) around a NP in (a) at 2300 fs. **(d)** Simulation

setup for lasing from line patches with \mathbf{e}_{pump} along y and \mathbf{e}_{line} reversed to be x . (e) Single-mode lasing emission $\lambda_{\text{SL}}^{\text{I}}$ from simulation at $k_{\parallel} = 0$. (f) Real-time evolution of population inversion at monitor A (left panel) and monitor B (right panel). Inset shows the spatial distribution of population inversion dN around a NP in (d) at 1250 fs.

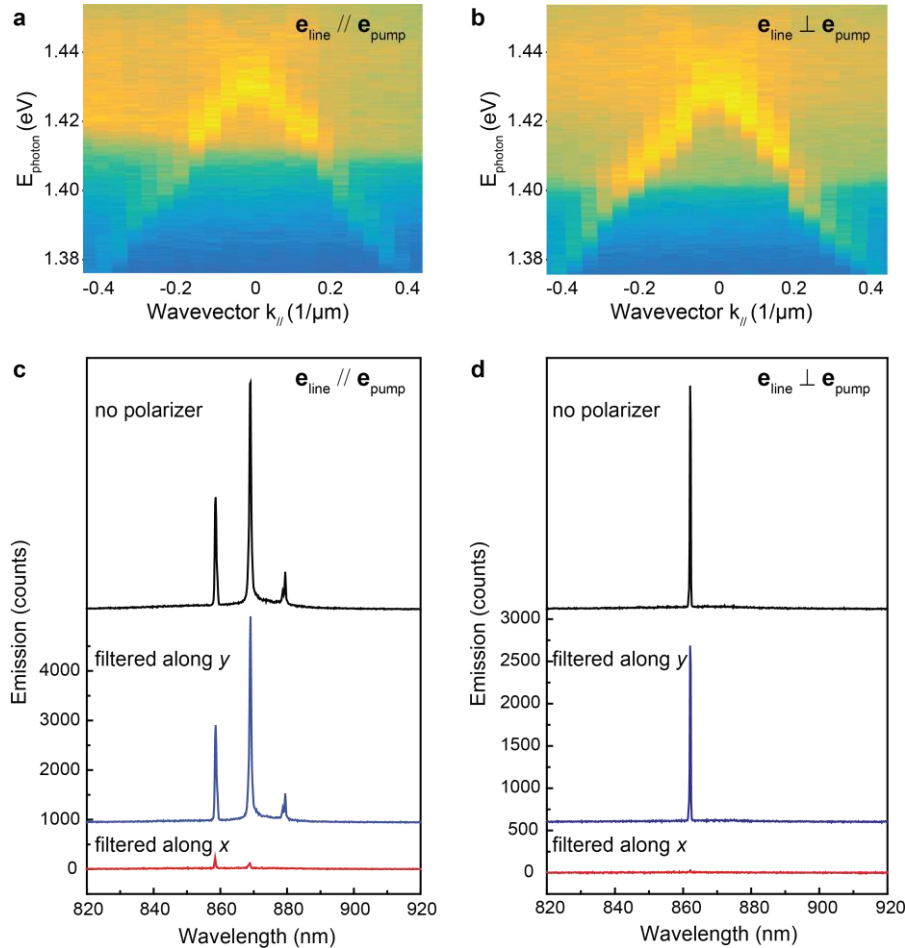


Figure 3.22. Polarization of output lasing emission was aligned with polarization of pump source. (a) Angle-resolved PL emission map from line patches with \mathbf{e}_{pump} along y and \mathbf{e}_{line} along y , and (b) \mathbf{e}_{pump} along y and \mathbf{e}_{line} along x . We used a near-CW laser (80 MHz) to pump the line patch sample at a $2 \times 2 \text{ mm}^2$ spot and 50 mW. (c) Measured multiple lasing modes from line patch with \mathbf{e}_{pump} along y , and \mathbf{e}_{line} orientated along y , and (d) \mathbf{e}_{pump} along y and \mathbf{e}_{line} orientated along x . We placed a linear polarizer between the spectrometer and lasing device to characterize the polarization direction of output beams.

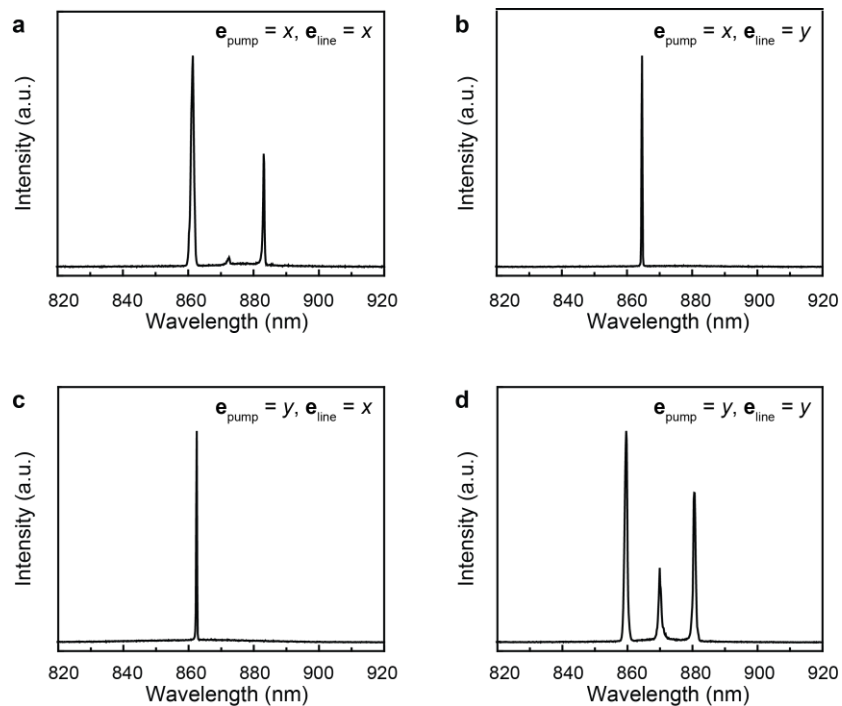


Figure 3.23. Orientation-dependent and polarization-dependent lasing were observed in NP line patches. Measured switchable lasing from line patches with (a) pump polarization direction e_{pump} and line axis e_{line} both along x , (b) e_{pump} along x and e_{line} along y , (c) e_{pump} along y and e_{line} along x , and (d) e_{pump} and e_{line} both along y . IR-140-DMSO concentration was 0.63 mM.

3.6 Microscale Superstrate Molding of Plasmonic NP Arrays

Plasmonic superlattices—finite-arrays of NPs (patches) grouped into microscale arrays—can support multiple band-edge modes at both zero and non-zero wavevectors for multi-modal lasing. However, NP superlattices with rationally designed microfeatures require stringent nanofabrication based on multiscale patterning processes.⁶ In addition, as-fabricated plasmonic superlattice samples showed fixed linear optical properties and band structures.⁵³ The configurable and unique engineering of optical band structures has arisen much interest recently. For example, one-directional edge modes in the band structure are critical in topological photonics.

For plasmonic NP arrays, a uniform index environment is critical in supporting the collective lattice plasmon resonances. The sharp, intense lattice plasmons can only accommodate to moderate index mismatch (< 0.1) between superstrate and substrate.^{12,52} Compared to exquisitely tailoring the position of NPs in an index-matching environment, the selective modulation of NP array superstrate can lead to tunable control of optical behaviors. For example, lattice-resonance metalenses for reconfigurable imaging have been realized by selective tuning of the index surrounding the NPs at the unit cell level.¹⁶⁰ For bare metal NPs in the air above a silica substrate, lattice modes are mostly damped; while for those embedded in SU8 polymers, index-matching with the silica substrate leads to well-defined lattice plasmons, and the dramatic phase-modulation at the wave front enables far-field manipulation in flat optics.

Here we demonstrated facile microscale molding of dielectric superstrate in plasmonic NPs for superlattice resonances. Contact lithography with a patterned Cr mask produced microscale photoresist patches on top of NP arrays, while the spacing areas between patches preserved clean NPs without photoresist residues for index contrast. We observed multiple superlattice plasmons from micro-photoresist molding in both transmission spectra and dispersion diagrams.

Polarization-dependent linear properties and band structures were achieved in symmetry-breaking line patches by superstrate molding. In addition, tunable superlattice resonances and band structures can be realized by rationally patterning of polymer superstrates with different patch spacings.

To create index contrast from molded superstrate, we first made single-lattice Au NP arrays with NP spacing $a_0 = 600$ nm coated with a 150-nm photoresist film (**Figure 3.24**). Contact lithography with a micropatterned Cr mask produced microscale photoresist patches on top, while the spacing areas between patches showed clean NPs without resist residues. Arbitrarily designed photoresist patterns are accessible as defined by the Cr masks. In contrast, PDMS masking on NP arrays produced decreased transmission signals in the visible regime due to the local microscale

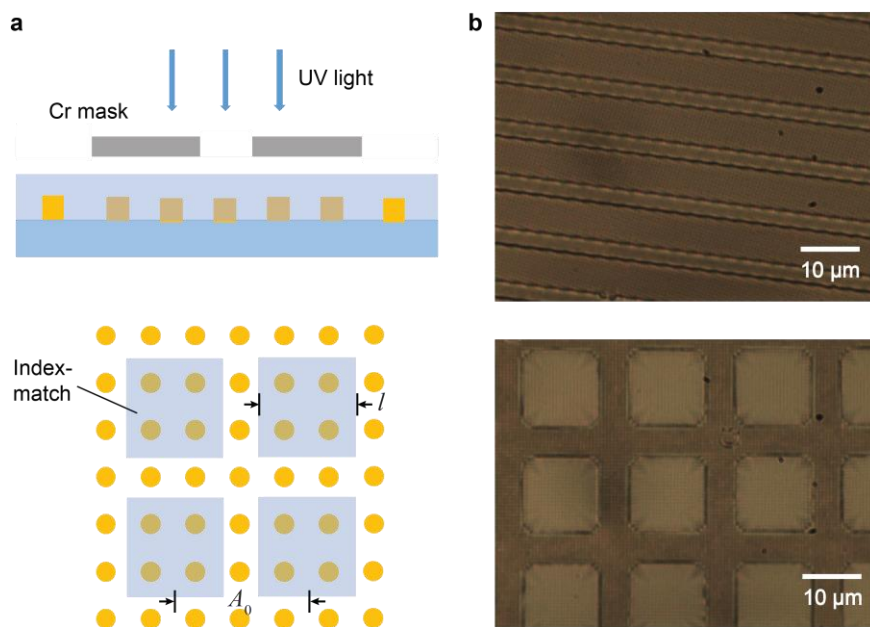


Figure 3.24. Microscale superstrate molding of plasmonic NP arrays. (a) Large scale superstrate patterning on Au NP arrays (b) The optical images of patterned superstrate with (6 μm , 9 μm) line patches and (12 μm , 18 μm) 2D arrays.

air gaps. Micropatterning by solvent assisted nanoscale embossing (SANE) showed protruding SU8 at the patch edge, without sufficient resist coating in the middle of patches.

Compared to superlattice arrays with depleted NPs in between patches, the selective superstrate molding for index-matching also achieved multiple superlattice resonances (**Figure 3.25**). For superlattice arrays ($l = 6 \mu\text{m}$, $A_0 = 9 \mu\text{m}$) in an index matching environment ($n = 1.5$), multiple superlattice resonances are observed at $\lambda = 944 \text{ nm}$ and $\lambda = 981 \text{ nm}$, as well as one weak resonance at $\lambda = 1056 \text{ nm}$. The multiple resonances come from the coupling of the localized surface plasmon of individual NPs to the $n = 15$, $n = 14$ and $n = 13$ orders of Bragg modes from the patch periodicity $A_0 = 9 \mu\text{m}$. In contrast, in molded superstrate NP arrays, the big index contrast in the patch spacing regions ($\Delta n = 0.5$ for $n_{\text{air}} = 1$, $n_{\text{substrate}} = 1.5$) cannot sustain strong lattice plasmons, and hence produced the microscale modulation between superstrate-defined patches. Multiple superlattice resonances are observed at $\lambda = 928 \text{ nm}$ and $\lambda = 976 \text{ nm}$ with slightly broadened resonance linewidth.

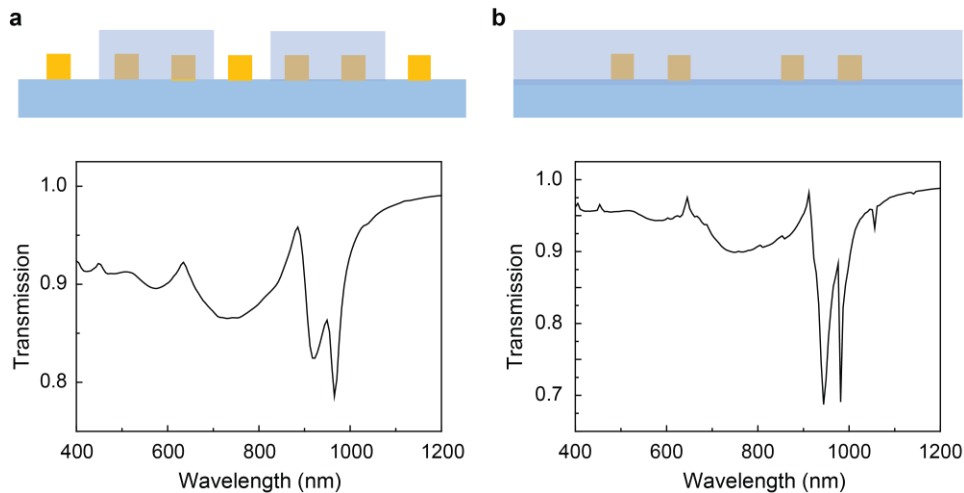


Figure 3.25. Superlattice plasmons from patterned superstrate on NPs. (a) Superlattice modes from patterned superstrate, (b) superlattice modes from spaced patches.

In experiments, multiple superlattice modes appeared in both transmission spectra and the dispersion diagram. For symmetry-breaking line patches by superstrate molding, polarization-dependent optical properties arose from the different coupling mechanism when the incident light was polarized along the x and y directions (**Figure 3.26**). We observed multiple lattice plasmon resonances when the polarization was along the same direction of the line axis (y), since NPs aligned perpendicular to the oscillation direction coupled strongly with each other and experienced microscale index modulation. The dispersion diagram under TE polarization exhibited both a primary mode from NP spacing $a_0 = 600$ nm that followed the $(\pm 1, 0)$ Bragg mode, and a satellite mode from the patch spacing $A_0 = 9$ μm . In contrast, polarization vertical to the direction of the line axis produced a single lattice plasmon resonance in both transmission spectra and the dispersion diagram that followed the $(0, \pm 1)$ Bragg modes, similar to a single-lattice NP array.

Flexible tuning of band structures could be achieved with rational engineering of the NP lattice superstrate features (**Figure 3.27**). Larger patch periodicity (from $A_0 = 9$ μm to $A_0 = 18$ μm) resulted in more high-order Bragg modes with smaller separations that fell within the resonance envelope of the single-patch lattice plasmons. Hence, closer mode spacings between superlattice resonances were observed from transmission spectra and band structures of superlattice arrays. Notably, the slightly decreased transmission intensity in the blue region came from absorption of the photoresist film.

In summary, the rational superstrate engineering on the metal NP array can create index contrast in multiple length scales for long-range plasmon interactions. Since the superstrate can be easily reconfigured by erasing and repatterning by lithography processes, the rational design and tuning of band structures are accessible. In addition, incorporation of active gain media such as dye molecules into superstrate polymers could induce side-by-side patterning of gain and loss

regions within NP arrays at multiple length scales, which offers prospects in parity-time symmetry breaking in a plasmonic nanoresonator system.

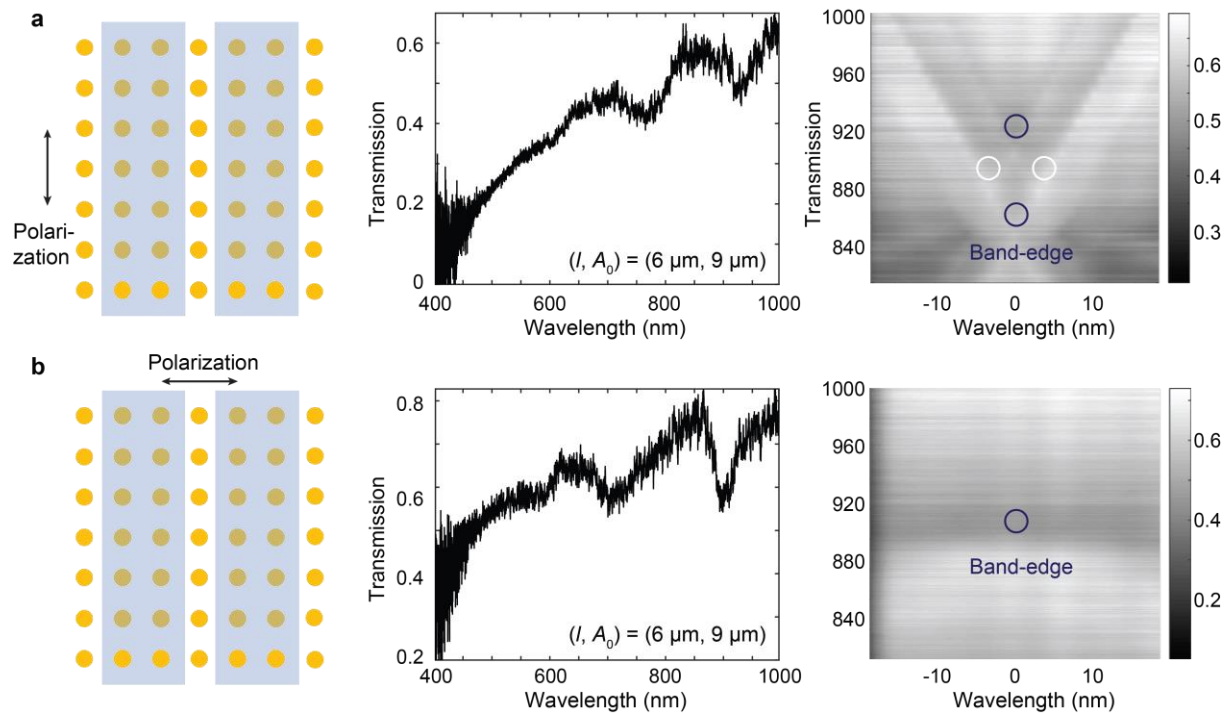


Figure 3.26. Polarization-dependent linear properties for symmetry-breaking line patches. (a) Superlattice resonance from molded line patches when the light was polarized parallel to the line axis, (b) single-lattice resonance when the light was polarized perpendicular to the line axis.

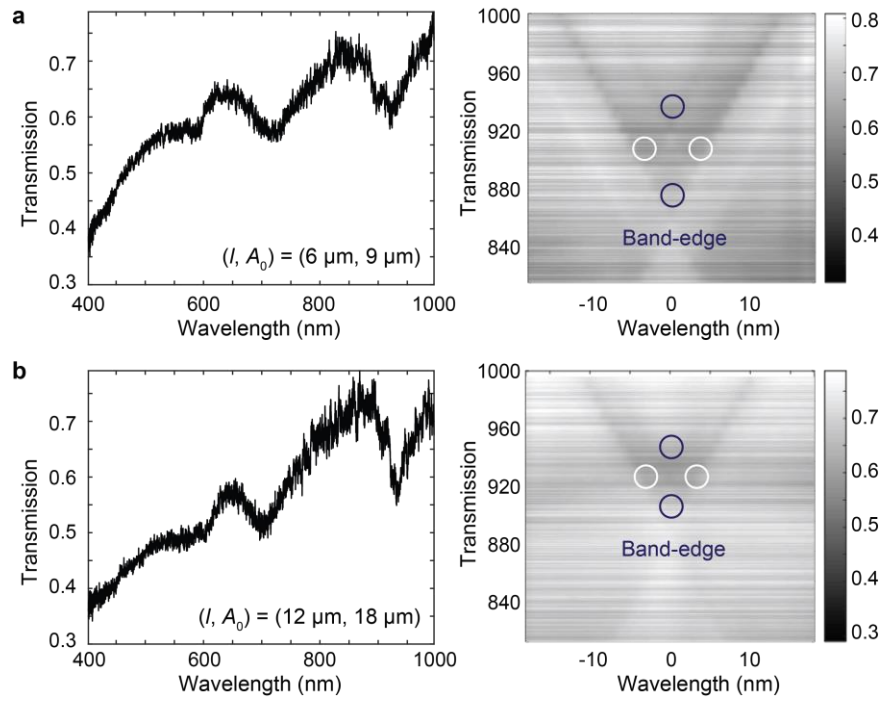


Figure 3.27. Tunable superlattice modes from flexible micro-photoresist molding.

3.7 Summary and Outlook

In summary, we realized superlattice plasmons in hierarchical Au NP arrays. Our multiscale patterning process offers a new approach for generating hierarchical NP arrays over large areas ($> \text{cm}^2$) with independent control over NP periodicity a_0 and patch periodicity A_0 . We found that superlattice plasmons could be described by the coupling of the single-patch lattice plasmons to different orders of Bragg modes from the patch periodicity. Superlattice plasmon resonances can be manipulated by tuning patch periodicity in addition to NP periodicity. We anticipate that superlattice plasmons, with their ultra-narrow resonance linewidths and multiple controllable resonant frequencies in the visible region, will be useful in areas such as ultrasensitive sensing as well as energy transfer and plasmon amplification processes in plasmonic cavities.

In addition, we demonstrated multi-modal nanolasing with controlled, large modal spacing from gold NP superlattices that support tunable, multiple band-edge modes at zero and non-zero wavevectors. Our model based on a four-level system coupled to FDTD calculations fully captured multi-modal lasing contributions from zero and off-normal angles. Compared to conventional micro- and nano-structured lasers, multi-modal lasing from NP superlattices showed strikingly different output emission behavior, spatial coherence, and ultrafast decay dynamics characteristics. Notably, the relative ratios of the different modes could be tuned by changing NP size and local gain concentration. Coherent nanoscale light sources with well-controlled mode position, spacing, and output characteristics offer possibilities for increasing information storage in on-chip photonic devices. Moreover, engineering slow light at multiple band-edges open prospects for manipulating strong light-matter interactions not only for lasing, but also for optical nonlinearities, quantum optics, and other optical processes.

Chapter 4. Scaling Behavior for Lasing from Plasmonic Nanocavity Arrays

Abstract

Small lasers are an emerging platform for generating coherent light for integrated photonics, in-vivo cellular imaging and solid-state lighting. Ultra-sharp lattice plasmons with suppressed radiative loss in strongly coupled plasmonic NP arrays can support lasing with high directionality and tunability. For compact photonic integration, a finite-sized laser is needed; however, the critical NP number N essential for a sub-wavelength laser is unknown. Here we show the critical N in a finite-sized NP array for lasing with a relatively low threshold at room temperature. We found that NP number in plasmonic nanocavity arrays plays a critical role in lasing actions in terms of ultrafast dynamics and lasing thresholds. Narrowing of lattice plasmon resonances associated with stronger near fields was observed with increased NP number. In experiments, lasing from a single patch showed smaller threshold with increased N . Semi-quantum modeling of lasing from a finite-sized patch reveals the dependence of population inversion dynamics and lasing thresholds on N .

Related references

Wang, D; Fumani, A.K.; Schatz, G.C.; Odom, T.W. "Scaling Behavior for Lasing from Plasmonic Nanocavity Arrays" *In preparation*

4.1 Introduction

Small lasers are an emerging platform for generating coherent light for integrated photonics^{22,131,161}, in-vivo cellular imaging,^{23,28} solid-state lighting, and fast 3D sensing in smartphones.^{162,163} Compared to conventional lasers with device size restricted by the diffraction limit, plasmonic nanolasers can confine the optical fields to sub-wavelength scales in at least one dimension. Spasers with single metal NPs can achieve nanoscale mode confinement in three dimensions, but are challenging in experimental realization due to large cavity losses.^{23,43} Nanowire-on-film lasers and nanodisk-on-film lasers utilized surface plasmon polaritons to confine the optical mode at the nanoscale in the vertical dimension.^{162,163} In strongly coupled plasmonic NP arrays, ultra-sharp lattice plasmons with suppressed radiative loss can support lasing with high directionality and tunability.^{12,52,53}

Compared to broad localized surface plasmons in individual NPs, strongly coupled plasmonic NP arrays showed ultra-sharp lattice plasmons with suppressed radiative loss, which can serve as optical feedback for lasing with high directionality and tunability.^{12,52,53} Lasing at room temperature has been observed in plasmonic NP arrays scalable to cm² scale.^{12,52,53} For compact integration with nanophotonics, a finite-sized laser device is needed; however, the critical NP number N essential for sub-wavelength lasing build-up is unknown.^{9,12,52,54} Plasmon nanodisk-on-film lasers showed faster modulation and lower lasing threshold than photonic lasers when the cavity size surpasses the diffraction limit.¹⁶⁴ In photonic distributed feedback lasers, the relationship between N and the resonance linewidth $\Delta\lambda$ has been found to follow the rule $\Delta\lambda \propto 1/N$.¹⁶⁵ Multiscale patterning⁶ facilitates the fabrication of finite-sized metal NP patches with tunable sizes, which enables varying of the NP number N in a single patch.

Here we show the critical NP number N needed in a finite-sized NP array for lasing with a relatively low threshold at room temperature. We found that the NP number in an array plays a dominant role in lasing action in terms of ultrafast dynamics and lasing thresholds. Narrowing of lattice plasmon resonances associated with stronger near fields was observed with increased NP number N within a single patch, and the near field enhancement reached saturation for more than 30×30 NPs. In experiments, lasing from a single patch showed smaller threshold with increased N . Semi-quantum modeling of lasing from a finite-sized patch reveals the dependence of population inversion dynamics and lasing thresholds on N .

4.2 Narrowed Lattice Plasmons with Increased NP Number

Figure 4.1 depicts the lattice plasmon resonances of a finite-sized patch with increased NP number N . For a lattice with diffractive coupling, the radiative loss is further suppressed with more

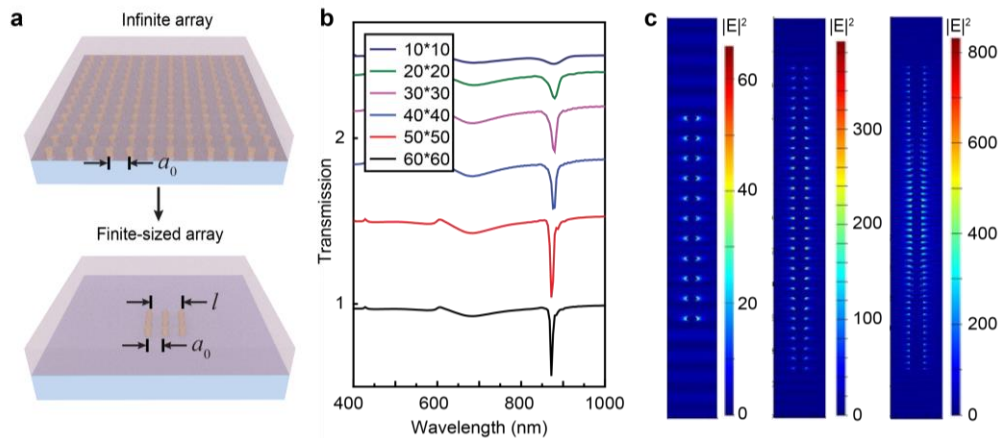


Figure 4.1. Lattice plasmons showed stronger resonances with increasing NP numbers in a finite-sized patch. (a) Scheme of infinite NP arrays to finite-sized NP arrays with spacing $a_0 = 600$ nm. (b) Simulated spectra of lattice plasmons in a single patch showed narrowed resonances with increased NP number N . (c) Near-field enhancement $|E|^2$ with increased N in a patch from 10×10 , 30×30 to 50×50 (left to right).

NPs present, which leads to a narrower, more intense resonance. The figure shows that the resonance linewidth $\Delta\lambda$ of the lattice plasmons shortens from 40 nm to 5 nm as N is increased from 10×10 to 60×60 within a single patch with $a_0 = 600$ nm (**Figure 4.1a**). The intensity of the transmission dips was stronger, and the near field $|\mathbf{E}|^2$ showed orders of magnitude enhancement ($|\mathbf{E}|^2/|\mathbf{E}_0|^2 = 50$ to $|\mathbf{E}|^2/|\mathbf{E}_0|^2 = 800$) as N is increased from 1 to 50×50 . Notably, the increase of near field enhancement nearly reached saturation for patches with more than 30×30 NPs.

Based on multiscale patterning processes,⁶ microscale single patches were made with varying patch size and >10 times larger patch separation to eliminate the coupling between patches: (i) far-spaced single patch ($300 \mu\text{m}$) with tunable patch side length (from $12 \mu\text{m}$ to $120 \mu\text{m}$); (ii) fixed

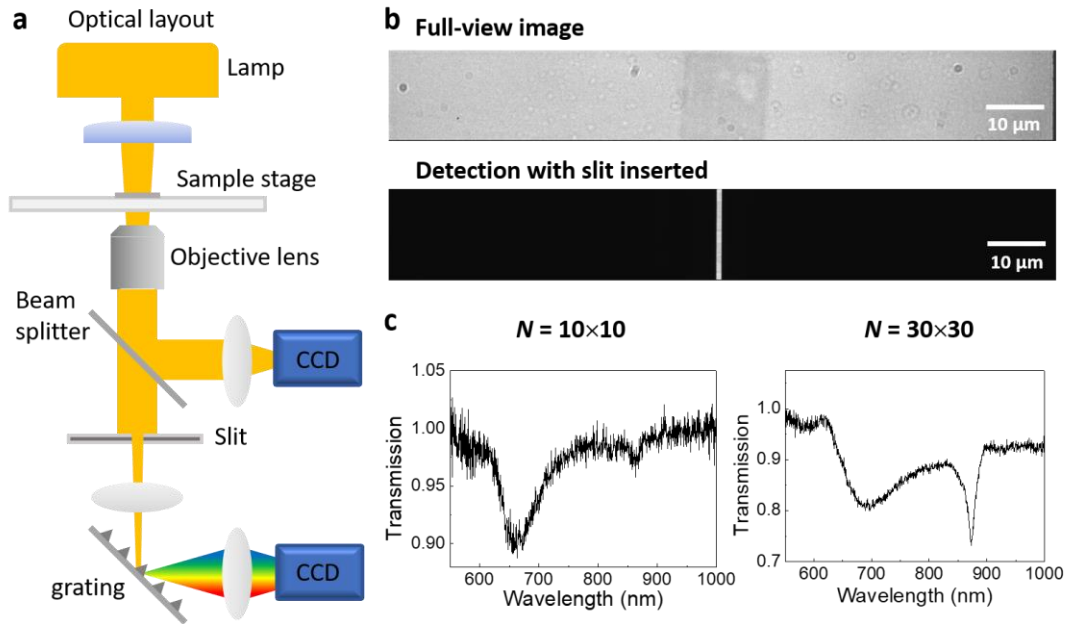


Figure 4.2. Sharper lattice plasmons were detected in experiments with increased NP numbers. (a) Optical setups of a dark-field microscope for imaging and spectroscopy. (b) Image of single patches with side length $l = 18 \mu\text{m}$ and patch spacing $A_0 = 180 \mu\text{m}$ under the microscope and the detection with an inserted slit. (c) Measured transmission spectra from single patches with varying N .

patch sizes ($18\ \mu\text{m}$) with increased patch spacing (from $18\ \mu\text{m}$ to $360\ \mu\text{m}$). With the single-particle microscope, we characterized the transmission spectra of finite-sized patches with increased NP number N (**Figure 4.2a**). Notably, the inserted slit in front of the detector is important for avoiding oblique scattering and detecting a narrow resonance linewidth (**Figure 4.2b**). Consistent with the simulation results, we observed that the lattice plasmons showed narrower and more intense resonances with more NPs in a patch ($\Delta\lambda = 16\ \text{nm}$ to $12\ \text{nm}$, for $N = 10 \times 10$ to 30×30 , **Figure 4.2c**).

4.3 Scaling Behavior for Lasing from Finite-sized Nanocavity Arrays

To characterize the lasing action from single NP patches, we built an optical set-up with an objective lens ($10\times$) to focus the pump laser beam to a controlled microscale region (spot diameter:

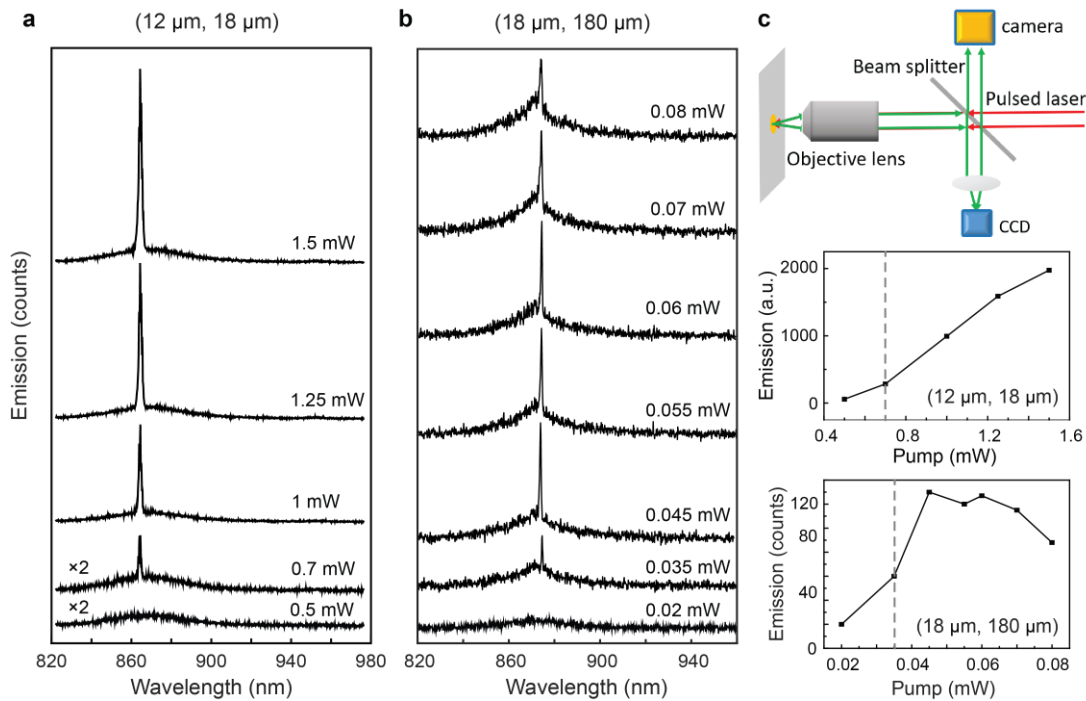


Figure 4.3. Lasing action from single patches of plasmonic nanoparticles. (a-b) Measured single lasing mode from a plasmonic lattice with patch size and patch spacing $(l, A_0) = (12\ \mu\text{m}, 18\ \mu\text{m})$ and $(18\ \mu\text{m}, 180\ \mu\text{m})$, respectively. (c) The optical set-up with an objective lens for beam focusing, and the input-output curves for the single plasmonic NP patches.

20-100 μm). We observed a single lasing mode from large-spaced plasmonic lattices (patch side length $l = 12 \mu\text{m}$ and periodicity $A_0 = 18 \mu\text{m}$, and $l = 18 \mu\text{m}$, $A_0 = 180 \mu\text{m}$, respectively). The far-spaced patches ($A_0 = 180 \mu\text{m}$) ensured that only a single patch was exposed and detected for lasing emission. For 20×20 NPs in a patch, we observed lasing emission at room temperature with a lasing threshold around 70 mJ/cm^2 , while the lasing threshold decreased to 3.9 mJ/cm^2 for 30×30 NPs. Saturation and decreasing of lasing intensity happened at high pump powers, similar to an infinite array. Notably, no lasing from dark modes was observed in a finite-sized patch⁵⁴ possibly due to the low dye concentration (2 mM) and NIR operation regimes.

Figure 4.4 shows that semi-quantum modeling of single-patch lasing reveals a N -dependent lasing build-up. We exploited a four-level system and a time-domain approach to simulate the time- and spatial- dependent lasing buildup in a finite-size array with perfectly matching layer boundaries. For a NP array with increasing number N under fixed pump power and dye concentration, lasing was observed from over 35×35 NPs with the characteristic time-dependent population inversion ($C = 1 \text{ mM}$, pump power 0.9 mJ/cm^2). With more NPs present, the stronger near fields also induced faster population inversion and shorter lasing rise time within the simulation window of 2 ps. Modeled single-patch lasing emission showed saturation behaviors at high powers, consistent with experiments.

4.4 Summary and Outlook

In conclusion, we determined a scaling behavior for the NP number N in plasmonic lattices for nanolasing at room temperature. This work offers critical insights into the relationship between NP number and lasing characteristics including thresholds and ultrafast dynamics in plasmonic

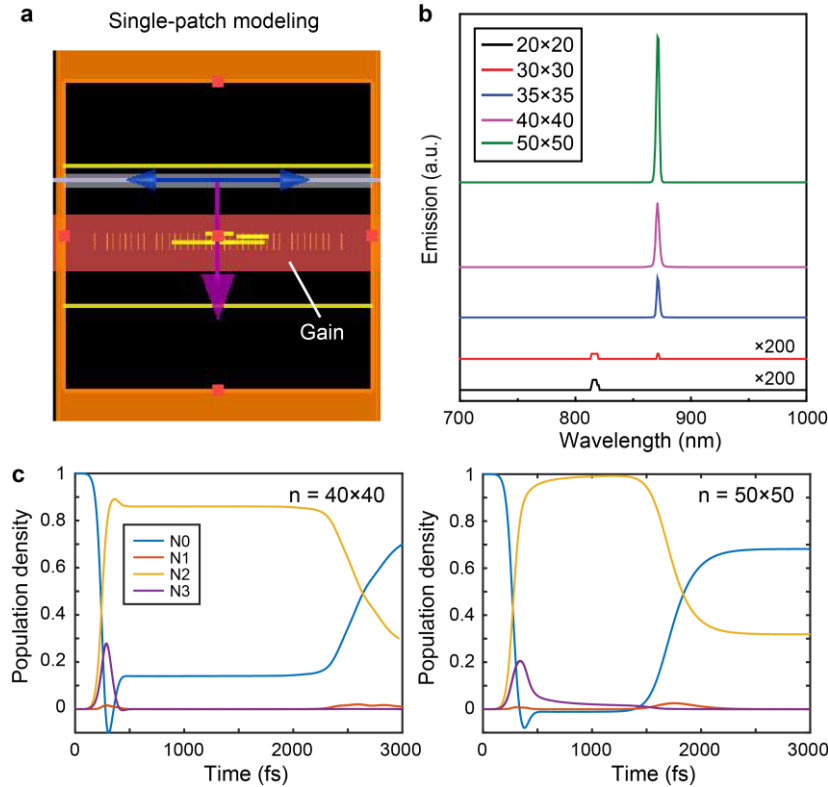


Figure 4.4. Lasing emission intensity and ultrafast dynamics depend strongly on NP number N within a single patch from simulations. (a) Set-up of FDTD simulation scheme. (b) N -dependent lasing build-up with a constant pump power of 0.9 mJ/cm^2 . (c) Time-dependent population inversion with different N .

nanocavity arrays. We expect that the scaling behavior of plasmonic nanocavity arrays will open possibilities for miniaturized on-chip photonic devices and in-situ bioimaging and therapeutics.

To provide perspective, in semi-quantum lasing simulations, we observed that the near-field coupling of NPs in unpumped regions contributed to enhanced lasing emission from dye-embedded regions (**Figure 4.5**). In addition, the lasing emission can propagate to bare NP regions not covered with gain; such energy transfer efficiency decreased with propagation distance. We expect that these long-range energy transfer processes assisted by delocalized lattice plasmons can offer new prospects for optical communications and quantum entanglements.

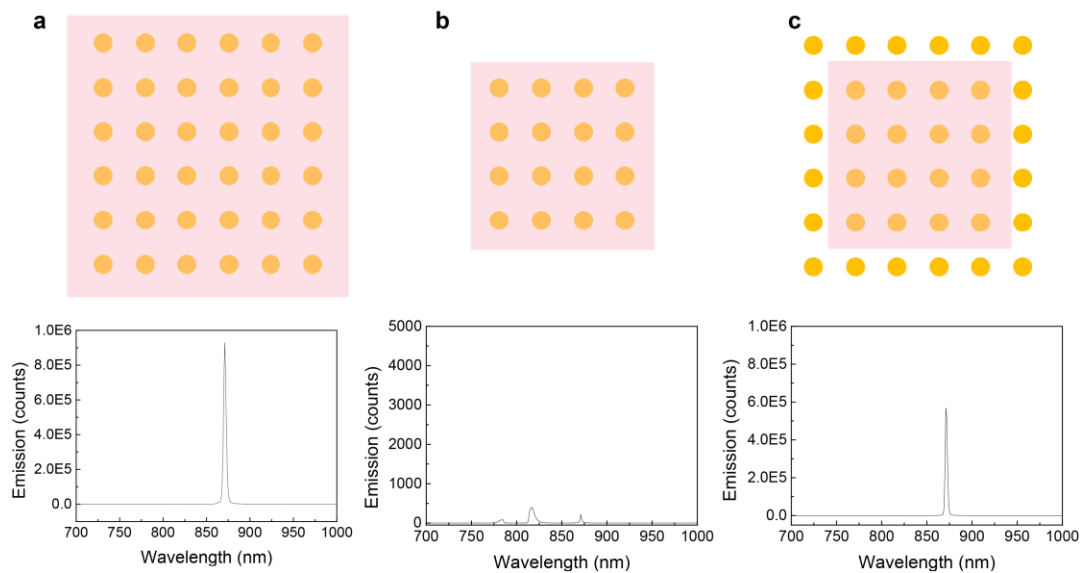


Figure 4.5. Near-field NP coupling in unpumped regions contributes to enhanced lasing emission. Simulated lasing emission from (a) a finite lattice arrays with 40×40 NPs all covered by dye solvent, (b) a finite lattice arrays with 30×30 NPs all covered by dye solvent and, (c) a finite 40×40 lattice array with 30×30 NPs covered by dye solvent.

Chapter 5. Continuous-wave Upconverting Plasmon Nanolasing

Abstract

Nanolasers that operate under continuous-wave pump and are robust in diverse environments will make possible compact optoelectronic devices, versatile bioimaging and theranostics, and large-scale quantum photonics. However, current nanolasers require low temperatures or pulsed excitation because their small mode volumes severely limit gain relative to cavity loss. Here, we show continuous-wave upconverting nanolasing at room temperature with record-low thresholds and high photostability even after six hours of constant operation. We achieved selective single-mode lasing from Yb³⁺/Er³⁺-co-doped upconverting nanoparticles conformally coated on silver nanopillar arrays supporting sharp lattice plasmon modes. The intense electromagnetic near-fields resulted in a threshold of 70 W/cm², orders of magnitude lower than other small lasers.

Related reference

Fernandez-Bravo, A.*; **Wang, D.***; Tajon, C.; Teitelboim, A.; Guan, J.; Schatz, G.C.; Cohen, B.E.; Chan, E.; Schuck, P.J.; Odom, T.W. “Continuous-wave upconverting plasmon nanolasing at room temperature,” *submitted* *equal contribution

5.1 Introduction

Miniaturized lasers are an emerging platform for generating coherent light for quantum photonics, in-vivo cellular imaging, solid-state lighting, and fast 3D sensing in smartphones.^{22,161,166} Continuous-wave (CW) lasing at room temperature is critical for integration with opto-electronic devices and optimal modulation of optical interactions.^{167,168} Plasmonic nanocavities integrated with gain can generate coherent light at sub-wavelength scales,^{12,36,49,53} beyond the diffraction limit that constrains mode volumes in dielectric cavities such as semiconducting nanowires.^{169,170} However, insufficient gain with respect to losses and thermal instabilities in nanocavities have limited all nanoscale lasers to pulsed pump sources and/or low-temperature operation.^{12,36,37,40,49,53,54,164}

Lanthanide-based UCNPs are photostable solid-state nonlinear emitters that are efficient at sequentially absorbing multiple near-infrared (NIR) photons and emitting at visible and shorter-NIR wavelengths.¹⁷¹⁻¹⁷⁴ Recently, UCNPs have been used as gain media in small lasers, and their integration with dielectric microcavities and hyperbolic metamaterials has resulted in multi-wavelength upconverted lasing.¹⁷⁵⁻¹⁷⁷ UCNPs also exhibit long radiative lifetimes (typically 100s of μs) compared to other gain materials,^{173,178,179} which leads to low saturation intensities that could facilitate CW pumping and population inversion build-up. Pump powers required for UCNP lasing are orders of magnitude lower than those for nanolasers based on quantum dots, dye molecules, or conventional nonlinear optical materials.^{12,177,180} Additionally, organic molecules exhibit triplet-state accumulation and limited photostability, and semiconductor nanomaterials undergo Auger recombination, which reduces population inversion under CW pump.^{70,167,181}

Multiphoton upconverting processes can be strongly enhanced by the intense electromagnetic fields from plasmonic nanostructures.¹⁸² However, surface plasmon resonances from single NPs are typically broadband with low mode quality. Spectral overlap with multiple, narrow UCNP energy bands results in reduced output efficiency at a single targeted mode because of internal energy transfer.^{183,184} Arrays of metal NPs can overcome these challenges because collective, coherent coupling can produce narrow lattice plasmon resonances (linewidths < 5 nm) with suppressed radiative loss and stronger near-field enhancements compared to single NPs.^{4,5} Previously, we demonstrated band-edge lattice plasmons as optical feedback for down-shifted dye nanolasing at room temperature with directional emission and tunable wavelengths.^{12,52,53,115} Compared to photonic microcavities that exhibit multiple cavity modes,¹⁷⁶ plasmonic nanocavity arrays with a single lattice spacing support a single, narrow mode that can, in principle, selectively enhance specific upconverting energy transitions.

Here we show CW upconverting lasing at room temperature with record-low thresholds and high photostability from sub-wavelength plasmons. We achieve selective, single-mode lasing from Yb³⁺/Er³⁺-co-doped upconverting nanoparticles (UCNPs) conformally coated on Ag nanopillar arrays that support a single, sharp lattice plasmon cavity mode and $> \lambda/20$ field confinement in the vertical dimension. The intense electromagnetic near-fields localized in the vicinity of the nanopillars result in a threshold of 70 W/cm², orders of magnitude lower than other small lasers. Our plasmon-nanoarray upconverting lasers provide directional, ultra-stable output at visible frequencies under near-infrared pumping, even after six hours of constant operation, which offers prospects in previously unrealizable applications of coherent nanoscale light. In addition, the upconverting nanolaser can achieve CW emission under both CW and pulsed pump conditions.

We used time domain, semi-quantum modeling to capture the characteristic population inversion and strong optical nonlinearities.

5.2 Low-threshold Upconverting Nanolasing

We designed nanolaser devices that integrate two key advances in order to enhance coupling between the nanocavity and the lanthanide (Ln) emitters, to lower upconverting lasing thresholds, and to improve device stability. First, we fabricated Ag nanopillar arrays with a lattice plasmon resonance that overlaps the red Er^{3+} upconverted emission transition ($^4\text{F}_{9/2}$ to $^4\text{I}_{15/2}$) in colloidal UCNPs doped with sensitizer Yb^{3+} ions / emitter Er^{3+} ions (**Figures 5.1a-c**). Second, we exploited core-shell UCNPs with high Ln content that are known to show significantly improved luminescence properties compared to canonical compositions.^{179,185} The high-Ln-content UCNPs are core-shell heterostructures with 13.9 ± 1.3 nm diameters comprised of 9.9-nm β -phase NaYF_4 cores doped with 20% Yb^{3+} / 20% Er^{3+} and 2-nm NaYF_4 shells (**Figure 5.2**).¹⁸⁶

In our all-solid-state system under ambient conditions, NIR pumping at 980 nm can excite Yb^{3+} ions in the UCNPs, which transfer energy to Er^{3+} ions to facilitate upconverted emission at multiple visible and NIR wavelengths, and lattice plasmon modes can be engineered to couple selectively to Er^{3+} emission (red) (**Figure 5.1d**). The plasmonic arrays consist of Ag nanopillars (80-nm diameter, 50-nm height) arranged in a square lattice with periodicity a_0 ranging from 450 – 460 nm depending on which transition within the Er^{3+} red emission manifold was of interest (Figures. 5.1a-c). For protection of these nanopillars, we used atomic layer deposition to deposit 5 nm Al_2O_3 around the nanopillar surface. As described previously,^{4,5} collective coupling of plasmonic nanopillar arrays produces a sharp lattice plasmon mode with a quality factor $Q = \frac{\lambda}{\Delta\lambda} > 200$ that is maintained after coating with UCNPs (**Figure 5.3**). UCNPs were drop-cast from

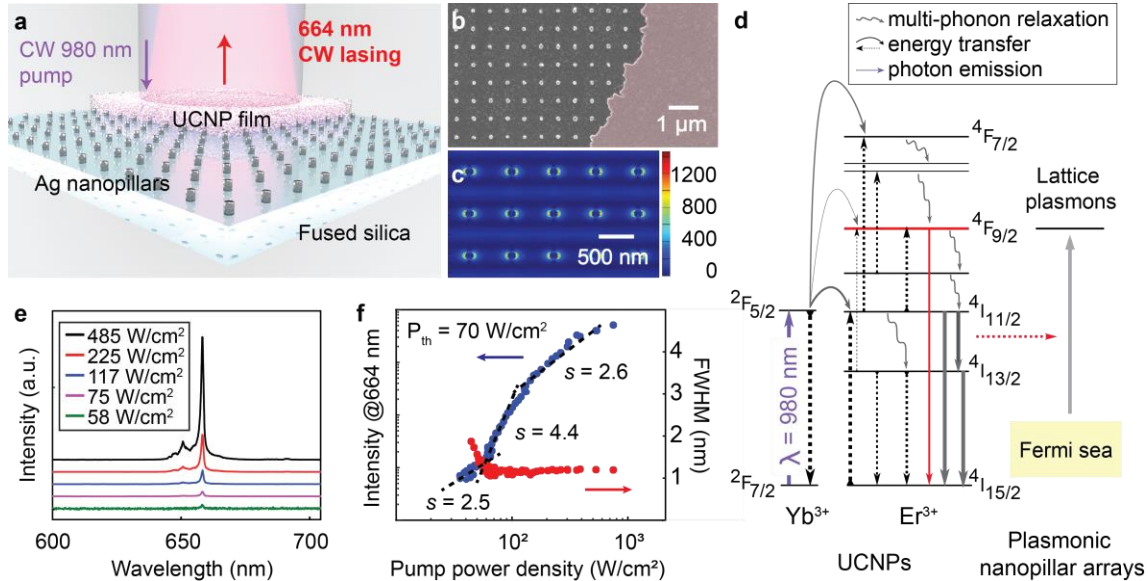


Figure 5.1. Continuous-wave (CW) upconverting nanolasing on Ag nanopillar arrays at room temperature. (a) Schematic of the upconverting nanoparticle (UCNP) coating on top of Ag arrays with spacing $a_0 = 450$ nm. Ag nanopillars are with 80-nm diameter, 50-nm height and scalable over cm^2 areas. The UCNP film is ca. 150 nm thick. (b) Scanning electron micrograph showing the Ag nanopillar array with partial conformal coating (right) with a film of 14 nm core-shell UCNPs ($\text{NaYF}_4:\text{Yb}^{3+}, \text{Er}^{3+}$). (c) Representative near-field $|E|^2$ plot for the 450-nm spaced Ag nanopillars at resonance ($n = 1.46$) from a finite-difference time-domain method simulation. (d) Yb^{3+} , Er^{3+} energy levels and coupling mechanism to the lattice plasmons. (e) Power-dependent lasing spectra from lattice plasmon resonances at $\lambda = 664$ nm for Ag nanopillar arrays with $a_0 = 450$ nm. (f) Input-output curves in log-log scale with emission linewidth narrowing, showing a low lasing threshold of 70 W/cm^2 .

solution onto the arrays to form conformal films of thickness ca. 150 nm, resulting in UCNPs that are situated at the nanoscale plasmonic hotspots within 25 nm surrounding each nanopillar surface (Figures 5.1a-c; near-field enhancement at the nanopillars, $|E|^2/|E_0|^2 > 1000$). Since the refractive index n of UCNPs ($n \sim 1.47$ @ 660 nm) closely matches that of the fused silica substrate ($n \sim 1.46$ @ 660 nm) (Figure 5.3), the Ag nanopillars were effectively embedded in a uniform index

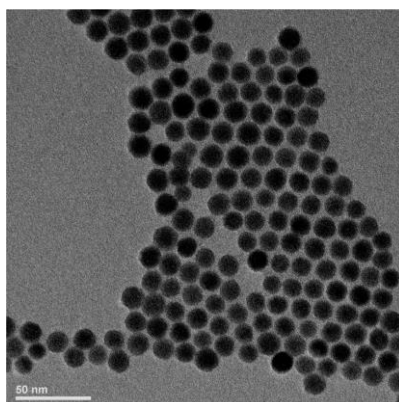


Figure 5.2. Transmission electron micrograph of core/shell UCNPs.

environment, which is critical for sustaining high-quality lattice plasmons. The dispersion diagram of lattice plasmons after UCNP coating showed that the plasmon resonance followed the Bragg mode defined by the lattice.

To determine whether UCNPs are coupled to the plasmonic nanocavities, we first characterized spontaneous emission from UCNPs on the plasmonic array at low (ca. 20 W/cm^2) pump intensities. Enhanced upconverted emission between 650-660 nm was resolved at each Ag nanopillar position (**Figure 5.4**). The fast Fourier transform of the output image evidenced the periodic spatial modification of the emission signals. As CW pump intensity increased beyond a threshold, lasing action occurred at the lattice plasmon resonance wavelength (**Figure 5.1e**). At threshold, we observed both a significant increase in rising slope ($s = 4.4$) in the input-output curve compared to spontaneous emission ($s = 2.2$; **Figure 5.5**) and simultaneous linewidth narrowing of the lasing mode to $< 1 \text{ nm}$ (**Figure 5.1f**). The lasing threshold of 70 W/cm^2 from the device in Fig. 5.1f represents a > 200 -fold improvement over that of upconverting microresonators¹⁷⁶ and orders of magnitude reduction over that of nanodisk-on-film^{39,164} or nanowire-on-film^{37,40} plasmon lasers at room temperature (**Table 5.1**). The low thresholds of our UCNP plasmon lasers (as low as 29

W/cm^2) can be attributed to both bright $\text{Yb}^{3+}/\text{Er}^{3+}$ -co-doped UCNPs favorable to CW pump and single-mode plasmon nanocavities with spectrally selective, strong optical enhancement ($|\mathbf{E}|^2/|\mathbf{E}_0|^2 > 10^3$).

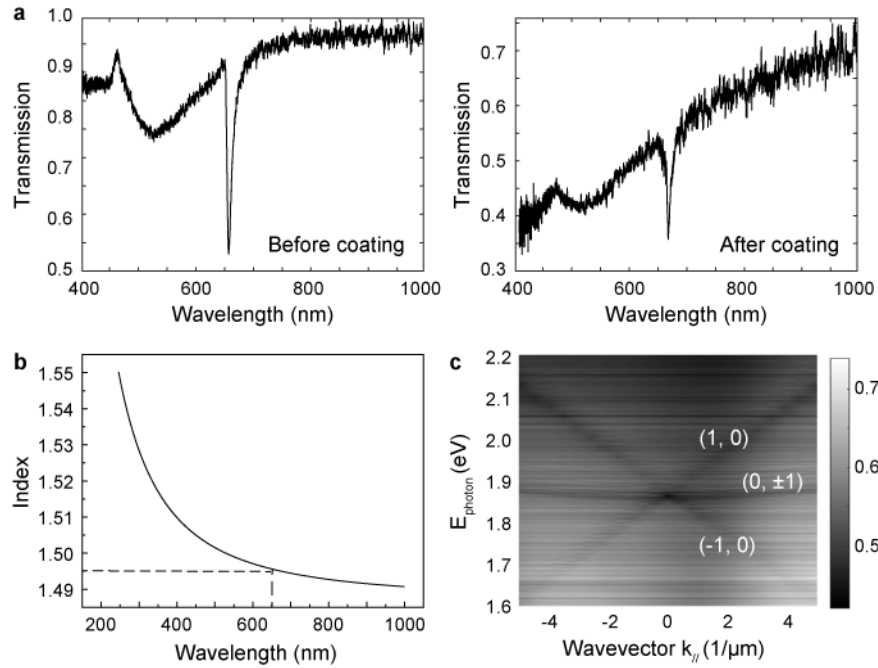


Figure 5.3. Preserved lattice plasmon resonances after coating Ag nanopillars with UCNP emitters. (a) The resonance lineshape and position of lattice plasmons showed only slight modifications after coating Ag NP arrays with $\text{Yb}^{3+}/\text{Er}^{3+}$ -based UCNPs. Measured transmission spectra of Ag nanopillar arrays with $a_0 = 450$ nm in DMSO (left) and coated with UCNPs (right). (b) The dispersion property of a thin Er-UCNP film measured by ellipsometry, suggesting that the refractive index of Er-UCNPs is close to the fused silica substrate ($n = 1.48$) at 650 nm ($n = 1.50$). (c) The dispersion diagram of lattice plasmons after UCNP coating shows that the plasmon resonance follows the Bragg mode defined by the lattice.

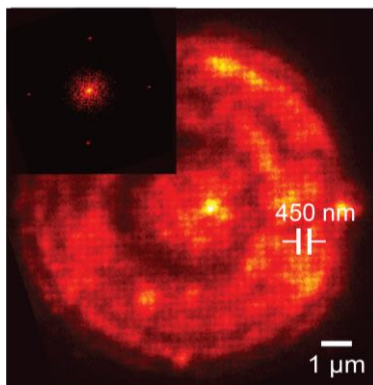


Figure 5.4. Resolving plasmon-enhanced emission from UCNP-coated Ag nanopillar arrays with high numerical aperture (NA) wide-field imaging. Wide-field image of Er^{3+} upconverted red emission (ca. 660 nm) enhanced at the local plasmonic hot spots surrounding each Ag nanopillar within the array. The inset shows the fast Fourier transform of the image evidencing the periodic nature of the emission distributions. The distance between Ag nanopillars can be resolved and measured in the image; $a_0 = 450$ nm for this case. The image was collected with a 100×0.95 NA objective at 17.8 W/cm^2 .

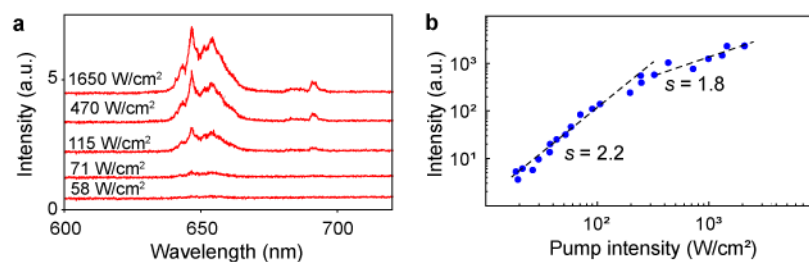


Figure 5.5. Er³⁺ red-band emission and pump intensity dependence for a UCNP film. (a) Intensity-dependent spectra of upconverted emission from the same UCNPs used in the lasing experiments. (b) Light-in-light-out curve for the emission intensity, showing the expected nonlinear behavior typical of a pseudo 2-to-3 photon process, followed by the onset of saturation at higher pump fluences. There is no Ag nanopillar array for this control measurement.

Laser type	Year	Pump (pulse length, operation frequency)	Temperature	Lasing Threshold
Plasmon nanowire-on-film laser ³⁶	2009	100 fs, 80 MHz	< 10 K	50 MW/cm ²
Plasmon microdisk-on-film laser ³⁹	2011	100 fs, 10 kHz	Room temperature	3000 MW/cm ² avg.*
Plasmon nanowire-on-film laser ⁴⁹	2012	CW	Liquid nitrogen	3.7 kW/cm ²
Plasmon nanoparticle array laser ¹²	2013	100 fs, 1 kHz	Room temperature	1 mJ/cm ²
Plasmon nanowire-on-film laser ³⁷	2014	150 fs, 800 kHz	Room temperature	0.2 mJ/cm ²
UV plasmon nanowire-on-film laser ⁴⁰	2014	10 ns, 100 kHz	Room temperature	1 MW/cm ² avg.*
Plasmon nanodisk-on-film laser ¹⁶⁴	2017	4.5 ns, 1 kHz	Room temperature	10 kW/cm ² avg.*
Photonic UCNP microbead laser ¹⁷⁶	2018	CW	Room temperature	50 kW/cm ²
Upconverting plasmon nanolaser (this work)	2019	CW	Room temperature	29 W/cm ²
				70 W/cm ²
		150 fs, 80 MHz		32 W/cm ² avg.*
				210 W/cm ² avg.*
300 W/cm ² avg.*				

Table 5.1. Summary metrics of previously reported plasmon and upconverting lasers in terms of types, pump modality, operation temperature and lasing thresholds. Our upconverting plasmon nanolasers showed the lowest lasing threshold while satisfying both continuous wave pump and room temperature operation for the first time¹. *For fair comparison, we note when average powers are reported for the pulsed excitation measurements, and peak power is left unlabeled.

Besides enabling low thresholds, plasmonic array nanocavities offer directional and highly-efficient coupling, in contrast to spherical and cylindrical cavity geometries based on whispering gallery modes, where input coupling is non-trivial and emission is less directional. The collective coupling between periodic Ag nanopillars results in directional, beam-like upconverted emission at the band-edge Γ point¹² with a low divergence angle of ca. 0.5° (**Figures 5.6a-b**). Additionally, the lasing beam is polarized along the same direction as the incident pump (**Figures 5.6c-d**). This polarization coherence is distinct from unpolarized spontaneous emission from UCNPs (regardless of excitation polarization) that results from energy transfer migration between dopant ions within a single UCNP over the long lifetimes of Ln^{3+} excited states¹⁷⁸ and random nanocrystal orientation.¹⁸⁷ Moreover, our upconverting nanolaser shows long-term stability, which is typically challenging for multiphoton lasing systems since high peak pump intensities are often required for nonlinear responses.¹⁷⁶ Our all-solid-state system operated at room temperature for more than 6 h under continuous irradiation, the longest operational period we tested (**Figures 5.6e-f**). Over this time, we did not observe any optical or thermal damage; the mode intensity remained constant, and only minimal shifts in mode frequency (< 0.15 nm) occurred. In contrast, CW lasing based on semiconductor NPs was not stable over 1 h under fluences similar to those used in this study.^{167,181}

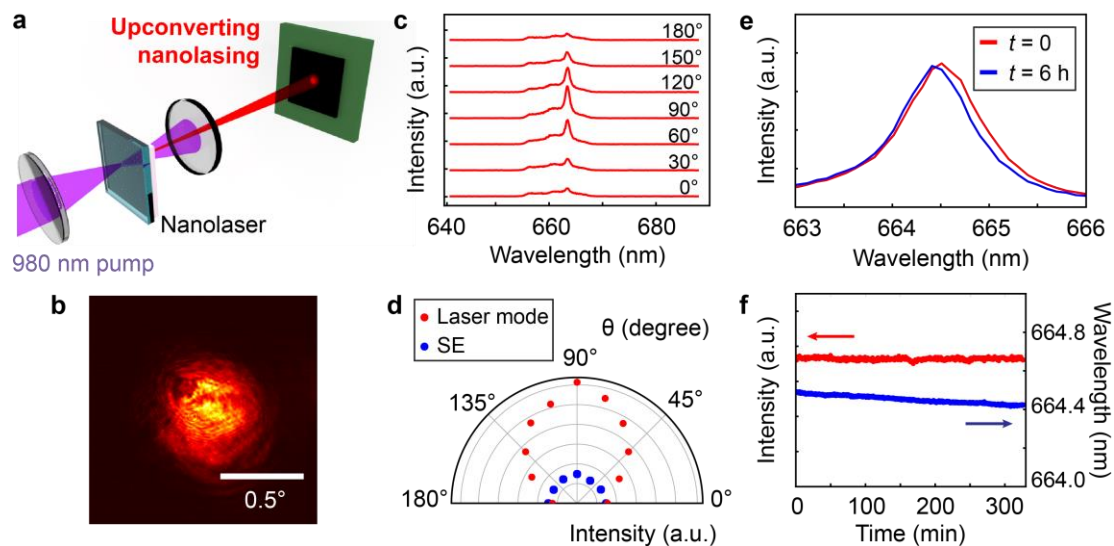


Figure 5.6. Upconverting nanolasing showed spatial and polarization coherence, as well as high photo-stability. (a) Schematic of the experimental optics setup to measure the far-field beam profile. The excitation beam is filtered out using a short pass 745 nm filter and 660/10 nm band pass filter, enabling the CMOS sensor to record only the emission from the plasmon nanolasing at 664 nm. (b) Far-field beam profile of lasing emission above threshold, with the camera detector placed 2 cm away from the sample plane, showing a beam divergence of ca. 0.5°. (c) Polarization-dependent lasing emission with pump polarized at 90°. (d) The polar plot represents the emission intensity of the 664 nm lasing mode and the spontaneous emission (SE) as a function of the polarization angle θ . (e-f) Stability of lasing spectra, intensity and wavelength (red and blue curves) over the course of 6 hours of uninterrupted irradiation, exhibiting stable emission intensity and modest mode shift (< 0.15 nm).

5.3 Upconverting Lasing under Pulsed Pumps

Interestingly, we find that CW lasing occurs even under pulsed pumping conditions in our upconverting plasmon nanolaser (**Figure 5.7**). This observation is consistent with excited state lifetimes that are much longer than both the pulse width and repetition period of the pulsed pump (~120 fs and ~13 ns, respectively). A second-order correlation measurement was implemented using a Hanbury-Brown and Twiss (HBT) setup with a 50/50 beam splitter and 2 MPD detectors to characterize the output temporal feature of upconverting nanolasers under a pulsed pump. The $g^{(2)}$ optical second-order cross correlation is defined as:

$$g^{(2)}(\tau) = \langle I_{det1}(t) \cdot I_{det2}(t+\tau) \rangle \quad (5.1)$$

where $I_{det1}(t)$ and $I_{det2}(t)$ are the signal intensities measured at the two detectors (the two discrete photon streams collected by the two channels). The brackets denote the expectation value and t and τ are the photon arrival time and delay. The counts in the $g^{(2)}$ histogram are the number of photon pairs detected for different delays using the two detectors (which means it should vary with the measurement length, selected bin size and signal intensity). The normalized $g^{(2)}$ is:

$$g^{(2)} = \frac{\langle I_{det1}(t) \cdot I_{det2}(t+\tau) \rangle}{(\langle I_{det1}(t) \rangle \cdot \langle I_{det2}(t+\tau) \rangle)} \quad (5.2)$$

which is the normalization by division of the mean signal of the two detectors. **Figure 5.8** depicts the $g^{(2)}$ histogram for the upconverted lasing at ca. 660 nm for above-threshold powers (CW and pulsed pumping schemes), showing that the normalized $g^{(2)}$ function is 1 for both pumping schemes. This demonstrates that there is no temporal correlation between the emitted photons, which is a signature of CW lasing. The CW output under a pulsed pump (80 MHz) is attributed to the ultra-long decay lifetime of UCNPs (~200 μ s) compared to the short pump pulses (12.5 ns).

The highly nonlinear scaling with power shows slopes as high as 10, and the simultaneous mode narrowing experienced at threshold powers indicates lasing behavior that happens in a CW fashion.

To highlight the ability of the system to select specific Er^{3+} transitions for lasing, we varied the nanopillar lattice constant a_0 , which modified the lattice plasmon nanocavity mode. Shifting the resonance from 650 nm ($a_0 = 450$ nm) to 660 nm ($a_0 = 460$ nm), we observed that the upconverted lasing emission followed the cavity mode resonance, demonstrating that single-mode upconverting lasing is directly determined by the plasmonic nanocavities (**Figure 5.7a**). We found similar lasing thresholds and power dependencies for both lattice spacings, including high nonlinearity in the gain portion of the input-output curves ($s = 5.3$ and 4.7 above the threshold for the devices with modes at 650 nm and 660 nm, respectively, **Figure 5.7b**). Note that the extreme saturation of excited states under pulsed excitation led to a smaller rising slope ($s = 1.2$) at high pump powers.

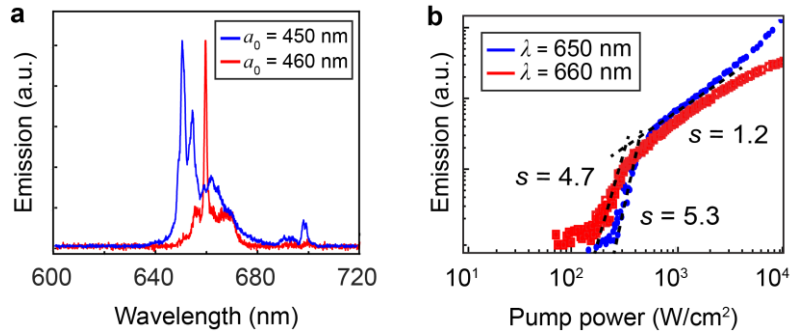


Figure 5.7. Upconverting CW nanolasing under a pulsed laser and semi-quantum modeling in the time domain. (a) Lasing spectra with lasing modes at $\lambda = 650$ and 660 nm from UCNPs coupled to Ag nanopillar arrays with spacing $a_0 = 450$ (blue) and 460 nm (red), respectively. The results show the selective coupling between Er^{3+} red emission from components of the ${}^4\text{F}_{9/2}$ level and the tailored plasmon resonances associated with collective Bragg modes of the Ag nanopillar arrays. (b) Input-output curves in log-log scale show a slightly lower laser threshold for the mode at 660 nm.

In addition, the lasing thresholds are similar in terms of average power with both CW and pulsed laser pumps (Table 5.1).

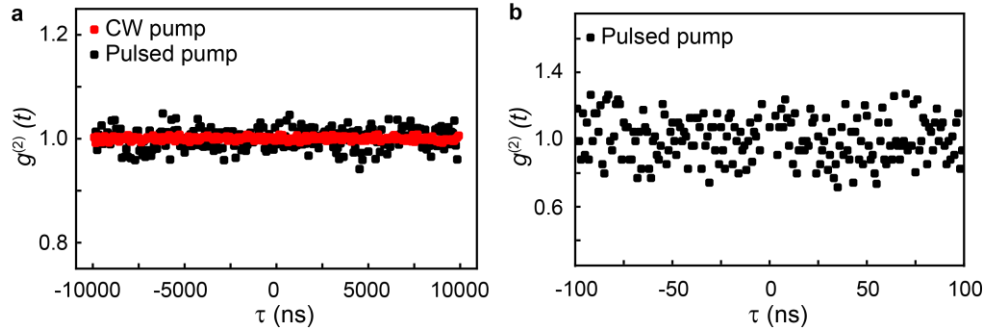


Figure 5.8. Temporal coherence of upconverting nanolasing by $g^{(2)}$ measurements under CW and pulsed pump. (a) $g^{(2)}(t)$ for 10000 ns window and bin size 100 ns for the plasmon laser at 664 nm under CW excitation above threshold (112 W/cm^2) in red, and pulsed excitation (230 W/cm^2) in black showing the values of 1 for the entire window. (b) $g^{(2)}(t)$ for 100 ns window and bin size 1 ns for the plasmon laser at 664 nm under pulsed excitation above threshold (230 W/cm^2), showing CW emission and no modulation with the 80 MHz excitation (12.5 ns delay between pulses) and with values close to 1 for the entire window.

5.4 Six-level System for Modeling Upconverting Lasing

To gain insight into the lasing mechanisms of these low-threshold CW nanolasers, we used a semi-quantum model and a time-domain approach to study the nonlinear optical build-up under a pulsed pump (**Figure 5.9**). The narrow lattice plasmon resonance provides selective enhancement only for the ${}^4F_{9/2}$ -to- ${}^4I_{15/2}$ red emission without directly affecting energy transfer processes at other energies. Therefore, we used a simplified six-level model to describe the two-photon optical pump process approximately. The rate equation depicts as follows:

$$\begin{aligned}
 \frac{dN_5}{dt} &= -\frac{N_5(1-N_4)}{\tau_{54}} - \frac{N_5(1-N_0)}{\tau_{50}} + \frac{1}{\hbar\omega_a} E \frac{dP_a N_3}{dt} \\
 \frac{dN_4}{dt} &= \frac{N_5(1-N_4)}{\tau_{54}} - \frac{N_4(1-N_1)}{\tau_{41}} + \frac{1}{\hbar\omega_e} E \frac{dP_e}{dt} + \frac{1}{\hbar\omega_a} E \frac{dP_a N_2}{dt} \\
 \frac{dN_3}{dt} &= -\frac{N_3(1-N_0)}{\tau_{30}} - \frac{N_3(1-N_2)}{\tau_{32}} + \frac{1}{\hbar\omega_a} E \frac{dP_a}{dt} - \frac{1}{\hbar\omega_a} E \frac{dP_a N_3}{dt} \\
 \frac{dN_2}{dt} &= \frac{N_3(1-N_2)}{\tau_{32}} - \frac{1}{\hbar\omega_a} E \frac{dP_a N_2}{dt} \\
 \frac{dN_1}{dt} &= \frac{N_4(1-N_1)}{\tau_{41}} - \frac{N_1(1-N_0)}{\tau_{10}} - \frac{1}{\hbar\omega_e} E \frac{dP_e}{dt} \\
 \frac{dN_0}{dt} &= \frac{N_5(1-N_0)}{\tau_{50}} + \frac{N_1(1-N_0)}{\tau_{10}} - \frac{1}{\hbar\omega_a} E \frac{dP_a}{dt} + \frac{N_3(1-N_0)}{\tau_{30}} \\
 N_t &= N_0 + N_2 + N_3
 \end{aligned} \tag{5.3}$$

In the semi-quantum system, we set the Ag nanopillar size $d = 80$ nm and height $h = 50$ nm, pump wavelength at $\lambda_a = 980$ nm, emission at $\lambda_e = 660$ nm and index $n = 1.42$, close to experimental conditions. The decay lifetimes were set as $t_{54} = t_{10} = 10$ fs, $t_{41} = 0.1$ ns, and $t_{50} = t_{32} = t_{30} = 1$ ns. We initially pumped the six-level system from the ground state (population density $N_0 = 1$, $N_1 = N_2 = N_3 = N_4 = N_5 = 0$) and collected all emitted flux with a plane monitor placed 0.3 μm away on top of the nanopillars. The calculations show a large exponentially rising slope ($s = 4.8$) above the lasing threshold, which is similar to nonlinear buildup seen in the experiments (**Figures 5.10a-b**). In contrast, the slow rise close to threshold ($s = 1.8$) corresponds to the intrinsic

two-photon emission of $\text{Yb}^{3+}/\text{Er}^{3+}$ -co-doped UCNPs. To capture the time-dependent lasing build-up, we tracked the evolution of population density in different energy levels and found a characteristic population inversion from ${}^4\text{F}_{9/2}$ to ${}^4\text{I}_{15/2}$ above threshold (**Figures 5.10c-d**). No population inversion was observed for upconverted emission below threshold, consistent with a slow rising slope (Figure 5.10c). The calculated lasing threshold occurred at an average power of 270 W/cm^2 (Figure 5.10b), comparable with experiments. Minor differences in threshold are likely because of unknown gain values for the UCNPs and the simplified Er^{3+} electronic structure in our model, where we included only select Er^{3+} excited states. Therefore, our semi-quantum model with a six-level system captured the characteristic population inversion and strong optical nonlinearities in upconverting lasing.

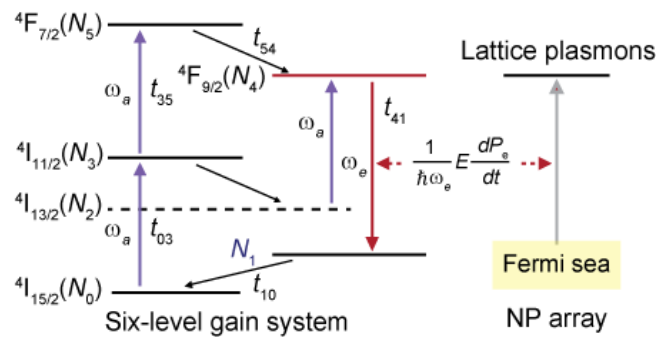


Figure 5.9. The semi-quantum system used for modeling the upconverting plasmon nanolasing in the time domain. The energy diagram showed that the six-level UCNP system was coupled to the lattice plasmon resonances.

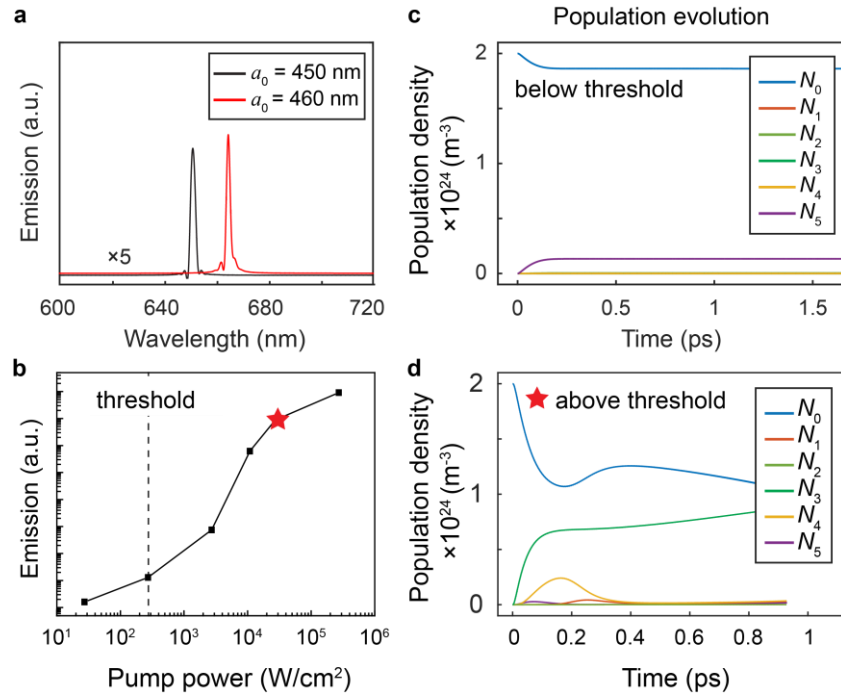


Figure 5.10. The semi-quantum system used for modeling the upconverting plasmon nanolasing in the time domain. (a) The simulated upconverting nanolasing showed single-mode lasing emission determined by the lattice constant a_0 of the array. (b) Simulated input-output curve showing a threshold-like power dependence with laser thresholds comparable to the experimental values. (c) No population inversion between different energy levels was observed in our semi-quantum simulations below the lasing threshold. (d) Simulated time-dependent evolution of population density describing upconverting nanolasing and the associated population inversion above threshold at $27 \text{ kW}/\text{cm}^2$ (marked star position).

5.5 Summary and Outlook

In summary, we demonstrated CW upconverting plasmon nanolasing at room temperature. We observed exceptionally stable lasing over long periods (> 6 h), with lasing thresholds as low as 29 W/cm², significantly lower than other plasmon and upconverting nanolasers. In addition, the upconverting nanolaser can achieve CW emission under both CW and pulsed pump conditions. Our time domain, semi-quantum modeling captured the characteristic population inversion and strong optical nonlinearities. Low-threshold upconverting nanolasers with NIR pump open possibilities for integration with compact, low-power circuits as well as in vivo applications including deep-tissue imaging, sensing, theranostics and optogenetic manipulation.¹⁸⁸ Looking forward, the large variety of available output wavelengths in the Ln series, the ability to couple plasmonic nanocavities with densely-packed quantum emitters, and the general nanocavity architectures provide an almost unlimited number of robust low-power coherent nanoscale light sources. Our all-solid-state nanolaser platform offers prospects to realize quantum-optical technologies and commercial lab-on-a-chip photonic devices.

Chapter 6. Emerging Applications of Strongly Coupled Nanocavities

Abstract

Because of their large figures of merit, lattice plasmons in metal nanoparticle arrays are very promising for chemical and biomolecular sensing, in both liquid and gas media. Due to its intrinsic surface-sensitivity and a power-law dependence on electric fields, second harmonic generation (SHG) spectroscopy can improve upon both the surface and volume sensitivities of lattice plasmons. In this chapter, we show that the SHG signal is greatly increased (up to 450 times) by the propagating lattice plasmons. We also demonstrate very narrow resonances in lattice plasmon intensity (~ 5 nm FWHM). We illustrate how the SHG resonances are highly sensitive to lattice plasmons by varying the fundamental wavelength, angle of incidence, nanoparticle material and lattice constant of the arrays. Finally, we identify an SHG resonance (10 nm FWHM) that is electric-dipole forbidden and can be attributed to higher-order multipoles, as enhanced by the strong near fields of lattice plasmons. Our results open up new and very promising avenues for chemical and biomolecular sensing, based on SHG spectroscopy of lattice plasmons.

Quantum emitters in two dimensional materials are promising candidates for studies of light-matter interaction and next generation, integrated on-chip quantum nanophotonics. However, the realization of integrated nanophotonic systems requires coupling of emitters to optical cavities and resonators. In this chapter, we show hybrid systems in which quantum emitters in 2D hexagonal boron nitride (hBN) are deterministically coupled to high-quality plasmonic nanocavity arrays. The plasmonic NP arrays offer a high quality, low loss cavity in the same spectral range as the

quantum emitters in hBN. As a result, the coupled emitters exhibit enhanced emission rates and reduced fluorescence lifetimes, consistent with Purcell enhancement in the weak coupling regime. Our results provide the foundation for a versatile approach for achieving scalable, integrated hybrid systems based on low loss plasmonic NP arrays and 2D materials.

In addition, photonic designs with rational integration of gain and loss can enable non-Hermitian photonic eigenstates with various applications such as loss-induced transparency, unidirectional invisibility, and nonreciprocal transmission. However, a well-defined, coupled plasmonic nanoresonator system is missing that can access the exceptional point and achieve PT symmetry phase transitions. This chapter shows that stacked plasmonic NP arrays can serve as a pair of coupled resonators and achieve transition between PT-symmetric and PT-broken phases by partial integration with gain media. Mode splitting was observed from the coupled nanoresonators that are stacked vertically with sub-wavelength spacings, associated with distinct phase distributions between two modes. The coupled plasmon resonator arrays can offer prospects in protected unidirectional optical communication, integrated nanophotonics and topological photonics.

Related references

Tran, T.T.*; **Wang, D.***; Xu, Z-Q.*; Yang, A.; Toth, M.; Odom, T.W.; Aharonovich, I. "Deterministic Coupling of Quantum Emitters in 2D Materials to Plasmonic Nanocavity Arrays," *Nano Letters* **17**, 2634-2639 *equal contribution

Hooper, D. C.; Kuppe, C.; **Wang, D.**; Wang, W.; Guan, J.; Odom, T.W.; Valev, V.K. "Second harmonic spectroscopy of surface lattice resonances," *Nano Letters* **19**, 165-172

Wang, D.; Bourgeois, M.R.; Schatz, G.C.; Odom, T.W. "PT Symmetry in Stacked Plasmonic Nanoresonator Arrays" *In preparation*

6.1 Enhanced Second Harmonic Generation from Propagating Lattice Plasmons

6.1.1 Introduction

Recently, nonlinear plasmonics has attracted significant research interest since nonlinear optical effects scale as a power law of the incident light and plasmonic nanostructures strongly concentrate the incident light into optical near-field “hotspots”.^{189,190} As a consequence, within such hotspots, nonlinear plasmonic effects are tremendously enlarged, offering prospects for new and improved applications. Because nonlinear optical effects can be used for tuning laser light, significant research interest has been devoted to nanostructure-enhanced frequency conversion, with increasing efficiency. Various strategies have been employed for enhancing frequency conversion, such as using all-dielectric nanostructures for increased damage threshold,¹⁹¹ plasmonic-dielectric hybrids where a plasmonic resonance enhances frequency conversion of the dielectric,^{192,193} and plasmonic nanostructures.¹⁹⁴ Nonlinear optical effects also find applications in multiphoton microscopy, which is useful for biological sciences and material characterization.¹⁹⁵

Plasmonic NPs have been the subject of numerous investigations with second harmonic generation (SHG),^{196,197} third harmonic generation,¹⁹⁸ and two-photon luminescence microscopy. Due to the frequency conversion, the measured signal in all these techniques is background free. The improved frequency conversion offered by plasmons can enable imaging with lower laser power and reduced photodamage to specimens (organic or inorganic).¹⁹⁹ The absence of signal background is also a key factor for the strong sensitivity of nonlinear optical effects, such as SHG chiral optical effects,²⁰⁰ or magnetization-induced SHG^{201,202} compared to their linear optical counterparts.²⁰³ Though considerable attention has been devoted to the SHG enhancements from

localized surface plasmons (LSP) and metasurfaces,^{204,205} lattice plasmons^{5,206} have received much less consideration.

Lattice plasmon resonances are more promising for sensing applications than LSPs because of their significantly narrower resonance linewidth (< 5 nm).^{207,208} Since the resonance wavelength depends on the refractive index of the environment,²⁰⁹ surface plasmons can be used for chemical and biological sensing, in both liquid and gaseous media. Whereas for LSPs the figure of merit (FOM) is typically on the order of a few units, for lattice plasmons it is much larger, (by one²¹⁰ and even two²⁰⁷ orders of magnitude) and the narrower resonance linewidth is attributed to the diffractive coupling between plasmonic NPs.⁴ Lattice plasmons occur on plasmonic NPs, arranged periodically, with a lattice constant of the order of the wavelength of incident light. Lattice plasmons result from the coupling of the broad LSPR with the narrow frequency of the Rayleigh anomaly, and hence exhibit a dual sensitivity – surface (on the NPs) and bulk (between the NPs).²¹¹

Here, we demonstrate SHG spectroscopy of lattice plasmons, where the SHG signal is enhanced up to 450 times by lattice plasmons, much above the previous reports of 10 and 30 times increase.^{212,213} The measured SHG resonances can be as sharp as 5 nm in FWHM, which is promising for sensing. Indeed, we show that the SHG signal is very sensitive to the factors determining lattice plasmons. We successfully tuned the SHG by varying the fundamental wavelength, the angle of incidence, the lattice parameter and the NP material. Importantly, we discover SHG spectroscopy resonances (10 nm FWHM) that are not associated with electric dipoles. We attribute these resonances to higher-order contributions, enhanced by the lattice plasmons. For individual NPs with diameter > 100 nm, retardation effects lead to higher-order terms (quadrupoles,¹¹⁵ octupoles, etc.²¹⁴⁻²¹⁶), at the second harmonic frequency. Whereas in

previous decades, such higher-order contributions did not play a major role in material properties, recent progress in nanofabrication has pushed them to the forefront of nonlinear plasmonics.²¹⁷

6.1.2 Determined SHG enhancement from lattice plasmons

We study four samples, where gold and silver plasmonic NPs are arranged into two square lattices each, with periodicities: 580 nm and 600 nm. The sample geometry is shown in **Figure 6.1a**. The NP arrays are fabricated using PEEL (a combination of photolithography, e-beam deposition, etching and lift-off). A scanning electron micrograph (SEM) of the 600 nm period array is shown in **Figure 6.1b**. An advantage of this fabrication technique is the ability to create large-area (cm²) uniform arrays, as demonstrated in **Figure 6.1c**, where the NP array appears green, due to its diffractive properties. The linear transmission spectra as a function of the angle of incidence for the 600 nm period gold array are shown in **Figure 6.1d**, revealing the location of the lattice plasmon band edges. The Rayleigh anomaly dispersion, denoted by the green lines in **Figure 6.1d**, is calculated using,²⁰⁹

$$\lambda_{(i,0)} = a_0 \left(\frac{n}{|i|} - \frac{\sin(\theta)}{i} \right), \quad (6.1)$$

where a_0 is the lattice periodicity, n is the refractive index of the surrounding environment, θ is the angle of incident, and i is an integer denoting the diffraction order. At the wavelength of the Rayleigh anomaly, the diffracted wave travels across the sample surface interacting with multiple NPs. When the wavelength undergoing a Rayleigh anomaly interferes with the broad LSPR of individual NPs, a Fano-type lattice plasmon resonance occurs (**Figure 6.2a**).

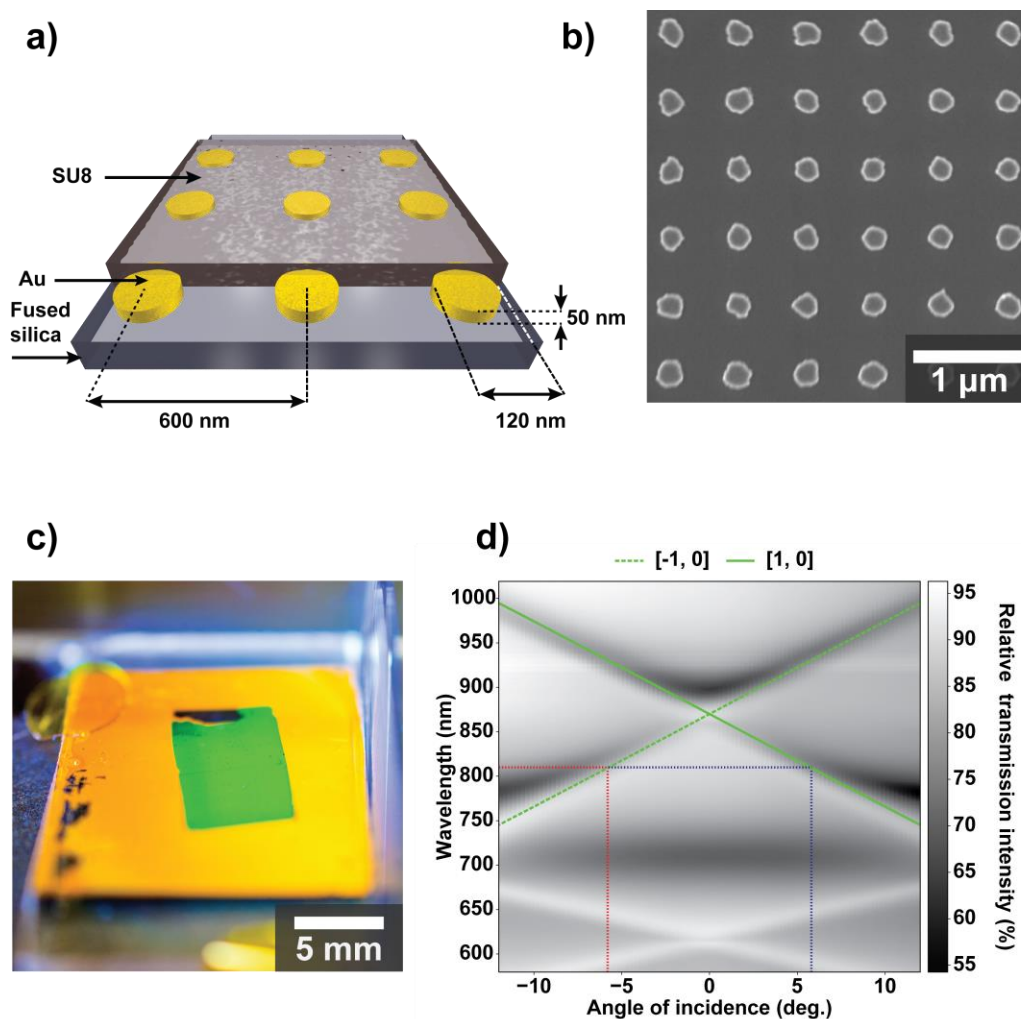


Figure 6.1. Our large-area gold nanoparticle arrays exhibit clear surface lattice resonances. (a) Sample schematic and dimensions showing gold nanoparticles on a fused silica substrate and capped with photoresist (SU8). (b) Scanning electron micrograph of the fabricated nanoparticle array before capping with SU8. (c) Photograph of an investigated sample, the large-area nanostructured array appears green. (d) Experimental mapping of transmission spectra versus changing angle of incidence, upon illumination with vertically polarized light (S_{IN}). The green lines show theoretical calculations of the diffraction beams that couple into surface lattice resonances. The red and blue dashed lines indicate the angles of incidence for enhancing the 810 nm fundamental light.

Figure 6.2a shows a numerically calculated transmission spectrum (performed using Lumerical) of the 600 nm period gold NP array, for normal incident light. The dip in transmission at 675 nm is attributable to the LSPR. The Rayleigh anomaly is at 870 nm and the lattice plasmon is at 872 nm. To illustrate the specific electromagnetic behavior of the lattice plasmon, we plot the results of numerical simulations at two different wavelengths—at the lattice plasmon and away from it. Specifically, these are electric field simulations, at the surface of a single NP, with periodic boundary conditions. In **Figure 6.2b**, at 780 nm, i.e. away from the lattice plasmon, the electric

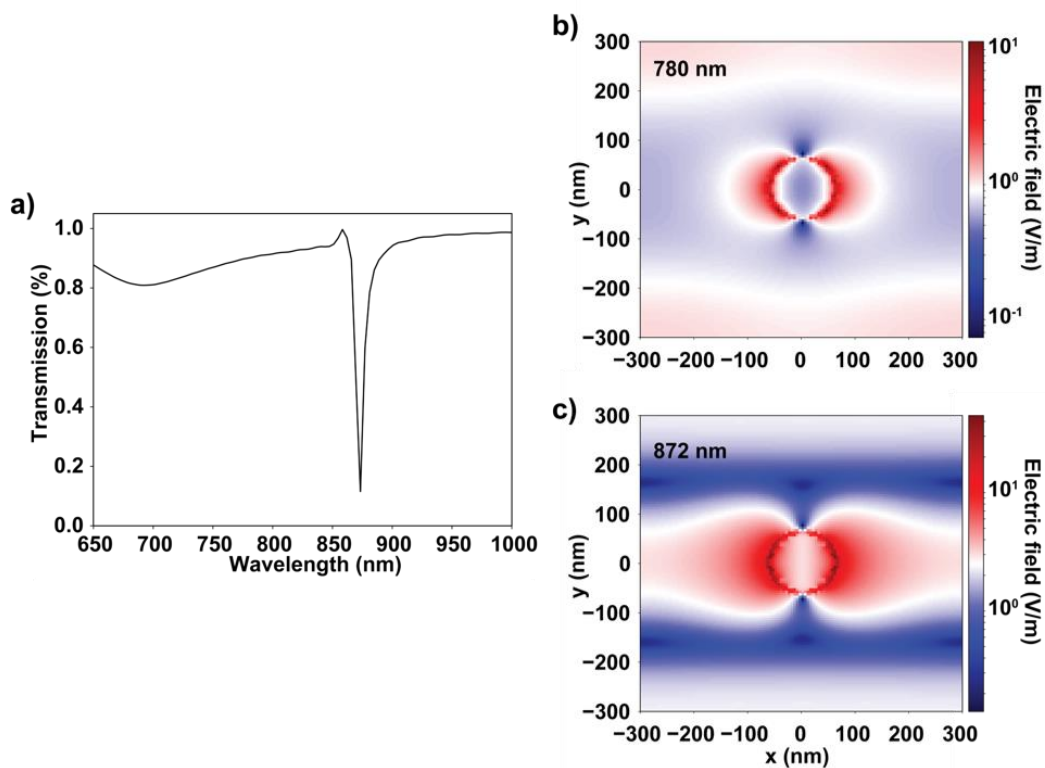


Figure 6.2. Numerical simulations illustrating the near-field enhancement at lattice plasmons. (a) For the 600 nm period gold array, the transmission at normal incidence clearly displays a lattice plasmon resonance at 872 nm. (b) The electric near-field at the surface of the nanoparticle, away from resonance at 780 nm. (c) The electric near-field at the surface of the nanoparticle, at 872 nm, the wavelength of lattice plasmon.

field is concentrated around the NP. By contrast, in **Figure 6.2c**, at 872 nm, i.e. at the wavelength of lattice plasmon, the electric field radiated by the NP extends to neighboring NPs. This is evidenced by the electromagnetic radiation from the dipole reaching beyond a single unit cell. The enhancement of the electric near-field at the lattice plasmon leads to an increased SHG signal.

Second harmonic generation is caused by a part of the material polarization that occurs and radiates at 2ω , i.e. twice the fundamental driving frequency ω . The total effective second-order nonlinear polarization can be expressed as,

$$P(2\omega) = P^D(2\omega) + P^Q(2\omega) \quad (6.2)$$

where $P^D(2\omega)$ is the dipole contribution to the second harmonic polarization, and $P^Q(2\omega)$ represents the contribution from quadrupoles. These two terms can then be written in full as,

$$P_i^D(2\omega) = \chi_{ijk}^{(2,D)} E_j(\omega) E_k(\omega) \quad (6.3)$$

$$P_i^Q(2\omega) = \chi_{ijkl}^{(2,Q)} E_j(\omega) \nabla_k E_l(\omega)$$

where summation over repeated indices is implied. The indices i, j , and k , take the Cartesian directions and $E(\omega)$ is the electric field of the incident light. Here, $\chi_{ijk}^{(2,D)}$ is a rank three tensor denoting the electric dipole susceptibility at the second harmonic, the first index designates the direction of the polarization and the final two indices are the directions of the input fields. The quadrupolar contribution is represented by the rank four tensor $\chi_{ijkl}^{(2,Q)}$. The expression for $P^Q(2\omega)$ in Equation 6.3 is obtained by a Taylor expansion and represents the quadrupolar contribution to the second order polarization. Electric dipole contributions to SHG are forbidden in systems with inversion symmetry. Our arrays of gold NPs possess C_{4v} symmetry and the corresponding $\chi_{ijk}^{(2,D)}$ tensor is

$$\chi_{ijk}^{(2,D)} = \begin{pmatrix} 0 & 0 & 0 & 0 & \chi_{xxz} & 0 \\ 0 & 0 & 0 & \chi_{xxz} & 0 & 0 \\ \chi_{zyy} & \chi_{zyy} & \chi_{zzz} & 0 & 0 & 0 \end{pmatrix} \quad (6.4)$$

This C_{4v} tensor is mathematically identical to the rotationally isotropic surface tensor. Equation 6.3 shows that the dipolar contribution to SHG scales as a power law of the electric field of incident light and that the quadrupolar contribution is proportional to gradients of that electric field. Notably, at lattice plasmons, the bulk and surface sensitivities are characterized by a long-range radiative dipole coupling (which scales as e^{ikr}/r) and by a short-range electric near-field (which scales as $1/r^3$ and is characterized by strong electric field gradients), respectively. In other terms, on the one hand, lattice plasmons are surface-sensitive: a spectral shift is induced in response to the refractive index change in the local environment. On the other hand, they are bulk-sensitive: the electromagnetic field is not confined to the plane of the array, it extends over a volume, tens of hundreds of nm across.²¹⁸ Consequently, combining lattice plasmons and SHG presents obvious advantages and SHG spectroscopy of lattice plasmons is currently of increasing interest.²¹⁹

Our experiments demonstrate two types of SHG enhancement mechanism: one dominated by dipolar contribution (sensitive to the amplitude of lattice plasmon enhanced near-fields) and one dominated by higher-order contributions (additionally sensitive to the gradients of enhanced near-fields). The SHG experimental set up is shown in **Figure 6.3a**. A tunable femtosecond pulsed laser provides the incident fundamental wavelength, the sample is mounted on an automated rotation stage to change the angle of optical incidence, and an analyzing polarizer is used to decompose the SHG signal into its vertically (S) and horizontally (P) polarized components.

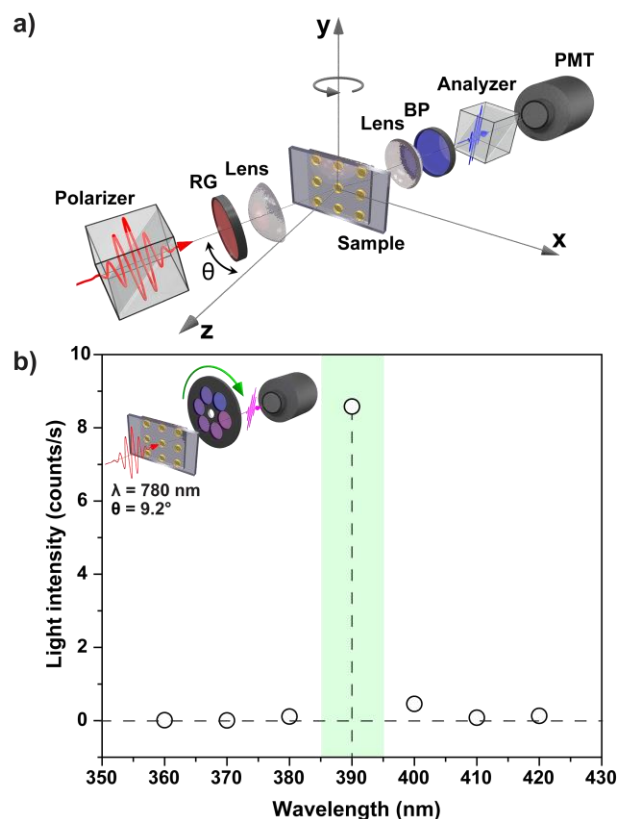


Figure 6.3. The second harmonic generation signal clearly stands out from the multiphoton background. (a) Experimental configuration for the SHG measurements, where θ is the angle of incidence, RG is an RG665 Schott glass filter, BP is bandpass filter and, PMT is a photomultiplier tube. (b) For illumination with 780 nm fundamental light, the multiphoton emission is plotted versus wavelength. A 10 nm FWHM bandpass filter was used for each detection wavelength, as indicated by the inset. The dashed vertical line shows the SHG signal.

First, it is important to establish that the measurements clearly correspond to SHG; for instance, three-photon luminescence could spectrally overlap with the detected SHG signal. To characterize the respective contributions from multiphoton luminescence and SHG, a series of bandpass filters are used (see **Figure 6.3b** inset). The filters are centered at 10 nm intervals, with 10 nm FWHM. In this experiment, the fundamental wavelength and the angle of incidence are kept constant at 780

nm and 9.2° , respectively. These values are close to the lattice plasmon resonance wavelength in the 600 nm period sample. As Figure 6.3b illustrates, the strongest signal occurs at 390 nm, which is the SHG. For wavelengths 380 nm and below, as well as for wavelengths 400 nm and above, there is a negligible signal, establishing that there is no contribution from multiphoton luminescence. The results unambiguously demonstrate that the signals we measure correspond to pure SHG.

The SHG signal is greatly enhanced by the lattice plasmons. We begin with the 600 nm period array of gold NPs, illuminated at 810 nm. In **Figure 6.4a**, the SHG intensity is plotted as a function of the angle of incidence, for the S_{IN} - P_{OUT} polarizer-analyzer configuration (i.e. vertical-in horizontal-out). Two strong SHG enhancements are observed at around $\pm 6^\circ$ angle of incidence. The red and green dashed lines in Figure 6.1d correspond to the calculated Rayleigh anomalies at $\pm 5.7^\circ$, which are shown by the black dashed lines in Figure 6.4a. For angles of incidence in between the peaks, there is no enhancement of SHG and the signal is below 0.2 counts per second. From these data, the SHG enhancement in the lattice plasmon peaks is over 150 times, due to the strong electric near-fields around the NPs provided by the lattice plasmons. Notably, this enhancement is already much greater compared to the previous reports of 10 and 30 times,^{212,213} but it can be even greater.

Next, we examine how the lattice plasmon enhancement of SHG is affected by fundamental wavelength, angle of incidence, array periodicity and NP material (**Figures 6.4b-d**). Specifically, NP arrays with periodicities of 600 nm and 580 nm are investigated, and four fundamental wavelengths are used, throughout various angles of incidence. For each fundamental wavelength and each sample periodicity, there is a corresponding peak in SHG versus angle of incidence. The figures show that as the fundamental wavelength is decreased, the corresponding SHG

enhancement shifts to greater angles of incidence. The SHG peaks track the angle of incidence at which a corresponding lattice plasmon occurs. Between Figure 6.4b and Figure 6.4c, the peaks are shifted in angle of incidence. This offset is due to the change in array periodicity, which affects the position of the lattice plasmons. It should be noted that all our sample arrays are covered with SU8, and that the difference in their behavior is therefore not due to differences in their refractive index environment. Moreover, because the azimuthal angle orientation of the arrays affects the dispersion of the Rayleigh anomalies, all sample lattices were oriented identically.

Furthermore, we investigated silver NP arrays with identical periodicities to those of the gold nanoarrays: 600 nm and 580 nm. In the case of silver, an SHG enhancement of up to 450 times is observed for the 600 nm period array, as shown in Figure 6.4d. This enhancement occurs for a fundamental wavelength of 760 nm, at 11.2° angle of incidence. The strength of this SHG enhancement can be attributed to a strong lattice plasmon resonance. Indeed, the SHG scales as the 4th power of the electric near-fields, which are enhanced at the lattice plasmons. In **Figure 6.5**, the deep black color near the intersection of the blue lines clearly indicates very low transmission through the arrays, i.e. a strong lattice plasmon resonance.

At maximum enhancement, an SHG conversion efficiency of $\eta_{SHG} = 1.5 \times 10^{-9}$ is obtained, where $\eta_{SHG} = P(2\omega)/P(\omega)$. Here, SHG enhanced by lattice plasmons results in conversion efficiencies comparable to previous studies on plasmonic nanostructures.²²⁰ Structures explicitly designed for efficient SHG can achieve much higher conversion efficiencies.²²¹ However, for sensing applications, the conversion efficiency is not the most crucial factor, but rather the relative contrast in SHG. Therefore, lattice plasmons provide an appealing platform for sensing given the dramatic variation in SHG demonstrated in this work.

In both Figure 6.3 and Figure 6.4, the SHG signal is electric-dipole allowed. The experimental geometries (polarizer-analyzer combinations and angles of optical incidence) address the non-zero tensor elements in Equation 6.4. In order to evidence the higher-order contributions to SHG, we must select an experimental geometry that is electric-dipole forbidden, i.e. one which addresses a zero-tensor component in Equation 6.4.

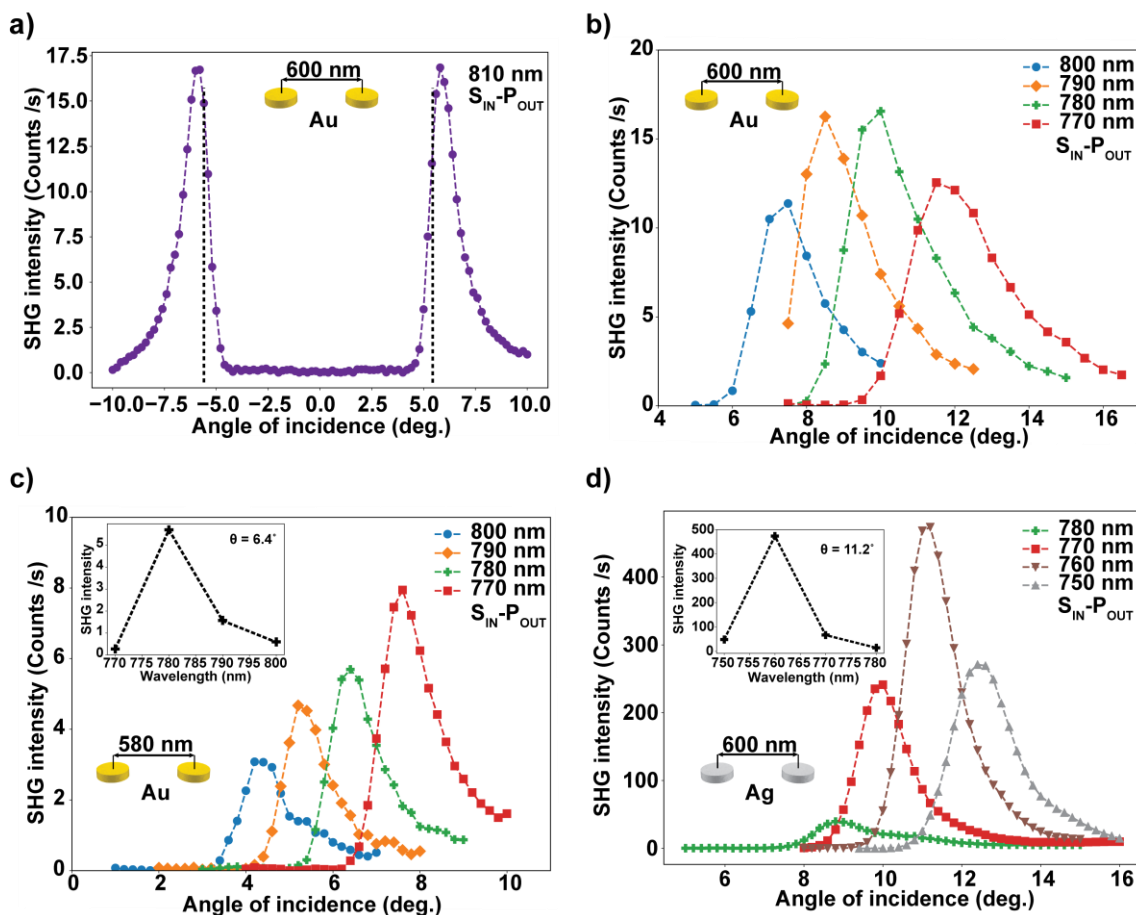


Figure 6.4. Due to the strong near-fields at lattice plasmons, SHG enhancements (up to 450 times) occur by tuning fundamental wavelength, angle of incidence and lattice constant of the arrays. **(a)** SHG enhancement from a lattice plasmon resonance occurs near the Rayleigh anomaly corresponding to the fundamental wavelength of 810 nm for the 600 nm period array. Enhancement occurs symmetrically for positive and negative angles of incidence. The 810 nm wavelength corresponds to the red and blue lines in Figure 6.1d. **(b-c)** Enhanced SHG at different fundamental wavelengths for the 600 nm and 580 nm period gold nanoparticle arrays, respectively. **(d)** Enhanced SHG at different fundamental wavelengths for the 600 nm period silver nanoparticle array. The strong enhancements follow the angles of incidence that correspond to a Rayleigh anomaly induced lattice plasmon resonance at the fundamental wavelength. The insets in (c) and (d) show the SHG intensity for different fundamental wavelengths at a single angle of incidence.

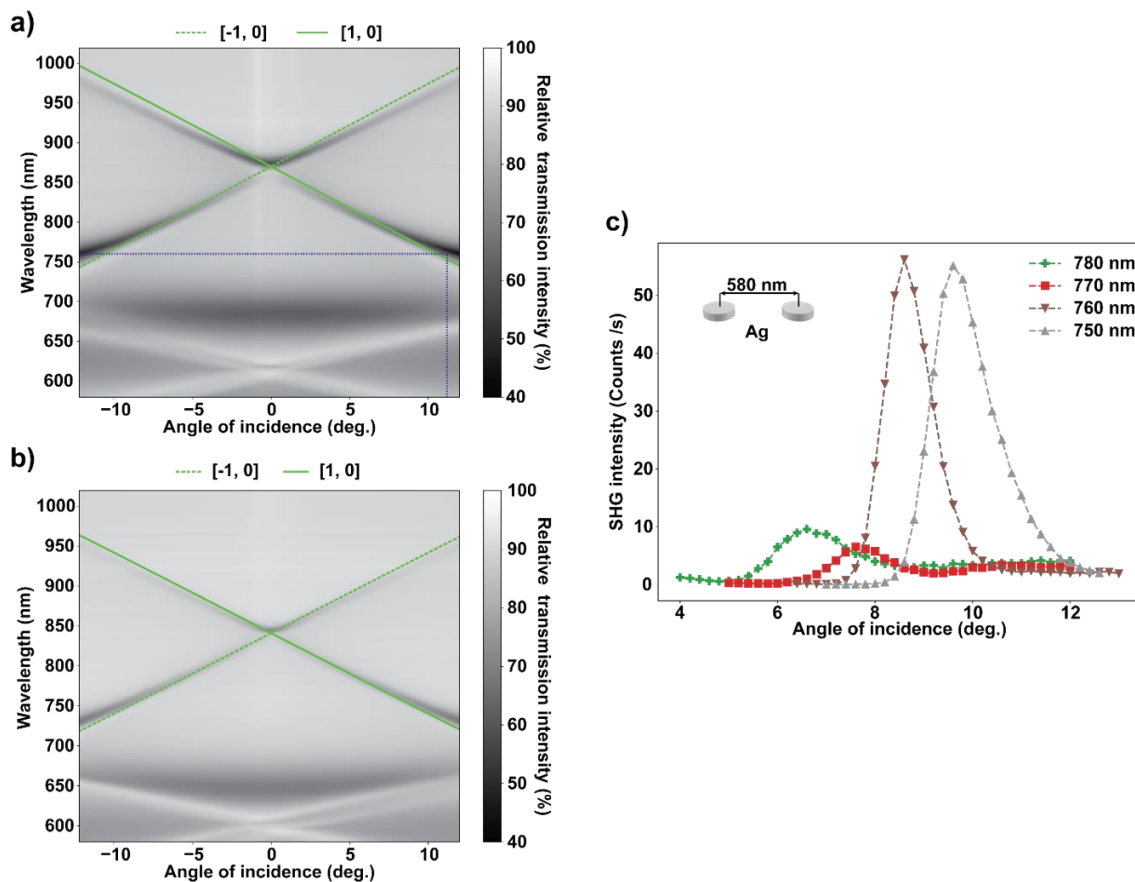


Figure 6.5. Measurements of silver nanoparticle arrays. (a-b) Transmission spectra versus angle of incidence, upon illumination with vertically polarized light (S_{IN}), for the 600 nm and 580 nm period arrays, respectively. The green lines show the calculated Rayleigh anomalies. The blue dashed lines in (a) indicate the angle of incidence and the corresponding fundamental wavelength (760 nm) for the measured lattice plasmons. (c) The SHG intensity, as a function of the angle of incidence, at different fundamental wavelengths for the 580 nm period silver nanoparticle array.

6.1.3 Enhanced SHG quadrupolar contributions from gold NP arrays

In the dipole approximation the material polarization at the second harmonic is:

$$P_i^D(2\omega) = \chi_{ijk}^{(2,D)} E_j(\omega) E_k(\omega), \quad (6.5)$$

where summation over repeated indices is implied, and the indices i, j, k can take any of the Cartesian components x, y, z . The term $\chi_{ijk}^{(2,D)}$ is a rank 3 tensor containing 27 complex components and represents the second-order nonlinear dipole susceptibility. For second harmonic generation with only a single laser beam, the input fields $E_j(\omega)$ and $E_k(\omega)$ are indistinguishable. This indistinguishability allows the indices of the input fields to be freely interchanged, causing the 27 independent components of $\chi_{ijk}^{(2,D)}$ to be reduced to 18 independent components. The symmetry of the sample can be applied to $\chi_{ijk}^{(2,D)}$ in order to further reduce the number of independent tensor components. For a 4-fold symmetric or isotropic surface, the material polarization at the second harmonic, in the dipole approximation can be written in full as:

$$\begin{pmatrix} P_x(2\omega) \\ P_y(2\omega) \\ P_z(2\omega) \end{pmatrix} = \begin{pmatrix} 0 & 0 & 0 & 0 & \chi_{XXZ} & 0 \\ 0 & 0 & 0 & \chi_{YYZ} & 0 & 0 \\ \chi_{ZXX} & \chi_{ZYY} & \chi_{ZZZ} & 0 & 0 & 0 \end{pmatrix} \begin{pmatrix} E_x^2(\omega) \\ E_y^2(\omega) \\ E_z^2(\omega) \\ 2E_y(\omega)E_z(\omega) \\ 2E_x(\omega)E_z(\omega) \\ 2E_x(\omega)E_y(\omega) \end{pmatrix}. \quad (6.6)$$

In equation 6.6, there only 3 independent tensor components: $\chi_{ZXX} = \chi_{ZYY}$, $\chi_{YYZ} = \chi_{XXZ}$, and χ_{ZZZ} .

Using the S_{IN} – S_{OUT} polarizer-analyzer combination, the input fields are polarized vertically along the y-direction and only the vertically (along y) polarized SHG signal is detected. This is equivalent

to directly measuring SHG from the χ_{YYY} tensor component. As can be seen above, the component $\chi_{YYY} = 0$ for the symmetry of the samples investigated. Therefore, dipolar contributions to SHG are forbidden under the $S_{IN} - S_{OUT}$ polarizer-analyzer combination. Consequently, because an SHG signal is observed, it can be attributed to higher order contributions.

For instance, the quadrupolar contribution to induced polarization $\mathbf{P}(2\omega)$ is determined by:

$$P_i^Q(2\omega) = \chi_{ijkl}^{(2,Q)} E_j(\omega) \nabla_k E_l(\omega), \quad (0.1) \quad (6.7)$$

where $\chi_{ijkl}^{(2,Q)}$ is a tensor of rank 4 with 81 components, representing the second-order nonlinear susceptibility associated with quadrupolar contributions to SHG. For a cubic or isotropic bulk (inside the NPs) symmetry, such as for amorphous gold or silver, the non-zero tensor elements are:

$$\begin{aligned} \chi_{XXXX} &= \chi_{YYYY} = \chi_{ZZZZ} \\ \chi_{XXYY} &= \chi_{YYXX} = \chi_{YYZZ} = \chi_{ZZYY} = \chi_{ZZXX} = \chi_{XXZZ} \\ \chi_{XXYY} &= \chi_{YYXX} = \chi_{YYZZ} = \chi_{ZZYY} = \chi_{ZZXX} = \chi_{XXZZ} \\ \chi_{XXYY} &= \chi_{YYXX} = \chi_{YYZZ} = \chi_{ZZYY} = \chi_{ZZXX} = \chi_{XXZZ} \end{aligned} \quad (6.8)$$

Upon substituting into equation 1.3 and subsequently expanding all terms, bearing in mind the vector identity $\nabla(A \cdot B) = (A \cdot \nabla)B + (B \cdot \nabla)A + A \times (\nabla \times B) + B \times (\nabla \times A)$ in order to expand $\nabla(E \cdot E)$, we arrive at:

$$\begin{aligned} \mathbf{P}(2\omega) &= (\chi_{XXXX} - \chi_{XXYY} - \chi_{XXYY} - \chi_{XXYY}) \sum_i \hat{e}_i E_i \nabla_i E_i \\ &\quad + \frac{\chi_{XXYY}}{2} \nabla(\mathbf{E} \cdot \mathbf{E}) + \chi_{XXYY} (\mathbf{E} \cdot \nabla) \mathbf{E} + \chi_{XXYY} \mathbf{E}(\nabla \cdot \mathbf{E}). \end{aligned} \quad (6.9)$$

This equation is often reproduced in the following form:

$$\begin{aligned} \mathbf{P}(2\omega) &= (\delta - \beta - 2\gamma)(\mathbf{E}(\omega) \cdot \nabla) \mathbf{E}(\omega) + \beta \mathbf{E}(\omega)(\nabla \cdot \mathbf{E}(\omega)) \\ &\quad + \gamma \nabla(\mathbf{E}(\omega) \cdot \mathbf{E}(\omega)) + \zeta \sum_i \hat{e}_i \mathbf{E}_i(\omega) \nabla_i \mathbf{E}_i(\omega). \end{aligned} \quad (6.10)$$

In this equation, the sum is over the Cartesian directions of the medium, \hat{e}_i are the corresponding unit vectors and δ , β , γ and ζ are phenomenological constants related to the symmetry of the sample. If we consider a single plane wave excitation, the first term is zero since we can write $(\mathbf{E} \cdot \nabla): -i(\mathbf{E} \cdot \mathbf{k})$, which is zero for a transverse electromagnetic wave, with \mathbf{k} being the wavevector of the source polarization. The second term cancels due to Maxwell's equations – the net electric charge inside a conducting metal is zero. The third term only gives rise to P-polarized SH light and it is isotropic. Since we measure S-polarized SHG, the only possible contribution is from the last term, which is allowed in all polarization combinations. It should be pointed out that this last term is known as the bulk anisotropic contribution and it originates from the fact that the material has finite dimensions, as opposed to an infinite centrosymmetric bulk. Consequently, our signal is attributable to this last term. Our SHG measures the sum of gradients along each of the 3 Cartesian directions, each multiplied by a combination of the four independent quadrupolar tensor components, i.e. $\zeta = \chi_{xxxx} - \chi_{yyx} - \chi_{xyy} - \chi_{xyx}$.

In **Figure 6.6**, we demonstrate the enhancement of the higher-order contributions to SHG by lattice plasmons. Here, the experimental geometry of interest is the S_{IN}-S_{OUT} (vertical-vertical) polarizer-analyzer configuration, at normal incidence. Under these conditions, within the electric dipole tensor, only the χ_{yyy} tensor component is addressed. As we can see in Equation 6.8, this component is zero, for our samples, i.e. SHG is from electric dipoles is forbidden. **Figure 6.6a** shows the SHG signal versus the angle of incidence, for a fundamental wavelength of 870 nm incident on the 600 nm period gold NP array. For the S_{IN}-S_{OUT} (vertical-vertical) polarizer-analyzer configuration, a distinct SHG peak can be seen (orange diamonds), centered at normal incidence,

i.e. precisely in the electric-dipole forbidden configuration. This enhancement at 870 nm is attributable to the lattice plasmons near normal incidence, as demonstrated by both theory and experiment. Numerically, we calculate the lattice plasmon position at 872 nm, see Figure 6.2c. Experimentally, in the $S_{\text{IN}}\text{-}P_{\text{OUT}}$ (vertical-horizontal) polarizer-analyzer configuration, which is electric-dipole allowed, we observe two peaks (blue dots) that are similar to the data in Figure 6.4a and are only 2° apart in angle of incidence.

Additionally, **Figure 6.6b** unambiguously demonstrates that the SHG enhancement in the electric-dipole forbidden configuration is due to the normal incidence lattice plasmons. The data were recorded for both gold NP samples, in the $S_{\text{IN}}\text{-}S_{\text{OUT}}$ (vertical-vertical) polarizer-analyzer configuration and at normal incidence. For each sample, the SHG spectra peak (10 nm FWHM) is at the wavelengths of lattice plasmons, which is red-shifted with respect to the wavelength of Rayleigh anomaly.

Physically, there is a direct link between lattice plasmons and the higher-order contributions to SHG. First, to avoid confusion, we point out that we do not discuss plasmonic quadrupolar modes in the NP. As can be seen from equation 6.7, the quadrupolar contribution to the second harmonic polarization is proportional to the gradients of the local electric field. At the lattice plasmons, such gradients of the local electric fields are very strongly pronounced, see Figure 6.2c. It should be pointed out that quadrupolar SHG can originate from the surface of the NPs.²²²

Our analysis of the SHG results in **Figure 6.5** is based on the assumption that we address the zero-tensor component in Equation 6.8, which implies 4-fold (or isotropic) symmetry. However, small shape imperfections of the nanostructures can break the isotropy leading to the appearance of electric-dipole allowed SHG at normal incidence.²²³ Moreover, lattice defects could also lead to electric-dipole allowed SHG. These hypothetical electric dipole contributions would usually be

very small but, in our experiments, they could be enhanced by the lattice plasmons and become measurable. However, as can be seen in **Figure 6.5a**, the SHG signal for $S_{IN-S_{OUT}}$ peaks at normal incidence and not at the angles corresponding to the SRLs, where electric dipole SHG attributable

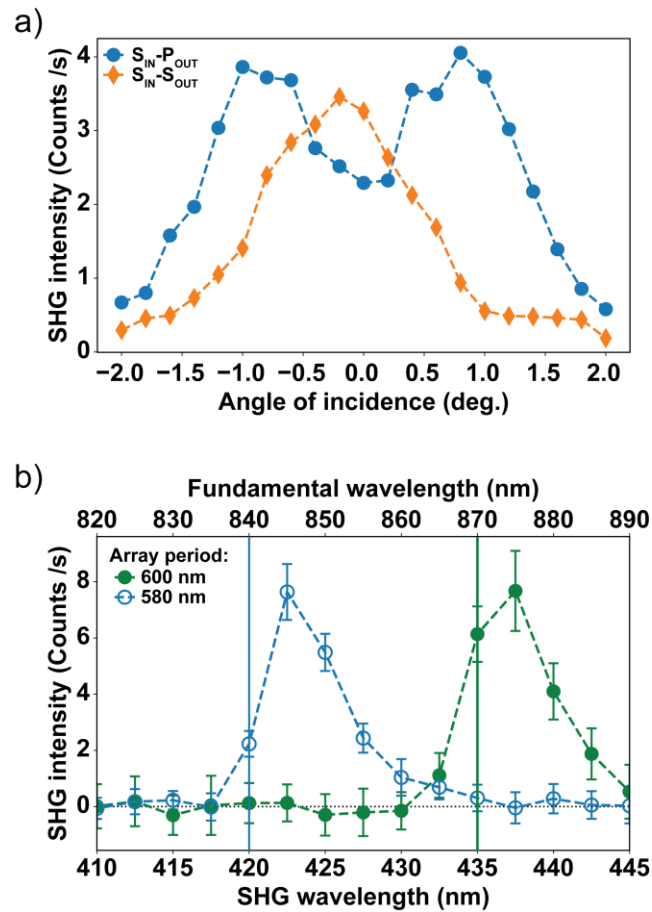


Figure 6.6. Lattice plasmon resonance causes an enhancement of the SHG quadrupolar contributions for the gold arrays. (a) For $S_{IN-P_{OUT}}$ (dots) the SHG signal is attributable to electric dipolar contributions. The fundamental light is at 870 nm (at the Rayleigh anomaly) and the peaks correspond to the lattice plasmons. For $S_{IN-S_{OUT}}$ (diamonds), the signal peaks at normal incidence, where the higher-order contributions to SHG appear. (b) Measuring SHG spectra, for $S_{IN-S_{OUT}}$ and at normal incidence, these higher-order contributions to SHG peak at the normal incidence lattice plasmon wavelength, for both the 600 nm and 580 nm period arrays. The blue and green solid lines indicate the Rayleigh anomalies for the 580 and 600 nm

to surface lattice resonantly-enhanced imperfections should have appeared ($\pm 1^\circ$). Therefore, the $S_{\text{IN}}-S_{\text{OUT}}$ signal cannot be attributed to a lattice plasmon enhanced electric dipolar contribution to SHG.

In conclusion, we demonstrate SHG spectroscopy from lattice plasmons, where the signal can be enhanced up to 450 times. We present both electric-dipole allowed (in Figure 6.4) and electric-dipole forbidden (in Figure 6.5) SHG resonances. We observe SHG resonances as narrow as 5 nm FWHM, which indicates that a high FOM can be achieved, opening new avenues for chemical and biosensing applications. Moreover, the SHG technique is intrinsically surface-sensitive, which can lead to improved near-field surface sensing, especially using higher-order resonances that originate from gradients in plasmonic near-fields, see equation 6.7. Equation 6.7 also demonstrates how SHG can improve upon the bulk sensitivity of lattice plasmons. This bulk sensitivity originates from far-field coupling between NPs and, for electric-dipole allowed SHG resonances, the sensitivity would additionally benefit from a power law dependence on the far-fields. It should also be pointed out that the SHG process occurs via virtual energy levels at ultrafast timescales. This process could therefore enable ultrafast probes of the refractive index and could be useful for monitoring chemical reactions, e.g. catalysis by the NPs. To explore the limits of these applications, future work can focus on the importance of the environment surrounding the NP arrays.

6.2 Deterministic Coupling of Quantum Emitters to Plasmonic Nanocavity Arrays

6.2.1 Introduction

Hybrid plasmonic – photonic systems are attracting increasing attention in studies of light-matter interaction at the nanoscale, coherent and incoherent light amplification, and as media for achieving enhanced emission and absorption rates.⁹⁴⁻⁹⁸ Quantum emitters in two-dimensional materials are promising candidates for studies of light-matter interaction and next generation, integrated on-chip quantum nanophotonics. To this extent, coupling of single photon emitters (SPEs), which are vital components of future quantum technologies,⁹⁹ to plasmonic cavities was demonstrated for 3D crystals including color centers in diamond,^{100,101} 1D carbon nanotubes (CNTs)¹⁰² and 0D quantum dots.¹⁰³⁻¹⁰⁵ Recently, isolated defects in two dimensional (2D) hexagonal boron nitride (hBN)¹⁰⁶⁻¹⁰⁹ have emerged as a new class of room temperature SPEs. These emitters are embedded in 2D flakes of layered hBN and therefore offer an excellent platform for integration with photonic elements, making them promising constituents of next-generation nanophotonics and optoelectronic devices.

One specific plasmonic resonator is a periodic metal NP array in a homogeneous dielectric environment.^{12,52} This platform supports narrow lattice plasmon resonances at the band-edge with suppressed radiative loss and strong sub-wavelength localized field enhancement around the NPs (< 50 nm). The plasmonic cavity modes can strongly enhance the emission rates of emitters in the hot spot regions, and the resonance wavelengths can be tailored by changing the NP periodicity and the dielectric environment.⁵² Additionally, compared to the limited pattern area in other plasmonic cavity designs fabricated by e-beam lithography (< 100 μm), these periodic metal NP arrays can be readily fabricated in cm^2 scale with a large-scale fabrication process based on soft

interference lithography (SIL).⁶ Thus, large-scale plasmonic NP arrays provide a flexible platform for coupling to SPEs without a need for precise control over the emitter location. Such lattices have been used to demonstrate strong light-matter coupling, directional emission and lasing actions.^{12,102,224} Integration of plasmonic NP arrays with deterministically selected quantum emitters in 2D materials will constitute a new platform for integrated on-chip flat optics.

In this work, we report for the first time a hybrid quantum system in which quantum emitters in 2D hexagonal boron nitride (hBN) are deterministically coupled to high-quality plasmonic nanocavity arrays. The plasmonic NP arrays offer a high quality, low loss cavity in the same spectral range as the quantum emitters in hBN. Specifically, we deterministically couple individual emitters of choice in 2D hBN hosts to gold or silver NP arrays (**Figure 6.7a**). We demonstrate an enhancement in the spontaneous emission rate, along with an enhanced count rate and reduced fluorescence lifetimes, consistent with Purcell enhancement in the weak coupling regime. Our results provide the foundation for a versatile approach for achieving scalable, integrated hybrid systems based on low loss plasmonic NP arrays and 2D materials.

6.2.2 Enhanced Single-photon Emission by Plasmonic Nanocavities

Figure 6.7b shows a scanning electron microscopy image of a pristine hBN flake on plasmonic arrays. The flakes were exfoliated using scotch tape from highly crystalline bulk hBN. To match the emission peaks (~ 560 nm – 700 nm), we select silver or gold NP arrays with a NP spacing of 400 nm. The corresponding optical image is shown in **Figure 6.7c**. Based on FDTD modeling (**Figure 6.7d**), the near-field electric field at lattice plasmon resonance is enhanced with respect to incident light in plasmonic hot spots. The electric field distribution along the vertical axis suggests that the field enhancement is still reasonably high for vertical distance of several tens of

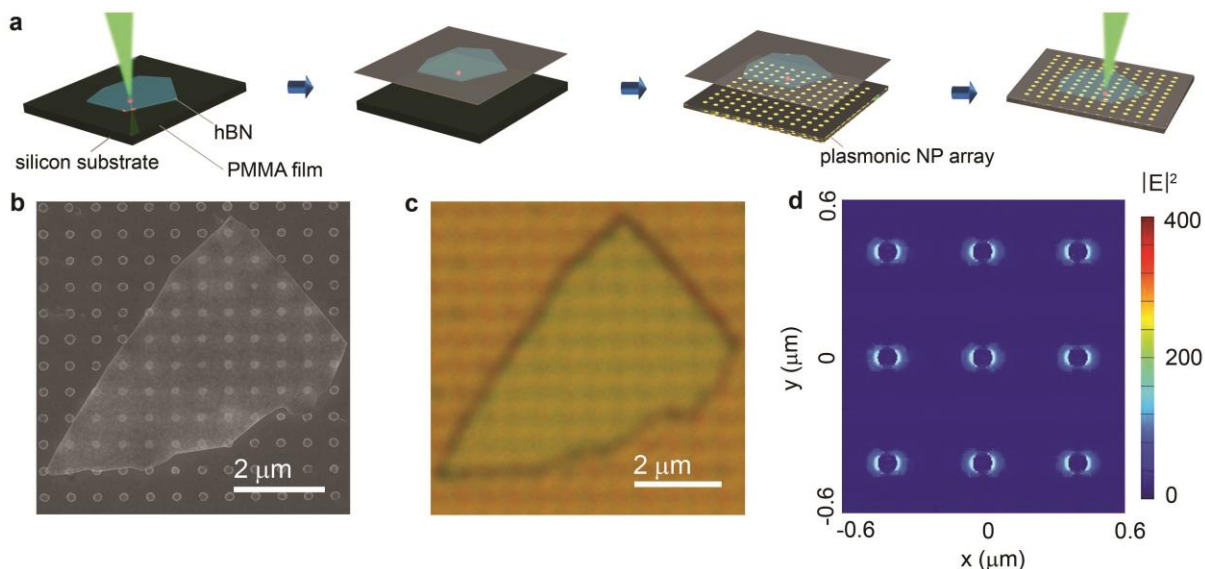


Figure 6.7. Hexagonal boron nitride flakes and their transfer process onto plasmonic lattice substrates. (a) Schematic illustration of the wet process used to transfer a selected hBN flake with an emitter of choice (exemplified by the red dot) from a thermal silicon oxide substrate onto a plasmonic NP array using PMMA as the carrier. (b) SEM image of the mechanically exfoliated hBN flake positioned atop of a silver plasmonic lattice on silica and, (c) optical image of the same flake on the plasmonic lattice. (d) FDTD simulation of the lateral (in-plane) electric field intensity distribution $|E|^2$ of a 400 nm-spaced silver NP lattices.

nanometers away from the edge of NPs. Such hot-spot regions are well-suited for the hBN flakes used in this study. Quantum emitters embedded in hBN flakes exhibit a broad distribution of zero-phonon lines (ZPL) in the range of $\sim 560\text{--}700$ nm, likely due to strain fields or inhomogeneity in the local dielectric environment.¹⁴ In order to match with this property of the emitters, we designed plasmonic arrays with lower Q factor than our previous work,¹⁸ and hence broader resonance width, covering most of the emission spectral range of the hBN emitters.

To transfer hBN flakes onto plasmonic NP arrays, we employed the wet transfer method depicted in Figure 6.7a.²²⁵ Briefly, an SPE at a frequency matching the plasmonic lattice array was

identified and pre-characterized. Overall, one out of ten emitters ($\sim 10\%$) will satisfy the criteria of being a single, bright and match the plasmonic resonance. A poly(methyl methacrylate) (PMMA) membrane was used to lift off the flakes and position them on top of a plasmonic lattice to achieve index-matching condition for high-quality lattice plasmon resonances. Basically, the substrates were gently floated on the surface of a 2M NaOH solution in a glass beaker. The beaker was then heated to 90°C for two hours to accelerate the silicon etching process. After that, the PMMA-coated hBN flakes were completely detached from the substrates and floating on the surface of the alkaline solution. The membranes were rinsed in deionized water, loaded onto plasmonic lattice substrates and dried at 40°C on a hot plate. The substrates were then baked at 120°C for 20 min to bring the emitters closer to the plasmonic surfaces and increase adhesion between the PMMA membrane and the substrate surface. Lithographically defined substrates enabled identification and characterization of the same emitter before and after the transfer process.

The optical properties of the emitters were recorded at room temperature using a home-built confocal microscope with a Hanbury Brown and Twiss interferometer. **Figure 6.8a** shows a confocal photoluminescence (PL) map of a pristine hBN flake with a selected single emitter, marked by a red circle. **Figure 6.8b** shows a transmission curve of the gold NP array (green) with the plasmonic resonance at 640 nm, a PL spectrum of the SPE circled in Figure 6.8a with a zero phonon line (ZPL) at ~ 600 nm and a phonon sideband at ~ 640 nm (red curve). While the exact crystallographic structure of the emitters is still under debate, it has been proposed to be associated with the antisite nitrogen vacancy defect ($\text{N}_\text{B}\text{V}_\text{N}$).¹⁰⁷ **Figure 6.8c** shows a second order correlation function, $g^2(\tau)$, from the emitter that dips to 0.02 at zero delay time (after background correction),²²⁶ thus confirming that the emitter is indeed a single photon source. The data are fit using a three-level model:

$$g^{(2)}(\tau) = 1 - (1 + a)e^{-\tau/t_1} + ae^{-\tau/t_2} \quad (6.11)$$

where t_1 and t_2 are lifetimes of the excited and metastable states, respectively, and a is a fitting parameter. We used the same model to fit all autocorrelation measurements in this work.

Once the selected emitter was pre-characterized, it was transferred onto the plasmonic lattice with a matching resonance at $\lambda = 641$ nm (green curve, Figure 6.8b). Inset of Figure 6.8a shows the SEM image of the same flake hosting the single emitter atop the gold array system. After being transferred atop the gold lattice, the emitter emission was enhanced by a factor of ~ 2.5 (blue curve, Figure 6.8b), while still maintaining its quantum nature, as evident from the $g^2(\tau)$ function (blue curve, Figure 6.8c). Because of better overlap of lattice plasmon resonance and the photon side band, we observed stronger enhancement (~ 3) than the peak at zero phonon line. To achieve a more quantitative analysis of the enhancement, a lifetime measurement of the emitter was recorded before and after the transfer using a pulsed laser. **Figure 6.8d** plots the lifetime results obtained using a picosecond pulsed laser. By using a double exponential fitting function, we obtained the values of $\tau_{1P} = 0.63$ ns, $\tau_{2P} = 3.4$ ns, and $\tau_{1C} = 0.42$ ns, $\tau_{2C} = 2.6$ ns for the pristine and coupled emitter, respectively. The PL intensity increase was in good agreement with the lifetime reduction for the emitter, confirming the coupling to the plasmonic array.

To further demonstrate the ability to couple quantum emitters from various host materials, we transferred solvent-exfoliated flakes onto a gold NP array with the center of resonance at 650 nm. The solution exfoliated flakes are only ~ 300 nm in lateral dimension and thus could represent as a much smaller host compared with that of tape-exfoliated flakes. Emitters from these small flakes have been shown to exhibit brighter and more stable emission compared to the tape exfoliated

ones.¹⁰⁷ Finally, the solvent exfoliated emitters also exhibit a larger ZPL distribution, therefore making it easier to find a matched emitter's wavelength to the plasmonic lattice resonance.

To match the SPE frequency with the plasmonic NP array, we chose an emitter emitting at 652 nm. The same unique features on the confocal maps taken for pristine and coupled emitters suggests that the same location of the emitter is addressed. **Figure 6.9a** shows a PL spectrum of the pristine SPE, and the same emitter coupled to the gold NP array. The emitter maintained its quantum nature, after being coupled to the plasmonic lattice, evident by the dips below 0.5 from the antibunching curves (**Figure 6.9b**). The reduction in the $g^{(2)}(0)$ value of the coupled emitter compared to the pristine emitter is due to background fluorescence from trace of PMMA residues after the transfer process. This effect is more obvious in the solvent hBN exfoliated rather than mechanically exfoliated flakes because of their smaller sizes compared to the laser spot size. From the time-resolved measurements, the lifetime of the emitter is reduced after being transferred onto the gold NP array - from 4 ns to 0.6 ns (**Figure 6.9c**). This reduction in lifetime implies that there is an increase in local density of optical states (LDOS) due to higher concentration of electric field surrounding the emitter. **Figure 6.9d** shows saturation measurements recorded from the pristine and the coupled flake, exhibiting saturation count rates of 0.37×10^6 and 0.89×10^6 counts/s, respectively, with an overall enhancement factor of 2.4. The data are fit to a three-level model, using $I = I_{\infty} \times P / (P + P_{sat})$ where I_{∞} and P_{sat} are the emission rate and excitation power at saturation, respectively. The higher brightness is thus in good agreement with the decrease in the lifetime of the emitter.

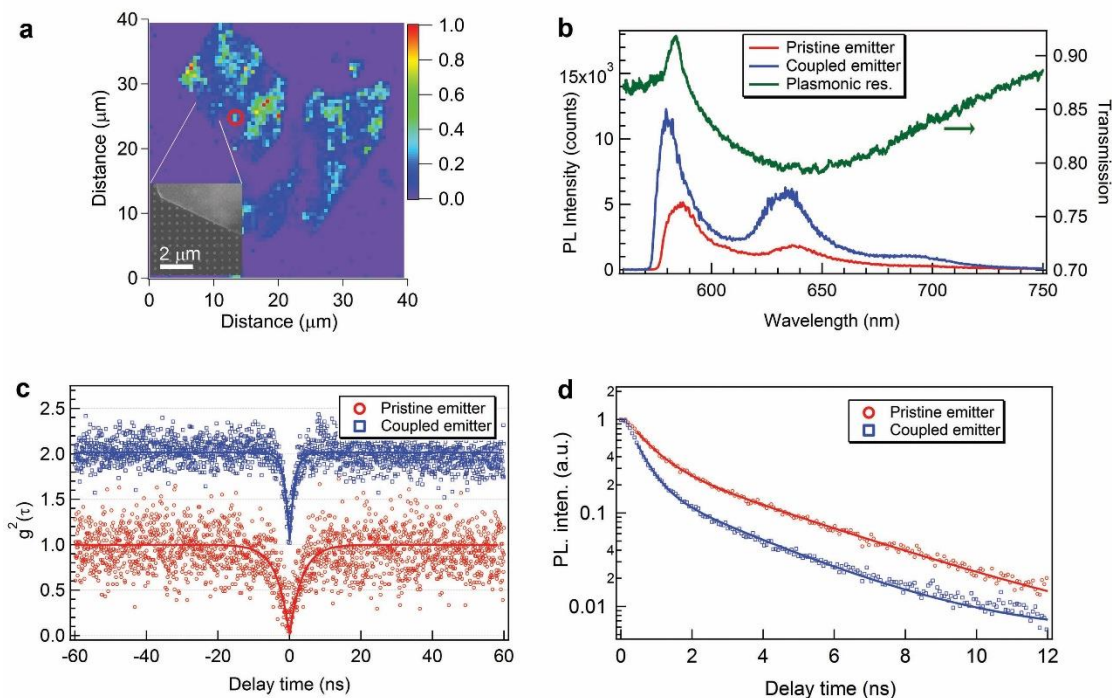


Figure 6.8. Coupling between a quantum emitter in a tape exfoliated hBN flake and a gold NP array on silica. (a) PL confocal map of a flake containing a single photon emitter (red circled). Inset, SEM image of part of the flake on top of the gold plasmonic lattice. (b) PL spectra of the pristine (red trace) and coupled (blue trace) single photon emitter, and a transmission spectrum of the plasmonic lattice (green trace) with the plasmonic resonance at 640 nm. (c) Second-order autocorrelation functions obtained from the pristine (red circles) and coupled (blue open squares) system. In both cases, the dip at zero delay time falling well below 0.5 implies single photon emission. Background correction was employed to correct the antibunching curves due to high PL background coming from the hBN flake. The $g^{(2)}(0)$ values for emission from pristine and coupled emitters are at 0.02 and 0.04, respectively. Red and blue solid lines are fits obtained using a three-level model. (d) Time-resolved PL measurements from the pristine (red open circles) and coupled (blue open squares) systems. Red and blue solid lines are double exponential fits. A 532 nm continuous-wave laser was used in (a), (b) and (c). A 512 nm pulsed laser with a repetition rate of 10 MHz and 100 ps pulse width was used in (d).

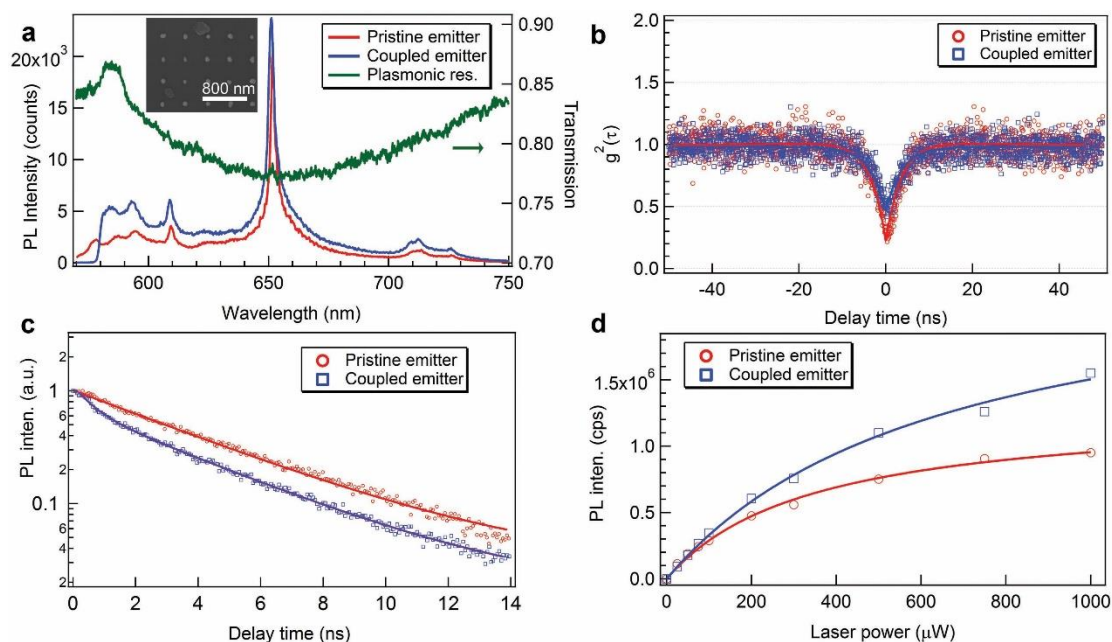


Figure 6.9. Coupling between a quantum emitter in a solvent exfoliated hBN flake and a gold NP array on a silica substrate. (a) PL spectra of a pristine (red trace) and coupled (blue trace) single photon emitter, and a transmission spectrum of the gold lattice (green trace). Inset: SEM image of the hBN flakes atop the gold NP array. (b) Second-order autocorrelation functions obtained from the pristine (red open circles) and coupled (blue open squares) systems. The $g^{(2)}(0)$ values for emission from pristine and coupled emitters are 0.23 and 0.47, respectively. In both cases, the dip at zero delay time falling well below 0.5 implies single photon emission. Red and blue solid lines are fits obtained using a three-level model. (c) Time-resolved PL measurements from the pristine (red open circles) and coupled (blue open squares) systems. Red and blue solid lines are double exponential fits. (d) Fluorescence saturation curves obtained from the pristine (red open circles) and coupled (blue open squares) systems. Red and blue solid lines are fits obtained using equation 2. A 532 nm continuous-wave laser was used in (a), (b) and (d). A 512 nm pulsed laser with a repetition rate of 10 MHz and 100 ps pulse width was used in (c).

While gold NP arrays can produce sharp lattice plasmon resonances in the NIR region, they suffer losses from interband transitions in the red region and thus exhibit broad resonances with lower quality factors. In contrast, silver NP arrays maintain narrow lattice plasmon resonances in the red spectral region with stronger near field enhancement, better mode quality and larger Purcell factor compared to gold NPs. We employed a silver NP array with 400 nm spacing coated with a 5-nm protective alumina layer. A strong resonance peak at $\lambda = 638$ nm with a FWHM of 50 nm was obtained from this structure (**Figure 6.10a**). To match this lattice, we identify a single emitter with a ZPL at 680 nm. The flake was then transferred onto the plasmonic array using the method shown in Figure 6.7c. Figure 6.10a shows a PL spectrum of the pristine single emitter, and the same emitter coupled to the silver plasmonic lattice array. **Figure 6.10b** confirms that the emitter is an SPE, and the non-classical emission is maintained after the transfer, with $g^{(2)}(0)$ at 0.06 and 0.29 before (red curve) and after (blue curve) the transfer, respectively.

The lifetime of the pristine emitter is $\tau_{1P} = 8.5$ ns while the lifetime of the same emitter coupled to the plasmonic lattice significantly reduced at a shorter time scale, to $\tau_{1C} = 0.27$ ns (**Figure 6.10c**), characteristic of the coupling to silver NP array. We note that the lifetimes of the pristine solvent-exfoliated and tape-exfoliated flakes may differ most likely due to the different dielectric environments in the materials. **Figure 6.10d** shows saturation measurements recorded from the pristine and the coupled flake, exhibiting saturation count rates of 0.33×10^6 and 0.85×10^6 counts/s, respectively, with an overall factor of 2.6 enhancement. The measured enhancement is lower than the one predicted from the ratios of the spontaneous decays before and after coupling to the plasmonic lattice ($E_F = \tau_{1P} / \tau_{1C} \approx 30$). This is likely due to less optimal spatial position of the

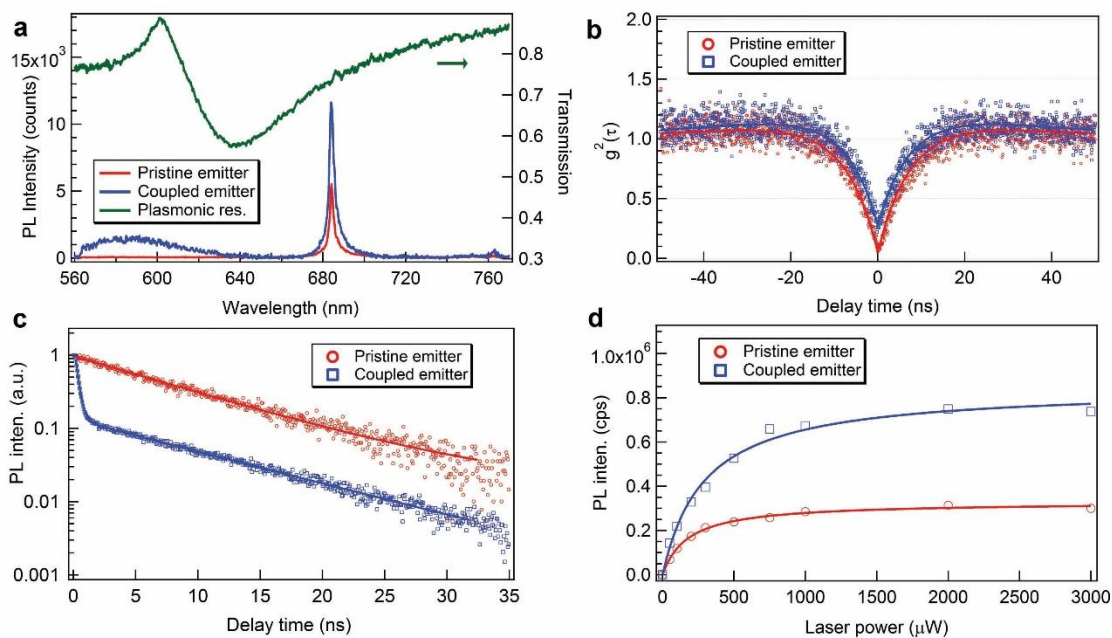


Figure 6.10. Coupling between a quantum emitter in a solvent exfoliated hBN flake and a silver NP array on a silica substrate. (a) PL spectra of a pristine (red trace) and coupled (blue trace) single photon emitter, and a transmission spectrum of the silver lattice (green trace). (b) Second-order autocorrelation functions obtained from the pristine (red open circles) and coupled (blue open squares) systems. In both cases, the dip at zero delay time falling well below 0.5 implies single photon emission. Red and blue solid lines are fits obtained using a three-level model. The $g^{(2)}(0)$ values for emission from pristine and coupled emitters are 0.06 and 0.29, respectively. (c) Time-resolved PL measurements from the pristine (red open circles) and coupled (blue open squares) systems. Red and blue solid lines are double exponential fits. (d) Fluorescence saturation curves for obtained from the pristine (red open circles) and coupled (blue open squares) systems. Red and blue solid lines are fits obtained using equation 2. A 532 nm continuous-wave laser was used in (a), (b) and (d). A 512 nm pulsed laser with a repetition rate of 10 MHz and 100 ps pulse width was used in (c).

emitters with respect to the hot cavity field and the spectral overlap between lattice plasmon resonance and hBN emission.

To summarize, we presented a robust and versatile approach to couple SPEs in 2D hBN to plasmonic nanocavity arrays. In particular, we developed a robust approach to transfer a pre-characterized quantum emitter of choice in hBN onto plasmonic gold and silver lattice arrays. An enhancement of a factor of ~ 2 is observed, associated with a fast lifetime reduction to demonstrate plasmonic-enhanced SPE emission. We note that the hBN emitters are already bright in their pristine form, with high QE and strong radiative component, which makes it more challenging to achieve high enhancement using plasmonic or dielectric cavities. The approach is an enabler to enhance emission from emitters in 2D materials and paves the way to hybrid planar quantum optics with 2D materials and plasmonic resonators. We expect that the delocalized surface plasmons can serve a versatile platform for long-range quantum entanglement and macroscale quantum coherence such as superradiance.

6.3 Topology and Parity-time Symmetry in Plasmonics

6.3.1 Introduction

The non-Hermitian Hamiltonian from parity–time symmetry opens a new era in quantum theories.^{117,119,120} Flexible photonic designs with rational integration of gain and loss have enabled the realization of non-Hermitian eigenstates in experiments, with various applications such as loss-induced transparency, unidirectional invisibility, and nonreciprocal transmission.^{118,227,228} A parity-time (PT) symmetric photonic system requires balanced loss and gain, where the Hamiltonian commutes with PT operators. The spatial dependence of the refractive index that leads to non-Hermitian eigenstates follows:

$$\text{Re}(n(x)) = \text{Re}(n(-x)) \quad (6.12)$$

$$\text{Im}(n(x)) = -\text{Im}(n(-x))$$

which can be achieved by spatial control of loss and gain. Coupled ring resonators with an active Er^{3+} -doped ring and a passive ring side by side can achieve the exceptional point by tailoring the coupling strength.^{118,119} Unidirectional light propagation is associated with the symmetry-broken phases, which is important for protected optical communications and on-chip photonics integration.^{117,120,121}

A well-defined, coupled plasmonic nanoresonator system is in need that can access exceptional point and achieve PT symmetry phase transitions. The balance of loss and gain in a plasmonic system is challenging due to the lossy plasmon damping, and stringent development of nanofabrication processes is required for defining active and passive resonators at sub-wavelength scale. In contrast, a plasmonic lattice with suppressed radiative loss^{4,5} could provide a platform for

spatial manipulation of gain and loss, and flexible tuning of resonator coupling efficiency for PT symmetry.

Here we show that the stacked plasmonic NP arrays can serve as a pair of coupled resonators and achieve transition between PT-symmetric and PT-broken phases by partial integration with the gain. Mode splitting was observed in simulation and experiment from the coupled nanoresonators that are stacked vertically with sub-wavelength spacings, associated with distinct phase distributions between two modes. The splitting modes followed the diffraction orders of a square array in the dispersion diagram, and were sensitive to NP size and interlayer spacing. In semi-quantum modeling, partial integration of gain in one layer induced the revival of single mode by changing interlayer spacing to control the coupling efficiency.

6.3.2 Mode Splitting in Stacked Plasmonic Nanoresonator Arrays

Figure 6.11 shows the mode splitting in stacked plasmonic NP arrays separated at sub-wavelength scales ($d = 330$ nm) without gain. A NP diameter of $D = 130$ nm was chosen to minimize the radiative loss. Mode splitting was observed at $\lambda_1 = 855$ nm and $\lambda_2 = 885$ nm, with the near-field enhancement following a dipolar pattern at both layers. Interestingly, mode λ_1 showed a reversed phase distribution between the top and bottom NP unit, and λ_2 showed the same phase distribution, similar to the bonding and anti-bonding modes in a dimer. The mode splitting and distinct phase distributions suggest that the stacked NP arrays can couple strongly with each other as a pair of coupled plasmon resonators.

In a coupled resonator system, the mode splitting is influenced by the oscillation strength of each resonator and the coupling efficiency between two resonators. For plasmonic arrays, the NP size and height influenced the resonance intensity and hence oscillation strength of lattice

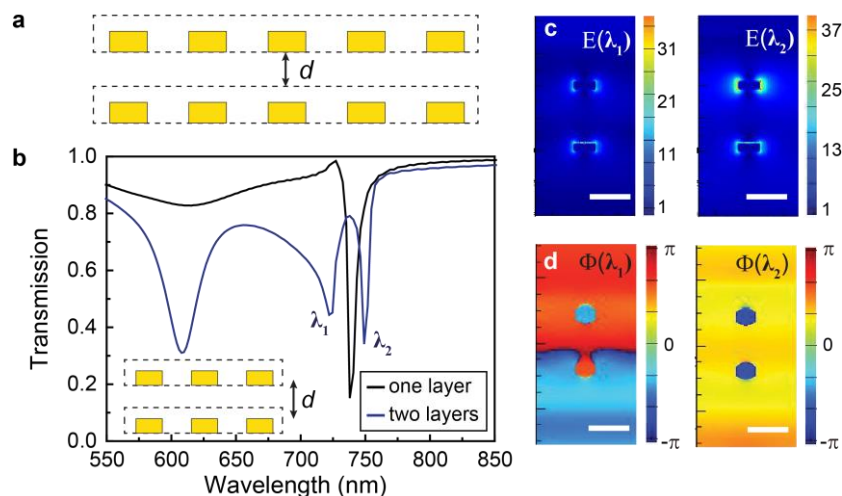


Figure 6.11. Splitting of modes in stacked plasmonic NP arrays. Near-field mode coupling in stacked NP arrays results in mode splitting in simulations. (a) Scheme of stacked NP arrays with gain in one layer for PT symmetry breaking. (b) Splitting modes were observed in stacked NP arrays without gain. (c-d) The near field and phase distributions suggest that NP arrays work as a pair of resonators with distinct phases between the two split modes.

plasmons. By tuning the NP diameter, we found that the two modes red-shifted and showed narrower splitting energy (**Figure 6.12**). In addition, tuning the interlayer spacing d modulated the coupling strength between two resonators. By changing d from 180 nm to 480 nm, we observed that the mode splitting was predominant at large spacings ($d > 330$ nm), while the splitting energy remained constant. The tuning of coupling strength by interlayer spacing d will be critical in accessing the exceptional point in a PT symmetric system.

To unveil the relationship between the splitting modes and the diffractive coupling in the stacked array without gain, we studied the dispersion properties at different wave vectors. For a single-lattice array, only a single lattice plasmon resonance existed at the red side of the Rayleigh anomaly. In contrast, two splitting modes appeared at the red and blue side of original single-lattice resonance at the Γ point (**Figure 6.13**). The splitting modes followed the $(\pm 1, 0)$ diffraction orders

under TE polarization, and followed low-dispersive ($0, \pm 1$) diffraction orders under TM polarization. Hence, the stacked NP arrays can open the bandgap at the original lattice plasmon wavelengths at Γ points, which offers a route to access the topological states in a plasmonic system.

To fabricate stacked plasmonic NP arrays, we spin coated SU8 on the Au NP arrays (thickness ~ 100 nm) and did a secondary Au NP deposition on top through a hole array mask. Both NP size

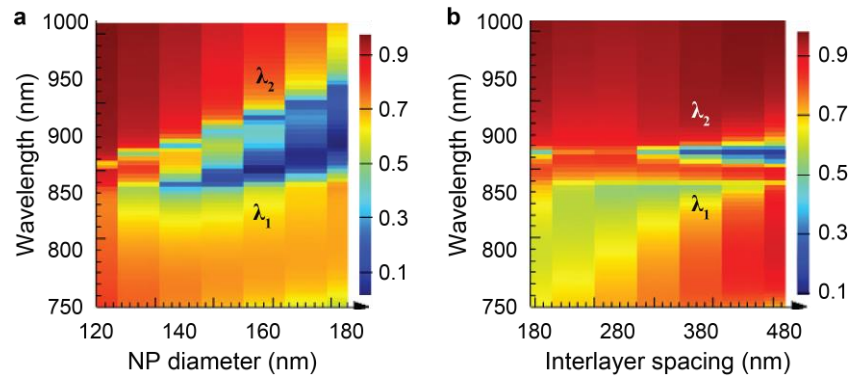


Figure 6.12. Mode splitting was sensitive to NP size and interlayer spacing in stacked arrays without gain. (a) Evolution of splitting modes with increased NP diameter, which enhanced the oscillator strength of NP array. (b) Evolution of splitting modes with increased interlayer spacing, which tuned the coupling efficiency.

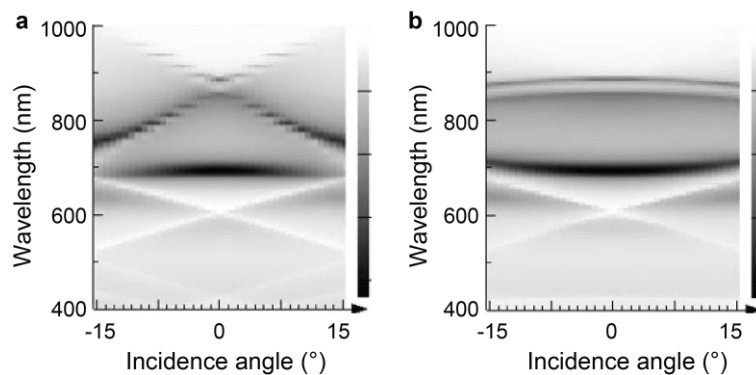


Figure 6.13. The split modes followed the diffraction orders of a square array at high incident angles. The dispersion diagrams under TE (a) and TM (b) polarization for NP diameter $D = 130$ nm and interlayer spacing $d = 330$ nm for stacked NP arrays without gain.

and interlayer spacing can be easily controlled in the nanofabrication process. In the experiments, the stacked arrays showed split modes under unpolarized light that followed the $(\pm 1, 0)$ and $(0, \pm 1)$ orders of Bragg modes (**Figure 6.14**). Interestingly, the splitting energy separation was smaller compared to simulations, and λ_1 appeared dark at $k_{\parallel} = 0$ while λ_2 appeared dominant at both zero

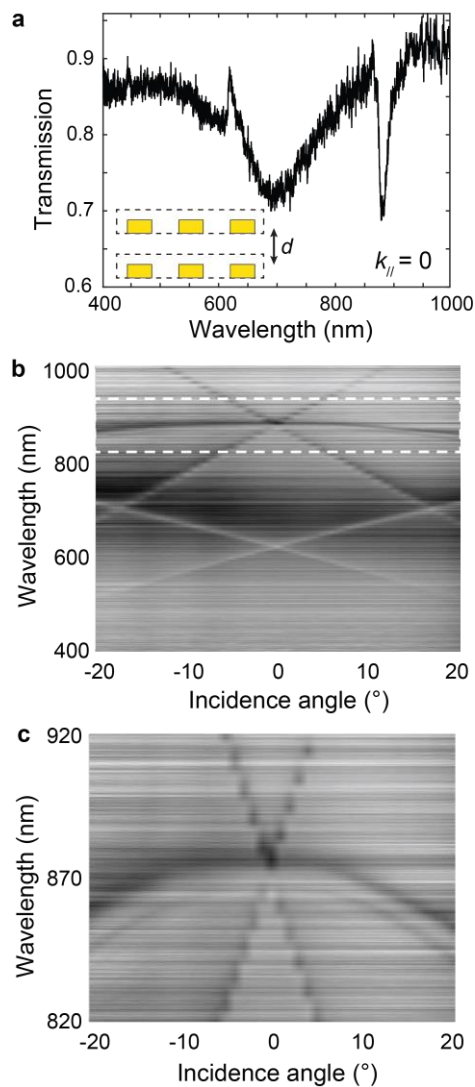


Figure 6.14. Mode splitting was observed in the dispersion diagram of stacked NP arrays. (a) Measured transmission spectrum at $k_{\parallel} = 0$ for stacked Au NP arrays with interlayer spacing around 100 nm. (b-c) Measured dispersion diagrams under unpolarized light. Panel c is a zoom-in of b at a smaller angular range.

and non-zero wavevectors, which might be attributed to the small interlayer distance (~ 100 nm) and tilted lattice angle.

6.3.3 Parity-time Symmetry with Spatially Engineered Gain and Loss

The spatial control of gain and loss in the stacked array system can be achieved by partial integration of gain in one of the NP array layers. In finite-different time-domain simulations, we integrated dye molecules in the upper NP layer as described by a four-level system (**Figure 6.15**). The loss in the coupled resonators can be balanced by the gain through flexible control over the dye concentration and pump power. To access the exceptional point in a PT symmetric system, the coupling strength between two NP arrays can be tuned by NP diameter, interlayer distance and lattice tilting angle. At small interlayer spacing $d = 330$ nm, we observed two enhanced peaks

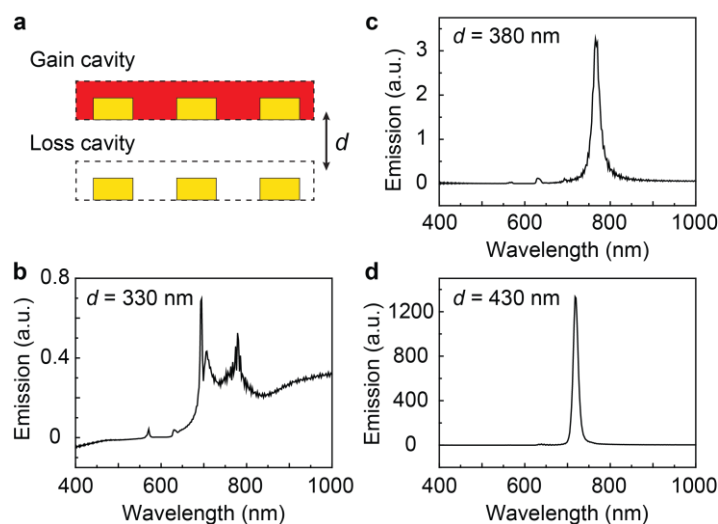


Figure 6.15. Revival of single mode with tunable NP interlayer spacing in semi-quantum modeling for stacked plasmonic NP arrays partly integrated with dyes. (a) Scheme of stacked NP arrays with dye molecule solvents in one layer. (b-d) Evolution from two modes to a single mode with increased interlayer spacing ($d = 330$ nm to 430 nm) to tune the coupling efficiency.

corresponding to the two splitting modes in the passive structure (Figure 6.15b). The revival of a single mode in the middle was achieved by increasing the layer spacing (from 330 nm to 430 nm, Figure 6.15d), which decreased the coupling efficiency k to surpass the exceptional point.

In conclusion, we demonstrated spatial tailoring of loss and gain in plasmon resonator system for PT symmetry breaking. The stacked NP arrays can serve as a new platform of coupled plasmon resonators that enables tunable coupling strength, and controlled gain and loss distributions. As a future outlook, the PT symmetry-broken phase in a plasmonic system can induce unidirectional propagating modes at the sub-wavelength scale, which is essential in protected optical communications and on-chip photonic integration.

6.4 Summary and Outlook

In summary, plasmonic NP arrays integrated with different photo-active materials provide a versatile, scalable platform for various light-matter interactions, such as nonlinear optics, quantum optics and PT symmetric photonics. The strong electric near-fields at the plasmon hot spots provide enhancement of SHG signals up to 450 times with wavelengths tunable by varying the fundamental wavelength, angle of incidence and lattice constant. Quantum emitters are deterministically coupled to high-quality plasmonic nanocavity arrays while preserving the single photon emission nature. As an outlook, the delocalized lattice plasmons can offer future prospects in long-range quantum entanglement and optical communications. A well-defined plasmonic nanoresonator system with rational integration of gain and loss can open possibilities for accessing exceptional points in PT symmetric systems, and achieving nontrivial topological states in a lossy, open environment.

References

- 1 Maier, S. A. *Plasmonics: Fundamentals and Applications*. (2007).
- 2 Barnes, W. L., Dereux, A. & Ebbesen, T. W. Surface plasmon subwavelength optics. *Nature* **424**, 824-830 (2003).
- 3 Henzie, J., Lee, J., Lee, M. H., Hasan, W. & Odom, T. W. Nanofabrication of plasmonic structures. *Annual Review of Physical Chemistry* **60**, 147-165 (2009).
- 4 Zou, S., Janel, N. & Schatz, G. C. Silver nanoparticle array structures that produce remarkably narrow plasmon lineshapes. *The Journal of chemical physics* **120**, 10871-10875 (2004).
- 5 Auguie, B. & Barnes, W. L. Collective resonances in gold nanoparticle arrays. *Physical Review Letters* **101**, 143902 (2008).
- 6 Henzie, J., Lee, M. H. & Odom, T. W. Multiscale patterning of plasmonic metamaterials. *Nature Nanotechnology* **2**, 549-554 (2007).
- 7 Chu, Y. Z., Schonbrun, E., Yang, T. & Crozier, K. B. Experimental observation of narrow surface plasmon resonances in gold nanoparticle arrays. *Appl. Phys. Lett.* **93**, 181108 (2008).
- 8 Auguie, B., Bendana, X. M., Barnes, W. L. & de Abajo, F. J. G. Diffractive arrays of gold nanoparticles near an interface: Critical role of the substrate. *Phys. Rev. B* **82** (2010).
- 9 Kravets, V. G., Schedin, F. & Grigorenko, A. N. Extremely narrow plasmon resonances based on diffraction coupling of localized plasmons in arrays of metallic nanoparticles. *Physical Review Letters* **101**, 087403 (2008).
- 10 Vecchi, G., Giannini, V. & Rivas, J. G. Surface modes in plasmonic crystals induced by diffractive coupling of nanoantennas. *Phys. Rev. B* **80** (2009).
- 11 Humphrey, A. D. & Barnes, W. L. Plasmonic surface lattice resonances on arrays of different lattice symmetry. *Phys Rev B* **90** (2014).
- 12 Zhou, W. *et al.* Lasing action in strongly coupled plasmonic nanocavity arrays. *Nature nanotechnology* **8**, 506-511 (2013).
- 13 Figotin, A. & Vitebskiy, I. Slow light in photonic crystals. *Wave Random Complex* **16**, 293-382 (2006).
- 14 Krauss, T. F. Why do we need slow light? *Nat. Photonics* **2**, 448-450 (2008).
- 15 Han, D., Lai, Y., Zi, J., Zhang, Z. Q. & Chan, C. T. Dirac spectra and edge states in honeycomb plasmonic lattices. *Physical Review Letters* **102**, 123904 (2009).

- 16 Weick, G., Woollacott, C., Barnes, W. L., Hess, O. & Mariani, E. Dirac-like plasmons in honeycomb lattices of metallic nanoparticles. *Physical Review Letters* **110**, 106801 (2013).
- 17 Klein J, K. J. The flexible research tool. *Nat. Photonics* **4** (2010).
- 18 Kukura, P., McCamant, D. W. & Mathies, R. A. Femtosecond stimulated Raman spectroscopy. *Annual Review of Physical Chemistry* **58**, 461-488 (2007).
- 19 Corkum, P. B. & Krausz, F. Attosecond science. *Nat. Phys.* **3**, 381-387 (2007).
- 20 E, M. The semiconductor laser: Enabling optical communication. *Nat. Photonics* **4** (2010).
- 21 Eichler, J. & Lenz, H. Laser applications in medicine and biology: a bibliography. *Appl Opt* **16**, 27 (1977).
- 22 Hill, M. T. & Gather, M. C. Advances in small lasers. *Nat Photonics* **8**, 908-918 (2014).
- 23 Ekaterina I. Galanzha, R. W., Dmitry A. Nedosekin, Mustafa Sarimollaoglu, Jacqueline Nolan, Walter Harrington, Alexander S. Kuchyanov, Roman G. Parkhomenko, Fumiya Watanabe, Zeid Nima, Alexandru S. Biris, Alexander I. Plekhanov, Mark I. Stockman & Vladimir P. Zharov. Spaser as a biological probe. *Nature Communications* **8**, 15528 (2017).
- 24 Murphy, S. V. & Atala, A. 3D bioprinting of tissues and organs. *Nat. Biotechnol.* **32**, 773-785 (2014).
- 25 J. Leuthold, C. H., S. Muehlbrandt, A. Melikyan, M. Kohl, C. Koos, W. Freude, V. Dolores, Calzadilla, M. Smit, I. Suarez, J. Martínez-Pastor, E.P. Fitrakis, and I. Tomkos. Plasmonic communications: Light on a wire. *Opt. Photon. News* **24**, 28-35 (2013).
- 26 Smit, M., van der Tol, J. & Hill, M. Moore's law in photonics. *Laser Photonics Rev* **6**, 1-+ (2012).
- 27 Kim, T. I. *et al.* Injectable, Cellular-Scale Optoelectronics with Applications for Wireless Optogenetics. *Science* **340**, 211-216 (2013).
- 28 Gather, M. C. & Yun, S. H. Single-cell biological lasers. *Nat. Photonics* **5**, 406-410 (2011).
- 29 Humar, M. & Yun, S. H. Intracellular microlasers. *Nat. Photonics* **9**, 572-576 (2015).
- 30 Zhang, Q., Ha, S. T., Liu, X., Sum, T. C. & Xiong, Q. Room-temperature near-infrared high-Q perovskite whispering-gallery planar nanolasers. *Nano. Lett.* **14**, 5995-6001 (2014).

- 31 Yu, Z. *et al.* Organic Phosphorescence Nanowire Lasers. *Journal of the American Chemical Society* **139**, 6376-6381 (2017).
- 32 Siegman, A. E. *Lasers*. (University Science Books, 1986).
- 33 Dridi, M. & Schatz, G. C. Lasing action in periodic arrays of nanoparticles. *Journal of the Optical Society of America B* **32**, 818 (2015).
- 34 Samuel, I. D. W., Namdas, E. B. & Turnbull, G. A. How to recognize lasing. *Nat. Photonics* **3**, 546-549 (2009).
- 35 Scrutinizing lasers. *Nat. Photonics* **11**, 139-139 (2017).
- 36 Oulton, R. F. *et al.* in *Nature* Vol. 461 629-632 (Nature Publishing Group, 2009).
- 37 Sidiropoulos, T. P. H. *et al.* in *Nat Phys* Vol. 10 870-876 (2014).
- 38 Bergman, D. & Stockman, M. Surface plasmon amplification by stimulated emission of radiation: quantum generation of coherent surface plasmons in nanosystems. *Phys. Rev. Lett.* **90**, 027402 (2003).
- 39 Ma, R. M., Oulton, R. F., Sorger, V. J., Bartal, G. & Zhang, X. Room-temperature sub-diffraction-limited plasmon laser by total internal reflection. *Nat Mater* **10**, 110-113 (2011).
- 40 Zhang, Q. *et al.* *Nature Communications* **5**, 4953 (2014).
- 41 Ma, R.-M., Ota, S., Li, Y., Yang, S. & Zhang, X. Explosives detection in a lasing plasmon nanocavity. *Nat Nano* **9**, 600-604 (2014).
- 42 Zheludev, N. I., Prosvirnin, S. L., Papasimakis, N. & Fedotov, V. A. Lasing spaser. *Nat Photonics* **2**, 351-354 (2008).
- 43 Stockman, M. I. Spasers explained. *Nat. Photonics* **2**, 327-329 (2008).
- 44 Stockman, M. I. in *J. Opt.* Vol. 12 024004 (IOP Publishing, 2010).
- 45 Gather, M. C. A rocky road to plasmonic lasers. *Nat. Photonics* **6**, 708-708 (2012).
- 46 Noginov, M. A. *et al.* *Nature* 460, 1110-1112 (2009).
- 47 Agio, M. & Alu, A. *Optical Antennas*. (2013).
- 48 Oulton, R. F., Sorger, V. J., Genov, D. A., Pile, D. F. P. & Zhang, X. A hybrid plasmonic waveguide for subwavelength confinement and long-range propagation. *Nat Photonics* **2**, 496-500 (2008).
- 49 Lu, Y. J. *et al.* Plasmonic nanolaser using epitaxially grown silver film. *Science* **337**, 450-453 (2012).

- 50 Lu, Y.-J. *et al.* All-color plasmonic nanolasers with ultralow thresholds: autotuning mechanism for single-mode lasing. *Nano Letters* **14**, 4381-4388 (2014).
- 51 Manjavacas, A., de Abajo, F. J. G. & Nordlander, P. Quantum Plexcitonics: Strongly Interacting Plasmons and Excitons. *Nano Letters* **11**, 2318-2323 (2011).
- 52 Yang, A. *et al.* Real-time tunable lasing from plasmonic nanocavity arrays. *Nature Communications* **6**, 6939 (2015).
- 53 Danqing Wang, A. Y., Weijia Wang, Yi Hua, Richard D. Schaller, George C. Schatz and Teri W. Odom. Band-edge Engineering for Controlled Multi-modal Nanolasing in Plasmonic Superlattices *Nature nanotechnology* (2017).
- 54 T. K. Hakala, H. T. R., A. I. Väkeväinen, J.-P. Martikainen, M. Nečada, A. J. Moilanen, P. Törmä. Lasing in dark and bright modes of a finite-sized plasmonic lattice. *Nature Communications* (2016).
- 55 Mohammad Ramezani, A. H., Antonio I. Fernández-Domínguez, Johannes Feist, Said Rahimzadeh-Kalaleh Rodriguez, Francisco J. Garcia-Vidal, and Jaime Gómez Rivas. Plasmon-exciton-polariton lasing. *Optica* **4**, 31 (2017).
- 56 Suh, J. Y. *et al.* *Nano Letters* **12**, 5769-5774 (2012).
- 57 Schokker, A. H. & Koenderink, A. F. Statistics of Randomized Plasmonic Lattice Lasers. *ACS Photonics* **2**, 1289-1297 (2015).
- 58 van Exter, M. P. *et al.* Surface plasmon dispersion in metal hole array lasers. *Opt. Express* **21**, 27422-27437 (2013).
- 59 Meng, X., Liu, J., Kildishev, A. V. & Shalaev, V. M. Highly directional spaser array for the red wavelength region. *Laser Photon. Rev.* **8**, 896-903 (2014).
- 60 Meng, X., Kildishev, A. V., Fujita, K., Tanaka, K. & Shalaev, V. M. Wavelength-tunable spasing in the visible. *Nano Letters* **13**, 4106-4112 (2013).
- 61 Yang, A. *et al.* Unidirectional Lasing from Template-Stripped Two-Dimensional Plasmonic Crystals. *ACS Nano* **9**, 11582-11588 (2015).
- 62 Yang, A. *et al.* Programmable and reversible plasmon mode engineering. *Proceedings of the National Academy of Sciences* **113**, 14201-14206 (2016).
- 63 Wang, D., Yang, A., Hryn, A. J., Schatz, G. C. & Odom, T. W. Superlattice Plasmons in Hierarchical Au Nanoparticle Arrays. *ACS Photonics* **2**, 1789-1794 (2015).
- 64 Turnbull, G. A., Andrew, P., Jory, M. J., Barnes, W. L. & Samuel, I. D. W. Relationship between photonic band structure and emission characteristics of a polymer distributed feedback laser. *Phys. Rev. B* **64** (2001).

- 65 Schokker, A. H. & Koenderink, A. F. Lasing in quasi-periodic and aperiodic plasmon lattices. *Optica* **3**, 686-693 (2016).
- 66 El-Kashef, H. The necessary requirements imposed on polar dielectric laser dye solvents-II. *Physica B* **311**, 376-379 (2002).
- 67 Gersborg-Hansen, M. & Kristensen, A. Tunability of optofluidic distributed feedback dye lasers. *Opt. Express* **15**, 137-142 (2007).
- 68 Heliotis, G. e. a. Two-dimensional distributed feedback lasers using a broadband, red polyfluorene gain medium. *J. Appl. Phys.* **96**, 6959-6965 (2004).
- 69 Gersborg-Hansen M, K. A. Optofluidic third order distributed feedback dye laser. *Appl. Phys. Lett.* **89**, 103518 (2006).
- 70 Samuel, I. D. & Turnbull, G. A. Organic semiconductor lasers. *Chem. Rev.* **107**, 1272-1295 (2007).
- 71 Stehr, J. *et al.* A low threshold polymer laser based on metallic nanoparticle gratings. *Adv. Mater.* **15**, 1726-+ (2003).
- 72 Kristensen, P. T. & Hughes, S. Modes and Mode Volumes of Leaky Optical Cavities and Plasmonic Nanoresonators. *ACS Photonics* **1**, 2-10 (2014).
- 73 Kristensen, P. T., Van Vlack, C. & Hughes, S. Generalized effective mode volume for leaky optical cavities. *Opt. Lett.* **37**, 1649-1651 (2012).
- 74 Griffiths, D. J. *Introduction to Electrodynamics.* (Pearson Education, 2014).
- 75 Cuerda, J., Ruting, F., Garcia-Vidal, F. J. & Bravo-Abad, J. Theory of lasing action in plasmonic crystals. *Phys Rev B* **91** (2015).
- 76 Nagra, A. S. & York, R. A. FDTD analysis of wave propagation in nonlinear absorbing and gain media. *Ieee T Antenn Propag* **46**, 334-340 (1998).
- 77 Yamada, A., Neuhauser, D. & Vallee, R. Path-selective lasing in nanostructures based on molecular control of localized surface plasmons. *Nanoscale* **8**, 18476-18482 (2016).
- 78 Bermel, P., Lidorikis, E., Fink, Y. & Joannopoulos, J. D. Active materials embedded in photonic crystals and coupled to electromagnetic radiation. *Phys Rev B* **73** (2006).
- 79 Chang, S. H. & Taflove, A. Finite-difference time-domain model of lasing action in a four-level two-electron atomic system. *Opt. Express* **12**, 3827-3833 (2004).
- 80 Chua, S. L., Chong, Y. D., Stone, A. D., Soljacic, M. & Bravo-Abad, J. Low-threshold lasing action in photonic crystal slabs enabled by Fano resonances. *Opt. Express* **19**, 1539-1562 (2011).

- 81 Huang, Y. Y. & Ho, S. T. Computational model of solid-state, molecular, or atomic media for FDTD simulation based on a multi-level multi-electron system governed by Pauli exclusion and Fermi-Dirac thermalization with application to semiconductor photonics. *Opt. Express* **14**, 3569-3587 (2006).
- 82 Teixeira, F. L. Time-domain finite-difference and finite-element methods for Maxwell equations in complex media. *IEEE T. Antenn. Propag.* **56**, 2150-2166 (2008).
- 83 Zhukovsky, S. V., Chigrin, D. N., Lavrinenko, A. V. & Kroha, J. Switchable lasing in multimode microcavities. *Physical Review Letters* **99** (2007).
- 84 Oskooi, A. F. *et al.* MEEP: A flexible free-software package for electromagnetic simulations by the FDTD method. *Computer Physics Communications* **181**, 687-702 (2010).
- 85 Dridi, M. & Schatz, G. C. Model for describing plasmon-enhanced lasers that combines rate equations with finite-difference time-domain. *Journal of the Optical Society of America B-Optical Physics* **30**, 2791-2797 (2013).
- 86 Scully, M. O. & Zubairy, M. S. *Quantum Optics*. (Cambridge University Press, 1999).
- 87 Sukharev, M., Freifeld, N. & Nitzan, A. Numerical Calculations of Radiative and Non-Radiative Relaxation of Molecules Near Metal Particles. *Journal of Physical Chemistry C* **118**, 10545-10551 (2014).
- 88 Sukharev, M. & Nitzan, A. Numerical studies of the interaction of an atomic sample with the electromagnetic field in two dimensions. *Physical Review A* **84** (2011).
- 89 Shan, G. C., Bao, S. Y., Zhang, K. & Huang, W. Theoretical study of photon emission from single quantum dot emitter coupled to surface plasmons. *Frontiers of Physics* **6**, 313-319 (2011).
- 90 Deinega, A. & Seideman, T. Self-interaction-free approaches for self-consistent solution of the Maxwell-Liouville equations. *Physical Review A* **89** (2014).
- 91 Deinega, A. & Seideman, T. Interaction of single quantum emitter and dark plasmon supported by a metal nanoring. *Journal of Chemical Physics* **140**, 5 (2014).
- 92 Sukharev, M., Seideman, T., Gordon, R. J., Salomon, A. & Prior, Y. Ultrafast Energy Transfer between Molecular Assemblies and Surface Plasmons in the Strong Coupling Regime. *Acs Nano* **8**, 807-817 (2014).
- 93 Lopata, K. & Neuhauser, D. Multiscale Maxwell-Schrodinger modeling: A split field finite-difference time-domain approach to molecular nanopolaritonics. *Journal of Chemical Physics* **130** (2009).

- 94 Benson, O. Assembly of hybrid photonic architectures from nanophotonic constituents. *Nature* **480**, 193-199 (2011).
- 95 Tame, M. S. *et al.* Quantum plasmonics. *Nat Phys* **9**, 329-340 (2013).
- 96 Koenderink, A. F., Alù, A. & Polman, A. Nanophotonics: Shrinking light-based technology. *Science* **348**, 516-521 (2015).
- 97 Schuller, J. A. *et al.* Plasmonics for extreme light concentration and manipulation. *Nat. Mater.* **9**, 193-204 (2010).
- 98 Akselrod, G. M. *et al.* Probing the mechanisms of large Purcell enhancement in plasmonic nanoantennas. *Nat. Photonics* **8**, 835-840 (2014).
- 99 Aharonovich, I., Englund, D. & Toth, M. Solid-state single-photon emitters. *Nat. Photonics* **10**, 631-641 (2016).
- 100 Schietinger, S., Barth, M., Alchele, T. & Benson, O. Plasmon-Enhanced Single Photon Emission from a Nanoassembled Metal-Diamond Hybrid Structure at Room Temperature. *Nano Letters* **9**, 1694-1698 (2009).
- 101 Choy, J. T. *et al.* Enhanced single-photon emission from a diamond-silver aperture. *Nat. Photonics* **5**, 738-743 (2011).
- 102 Zakharko, Y., Graf, A. & Zaumseil, J. Plasmonic Crystals for Strong Light–Matter Coupling in Carbon Nanotubes. *Nano Letters* **16**, 6504-6510 (2016).
- 103 Hoang, T. B., Akselrod, G. M. & Mikkelsen, M. H. Ultrafast Room-Temperature Single Photon Emission from Quantum Dots Coupled to Plasmonic Nanocavities. *Nano Letters* **16**, 270-275 (2016).
- 104 Demory, B. *et al.* Plasmonic Enhancement of Single Photon Emission from a Site-Controlled Quantum Dot. *ACS Photonics* **2**, 1065-1070 (2015).
- 105 Russell, K. J., Liu, T.-L., Cui, S. & Hu, E. L. Large spontaneous emission enhancement in plasmonic nanocavities. *Nat. Photonics* **6**, 459-462 (2012).
- 106 Tran, T. T. *et al.* Robust Multicolor Single Photon Emission from Point Defects in Hexagonal Boron Nitride. *ACS Nano* **10**, 7331-7338 (2016).
- 107 Tran, T. T., Bray, K., Ford, M. J., Toth, M. & Aharonovich, I. Quantum emission from hexagonal boron nitride monolayers. *Nature Nanotechnology* **11**, 37-41 (2016).
- 108 Jungwirth, N. R. *et al.* Temperature Dependence of Wavelength Selectable Zero-Phonon Emission from Single Defects in Hexagonal Boron Nitride. *Nano Letters* **16**, 6052-6057 (2016).

- 109 Chejanovsky, N. *et al.* Structural Attributes and Photodynamics of Visible Spectrum Quantum Emitters in Hexagonal Boron Nitride. *Nano Letters* **16**, 7037-7045 (2016).
- 110 Harari, G. *et al.* Topological insulator laser: Theory. *Science* **359** (2018).
- 111 Khanikaev, A. B. & Shvets, G. Two-dimensional topological photonics. *Nat. Photonics* **11**, 763-773 (2017).
- 112 Noh, J. *et al.* Topological protection of photonic mid-gap defect modes. *Nat. Photonics* **12**, 408-415 (2018).
- 113 Lu, L., Joannopoulos, J. D. & Soljacic, M. Topological states in photonic systems. *Nat. Phys.* **12**, 626-629 (2016).
- 114 Bahari, B. *et al.* Nonreciprocal lasing in topological cavities of arbitrary geometries. *Science* **358**, 636-639 (2017).
- 115 Wang, D. *et al.* Stretchable Nanolasing from Hybrid Quadrupole Plasmons. *Nano Lett.* **18**, 4549-4555 (2018).
- 116 Wang, Z., Chong, Y., Joannopoulos, J. D. & Soljacic, M. Observation of unidirectional backscattering-immune topological electromagnetic states. *Nature* **461**, 772-775 (2009).
- 117 El-Ganainy, R. *et al.* Non-Hermitian physics and PT symmetry. *Nat. Phys.* **14**, 11-19 (2018).
- 118 Hodaei, H., Miri, M. A., Heinrich, M., Christodoulides, D. N. & Khajavikhan, M. Parity-time-symmetric microring lasers. *Science* **346**, 975-978 (2014).
- 119 Peng, B. *et al.* Parity-time-symmetric whispering-gallery microcavities. *Nat. Phys.* **10**, 394-398 (2014).
- 120 Feng, L., El-Ganainy, R. & Ge, L. Non-Hermitian photonics based on parity-time symmetry. *Nat. Photonics* **11**, 752-762 (2017).
- 121 Feng, L. *et al.* Nonreciprocal light propagation in a silicon photonic circuit. *Science* **333**, 729-733 (2011).
- 122 Choi, J. H. *et al.* A high-resolution strain-gauge nanolaser. *Nat. Commun.* **7**, 11569 (2016).
- 123 Shih, M. H. *et al.* Compact Tunable Laser With InGaAsP Photonic Crystal Nanorods for C-Band Communication. *Ieee J Sel Top Quant* **21** (2015).
- 124 Rogers, J. A., Someya, T. & Huang, Y. Materials and mechanics for stretchable electronics. *Science* **327**, 1603-1607 (2010).
- 125 Kaltenbrunner, M. *et al.* An ultra-lightweight design for imperceptible plastic electronics. *Nature* **499**, 458-463 (2013).

- 126 Kang, D. *et al.* Ultrasensitive mechanical crack-based sensor inspired by the spider sensory system. *Nature* **516**, 222-226 (2014).
- 127 Desai, S. B. *et al.* Strain-induced indirect to direct bandgap transition in multilayer WSe₂. *Nano Lett.* **14**, 4592-4597 (2014).
- 128 Lu, T. W., Wang, C., Hsiao, C. F. & Lee, P. T. Tunable nanoblock lasers and stretching sensors. *Nanoscale* **8**, 16769-16775 (2016).
- 129 Yu, C. L. *et al.* Stretchable photonic crystal cavity with wide frequency tunability. *Nano Lett.* **13**, 248-252 (2013).
- 130 Sun, T. M. *et al.* Stretchable Random Lasers with Tunable Coherent Loops. *ACS Nano* **9**, 12436-12441 (2015).
- 131 Wang, D., Wang, W., Knudson, M. P., Schatz, G. C. & Odom, T. W. Structural Engineering in Plasmon Nanolasers. *Chem. Rev.* **118**, 2865-2881 (2018).
- 132 Yang, A. K., Wang, D. Q., Wang, W. J. & Odom, T. W. Coherent Light Sources at the Nanoscale. *Annu. Rev. Phys. Chem.* **68**, 83-99 (2017).
- 133 Kwon, S. H. *et al.* Subwavelength plasmonic lasing from a semiconductor nanodisk with silver nanopan cavity. *Nano Lett.* **10**, 3679-3683 (2010).
- 134 Daskalakis, K. S., Vakevainen, A. I., Martikainen, J. P., Hakala, T. K. & Torma, P. Ultrafast Pulse Generation in an Organic Nanoparticle-Array Laser. *Nano Lett.* **18**, 2658-2665 (2018).
- 135 Cui, Y., Zhou, J., Tamma, V. A. & Park, W. Dynamic tuning and symmetry lowering of Fano resonance in plasmonic nanostructure. *ACS Nano* **6**, 2385-2393 (2012).
- 136 Weijia Wang, M. R., Aaro I. Väkeväinen, Päivi Törmä, Jaime Gómez Rivas, Teri W. Odom. The rich photonic world of plasmonic nanoparticle arrays. *Materials Today* (2017).
- 137 Henzie, J., Barton, J. E., Stender, C. L. & Odom, T. W. Large-area nanoscale patterning: chemistry meets fabrication. *Acc. Chem. Res.* **39**, 249-257 (2006).
- 138 Odom, T. W., Love, J. C., Wolfe, D. B., Paul, K. E. & Whitesides, G. M. Improved pattern transfer in soft lithography using composite stamps. *Langmuir* **18**, 5314-5320 (2002).
- 139 Hao, F., Larsson, E. M., Ali, T. A., Sutherland, D. S. & Nordlander, P. Shedding light on dark plasmons in gold nanorings. *Chem. Phys. Lett.* **458**, 262-266 (2008).
- 140 Andrey B. Evlyukhin, C. R., Urs Zywietz, and Boris N. Chichkov. Collective resonances in metal nanoparticle arrays with dipole-quadrupole interactions. *Phys. Rev. B* **85**, 245411 (2012).

- 141 Evlyukhin, A. B., Reinhardt, C., Seidel, A., Luk'yanchuk, B. S. & Chichkov, B. N. Optical response features of Si-nanoparticle arrays. *Phys. Rev. B* **82** (2010).
- 142 Lopez, N., Reichertz, L. A., Yu, K. M., Campman, K. & Walukiewicz, W. Engineering the electronic band structure for multiband solar cells. *Physical review letters* **106**, 028701 (2011).
- 143 Withers, F. *et al.* Light-emitting diodes by band-structure engineering in van der Waals heterostructures. *Nat. Mater.* **14**, 301-306 (2015).
- 144 Qian, F. *et al.* Multi-quantum-well nanowire heterostructures for wavelength-controlled lasers. *Nat. Mater.* **7**, 701-706 (2008).
- 145 Painter, O. *et al.* Two-dimensional photonic band-Gap defect mode laser. *Science* **284**, 1819-1821 (1999).
- 146 Pickering, T., Hamm, J. M., Page, A. F., Wuestner, S. & Hess, O. Cavity-free plasmonic nanolasing enabled by dispersionless stopped light. *Nat. Commun.* **5**, 4972 (2014).
- 147 Schokker, A. H. & Koenderink, A. F. Lasing at the band edges of plasmonic lattices. *Phys. Rev. B* **90** (2014).
- 148 Fan, F., Turkdogan, S., Liu, Z., Shelhammer, D. & Ning, C. Z. A monolithic white laser. *Nature nanotechnology* **10**, 796-803 (2015).
- 149 Ma, R. M., Yin, X., Oulton, R. F., Sorger, V. J. & Zhang, X. Multiplexed and electrically modulated plasmon laser circuit. *Nano Lett.* **12**, 5396-5402 (2012).
- 150 Kichin, G. *et al.* Metal-dielectric photonic crystal superlattice: 1D and 2D models and empty lattice approximation. *Physica B* **407**, 4037-4042 (2012).
- 151 Odom, T. W., Gao, H. W., McMahon, J. M., Henzie, J. & Schatz, G. C. Plasmonic superlattices: Hierarchical subwavelength hole arrays. *Chem. Phys. Lett.* **483**, 187-192 (2009).
- 152 Zentgraf, T. *et al.* Metallodielectric photonic crystal superlattices: Influence of periodic defects on transmission properties. *Phys. Rev. B* **73** (2006).
- 153 Young, K. L. *et al.* Using DNA to design plasmonic metamaterials with tunable optical properties. *Adv. Mater.* **26**, 653-659 (2014).
- 154 Ross, M. B., Ku, J. C., Vaccarezza, V. M., Schatz, G. C. & Mirkin, C. A. Nanoscale form dictates mesoscale function in plasmonic DNA-nanoparticle superlattices. *Nature nanotechnology* (2015).
- 155 Macfarlane, R. J. *et al.* Nanoparticle superlattice engineering with DNA. *Science* **334**, 204-208 (2011).

- 156 Sung, J., Hicks, E. M., Van Duyne, R. P. & Spears, K. G. Nanoparticle spectroscopy: Plasmon coupling in finite-sized two-dimensional arrays of cylindrical silver nanoparticles. *Journal of Physical Chemistry C* **112**, 4091-4096 (2008).
- 157 Henzie, J., Kwak, E. S. & Odom, T. W. Mesoscale metallic pyramids with nanoscale tips. *Nano Lett.* **5**, 1199-1202 (2005).
- 158 Gao, H., Henzie, J. & Odom, T. W. Direct evidence for surface plasmon-mediated enhanced light transmission through metallic nanohole arrays. *Nano Lett.* **6**, 2104-2108 (2006).
- 159 Trivedi, D. J., Wang, D. Q., Odom, T. W. & Schatz, G. C. Model for describing plasmonic nanolasers using Maxwell-Liouville equations with finite-difference time-domain calculations. *Physical Review A* **96** (2017).
- 160 Hu, J. *et al.* Lattice-Resonance Metalenses for Fully Reconfigurable Imaging. *ACS Nano* (2019).
- 161 Ma, R. M. & Oulton, R. F. Applications of nanolasers. *Nature nanotechnology* **14**, 12-22 (2019).
- 162 Wierer, J. J., Tsao, J. Y. & Sizov, D. S. Comparison between blue lasers and light-emitting diodes for future solid-state lighting. *Laser Photonics Rev* **7**, 963-993 (2013).
- 163 Nelis, J., Elliott, C. & Campbell, K. "The Smartphone's Guide to the Galaxy": In Situ Analysis in Space. *Biosensors* **8**, 96 (2018).
- 164 Wang, S. *et al.* Unusual scaling laws for plasmonic nanolasers beyond the diffraction limit. *Nature Communications* **8**, 1-8 (2017).
- 165 Ghafouri-Shiraz, H. *Distributed feedback laser diodes and optical tunable filters*. (John Wiley, 2003).
- 166 Wang, D., Wang, W., Knudson, M. P., Schatz, G. C. & Odom, T. W. Structural Engineering in Plasmon Nanolasers. *Chem. Rev.* **118**, 2865-2881 (2017).
- 167 Fan, F. J. *et al.* Continuous-wave lasing in colloidal quantum dot solids enabled by facet-selective epitaxy. *Nature* **544**, 75-79 (2017).
- 168 Tamboli, A. C. *et al.* Room-temperature continuous-wave lasing in GaN/InGaN microdisks. *Nat. Photonics* **1**, 61-64 (2007).
- 169 Zhu, H. *et al.* Lead halide perovskite nanowire lasers with low lasing thresholds and high quality factors. *Nat. Mater.* **14**, 636-642 (2015).
- 170 Huang, M. H. *et al.* Room-temperature ultraviolet nanowire nanolasers. *Science* **292**, 1897-1899 (2001).

- 171 Zhou, B., Shi, B., Jin, D. & Liu, X. Controlling upconversion nanocrystals for emerging applications. *Nature nanotechnology* **10**, 924-936 (2015).
- 172 Gargas, D. J. *et al.* Engineering bright sub-10-nm upconverting nanocrystals for single-molecule imaging. *Nature nanotechnology* **9**, 300-305 (2014).
- 173 Wu, S. *et al.* Non-blinking and photostable upconverted luminescence from single lanthanide-doped nanocrystals. *Proc. Natl. Acad. Sci.* **106**, 10917-10921 (2009).
- 174 Anderson, R. B., Smith, S. J., May, P. S. & Berry, M. T. Revisiting the NIR-to-visible upconversion mechanism in β -NaYF₄:Yb³⁺,Er³⁺. *Journal of Physical Chemistry Letters* **5**, 36-42 (2014).
- 175 Zhu, H. *et al.* Amplified spontaneous emission and lasing from lanthanide-doped upconversion nanocrystals. *ACS Nano* **7**, 11420-11426 (2013).
- 176 Fernandez-Bravo, A. *et al.* Continuous-wave upconverting nanoparticle microlasers. *Nat. Nanotechnol.* **13**, 572-577 (2018).
- 177 Haider, G. *et al.* A Highly-Efficient Single Segment White Random Laser. *ACS Nano* **12**, 11847-11859 (2018).
- 178 Ostrowski, A. D. *et al.* Controlled synthesis and single-particle imaging of bright, sub-10 nm lanthanide-doped upconverting nanocrystals. *ACS Nano* **6**, 2686-2692 (2012).
- 179 Tian, B. *et al.* Low irradiance multiphoton imaging with alloyed lanthanide nanocrystals. *Nat. Commun.* **9**, 3082 (2018).
- 180 Schuck, P. J., Willets, K. A., Fromm, D. P., Twieg, R. J. & Moerner, W. E. A novel fluorophore for two-photon-excited single-molecule fluorescence. *Chem. Phys.* **318**, 7-11 (2005).
- 181 Grim, J. Q. *et al.* Continuous-wave biexciton lasing at room temperature using solution-processed quantum wells. *Nature Nanotechnology* **9**, 891-895 (2014).
- 182 Nielsen, M. P., Shi, X. Y., Dichtl, P., Maier, S. A. & Oulton, R. F. Giant nonlinear response at a plasmonic nanofocus drives efficient four-wave mixing. *Science* **358**, 1179-1181 (2017).
- 183 Yuan, P. *et al.* Plasmon enhanced upconversion luminescence of NaYF₄:Yb,Er@SiO₂@Ag core-shell nanocomposites for cell imaging. *Nanoscale* **4**, 5132-5137 (2012).
- 184 Sun, Q. C. *et al.* Plasmon-enhanced energy transfer for improved upconversion of infrared radiation in doped-lanthanide nanocrystals. *Nano Lett.* **14**, 101-106 (2014).
- 185 Liu, Q. *et al.* Single upconversion nanoparticle imaging at sub-10 W cm⁻² irradiance. *Nat. Photonics* **12**, 548-553 (2018).

- 186 Tajon, C. A. *et al.* Photostable and efficient upconverting nanocrystal-based chemical sensors. *Opt. Mater.* **84**, 345-353 (2018).
- 187 Teitelboim, A. *et al.* Energy Transfer Networks within Upconverting Nanoparticles Are Complex Systems with Collective, Robust, and History-Dependent Dynamics. *J. Phys. Chem. C* **123**, 2678-2689 (2019).
- 188 Chen, S. *et al.* Near-infrared deep brain stimulation via upconversion nanoparticle-mediated optogenetics. *Science* **359**, 679-684 (2018).
- 189 Kauranen, M. & Zayats, A. V. Nonlinear plasmonics. *Nat. Photonics* **6**, 737-748 (2012).
- 190 Butet, J., Brevet, P. F. & Martin, O. J. Optical Second Harmonic Generation in Plasmonic Nanostructures: From Fundamental Principles to Advanced Applications. *ACS Nano* **9**, 10545-10562 (2015).
- 191 Shibanuma, T., Grinblat, G., Albella, P. & Maier, S. A. Efficient Third Harmonic Generation from Metal-Dielectric Hybrid Nanoantennas. *Nano Lett* **17**, 2647-2651 (2017).
- 192 Bautista, G. *et al.* Collective Effects in Second-Harmonic Generation from Plasmonic Oligomers. *Nano Lett.* **18**, 2571-2580 (2018).
- 193 Valev, V. K. *et al.* Plasmon-enhanced sub-wavelength laser ablation: plasmonic nanojets. *Adv. Mater.* **24**, OP29-35 (2012).
- 194 Chen, S. *et al.* Symmetry-selective third-harmonic generation from plasmonic metacrystals. *Physical Review Letters* **113**, 033901 (2014).
- 195 Bautista, G. & Kauranen, M. Vector-Field Nonlinear Microscopy of Nanostructures. *ACS Photonics* **3**, 1351-1370 (2016).
- 196 Valev, V. K. *et al.* Distributing the optical near-field for efficient field-enhancements in nanostructures. *Adv. Mater.* **24**, OP208-215, OP272 (2012).
- 197 Valev, V. K., Baumberg, J. J., Sibilia, C. & Verbiest, T. Chirality and chiroptical effects in plasmonic nanostructures: fundamentals, recent progress, and outlook. *Adv. Mater.* **25**, 2517-2534 (2013).
- 198 Hooper, D. C. *et al.* Strong Rotational Anisotropies Affect Nonlinear Chiral Metamaterials. *Adv. Mater.* **29** (2017).
- 199 Belardini, A. *et al.* Circular dichroism in the optical second-harmonic emission of curved gold metal nanowires. *Physical Review Letters* **107**, 257401 (2011).
- 200 Valev, V. K. *et al.* Nonlinear Superchiral Meta-Surfaces: Tuning Chirality and Disentangling Non-Reciprocity at the Nanoscale. *Adv. Mater.* **26**, 4074-4081 (2014).

- 201 Lee, J. *et al.* Giant nonlinear response from plasmonic metasurfaces coupled to intersubband transitions. *Nature* **511**, 65-69 (2014).
- 202 Almeida, E., Shalem, G. & Prior, Y. Subwavelength nonlinear phase control and anomalous phase matching in plasmonic metasurfaces. *Nat. Commun.* **7**, 10367 (2016).
- 203 Li, G., Zhang, S. & Zentgraf, T. Nonlinear photonic metasurfaces. *Nat. Rev. Mater.* **2** (2017).
- 204 Schlickriede, C. *et al.* Imaging through Nonlinear Metalens Using Second Harmonic Generation. *Adv. Mater.* **30** (2018).
- 205 Chen, J. W. *et al.* Tungsten Disulfide-Gold Nanohole Hybrid Metasurfaces for Nonlinear Metalenses in the Visible Region. *Nano Letters* **18**, 1344-1350 (2018).
- 206 Zou, S. & Schatz, G. C. Narrow plasmonic/photonic extinction and scattering line shapes for one and two dimensional silver nanoparticle arrays. *The Journal of chemical physics* **121**, 12606-12612 (2004).
- 207 Spackova, B. & Homola, J. Sensing properties of lattice resonances of 2D metal nanoparticle arrays: An analytical model. *Opt. Express* **21**, 27490-27502 (2013).
- 208 Kravets, V. G., Schedin, F., Kabashin, A. V. & Grigorenko, A. N. Sensitivity of collective plasmon modes of gold nanoresonators to local environment. *Opt. Lett.* **35**, 956-958 (2010).
- 209 Lee, K. S. & El-Sayed, M. A. Gold and silver nanoparticles in sensing and imaging: sensitivity of plasmon response to size, shape, and metal composition. *J Phys Chem B* **110**, 19220-19225 (2006).
- 210 Offermans, P. *et al.* Universal scaling of the figure of merit of plasmonic sensors. *ACS Nano* **5**, 5151-5157 (2011).
- 211 Li, J. Q. *et al.* Revisiting the Surface Sensitivity of Nanoplasmonic Biosensors. *ACS Photonics* **2**, 425-431 (2015).
- 212 Michaeli, L., Keren-Zur, S., Avayu, O., Suchowski, H. & Ellenbogen, T. Nonlinear Surface Lattice Resonance in Plasmonic Nanoparticle Arrays. *Physical Review Letters* **118**, 243904 (2017).
- 213 Czaplicki, R. *et al.* Surface lattice resonances in second-harmonic generation from metasurfaces. *Opt. Lett.* **41**, 2684-2687 (2016).
- 214 Butet, J. *et al.* Interference between Selected Dipoles and Octupoles in the Optical Second-Harmonic Generation from Spherical Gold Nanoparticles. *Physical Review Letters* **105** (2010).

- 215 Nappa, K., Russier-Antoine, I., Benichou, E., Jonin, C. & Brevet, P. F. Wavelength dependence of the retardation effects in silver nanoparticles followed by polarization resolved hyper Rayleigh scattering. *Chem. Phys. Lett.* **415**, 246-250 (2005).
- 216 Russier-Antoine, I., Benichou, E., Bachelier, G., Jonin, C. & Brevet, P. F. Multipolar contributions of the second harmonic generation from silver and gold nanoparticles. *Journal of Physical Chemistry C* **111**, 9044-9048 (2007).
- 217 Smirnova, D. & Kivshar, Y. S. Multipolar nonlinear nanophotonics. *Optica* **3**, 1241-1255 (2016).
- 218 Vecchi, G., Giannini, V. & Gomez Rivas, J. Shaping the fluorescent emission by lattice resonances in plasmonic crystals of nanoantennas. *Physical Review Letters* **102**, 146807 (2009).
- 219 Huttunen, M. J., Rasekh, P., Boyd, R. W. & Dolgaleva, K. Using surface lattice resonances to engineer nonlinear optical processes in metal nanoparticle arrays. *Physical Review A* **97** (2018).
- 220 Aouani, H. *et al.* Multiresonant Broadband Optical Antennas As Efficient Tunable Nanosources of Second Harmonic Light. *Nano Lett.* **12**, 4997-5002 (2012).
- 221 Dong, Z. *et al.* Second-Harmonic Generation from Sub-5 nm Gaps by Directed Self-Assembly of Nanoparticles onto Template-Stripped Gold Substrates. *Nano Lett.* **15**, 5976-5981 (2015).
- 222 Guyot-Sionnest, P. & Shen, Y. R. Bulk contribution in surface second-harmonic generation. *Phys Rev B Condens Matter* **38**, 7985-7989 (1988).
- 223 Bachelier, G., Russier-Antoine, I., Benichou, E., Jonin, C. & Brevet, P. F. Multipolar second-harmonic generation in noble metal nanoparticles. *Journal of the Optical Society of America B-Optical Physics* **25**, 955-960 (2008).
- 224 Boulesbaa, A. *et al.* Ultrafast Dynamics of Metal Plasmons Induced by 2D Semiconductor Excitons in Hybrid Nanostructure Arrays. *ACS Photonics* (2016).
- 225 Xu, Z.-Q. *et al.* Synthesis and Transfer of Large-Area Monolayer WS₂ Crystals: Moving Toward the Recyclable Use of Sapphire Substrates. *ACS Nano* **9**, 6178-6187 (2015).
- 226 Beveratos, A., Brouri, R., Gacoin, T., Poizat, J.-P. & Grangier, P. Nonclassical radiation from diamond nanocrystals. *Physical Review A* **64**, 061802 (2001).
- 227 Shi, C. *et al.* Accessing the exceptional points of parity-time symmetric acoustics. *Nat. Commun.* **7**, 11110 (2016).
- 228 Feng, L., Wong, Z. J., Ma, R. M., Wang, Y. & Zhang, X. Single-mode laser by parity-time symmetry breaking. *Science* **346**, 972-975 (2014).

Danqing Wang

• danqingwang2018@u.northwestern.edu • +1 (224) 420-6869

EDUCATION

Northwestern University , Evanston, IL Ph.D. candidate in Applied Physics	2013 – 2019
Nanjing University , Nanjing, China B.S. in Physics	2009 – 2013

RESEARCH EXPERIENCE

Northwestern University, Evanston, IL

- Graduate research co-advised by Prof. Teri W. Odom and Prof. George C. Schatz

Highlight activities include:

- Achieved controlled multi-modal nanolasing in multi-scale plasmonic superlattice arrays and unveiled the origin from multiple band-edge modes
- Exploited hybrid quadrupole plasmons as a new lasing feedback mechanism and realized stretchable nanolasing based on metal nanoparticles on a flexible, polymer matrix
- Established a robust computational approach in finite-difference time-domain to investigate time- and spatial- dependent lasing buildup in plasmonic nanocavities
- Collaboratively realized deterministic coupling of quantum emitters in hexagonal boron nitride to plasmonic nanocavities for enhanced single-photon emission

Nanjing University, Nanjing, China

- Undergraduate project titled “*Enhanced Light Propagation in Hybrid Nonlinear Waveguides*” in *National Laboratory of Solid State Microstructures*

AWARDS

- 2019 Miller Research Fellowship, University of California, Berkeley
- 2018 Material Research Society Graduate Student Award (GSA) Silver Award
- 2018 Excellent Poster Award, Gordon Research Conference on Lasers in Micro, Nano and Bio Systems
- 2018 International Precious Metals Institute (IPMI) Student Award Honorable Mention
- 2018 Chinese Government Award for Outstanding Self-Financed Students Abroad
- 2017 Outstanding Research Award (International Institute for Nanotechnology, Northwestern University)

2013 Excellence Prize in Chinese Undergraduate Innovation Program (*national level*)

2013 Shengda and Renmin Fellowships, Nanjing University

PUBLICATIONS

1. **Wang, D.**; Bourgeois, M.R.; Lee, W.; Li, R.; Trivedi, D.; Knudson, M.P.; Wang, W.; Schatz, G.C.; Odom, T.W. "Stretchable Nanolasing from Hybrid Quadrupole Plasmons," *Nano Letters* **18**, 4549–4555 (June 18, 2018) DOI: 10.1021/acs.nanolett.8b01774
2. **Wang, D.**; Wang, W.; Knudson, M.P.; Schatz, G.C.; Odom, T.W. "Structural Engineering in Plasmon Nanolasers," *Chemical Reviews* **118**, 2865–2881 (October 17, 2017) DOI: 10.1021/acs.chemrev.7b00424
3. **Wang, D.**; Yang, A.; Wang, W.; Hua, Y.; Schaller, R.D.; Schatz, G.C.; Odom, T.W. "Band-edge Engineering for Controlled Multi-modal Nanolasing in Plasmonic Superlattices," *Nature Nanotechnology* **12**, 889 (July 10, 2017) [**Highlighted in News and Views Nature Nanotechnology** **12**, 838 (September 6, 2017)] DOI: 10.1038/nnano.2017.126
4. Tran, T.T.*; **Wang, D.***; Xu, Z-Q.*; Yang, A.; Toth, M.; Odom, T.W.; Aharonovich, I. "Deterministic Coupling of Quantum Emitters in 2D Materials to Plasmonic Nanocavity Arrays," *Nano Letters* **17**, 2634–2639 (March 20, 2017) *equal contribution DOI: 10.1021/acs.nanolett.7b00444
5. **Wang, D.**; Yang, A.; Hryn, A.J.; Schatz, G.C.; Odom, T.W. "Superlattice Plasmons in Hierarchical Au Nanoparticle Arrays," *ACS Photonics* **2**, 1789 (November 24, 2015) DOI: 10.1021/acsp Photonics.5b00546
6. Hu, J.; **Wang, D.**; Bhowmik, D.; Liu, T.; Deng, S.; Knudson, M.P.; Ao, X.; Odom, T.W. "Lattice-Resonance Metalenses for Fully Reconfigurable Imaging," *ACS Nano, ASAP* (March, 2019)
7. Knudson, M.P.; Li, R.; **Wang, D.**; Wang, W.; Schaller, R.D.; Odom, T.W. "Polarization-Dependent Lasing Behavior from Low-Symmetry Nanocavity Arrays," *ACS Nano ASAP* DOI: 10.1021/acsnano.9b01142
8. Liu, J.; Wang, W.; **Wang, D.**; Hu, J.; Ding, W.; Schaller, R.D.; Schatz, G.C.; Odom, T.W. "Spatially Defined Molecular Emitters Coupled to Plasmonic Nanoparticles," *Proc. Natl. Acad. Sci.* **116**, 5925–5930 (March, 2019) DOI.org/10.1073/pnas.1818902116
9. Hooper, D. C.; Kuppe, C.; **Wang, D.**; Wang, W.; Guan, J.; Odom, T.W.; Valev, V.K. "Second harmonic spectroscopy of surface lattice resonances," *Nano Letters* **19**, 165–172 (January, 2019) DOI: 10.1021/acs.nanolett.8b03574
10. **Wang, D.**; Wang, W.; Odom, T.W et al. "Roadmap on Plasmonics: Nanoarray Lasing Spasers," *Journal of Optics* **20**, 043001 (March 9, 2018) DOI: 10.1088/2040-8986/aaa114

11. Trivedi D.; **Wang, D.**; Odom, T.W.; Schatz, G.C. "Model for Describing Plasmonic Nanolasers Using Maxwell-Liouville Equations with Finite-difference Time-domain Calculations," *Phys. Rev. A*. **96**, 053825 (November 10, 2017) DOI: 10.1103/PhysRevA.96.053825
12. Yang, A.; **Wang, D.**; Wang, W.; Odom, T. W. "Coherent Light Sources at the Nanoscale," *Annu. Rev. Phys. Chem.* **68**, 83-99 (January 30, 2017) DOI: 10.1146/annurev-physchem-052516-050730
13. Wang, S.; **Wang, D.**; Hu, X.; Li, T.; Zhu, S. "Compact Surface Plasmon Amplifier in Nonlinear Hybrid Waveguide," *Chinese Physics B* **25**, 7 (May 27, 2016)
14. Fernandez-Bravo, A.*; **Wang, D.***; Tajon, C.; Teitelboim, A.; Guan, J.; Schatz, G.C.; Cohen, B.E.; Chan, E.; Schuck, P.J.; Odom, T.W. "Continuous-wave upconverting plasmon nanolasing at room temperature," *submitted to Nature Materials* *equal contribution
15. Li, R.; **Wang, D.**; Guan, J.; Wang, W.; Ao, X.; Schatz, G.C.; Schaller, R.D.; Odom, T.W. "Plasmon Nanolasing with Aluminum Nanoparticle Arrays," *submitted to J. Opt. Soc. Am. B*

PRESS RELEASES

1. "[The chameleon and the crystal maze](#)", *Laboratory News, UK* (Sept. 2018) [**Highlighted** as the featured article and the cover story]
2. "[Mimicking the Master of Camouflage](#)", *Chicago Biomedical Consortium Success Story* (July 2018)
3. "[Nanolaser Changes Color when Stretched](#)", *Chemical & Engineering News* (July 2018)
4. "[Chameleons Inspire Mechanochromic Nanolaser](#)", *Physics World* (June 2018)
5. "[Chameleon-inspired Nanolaser Changes Colors](#)", *ScienceDaily* (June 2018)
6. "[Chameleon-inspired Nanolaser Changes Colors](#)", *Northwestern Now* (June 2018)
7. "[Chameleon-inspired Nanolaser Changes Colors](#)", *National Science Foundation's homepage* (June 2018)
8. "[Northwestern's New Chameleon-Inspired Laser Changes Colors](#)", *WTTW* (June 2018)
9. "[Nanolasing: Multimode Superlattice Arrays](#)", *Nature Nanotechnology News and Views* (September 2017)
10. "[New Laser Design Offers More Inexpensive Multi-color Output](#)", *Northwestern Now* (July 2017)
11. "[Controlling Multi-modal Nanolasing with Plasmonic Superlattices](#)", *Nanowerk News* (July 2017)

CONFERENCES AND PRESENTATIONS

1. **MRS Fall Meeting** Boston, MA 2018
Talk: "Stretchable Nanolasing from Hybrid Quadrupole Plasmons"
2. **Gordon Conference** Waterville Valley, NH 2018
Poster: "Structural Engineering in Plasmon Nanolasers"
3. **Nanjing University Tiandi Symposium** Nanjing, China 2017
Invited talk: "Structural Engineering in Plasmon Nanolasers"
4. **MRS Fall Meeting** Boston, MA 2017
Talk: "Band-edge Engineering for Controlled Multi-modal Nanolasing in Plasmonic Superlattices"
5. **Northwestern SPIE-MRSEC Student Seminar Series** Evanston, IL 2017
Invited talk: "Structural Engineering in Plasmon Nanolasers"
6. **OSA Incubator on Science & Applications of Nanolasers** Washington, DC 2016
Invited talk: "Lasing from Plasmonic Nanocavity Arrays"
7. **Gordon Conference** Newry, ME 2016
Poster: "Band-edge Engineering in Hierarchical Plasmonic Nanolasers"
8. **APS March Meeting** San Antonio, TX 2015
Poster: "Superlattice Plasmons in Finite Nanoparticle Arrays"

PROFICIENCIES AND SKILLS

Nanofabrication

Bench-top Multi-scale Pattern Transferring, Phase-shift Photolithography, Vapor Deposition, Reactive Ion Etching, Deep Reactive Ion Etching, Scanning Electron Microscopy

Optical characterization

Optical Set-up, Lasing Detection, Time-resolved Photoluminescence, Angle-resolved Spectroscopy, Dark-field Microscopy

Modeling and Computation

Finite-Difference Time-Domain (FDTD) Modeling, COMSOL Multiphysics, MATLAB, Adobe Illustrator, Blender 3D Software

LEADERSHIP POSITIONS

- 2016-18 Laser Instrument Manager, the Odom Group
- 2015-17 Rotational-stage Spectrometer Manager, the Odom Group
- 2016 Management for Scientists and Engineers Certificate, Northwestern University, Kellogg School of Management

2014-16 McCormick Graduate Leadership Council, Professional Development Co-chair

2014-15 Cleanroom Manager, the Odom Group

REFERENCE CONTACTS

Prof. Teri W. Odom

Department of Chemistry, Department of Materials Science and Engineering, Northwestern University

Email: todom@northwestern.edu

Phone: 01-847-491-7674

Prof. George C. Schatz

Department of Chemistry, Department of Biological Engineering, Northwestern University

Email: g-schatz@northwestern.edu

Phone: 01-847-491-5657